ORNL-2632
C-84 – Reactors–Special Features
of Aircraft Reactors
M-3679 (22nd ed.)

METALLURGY DIVISION

ANNUAL PROGRESS REPORT

FOR PERIOD ENDING OCTOBER 10, 1958

OAK RIDGE NATIONAL LABORATORY
operated by
UNION CARBIDE CORPORATION
for the
U.S. ATOMIC ENERGY COMMISSION

[redacted]

ORNL-2632
C-84 -- Reactors--Special Features
of Aircraft Reactors
M-3679 (22nd ed.)

This document consists of 220 pages.

Copy 126 of 292 copies. Series A.

Contract No. W-7405-eng-26

METALLURGY DIVISION

ANNUAL PROGRESS REPORT

for Period Ending October 10, 1958

J. H. Frye, Jr., Director
W. D. Manly, Associate Director
J. E. Cunningham, Assistant Director

DATE ISSUED

DEC 1 1958

OAK RIDGE NATIONAL LABORATORY
Oak Ridge, Tennessee
operated by
UNION CARBIDE CORPORATION
for the
U. S. ATOMIC ENERGY COMMISSION

[redacted]

[redacted]

CONTENTS

[redacted]

[redacted]

REACTOR METALLURGY

[redacted]

APPLIED METALLURGY

[redacted]

METALLURGY DIVISION ANNUAL PROGRESS REPORT

SUMMARY

FUNDAMENTAL METALLURGY

Physicometallurgical Research

The reorientations which take place during deformation have been studied in aluminum rods, cold-swaged for varying amounts from an initial orientation of <001>, 88% <111>–12% <001>, or <118>. In all instances a major <001> texture developed due to room-temperature recrystallization after approximately 50 to 70% reductions in area. The <001> orientation was observed to be relatively stable, and some material retained this texture after a reduction of 99%. A tendency for movement away from the <111> position was noted after a reduction of 96.1% in the specimen containing a strong initial <111> texture.

In cerium a study was made of the reversion of the hexagonal close-packed phase to the face-centered cubic (fcc) structure at 388°K. No isothermal transformation was found, but it was noted that the relief of transformation stresses caused a small amount of additional transformation. Metallic clicks were detected in the temperature range (95–77°K) where the fcc-to-fcc′ transformation occurs, which is usually interpreted as resulting from rapid, cooperative atom movements during the transformation. Thermal cycling cerium 100 times between 293 and 77°K was found to produce large amounts of the hexagonal phase and to cause suppression of the collapsed cubic phase upon further cooling.

The low-temperature specific heats of group IVA elements, titanium and zirconium, have been measured to precisions better than 1%. The heat capacity in each case was found to be of the form $aT + bT^3$ over the range 1.2 to 4.5°K with a relatively high density of states observed in each of these transition elements. Measurements of the electronic specific heat of indium-zirconium alloys have shown that indium increases the density of states in a nearly linear manner from 0 to 8 at. % In. The effect of indium on the Debye temperature was a gradual decrease with increased alloying. Physical and chemical impurities introduced into zirconium by arc casting or quenching through the allotropic transition did not have any measurable effect on the specific heat.

In the zirconium-gallium system, supporting evidence has been found for the intermediate phase Zr_3Ga and the eutectic, liquid $\rightleftharpoons Zr_5Ga_3 + \beta$, reported by Anderko. The solubility of gallium in β-zirconium is approximately one-third that of aluminum or indium in β-zirconium.

Vapor pressure measurements of zirconium-cadmium alloys show that the free energy of formation of the beta phase can be represented within the accuracy of the experiments by

$$X(-2780)\,R + RT[X \ln X + (1 - X) \ln (1 - X) + 2.22X] ,$$

where X is the mole fraction of cadmium in the range $0 < X < 0.1$ and the temperature is in the range 1175 to 1325°K. It should be noted in the above expression that the reaction between zirconium and cadmium to form the beta alloy is exothermic and that the entropy observed is less than that for ideal mixing. Similar results have not yet been obtained for the alpha phase, although the pressure measurements have shown that diffusion of cadmium in α-zirconium is very much slower than the diffusion in β-zirconium.

X-Ray Diffraction

In addition to the normal service activities of the X-Ray Laboratory, progress in the more special problems of high-temperature structures, transition-metal scattering factors, and aging behavior in zirconium-columbium alloys is reported.

More accurate methods of temperature estimation have been used with the Laboratory's high-temperature x-ray diffraction apparatus, enabling the thermal expansion curves for Zircaloy-2 and a Cu–15 at. % Al alloy to be measured.

Relative scattering factors of $3d$ transition elements are being determined to check recent results suggesting abnormally low $3d$ electron concentrations in a metallic α-iron and chromium.

Single-crystal aging experiments with a series of zirconium-columbium alloys have shown the following: the structure of the metastable omega phase formed on low-temperature aging of a beta-quenched alloy is hexagonal, aging at somewhat higher temperature causes reversion of the omega phase, and the

[redacted]

$\beta \rightarrow \beta_1 + \beta_2$ dissociation in the miscibility gap of the zirconium-columbium system proceeds rapidly in the case of the 25% Cb alloy without apparent formation of intermediate structures.

Microstresses in Crystals

The x-ray diffraction maxima of Cu_2O surface films grown on copper single crystals have been detected for films as thin as 188 Å. A theory has been developed to interpret the shapes of these maxima in terms of the film thickness and the imperfections present in the crystal lattice. First efforts to fit theory with experiment appear promising.

In an effort to understand the effect of reactor radiation on the alloy Cu–16 at. % Al, diffuse x-ray scattering measurements have been made before and after exposure in the reactor. In both cases, a significant degree of short-range order was observed. A model for the short-range-order arrangement has been devised which agrees well with experiment.

The diffraction theory for disordered substitutional solid solutions containing atoms of different sizes has been modified to give a simpler and more accurate expression for the size-effect diffuse scattering. A comparison of the theory with diffuse scattering measurements for Cu_3Au shows good agreement.

High-Temperature Reactions

Studies have been made of the optical absorption spectrum of the nitrate ion in a large number of fused salt media. These measurements show that the lowest-energy electronic transition is quite sensitive to the electrostatic fields of neighboring ions, both cations and anions.

Progress has been made on the problem of the quantitative analysis of spectra consisting of broad overlapping bands. Present work indicates the skew-symmetric Gaussian as a proper function for fitting.

Measurements of the densities of a large number of fused salt solutions have been made.

The nuclear magnetic resonance of the fluoride ion has been measured in several inorganic fluoride melts.

Studies of the effect which the mode of diffusion has on the protectiveness of oxide films were continued with electron-optical studies of the oxidation of vanadium and titanium.

The development of thickness inhomogeneities in thin-film oxidation has been studied on selected faces of single crystals of copper.

Preliminary work is reported on the effect of nuclear radiation on the oxidation of columbium.

HRP METALLURGY

Zirconium-columbium-X ternary alloys have shown promise in having an in-pile corrosion resistance to uranyl sulfate solutions superior to that of Zircaloy-2. The transformation kinetics and morphology of a number of Zr–15% Cb–X and Zr–20% Cb–X alloys have been determined. The transformation products and mechanisms have been partially identified. The age hardening of beta-quenched material was found to be due to the formation of omega phase, analogous to the omega phase of the β-titanium alloys. The martensitic Widmanstatten platelet phase observed in beta-quenched material was identified as having a body-centered tetragonal structure and to exist only on the (100) planes of the matrix. Both the Widmanstätten phase and the omega phase will regress to form the beta phase on heating to temperatures above that of their formation. The most potent ternary alloying element for delaying the formation of omega phase is molybdenum, the addition of 2 wt % Mo delaying the reaction for approximately 4 hr at 400°C, permitting multipass welding of beta-quenched plate.

In-pile corrosion studies of the Zr-Cb-X alloys have shown that the optimum columbium content is 15 wt % Cb, that ½% Cu is the most potent ternary addition for improving the corrosion resistance, followed by Pd, Mo, Pt, Fe, Ni, Cr, and V, and that heat treatment to produce stable structures with corresponding high strengths and moderate ductilities decreases the corrosion resistance of the ternary alloys.

The $\alpha/(\alpha + \beta)$ temperatures of Zircaloy-2 have been determined by resistance-temperature measurements, being 815°C for material containing 40 to 50 ppm H_2 and 832°C for material with less than 5 ppm H_2.

In a study of the fabrication variables of Zircaloy-2 it was demonstrated that the anisotropy of plate material can be shown by an analysis of the size and shape of cross sections of fractured round tensile specimens, but not from the conventional tensile values. The data determined (incomplete) permit the conclusion that there is

[redacted]

no justification as yet for modifying the presently used HRP fabrication schedule.

With two plates, studied in considerable detail, the results of the fracture shape studies were confirmed by standard impact tests. It was shown that in an impact test the notch orientation is more critical than the specimen orientation. Many of the usual rules of thumb developed for steels do not hold when applied to Zircaloy-2, the presence or absence of shear lip being dependent upon notch orientation rather than upon break temperature or the transition location. Ductile-appearing fractures were obtained which had required less fracture energy than had other brittle-appearing fractures, orientation again seeming to be the most critical variable.

By slant polishing surface layers of hydride on Zircaloy-2 specimens, the hydrided needles reported by other investigators to exist within the alpha grains immediately under the hydride surface layer were found to be lenticular twins caused by the deformation occurring in the formation of the surface hydride.

Nickel was successfully deposited from a Kanigen bath on anodized Zircaloy-2 for edge protection of corrosion samples. However, no deposits were made successfully on the rather heavy air-formed oxides. Hydriding studies of Zircaloy-2 have also shown that the hydride forms in patches on the surface at temperatures of 400°C and less, instead of occurring as a uniform layer.

In measuring the mechanical properties of Ti A-40, an irregularity in the temperature dependence of impact strength was observed. This behavior is thought to be due to a strain-aging phenomenon; however, this property appears to be independent of long-time aging.

Creep tests of 4800 hr for Ti A-40 and A-110AT and 7200 hr for Zircaloy-2 indicate that a gradual transition occurs from second- to third-stage creep.

Studies of the changes in mechanical properties as a result of exposure to fissioning uranyl sulfate in high-temperature in-pile loops have been made of various materials of interest to the HRP. With both crystal-bar zirconium and zirconium alloys, only very small changes in either tensile or impact properties were noted at fast-neutron exposures of up to 10^{19} *nvt*. Small increases were found in yield points, with small decreases in elongation and, primarily, in the uniform elongation. Titanium alloys have shown larger changes than have the zirconium alloys but they are still small. Small increases were noted in both yield and tensile strength, with a decrease in necking elongation. With neither material were any changes noted in impact strength.

Titanium welds of quality comparable with those made in a dry box have been prepared in air by using a tungsten-arc inert-gas torch. Special requirements include the use of a cup of sufficient size to cover molten metal and that portion of base metal heated to high temperatures. Also, the surface of each weld pass must be conditioned by grinding to remove any surface oxidation prior to succeeding passes.

The quality of titanium welds prepared with root inserts of various geometries was evaluated. Root inserts of square cross section gave welds of acceptable hardness but contained porosity of unknown origin and had an over-all quality inferior to hand-fed wire welds.

The properties of weldments in Ti A-110AT alloy have been found to be dependent on the distribution of a grain-boundary phase present in the base metal. Acceptable welds have been made in Ti A-110AT pipe stock.

The possibility of torch-brazing titanium has been examined by using silver, platinum, and gold. The protective properties of the fluxes studied were lost at temperatures below those necessary to melt the filler wire.

Air welds comparable in properties with those made in a dry box have been made on Zircaloy-2 under the conditions listed above for titanium.

In work carried out by subcontract, it has been shown that if titanium or zirconium or their alloys are fractured in an atmosphere of high-pressure oxygen, ignition of and complete consumption of the sample will occur. In pure oxygen under dynamic conditions, pressures as low as 50 psi are sufficient for the ignition. Data are presented showing that the limiting conditions vary with oxygen pressure, total pressure, and velocity. Once ignition occurs, much lower pressures are sufficient to sustain it. No ignition could be made to occur under a liquid surface. It has been shown that similar reactions occur between molten zirconium and water and with oxygenated uranyl sulfate solution.

[redacted]

REACTOR METALLURGY

Dynamic Corrosion and Inspection

In the present concept of the ORNL Gas-Cooled Reactor, one important technical consideration is the compatibility of the cooling gas with the graphite moderator, the canning material used in the fuel element, and the other structural components. Since helium, an inert gas, was selected for the cooling medium, the main concern is with reactions between contaminants in the helium and the component parts. Thus a program was initiated to study the amounts and types of gases evolved from various grades of graphite when heated to the service temperature and to study the possible reactions between these contaminants and the structural metals. Equipment was developed to permit such studies to be conducted under static and dynamic conditions of gas flow.

Analyses of the gases evolved during these tests show that substantial amounts of hydrogen, nitrogen, carbon dioxide, and water vapor are released from the graphite. No significant differences were noted in the amounts released or in the rate of attack on the metal specimens between the static and dynamic types of tests. As would be expected, zirconium and zirconium-base alloys were grossly attacked by the contaminated helium, whereas the nickel-base alloys and iron-base alloys showed little attack.

The use of a molten salt as a carrier for fuel in a homogeneous circulating-fluid reactor requires structural alloys so resistant to corrosion attack of the salt that a useful operating life of 20 years can be achieved. Inconel, a well-known high-temperature alloy, has been extensively studied in the past, and although the rate at which it is corroded renders it unattractive for structural purposes, it remains a valuable material for studying corrosion mechanisms. A number of salt mixtures, based on both zirconium and beryllium fluorides, have been evaluated in terms of such variables as temperature, time, and flow rate. An alloy developed by the Metallurgy Division, INOR-8, has been found to be very resistant to attack by the fused salt systems at test times approaching a year.

The careful screening of all metal, particularly tubing, by nondestructive testing techniques has resulted in the rejection of material which would cause failure in operation or would unnecessarily complicate post-test analysis. Thus a considerable saving in effort and expense has been achieved. Also, a variety of fabricated test parts and assemblies were inspected before test to avoid fractures resulting from defective parts. Welded joints received the major share of attention. Specifications for various welding designs have been evolved based on experience and failure analyses.

General Corrosion

Various experimental techniques have been studied in an effort to determine which methods are most effective in reducing the nitrogen and oxygen content of lithium metal.

Static corrosion testing of a variety of materials of interest has been conducted in lithium at elevated temperatures. Materials tested include yttrium, beryllium, columbium, zirconium-columbium alloys, and a variety of refractory-metal-base brazing alloys. Zirconium- and titanium-base brazing alloys appear to have good corrosion resistance to 1700°F lithium in 500-hr static tests.

A series of molybdenum-lithium seesaw furnace tests has been conducted at hot-zone temperatures of 1700, 1800, and 1900°F for periods of 100 and 500 hr. One seesaw test of lithium in a columbium system has also been made.

Two columbium-lithium thermal-convection loops have been tested in the stainless steel vacuum chamber, and the results are given.

A summary of the solution-rate studies of various materials in lithium conducted by the Nuclear Development Corporation of America on a subcontract is included.

Several cermet-metal joints formed by fusing or brazing of TiC-Ni, WC-Co, and $WTiC_2$-Co cermets to metals were found to be corrosion resistant to molten sodium and NaF-ZrF_4-UF_4 (50-46-4 mole %, fuel 30) in 100-hr exposures at 1500°F. These cermet-metal joints were developed to permit these types of cermets to be jointed to Inconel by brazing.

An examination was made of the rare-earth-oxide ceramic cylinders that constituted a prototype ART control rod and that were exposed to molten sodium for 3000 hr in a rigorous test of the control rod and its drive system. Some of the ceramic pieces were broken as a result of rather large thermal changes. There was no detectable corrosion of the ceramic cylinders by the sodium. Despite the breakage of some of the cylinders, the rod would have been satisfactory for ART operation because there was no change in the location of the cylinders.

[redacted]

Preliminary carburization tests involving NaF-ZrF_4-UF_4 (50-46-4 mole %, fuel 30), Inconel, and graphite indicate that the Inconel does not appear to carburize in 1000 hr in thermal-convection loops with hot legs at 1300°F. However, a thin Cr_3C_2 film formed on a graphite specimen in the hot leg of a thermal-convection loop.

Inconel and INOR-8 tensile specimens were carburized in the sodium-graphite system and then tensile- and creep-tested at room and elevated temperatures to determine what detrimental effects, if any, carburization has on the mechanical properties of these materials.

A comprehensive test involving INOR-8, graphite, and fuel 130 has been terminated after operation for 2000 hr at 1300°F. From mechanical tests and chemical analyses conducted on specimens from this test, it appears that the INOR-8 exposed to fuel 130 in contact with bare graphite is carburized enough to slightly alter the mechanical properties of the material.

Uranium in the form of UO_2 precipitated in appreciable quantities from LiF-BeF_2-UF_4 (62-37-1 mole %, fuel 130) in contact with graphite at 1300°F under a vacuum of <0.1 μ. This occurred even though the graphite specimens had been degassed well, flooded with argon, and subsequently exposed to room atmosphere for less than 3 min prior to testing.

Silver-base brazing alloys had limited corrosion resistance to fuel 130 in 500-hr static tests at 1300°F. A gold-base alloy (75 Au–20 Cu–5 Ag) showed excellent resistance to fuel 130 under the same conditions.

Fabrication

The production of seamless columbium tubing for corrosion testing and fabrication of corrosion loops is now well understood. Techniques for the co-extrusion of columbium and heat-resistant alloys are being studied. The reactions of columbium with gases at low pressures and high temperatures are being determined. The protection of columbium structures in air by braze coating with nickel-base alloys has been studied. The effects of heat treatment on the cold workability of cast columbium were evaluated. Alloying additions of elements known to form very stable oxides have been proposed for improving cold fabricability. Alloys with small additions of these elements are being studied.

The process for the production of high-purity yttrium metal was carried to a reasonable degree of perfection on a laboratory scale. Evaluation of material produced indicated that the process should be capable of quantity production of high-purity metal. A facility for the production of 20-lb ingots has been installed and is undergoing test operation. The physical properties of high-purity yttrium and improved procedures for hydriding the metal are being studied.

The selection of the fuel capsule material for the GCR-2 was confirmed by extensive surveys and tests. The reactions of type 304 stainless steel with impure argon and with CO_2 are being studied in detail. The fabricability of seamless tubing from an iron-aluminum alloy (DB-2) was investigated, with discouraging results. Control rod materials for the GCR-2 were surveyed, and a proposed materials choice and control rod design were recommended.

The specified composition of INOR-8 was confirmed by extensive metallographic and mechanical property investigation of a series of alloys similar to INOR-8. The production of INOR-8 products, including rod, sheet, heavy plate, and seamless tubing, has been accomplished satisfactorily.

Liquid-Metal Research

In an effort to ascertain the principles governing the mass transfer of container materials exposed to liquid-metal coolants, both theoretical and experimental studies have been made. Equations have been derived in the theoretical studies which relate the rate-controlling step of the mass transfer process to the distribution of corrosive attack. Equations were also derived for the maximum stress at the base of a crystal under both static and turbulent flow conditions. A correlation was made of existing data on self-diffusion coefficients of liquid metals.

The experimental studies included the investigation of the factors that govern the rate of mass transfer of benzoic acid in water in a pump loop with a temperature gradient. Analysis of the data showed that the mass transfer rate was very sensitive to changes in the flow rate, but rather insensitive to temperature changes as large as 40°C. The over-all rate of mass transfer was controlled by both hot-zone and cold-zone processes.

A thermal-convection loop for mass transfer experiments under controlled conditions has been designed and constructed.

Nondestructive Test Development

A new, improved transistorized version of the metal identification meter has been developed

[redacted]

which is more versatile and portable than the former instrument.

Studies on the eddy-current measurement of cladding thickness on MTR-type fuel plates have revealed the causes and a possible solution to the problem of measurement discrepancies. A new technique has been developed for measuring the thickness of a nonmagnetic metallic cladding on a ferromagnetic base.

Studies of the eddy-current inspection of GCR fuel-capsule tubing with developed equipment indicate that an eddy-current inspection may suffice as a primary inspection method. The results of the study will be used in formulating improved inspection procedure specifications.

Radiographic images formed by an x-ray-sensitive closed-circuit television system indicate that the system has development promise for high-resolution remote x-ray viewing.

An ultrasonic technique has been developed for measuring liquid flow rates in small tubing.

Investigations are being made on the application of pulse-echo ultrasonic techniques to the inspection of weldments, and a considerable amount of data on the interpretation of defect indications has been assimilated. Although defects in a 4-in.-thick mild steel test weld were successfully detected and located, difficulty has been encountered in austenitic stainless steel welds because of severe ultrasonic attenuation.

A program of study of the attenuation of ultrasound in reactor construction materials has been initiated. Equipment has been procured, measuring techniques have been established, and a small amount of data has been assimilated on austenitic stainless steels, martensitic stainless steel, carbon steel, and Zircaloy-2. These studies are producing a better understanding of the transmission of ultrasound in metals and will facilitate the development of improved inspection techniques.

An improved technique has been developed for inspecting thin sections by the ultrasonic "through-transmission" method. The new technique allows inspection with one transducer where two were formerly required. Basic studies of the nature of ultrasonic vibrational modes in elastic plate structures are revealing many new avenues for developing simplified inspection techniques for the detection of laminar discontinuities in thin sheet and poor-quality bonding in clad structures.

Mechanical Properties

Cylinders of type 304 stainless steel were studied to determine the factors which would limit the mechanical life of fuel elements designed for the Gas-Cooled Reactor. Buckling due to creep-induced structural instabilities was found to be a critical problem.

The mechanical properties of INOR-8 from room temperature to 1600°F are under study. The extrapolation of short-time data to values for 10 and 20 years predict strength values approximating that of type 316 stainless steel at the operating temperature. No marked deterioration in strength properties has been noted in tests where the metal is exposed to a fused-salt environment.

Equipment was designed and built to permit the testing of materials at temperatures above 1800°F. Further study of Inconel at 1500°F revealed that creep rates for the multiaxial-stress state can be predicted from uniaxial-stress tests. A correlation between thermal fatigue and mechanical fatigue was found to exist at elevated temperatures on the basis of the plastic strain induced per cycle. Failure can be predicted with the use of a simple equation; however, structural and test variables have a marked effect on the constants used in this relationship.

Welding and Brazing

The progress of the Welding and Brazing Group during the past year has been published in the Reactor Projects Division progress and design reports and in various topical reports. The investigations have been highly diversified in scope and cannot be summarized under a general subject. Abstracts covering the pertinent results of each study are presented under individual headings.

APPLIED METALLURGY

Process Metallurgy

The major effort during the past year has been centered on the development of new core components for the Army Package Power Reactor, investigation of suitable alloy and powder-metallurgy techniques for manufacturing plate-type aluminum fuel elements containing uranium enriched to 20% U^{235}, and metallurgical support work for the Maritime Reactors Branch in connection with the reactor core for the NS "Savannah."

[redacted]

The APPR development has been aimed primarily at improvements in future core loadings for the reactor at Fort Belvoir, Virginia, as well as for future reactors of this general type. Potential irradiation damage to the boron-iron absorber section of the control rod has spurred the development of a 38 wt % dispersion of Eu_2O_3 in stainless steel. The previously reported reaction between the europium oxide and the silicon in stainless steel was prevented by the use of chromium with less than 0.003% silicon. Consequently, it was necessary to prepare the powder mixture with elemental iron, nickel, and chromium powders instead of prealloyed stainless steel powder.

The buildup of gamma activity in the primary loop system of APPR-1 has been generally traced to cobalt, a tramp constituent in the stainless steel. This condition stimulated procurement of an austenitic stainless steel with a cobalt content of 0.005 wt % for the second core loading of APPR-1. It was demonstrated that, by exercising careful control in selection of materials, a low-cobalt type 304L stainless steel can be obtained economically.

Although it is desirable to double the boron content in fuel elements for core II of APPR-1, studies of the effect of this increase on the reaction and diffusion of boron into the protective cladding of the plate indicated that neither B_4C, ZrB, nor BN is satisfactory as a burnable-poison compound. Additional investigations aimed at incorporating the boron in the fuel core by means of a master-alloy additive consisting of stainless steel powder containing 0.25 wt % of highly enriched boron revealed that significant boron losses occurred during sintering under hydrogen. Results obtained from vacuum and inert-atmosphere sintering indicated that either negligible or no losses occurred.

In the development and selection of an optimum materials combination for the plate-type aluminum research-reactor fuel element requiring 20% enriched uranium, it was demonstrated that a 35 to 48 wt % U–Al alloy containing 3 wt % silicon was suitable but rather expensive. A powder-metallurgical method in which UC_2 is dispersed in aluminum was successfully developed but has the disadvantage that, in the event of a cladding failure, the fuel mixture will corrode catastrophically. Fuel element fabrication procedures have been developed for incorporating 37 vol % U_3O_8 in aluminum by powder-metallurgy techniques, roll cladding into composite plates, and brazing into fuel elements. A test element, containing 195 g of U^{235} and approximately 1200 g of U_3O_8, is currently under test in the active lattice of the MTR.

Other investigations aimed at optimization of the plate-type aluminum fuel element included an examination of surface contamination of composite plates by uranium, the utility of high-strength aluminum as a substitute for type 1100, and the development of a cheap but reliable method for mechanically joining the plates into fuel assemblies. If care is exercised during cleaning and storage of aluminum fuel-plate composites, it appears possible to limit uranium contamination on the surfaces to approximately 0.4 ppm. Testing of fuel elements in which types 5050, 6951, and 6061 aluminum were substituted for type 1100 aluminum revealed that greater resistance to pressure differentials occurs and that superior metal-to-water ratios and higher fuel loadings are possible with such elements. A mechanical joining method in which the plates are joined to the side plates in one operation appears economically attractive. Subsize fuel elements have been joined in this manner and have a joint strength of 200 lb per lineal inch.

As a result of development reported previously, a full loading of enriched fuel elements for the spherical core of the Tower Shielding Reactor was successfully produced.

Postirradiation examination of an MTR-type fuel element containing a 10 wt % Pu–Al alloy prepared at ORNL with the cooperation of LASL revealed no signs of gross irradiation damage.

Support of the Maritime Ship Reactor program has been primarily directed at assistance to MRB in evaluation of problems encountered by Babcock & Wilcox in the development of fuel components for the NS "Savannah." Methods for welding caps to the fuel tubes as well as for brazing the tubes into bundles were investigated. It was demonstrated that closures made by using inverted cups or plugs were equally sound for encapsulating the UO_2 pellets within the tubes. Nicrobraz No. 50 brazing alloy also appeared to be an acceptable selection for joining tubes into bundles.

Two methods for incorporating the burnable poison into the fuel element were examined. The primary method of utilizing wrought boron–stainless steel tubing is subject to the possibility of boron losses during heat treatments in hydrogen. Preliminary work indicated that annealing either in vacuum or argon was effective in maintaining the boron level.

[redacted]

[redacted]

Attempts to incorporate boron in the UO_2 pellet met with little success; this is discussed in detail in the "Ceramics Research" section of this report.

Advanced Engineering and Development of Reactor Materials

A program for studying the effects of irradiation on reactor fuels has been initiated. The first phase is a study of the behavior of stainless steel–uranium dioxide dispersion fuels as a function of burnup and irradiation temperature. Duplicate specimens will be irradiated at low temperatures and subjected to postirradiation annealing treatments. Comparison of the data will establish the extent to which low-temperature irradiations can be used to indicate the effects of irradiation at high temperature. Fabrication techniques are being developed for miniature fuel specimens. An instrumented capsule for high-temperature irradiation in the assigned ORR facility is being designed and tested.

Fuel element decladding studies to assist in recovery of uranium from spent fuels have shown that zirconium or Zircaloy-2 cladding can be penetrated intergranularly with magnesium. The brittleness of the penetrated material allows the cladding to be removed by mechanical methods. Chemical methods of removal were not conclusive.

A survey of potential solid moderators was completed. Moderating ratios and neutron ages were calculated and a literature survey made on some of the promising hydrides.

Compatibility and growth studies on dispersions of U_3O_8 in aluminum were continued; U_3O_8 appears to react with aluminum at 600°C in the following step reaction:

$$3U_3O_8 + 4Al = 9UO_2 + 2Al_2O_3$$

$$3UO_2 + 16Al = 3UAl_4 + 2Al_2O_3$$

The reaction of UO_2 with aluminum is the same as in step 2 of the U_3O_8-Al reaction. The ultimate growth of U_3O_8-Al fuel plates after 3000 hr at 600°C is ~4%. Growth of 20 to 26% was observed in UO_2-Al fuel plates after 24 hr at 600°C. The growth rate of UO_2-Al plates decreases with temperature, but the ultimate growth may be greater. Pressed UO_2-Al compacts showed an average 76% reaction after 80 hr of vacuum heat treatment at 600°C.

Ceramics Research

Incorporation of selected additives in high-density BeO was investigated. A number of borides were synthesized and incorporated in BeO, and the stability of the resulting ceramic bodies was then studied in air at 1300°C. Several additives designed to enhance densification were studied and reported. Investigations into necessary hot-pressing temperatures to obtain very high densities were carried out.

An explanation of the theory and procedures of forming UO_2 pieces for the Gas-Cooled Reactor Program was made. Typical types of failures in fabrication processes are described and explained. Studies on the cold pressing of GCR slugs showed that pressures of 7500 psi and a length-to-diameter ratio of ~0.65 yield a slug with a green density of ~48%. Sintering temperatures of 1750°C, with a soaking period of 1 hr, were sufficient to attain densities desired. The optimum atmosphere for sintering was a mixture of hydrogen and nitrogen in a ratio of 7:3. General specifications for the UO_2 powder, together with two general flowsheets for its preparation, are given. Thermogravimetric and differential thermal analyses were used as a control in the testing of the UO_2 powders. Fabrication of GCR irradiation test specimens is in progress. A method to monitor pellet temperature during irradiation by incorporating metal wires of widely different melting points appears attractive. Gold, nickel, vanadium, platinum, and columbium were selected for this purpose, but platinum was rejected because it apparently reacts with UO_2 under the established sintering conditions.

It has been shown that contamination of powdered ThO_2 at 1600°C by alumina containers is negligible. Investigations have not revealed the reason for lumping in the calcined thoria product.

Possible procedures for controlling several parameters in the fabrication of Si-SiC fuel elements are given. Bars of Si-SiC with a loading of 0.44 and 0.88 g of fully enriched UO_2 were forwarded for irradiation in the ORR. Samples with fuel loadings as high as 10% have been successfully prepared.

Conclusions on the sintering and densities of 13 rare-earth oxides are given.

[redacted]

[redacted]

Metallography

In addition to handling the bulk of the metallographic work required in support of the various research and development programs under way, some effort of the section is directed toward devising new equipment and metallographic techniques to aid the over-all Laboratory program. In this regard, an attempt is being made to utilize color in electron microscopy and to correlate patterns observed on anodized aluminum surfaces with the topography of the base metal by electron microscopy. Thermal effects on the microstructure and the expansion and contraction of metals are under investigation by means of hot- and cold-stage microscopy and dilatometry. Another technique involves the use of an ultrasonic chisel to remove inclusions from the microstructure for subsequent identification. Data are reported on failure analysis, stress-corrosion cracking, molten-salt corrosion, and other related phenomena encountered in the performance testing of equipment for the Homogeneous, Gas-Cooled, Molten-Salt, and Aircraft-Nuclear Reactor Programs.

[redacted]

FUNDAMENTAL METALLURGY

PHYSICOMETALLURGICAL RESEARCH

L. K. Jetter

C. J. McHargue J. O. Betterton, Jr. G. D. Kneip, Jr.

STRUCTURE OF METALS

C. J. McHargue

Changes in Orientation During Deformation of Aluminum Rod

One of the areas of investigation needed in order to test the validity of assumptions concerning deformation texture formation is the relative stability of various orientations under the influence of an applied stress. For the most part this problem has been approached by observing the change in orientation of single crystals with different initial orientations during cold rolling. However, there appear to be no data concerning reorientations which occur during essentially uniaxial flow of face-centered cubic metal wires or rods. Although the reorientation of single crystals loaded in tension is well known, the movements would be expected to differ in the forming of wires and rods because of their circular array of radial compressive stresses resulting from the die walls or the rolls. Moreover, it is necessary for a circular cross section to be retained, whereas the cross section of a single crystal pulled in tension is often observed to become elliptical due to the anisotropy of the flow mechanism.

The results of a previous study[1] of the preferred orientation developed in aluminum rod under different fabricating conditions showed that a variety of as-extruded textures could be obtained. A study was made of the change in orientation during deformation by subjecting polycrystalline aluminum rods with varying initial orientations to a series of reductions by swaging at room temperature. Thus far, rods with initial orientations of near <001>, <118>, and 88% <111> – 12% <001> have been examined.

Initial Orientation, <001>. – Back-reflection Laue x-ray photographs showed that aluminum ingots cast under the conditions commonly used by the Melting and Casting Section have a preferred orientation which can be described as <001>. Figure 1*a* shows that 18 of 21 grains in the cross section examined had a <001> direction within 20° of the longitudinal axis. The three deviating grains were oriented near <133>. The orientations of specimens taken from a rod swaged from this ingot after 20, 40, 60, 70, 80, 90, 95, and 99% reductions in area are shown in Fig. 1*b* to 1*i*.

For 20 and 40% reductions in area there is little change in the material oriented near <001>. There is a peak in the axis density 5 to 8° from <001> which corresponds to a group of five grains in the ingot cross-section area examined. The center of this peak moves toward <001> with increasing deformation. The movement of the group of grains initially near <133> is shown on the stereographic projection of Fig. 2. A single crystal with such an initial orientation would be expected to move toward <112> along path I when deforming under a simple tensile stress. If, due to restraints, duplex slip occurs on the two most favored systems, the path of reorientation would be that marked II. The concentrations after 20 and 40% reduction in area lie near the path for duplex slip.

It is obvious, of course, that the stress system producing the deformation was much more complicated than a simple tensile stress. The work of Vargha and Wassermann[2] and of Barrett and Levenson[3] seems to show that the major flow component is more important in determining textures than the manner in which the stress is applied. Thus in swaging there is a secondary tensile stress along the rod axis, although the deformation is caused by radial compressive stresses. During the early stages of deformation the radial compressive stresses probably have little influence toward developing a radial texture. The reorientation of the group of grains shown in Fig. 2 can be accounted for by duplex slip, with slightly more slip occurring on the most favored system, path I. The onset of duplex slip inside the unit triangle could be caused by the restraints imposed by neighboring grains or by the restraints imposed by the dies in maintaining a circular cross section.

---

[1] C. J. McHargue and L. K. Jetter, *Met. Ann. Prog. Rep. Oct. 10, 1957*, ORNL-2422, p 212.

[2] G. V. Vargha and G. Wassermann, *Z. Metallk.* **25**, 310 (1933).

[3] C. S. Barrett and L. H. Levenson, *Trans. Am. Inst. Mining Met. Engrs.* **135**, 327 (1939).

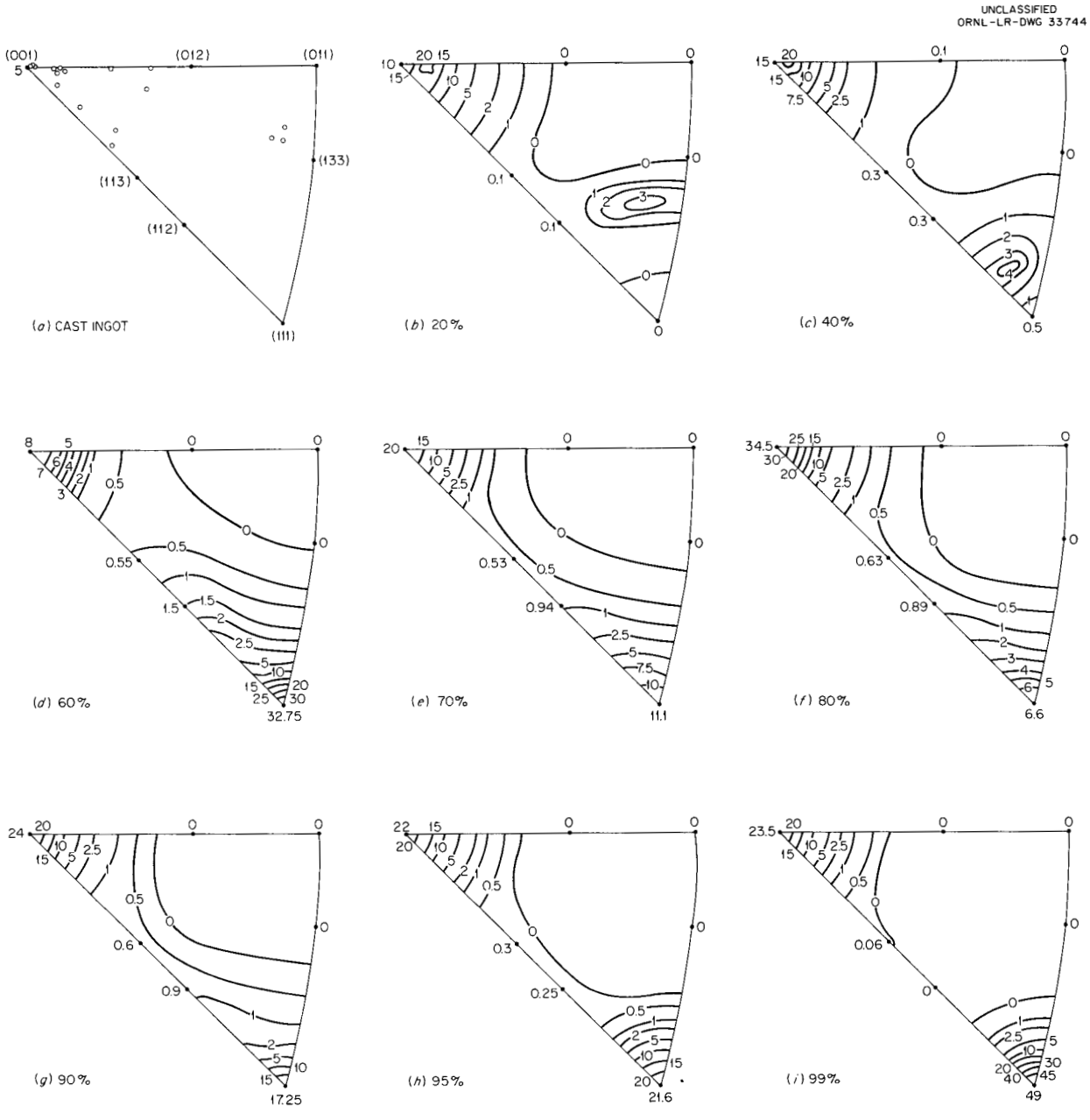

Fig. 1. Axis Distribution Charts for Aluminum Ingot Swaged to Indicated Reduction in Area.

After a reduction of 60% there is a well-developed <111> texture component, as well as the <001> texture. There is also considerable material with orientations on the <110> zone between <112> and <111>. It was found that 38% of the volume was associated with the <001> component and that 62% was in the <112> – <111> orientations.

Further deformation resulted in a decrease in the intensity of the peak at <111> and a decrease (to 42% after 70% reduction in area) in the volume of material associated with the component. There was a corresponding increase in the <001> component. These changes were attributed to the onset of room-temperature recrystallization for reductions between 60 and 70%. There was metallographic evidence of recrystallized grains with the <001> orientation, as well as fragments of original <001> grains. The amount of <001> component increased

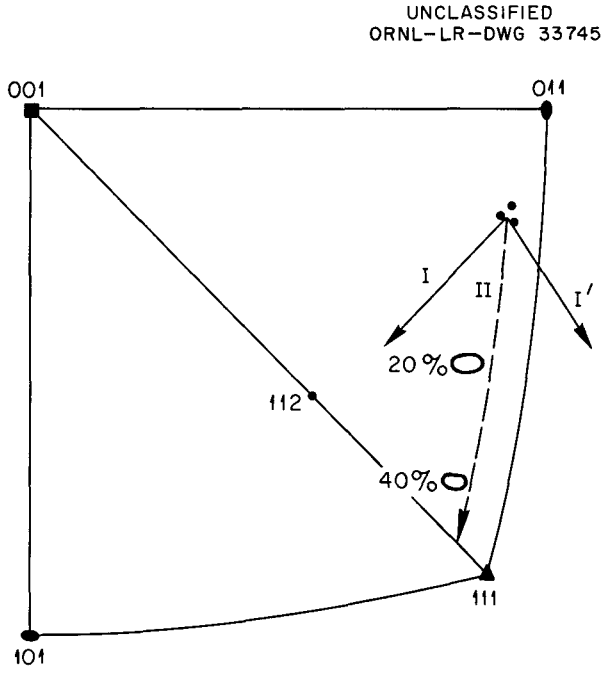

Fig. 2. Sterographic Projection Showing Reorientation of a Group of Grains in a Cast Ingot During Deformation. (I) Path for single slip on most favored system; (I′) path for single slip on next favored system; (II) path for duplex slip.

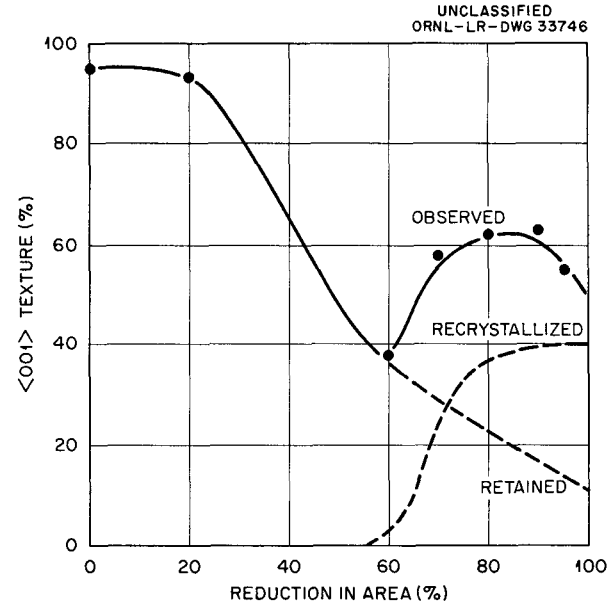

Fig. 3. Schematic Representation Showing the Relative Amount of an Observed <001> Texture Due to Room-Temperature Recrystallization and the Amount Due to Retained Initial Texture.

for reductions up to ~85%, then decreased again. A schematic drawing is shown in Fig. 3 which separates the observed <001> component into that retained from the original cast texture and that resulting from recrystallization during deformation.

Initial Orientation, 88% <111> – 12% <001>. – A section taken from the front end of an aluminum rod prepared by extruding at 450°F at a rate of 615 fpm and found to have a texture described as 88% <111> – 12% <001> was swaged at room temperature to further reductions in area of 59.7, 78.7, 92.1, and 96.1%. The axis distribution charts of specimens taken from these rods are shown in Fig. 4*a* to 4*e*.

Despite the marked changes which occur in the values of the axis density at the peak position, there is little change in the amount of material associated with each component for reductions up to 92.1%. There is a marked sharpening of the <111> component at first to give an extremely sharp texture after the reduction of 59.7%. Further deformation causes a spreading of this texture, and after a reduction of 96.1% there is a noticeable shift along the <$1\bar{1}0$> zone toward <112>. After a reduction of 96.1%, 80% of the volume is associated with <111>, 12% with <001>, and the remaining 8% near <112>.

The initial buildup at <001> in Fig. 4*b* is probably due in part to room-temperature recrystallization. For higher amounts of deformation there is a gradual decrease in the sharpness of this component. Although the axis distribution charts show that relative amounts of the texture components remain about the same for reductions up to 92.1%, this does not necessarily imply that there are no orientation changes in the individual grains. This may result from the rate of change due to deformation being equal to the rate of recrystallization, which produces a <001> texture. A metallographic study which is being made may show how much of the <001> component is due to recrystallization.

Initial Orientation, <118>. – A rod extruded at a fast rate at 850°F was completely recrystallized and contained the single <118> texture shown in Fig. 5*a*. The axis distribution charts for specimens reduced 59.7, 78.7, 92.1, and 96.1% by swaging at room temperature are given in Fig. 5*b* to 5*e*.

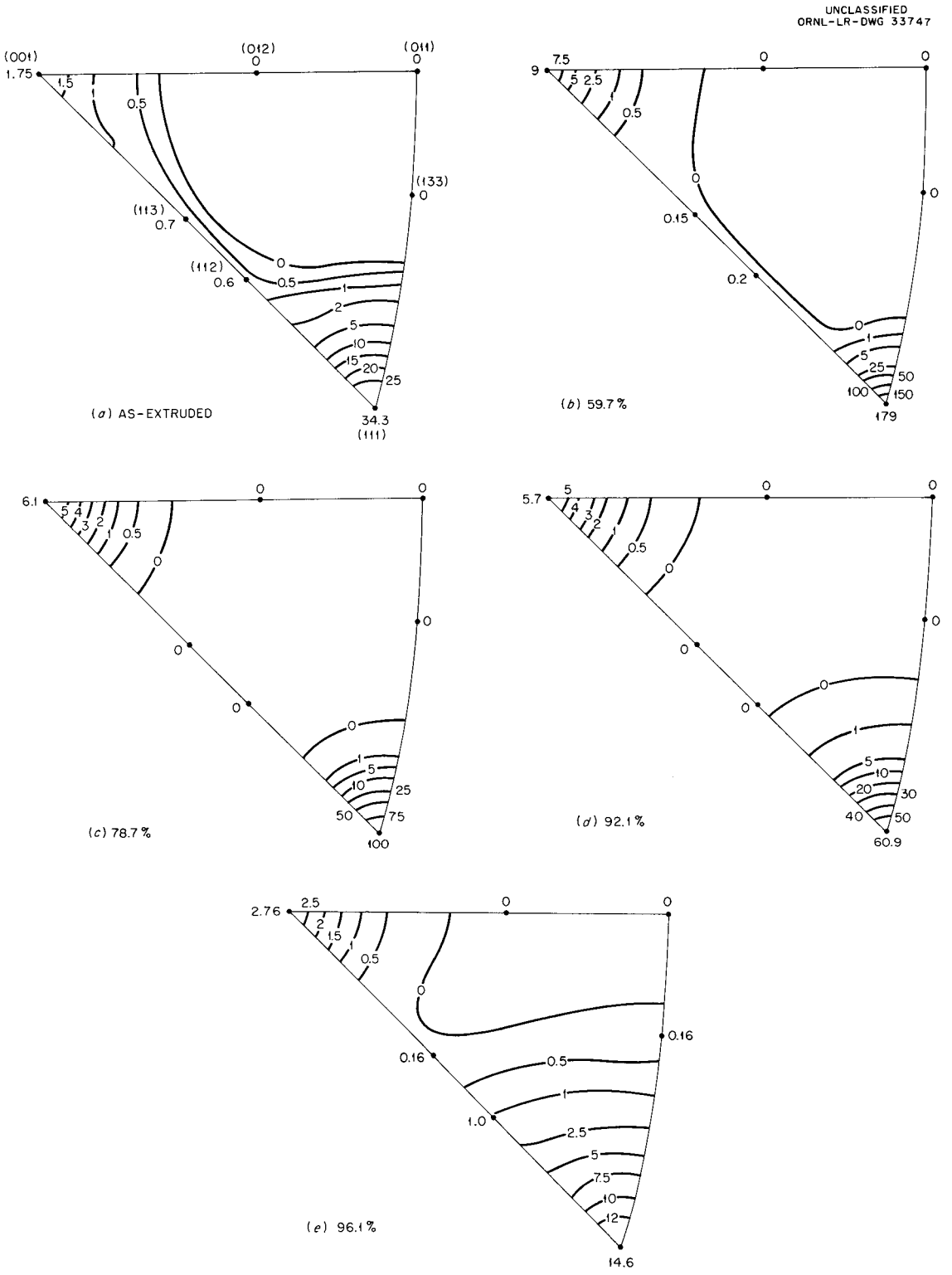

Fig. 4. Axis Distribution Charts for Aluminum Rods Swaged from One Containing an Initial 88% <111> – 12% <001> Texture.

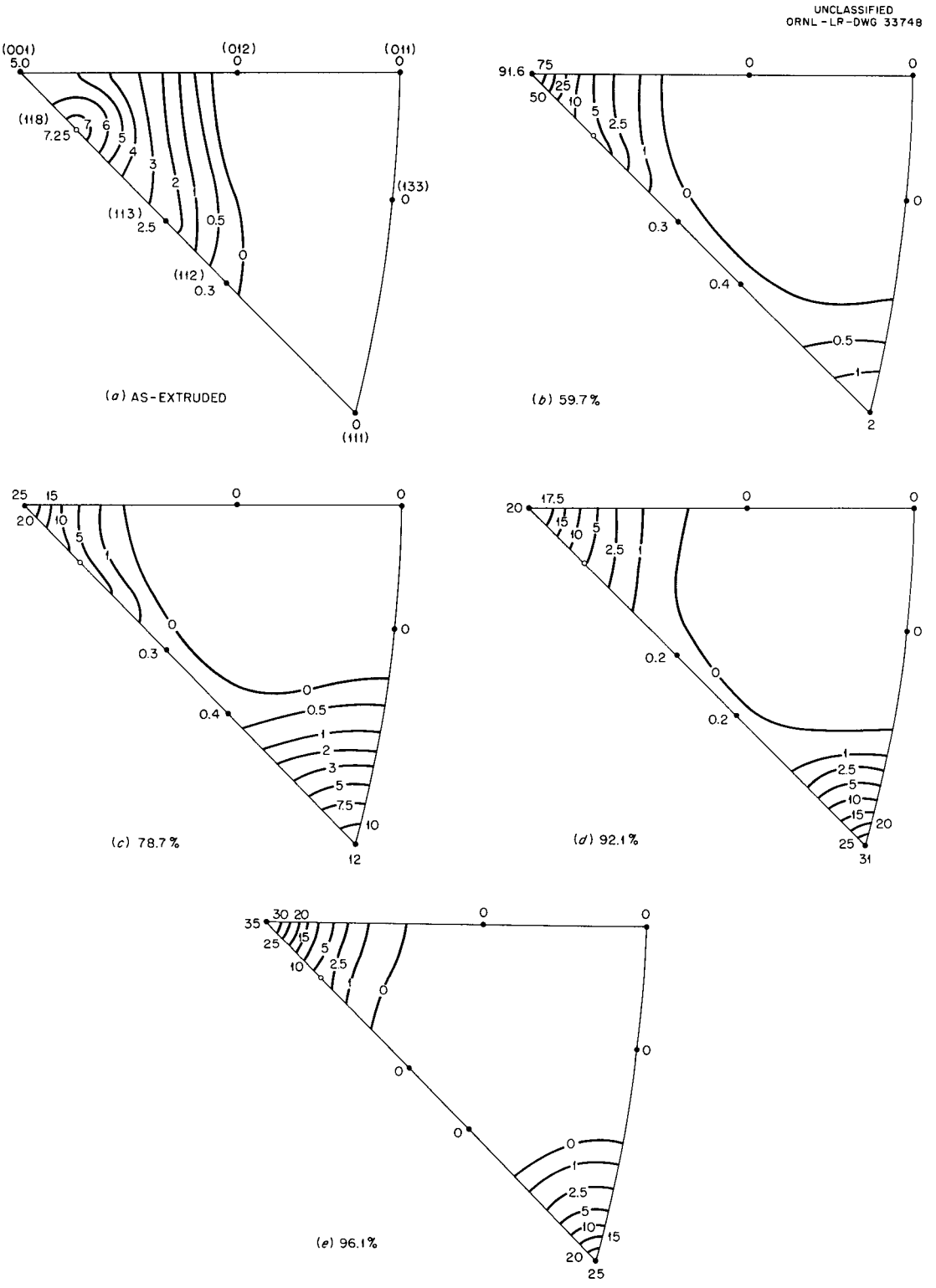

Fig. 5. Axis Distribution Charts for Aluminum Rods Swaged from One Containing an Initial <118> Texture.

After a reduction of 59.7%, there was a marked increase in the peak intensity at <001> ($T_0 = 5$ to $T_0 = 92$), whereas the value at <118> remained constant. A small amount (~3%) of material moved to <111>. With more deformation, the amount of material near <001> and the peak intensity at <001> decreased and there was a build-up of the <111> texture. After a reduction of 92.1%, 40% of the volume had the <111> texture and 60% the <118>–<001> textures. Room-temperature recrystallization apparently began for reductions between 92.1 and 96.1%.

Discussion. – The study of reorientations occurring during the deformation of aluminum rod is handicapped by the occurrence of room-temperature recrystallization. The amount of prior deformation necessary to cause such recrystallization apparently is related to the initial orientation. This relation is a manifestation of some other factor, such as different rates of work-hardening for different orientations.

An initial <001> orientation shows a relatively high degree of stability under further deformation, if such stability is measured by the amount of initial texture left after heavy reductions. In the present study it was found that ~10% of an initial <001> texture was retained after a 99% reduction in area. It was noted that some material, probably that farthest from the <001> peak position, first started to move away after a reduction of ~20%.

From the study of a specimen with an initial <118> orientation, it is tentatively concluded that material oriented on the <100> zone within about 20° of <001> first moves to the <001> position.

In no case was a concentration of axes noted along the <110> zone between <113> and <112>. One interpretation of this behavior is that the change in orientation from near <001> to near <111> takes place in a sudden and complete manner, such as occurs in kink-band formation. Another interpretation, which is possible but not very likely, is that there is a continuous change in orientation along the <110> zone at such a rate that there is always about the same volume of material with a given orientation.

With an initial <111> orientation a sharpening of this component was noted at first with increasing amounts of deformation, but after reductions of approximately 80%, there was a decrease in sharpness. After a reduction of 96.1%, a component on the <110> zone between <111> and <112> may tend to develop.

Phase Transformations in Metallic Cerium

In a previous report[4] initial results of a study of the phase transformations in high-purity metallic cerium were given for the range 77 to 425°K. It was reported that a previously uncooled specimen of cerium which had been annealed at 625°K had a face-centered cubic (fcc) crystal structure at ambient temperatures with $a_0 = 5.15$ Å. Transformation to a four-layer repeat hexagonal close-packed (hcp) structure ($c/a = 3.239$) began upon cooling at 263 ± 10°K. No isothermal transformation was observed, and the amount of hexagonal phase depended only upon the temperature difference between T_s (263°K) and the observation temperature. At 96 ± 5°K, the fcc phase which had not transformed to the hcp phase began to transform to a second fcc phase ($a_0 = 4.85$ Å at 77°K) with a volume decrease of 16.5%. Plastic deformation at any temperature was found to suppress the fcc → hcp transformation, and sufficient deformation could lead to its complete suppression.

This investigation has been continued in order to study the nature, kinetics, and effects of prior treatments on the transformations. The only detected impurities in the cerium, which was obtained from the Institute for Atomic Research, Ames, Iowa, and was vacuum-melted, were 260 ppm of O_2, 40 ppm of H_2, 15 ppm of N_2, 140 ppm of Fe, and 60 ppm of Mg.

The hcp-to-fcc Transformation. – A study was made of the nature of the reversion of the hcp phase to the fcc structure at higher temperatures. It was previously reported that this transformation began at 375 ± 5°K and was complete at 411 ± 10°K and appeared to have martensitic characteristics. Masson and Barrett[5,6] report that the martensitic hcp phase produced by deformation of the body-centered cubic (bcc) AgCd *beta* phase reverts to the original bcc structure by a thermally activated process. In view of these results in the AgCd system, it seemed desirable to confirm the earlier conclusion that the hcp → fcc transformation does not proceed isothermally.

A specimen of cerium was annealed for 1 hr at 625°K and cooled to 77°K in the x-ray camera. At

[4] C. J. McHargue, H. L. Yakel, Jr., and L. K. Jetter, *Met. Ann. Prog. Rep. Oct. 10, 1957*, ORNL-2422, p 207.

[5] D. B. Masson and C. S. Barrett, *Trans. Am. Inst. Mining Met. Petrol. Engrs.* 212, 260 (1958).

[6] D. B. Masson and C. S. Barrett, unpublished work at the University of Chicago.

this temperature the specimen contained 12% fcc phase, 30% hcp phase, and 58% fcc′ (collapsed cubic) phase. Upon being heated, the specimen was found to be composed of 45% fcc phase and 55% hcp phase at 296°K. Heating was continued and the hcp → fcc transformation was observed to begin at 373°K, in agreement with earlier studies. The temperature was raised to 388°K, where it was held (±2°) for 6 hr; during this time an appropriate range of Bragg angle was repeatedly scanned. Calculations based on the integrated intensities of the (10.2) and (10.3) reflections of the hcp phase and the (200) reflection of the fcc phase showed the amounts of fcc and hcp phases to be 54% and 46%, respectively, 5 min after the temperature of 388°K was reached. During the next 25 min, the amount of fcc phase increased to 60% and the hcp phase decreased to 40%. No further change was noted during the next 6 hr at this temperature. At the end of 6 hr the temperature was raised by 6° to 394°K, and it was noted that an additional 8% of the hcp phase transformed during the first 10 min at this temperature. These data strongly indicate that there is no isothermal reversion of hcp cerium to the fcc form. The initial increase in cubic cerium during the first 30 min at 388°K is attributed to the relief of transformation stresses in the polycrystalline sample.

Sonic Activity. – Processes in solids involving the rapid cooperative movements of atoms in phase, such as those occuring in typical martensitic transformations and deformation twinning, produce sound. In order to obtain information regarding the nature of the fcc → hcp and fcc → fcc′ transformations, experiments have been conducted on the detection of sonic activity in cerium specimens being cooled or heated.

A cerium specimen was attached to a long copper rod to which a small phonographic crystal pickup was secured. A copper-constantan thermocouple was attached to the specimen. The assembly was mounted over a large, deep Dewar partially filled with liquid nitrogen. The signal from the pickup was amplified with a Bogen LX30 amplifier and was transmitted by an 8-in. speaker. The operation of the apparatus was checked by mechanically deforming a specimen of indium. The clicks accompanying the mechanical twinning were clearly detected. In order to attain the lowest temperatures, it was desirable to bring the specimen into contact with the liquid nitrogen. When the specimen was submerged, the boiling of the nitrogen at the specimen surface caused a high background noise. This noise was eliminated by placing a large copper block in the bottom of the flask with its surface just above the surface of the liquid and then, after the block had come into thermal equilibrium with the nitrogen, cooling the specimen assembly by clamping it to the block.

In a series of runs no sonic activity was detected in the temperature range where the cubic-to-hexagonal transformation occurs. That such a transformation had occurred was confirmed by x-ray examination of a specimen after one run.

Metallic clicks were heard upon both cooling and heating in the temperature range where the cubic-to-cubic transformation occurs. In all cases sonic activity was detected on cooling, but not upon heating unless the heating rates were very rapid.

Such sounds are usually interpreted to mean that volume elements change structure by a rapid shearing motion similar to twinning. In the present case, however, where the two phases have the same crystal structure and differ only in the size of the unit cell, it is difficult to imagine any cooperative shearing motion which would convert one into the other. It is intended that the crystallographic relationships between the phases and possible atom movements be investigated by means of such treatments as that developed by Wechsler, Lieberman, and Read[7] and by observation of habit plane relationships.

Effect of Thermal Cycling. – Lock[8] observed that the change in magnetic susceptibility associated with the fcc → fcc′ transformation and a second discontinuity at 12.5°K were markedly affected by thermal cycling between 293 and 4.2°K. From these data Lock concluded that less of the normal cubic phase transformed on each subsequent cycle, but since he made no observation regarding the fcc → hcp transformation, he concluded that the fcc phase becomes antiferromagnetic at 12.5°K.

A specimen of annealed cerium which was found to have only the normal cubic phase present at room temperature was alternately cooled to 77°K and warmed to room temperature. The relative

---

[7]M. S. Wechsler, D. S. Lieberman, and T. A. Read, *Trans. Am. Inst. Mining Met. Engrs.* 197, 1503 (1953).

[8]J. M. Lock, *Proc. Phys. Soc. (London)* B70, 566 (1957).

amount of each phase present under various conditions is shown in Table 1. The results at 293 and 77°K after the first two cycles are consistent with those reported earlier.[9] It is seen that cycling 105 times has greatly increased the amount of hcp phase present at room temperature and that the collapsed cubic phase was completely absent upon the next cooling. This behavior is similar to that found by M. K. Wilkinson and H. R. Child of the Physics Division, who are making a neutron diffraction study in collaboration with these x-ray studies. When they cycled the specimen 100 times between 293 and 4°K, they found that there was complete suppression of the fcc → fcc′ transformation and that there were large amounts of the hexagonal phase.[10] Thus it appears that Lock's magnetic measurements after 100 or more thermal cycles may have been made on a specimen containing primarily the hexagonal phase rather than the fcc phase.

The specimen which contained 15% fcc phase and 85% hcp phase at 77°K after 107 coolings was plastically deformed in the x-ray camera at that temperature. Interestingly, this deformation resulted in the appearance of the collapsed cubic phase (in the amount of 50% of the total volume). Upon further heating and cooling, the specimen behaved in a manner similar to one which had not been thermally cycled. It is not yet clear whether the deformation causes the hexagonal phase to transform back to the normal cubic form, which then transforms to the collapsed cubic phase, or whether it causes the hexagonal phase to go directly to the collapsed cubic form. At temperatures above T_s for the fcc → fcc′ reaction, the former behavior was observed,[8] but, as is discussed below, between 77 and 4°K the hexagonal phase appears to go to the collapsed cubic phase without the benefit of plastic deformation.

Effect of Cooling to 4.2°K. – Apparatus has been constructed so that an x-ray specimen can be cooled to liquid-helium temperature and has been mounted on a G-E XRD-5 x-ray spectrometer. The specimen is cooled to 4.2°K and the diffraction pattern recorded as the specimen heats to room temperature.

A specimen of cerium annealed at 625°K which was observed to contain only the fcc phase at room temperature was cooled first to 77°K and then to 4.2°K. At 77°K the specimen contained ~60% collapsed cubic phase, 30% hcp phase, and 10% normal fcc phase. At 4.2°K, only the collapsed cubic phase was found to be present, indicating that both the hcp structure and the fcc structure had transformed to the collapsed cubic structure. The changes in the amounts of the phases present

[9] C. J. McHargue, H. L. Yakel, Jr., and L. K. Jetter, *Met. Ann. Prog. Rep. Oct. 10, 1957*, ORNL-2422, p 207.

[10] To be reported by M. K. Wilkinson *et al.* in the *Phys. Semiann. Prog. Rep. Sept. 20, 1958*, ORNL-2610 (in press).

Table 1. Effect of Thermal Cycling on Transformations in Cerium

At 293°K specimen in annealed condition was 100% fcc

Stage of Observation	Observation Temperature (°K)	Transformations (%)		
		fcc	hcp	fcc′
After 1 cycle	293	80	20	
Second cooling	77	10	40	50
After 105 cycles	293	30	70	
106th cooling	77	15	85	
After 106 cycles	293	25	75	
107th cooling	77	15	85	
Specimen worked while being cooled to 77°K for 107th time		10	50	40
Specimen then heated back to 293°K		50	50	
Specimen cooled again to 77°K		10	55	35

as the temperature was raised are shown in Fig. 6. At ~125°K the fcc′ phase starts to revert to the hcp phase, and this transformation appears to cease at 195°K, with only 20% of the specimen being in the hexagonal form. The transformation from fcc′ to fcc takes place over the range 150 to 210°K.

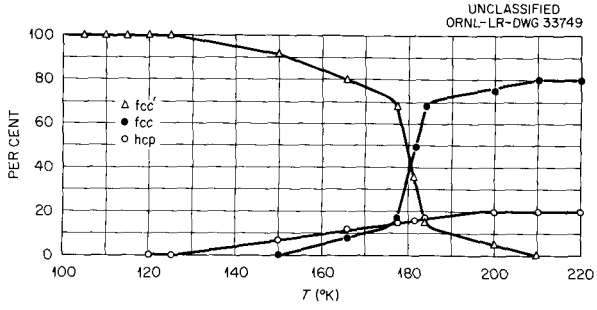

Fig. 6. Per Cent of Each Phase Present upon Heating an Annealed Specimen of Cerium Cooled to 4.2°K.

The specimen from the above series of experiments which contained 80% fcc phase and 20% hcp phase at 293°K was again cooled. The amounts of phases present at 77°K were 75% fcc′, 17% hcp, and 8% fcc, and at 4.2°K there was a trace of hcp present in addition to the fcc′ phase. The surface of the specimen was plastically deformed at 4.2°K by scratching with a tool built into the x-ray camera. This work caused no detectable change in the x-ray diffraction pattern. Again the collapsed cubic phase transformed to both hexagonal and normal cubic structure, and at 293°K the specimen consisted of 80% fcc and 20% hcp.

Results on a second annealed specimen were essentially the same as for the above specimen.

These data show that the hcp phase will transform to the collapsed cubic form at a sufficiently low temperature. However, there appears to be some factor which differentiates the collapsed cubic phase originating in the hexagonal phase from that coming from the normal cubic phase. Thus a specimen which is entirely in the fcc′ form will revert to fcc and hcp in approximately the same ratio that existed before these phases transformed to fcc′ upon cooling. This "memory" effect could possibly be caused by a characteristic distribution of stacking faults in the fcc′ phase. A careful study of the stacking faults present in all three phases is now being conducted.

THEORY OF ALLOYING

Specific Heats of Zirconium Alloys at Low Temperatures

G. D. Kneip, Jr. J. O. Betterton, Jr.
J. O. Scarbrough

The primary substitutional solid solutions of the group IVA metals of the periodic table, with other metals as the solutes, are particularly interesting from the standpoint of alloying theory. Two of the four valence electrons in the free atoms are *s* electrons, and the other two are *d* electrons. Chemically, these elements almost invariably are quadrivalent, indicating little difference in energy between the electronic states of the valence electrons. Recent evidence has shown that as far as the effects of various solutes on the allotropic transformations are concerned the group IVA elements may be considered to be divalent.[11] The band structure of these metals has not been satisfactorily solved, but in view of the difference in the valence exhibited in solid solutions as compared with the chemical valence, it seems likely that the band structure is complicated and consists of overlapping *s* and *d* bands. The variation of the axial ratios of zirconium and titanium that occurs when they are alloyed has been interpreted in terms of Brillouin zone overlaps,[12,13] indicating that the shape of the curve for the density of states may have maxima and minima.

One experimental approach to the study of the characteristics of the electronic energy bands is the measurement of the electronic specific heat. Since only the electrons at the top of the occupied region can be thermally excited into vacant energy states, their heat capacity is a measure of the density of states at the top of the filled region of the energy band. This electronic heat capacity is proportional to temperature and, at normal temperatures, is small compared with the vibrational heat capacity of the atoms. At sufficiently low temperatures, however, where the vibrational heat capacity is proportional to the cube of the temperature, the electronic specific heat is an appreciable

[11] J. O. Betterton, Jr., and J. H. Frye, Jr., *Acta Met.* 6, 205 (1958).

[12] J. M. Denny, *A Study of Electron Effects in Solid Solution Alloys of Titanium*, Sixth Technical Report, Physical Metallurgy Laboratory, California Institute of Technology, January 1955.

[13] J. O. Betterton, Jr., *Met. Semiann. Prog. Rep. April 10, 1956*, ORNL-2080, p 228.

part of the total. In general, in the liquid-helium temperature range, the total specific heat can be expressed as[14]

$$\frac{C_v}{T} = \frac{\pi^2}{3} k^2 N(E_{max}) + \frac{12}{5} \pi^4 N_0 k \frac{T^2}{\theta_D^3} ,$$

where $N(E_{max})$ is the density of states at the top of the occupied portion of the band and θ_D is the Debye temperature. Furthermore, the difference between C_p and C_v at these temperatures is negligible, so that if the experimentally determined values of the specific heat are plotted in the form C/T vs T^2, the density of states and the Debye temperature can be obtained from the intercept and the slope, respectively, of the resulting linear plot.

The details of the apparatus used to measure the specific heats of alloy specimens in the liquid-helium temperature range were described earlier.[15] The heat capacity is determined by measuring the temperature drift of the specimen as a function of time and applying known heat inputs at appropriate intervals. The heat capacity, then, is the energy input divided by the temperature rise.

A semiconducting carbon resistance thermometer is used as the temperature-sensing element for the heat-capacity measurements. The resistance thermometer is calibrated against the vapor pressure of liquid helium by use of the vapor-pressure temperature scale (T_{55E}) of Clement, Logan, and Gaffney[16] prior to the heat-capacity measurements on each specimen. In order to facilitate the thermometer calibration, a resistance temperature, T_R, is defined by the equation

$$\frac{\log R}{T_R} = (0.60521 - 1.05028 \log R)^2 ,$$

and the thermometer calibration then consists in establishing $T_{55E} - T_R$ as a function of T_R. Above the lambda point of liquid helium the vapor pressure of the liquid helium is measured with a helium-vapor-pressure thermometer whose bulk is an integral part of the specimen contained, in order to avoid the uncertainties involved in making a hydrostatic heat correction.

Below the lambda point the vapor pressure is assumed to be equal to the pressure over the bath, since the high thermal conductivity of helium II assures the equality of temperature throughout the bath. The thermometer deviation curve and its slope are then used to correct the observed mean temperatures and ΔT's, respectively, for each measurement of the heat capacity. Figure 7 shows the thermometer resistance as a function of temperature, and Fig. 8 shows several deviation curves. Slight shifts in the $T_{55E} - T_R$ curve are seen to occur when the thermometer and heater assembly is shifted from one specimen to another. No apparent changes in the thermometer were found, however, on several occasions when the thermometer was warmed to room temperature and then recooled without removing the thermometer assembly from the specimen. The cryostat holds

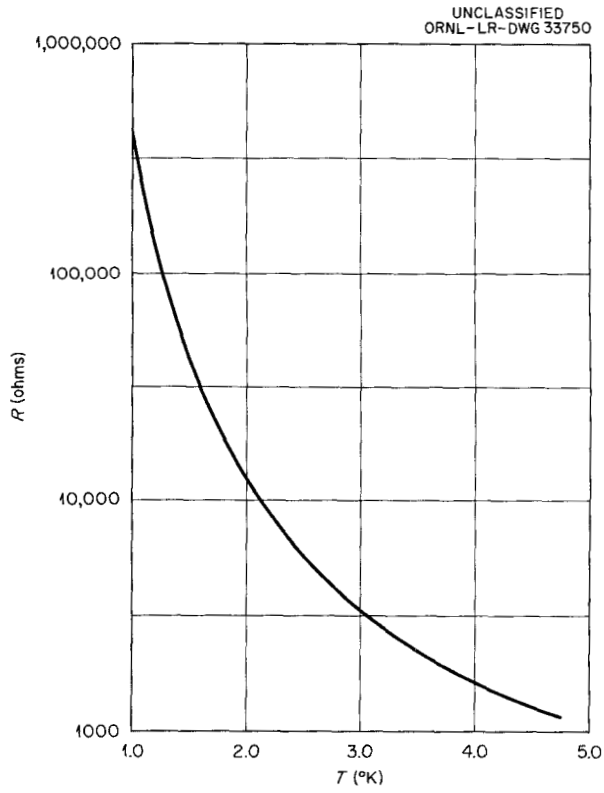

Fig. 7. Thermometer Resistance as a Function of Temperature.

[14] N. F. Mott and H. Jones, *The Theory of the Properties of Metals and Alloys*, pp 4, 179, Clarendon Press, Oxford, 1936.

[15] G. D. Kneip, Jr., and J. O. Betterton, Jr., *Met. Ann. Prog. Rep. Oct. 10, 1957*, ORNL-2422, p 214.

[16] J. R. Clement, J. K. Logan, and J. Gaffney, *Phys. Rev.* 100, 743 (1955).

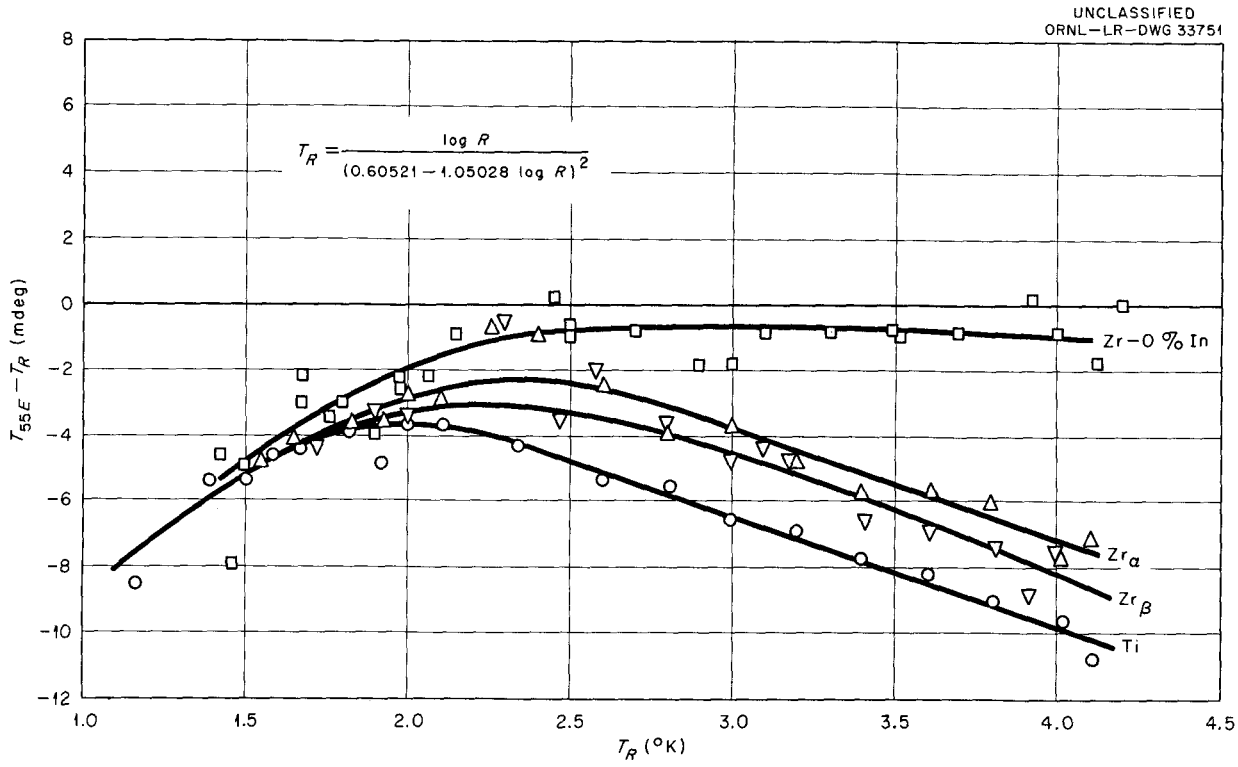

Fig. 8. Thermometer Deviation Curves.

sufficient liquid helium to last for over 24 hr, thus making it feasible to spread the thermometer calibration and heat-capacity measurements over several days.

In order to correct the alloy specific heats for the heat capacity of the thermometer and heater assembly, the heat capacity of the addendum has been measured separately, and the results are shown in Fig. 9. It can be seen that the experimental data fit a straight line when plotted in the form C/T vs T^2. The value of the coefficient of the electronic term, determined experimentally (1199 ergs/deg^2), is in very good agreement with the value computed for the sum of the metal parts of the assembly, 1205 ergs/deg^2, from the known specific heats of zirconium and copper and an estimated value for Manganin. The close agreement for these two values indicates that the graphite thermometer and the organic cement used to hold the thermometer and the heater winding to the zirconium plug have a very low electronic specific heat, as would be expected. Unfortunately, no attempt can be made to compute an effective Debye temperature because of the lack of information about the specific heats and molecular weights of the organic materials.

Figure 10 shows a typical recording of the thermometer potential drop as a function of time. The lower part of the curve corresponds to the sample

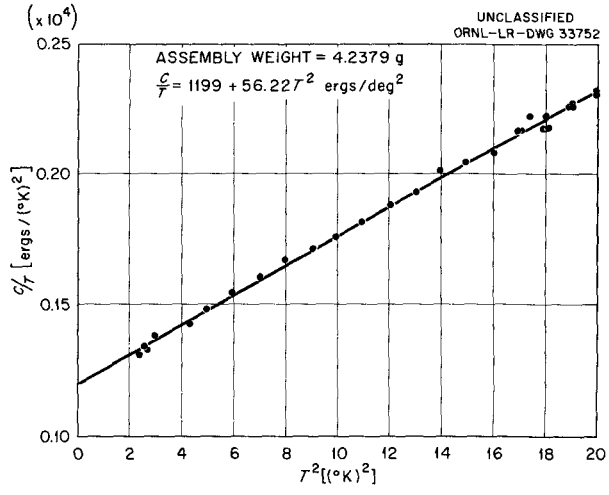

Fig. 9. Heat Capacity of the Heater and Thermometer Assembly.

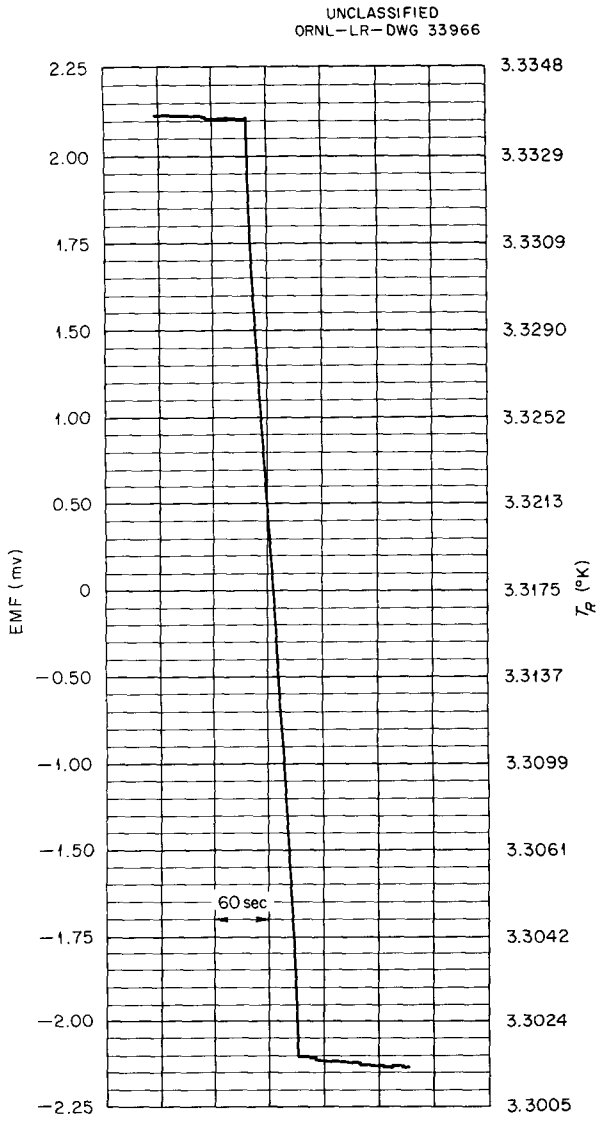

Fig. 10. Typical Heating Curve for 0.7649-mole Zirconium Specimen. Heater current, 60 μa; heater voltage, 97.277 mv; time, 54.208 sec.

drift before the heating pulse, the rapid rise in the curve corresponds to the heating pulse, and the upper portion corresponds to the drift after the heating pulse. The temperature rise caused by the heat input is determined by extrapolating the initial and final portions of the curve back to the middle of the heating period, calculating the thermometer resistance at these two points, and then computing the mean temperature and the temperature increase from these two resistance values. It can be seen from Fig. 10 that this is easily done as long as the drift rates are small compared with the value of ΔT. Figure 11 shows the observed thermal coupling between the specimen and the bath for two experiments. When the specimen and the bath are at the same temperature, the specimen warms up slowly as a result of the power input to the thermometer. After the specimen has been warmed above the bath temperature by several heating pulses, the net heat flow tends to cool the specimen back toward the temperature of the bath, and the heat conduction through a unit length of No. 60 cotton thread is estimated to be 10^{-2} to 10^{-3} times that of a unit length of 2-mil columbium wire.

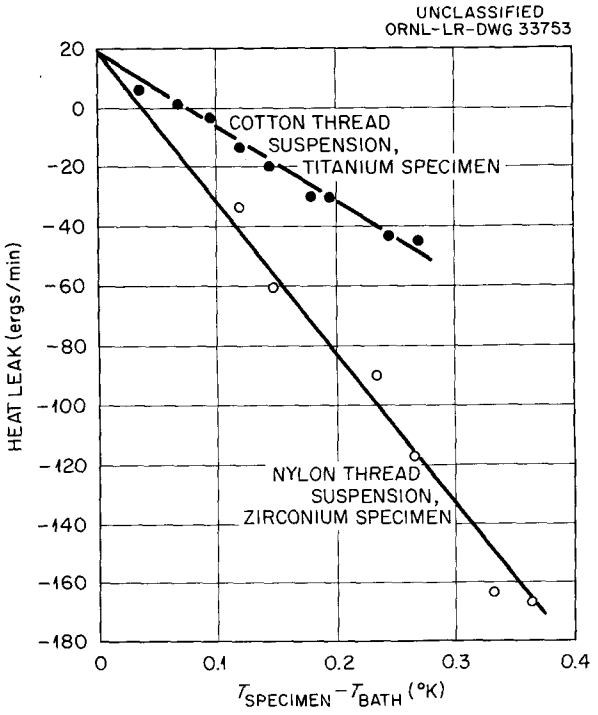

Fig. 11. Thermal Heat Leak Between Specimen and Bath.

Specimens of iodide titanium and iodide zirconium, from which the hydrogen had been removed by vacuum-annealing at 1100°C and 10^{-7} mm Hg, were machined for the calorimetric studies. After the machining operation the specimens were alpha-annealed and slowly cooled to remove any residual stresses. The typical impurity contents and the hardness of these materials are listed in Table 2. Two additional zirconium specimens were made.

Table 2. Impurity Content and Hardness of Iodide Titanium and Zirconium

Impurity	Concentration* (ppm)	
	Zr	Ti
Ti	80 ± 50	Balance
Zr	Balance	200–500
Hf	130 ± 50	
Cr	5	10
Fe	45	55
Ni	10	5
Si	10	
All others	<5	<10
C	20–175	10
O_2	50–350	20
N_2	4–5	20
H_2	<5	<5
Hardness	63 DPH	63 DPH

*Average values from spectrographic and activation analyses; H_2, N_2, O_2 from vacuum fusion analyses.

One specimen was annealed and quenched from the beta-phase region so that the effects of residual stresses could be observed. The other specimen was arc-melted, homogenized in the beta-phase region, and annealed in and quenched from the alpha-phase region; then a hole was machined for the addendum. This specimen was investigated in order to show the absence of significant impurity contamination occurring during the melting and annealing treatments. The latter procedure was also used for preparing the zirconium-indium alloys discussed below.

The specific heats of the alpha-annealed iodide titanium and zirconium plotted as C/T vs T^2 are shown in Figs. 12 and 13, respectively. The scatter of the individual measurements from the best straight-line fit determined by the method of least squares is well under 1%, as shown in Fig. 14. The systematic deviation of the data from the linear equation for C/T vs T^2 below ~2.6°K is within the uncertainty of the helium-vapor-pressure temperature scale. The coefficients of the electronic terms and the Debye temperatures for titanium and zirconium are shown in Table 3.

The observed densities of states of both titanium and zirconium are considerably higher than would be estimated by assuming the valence electrons to

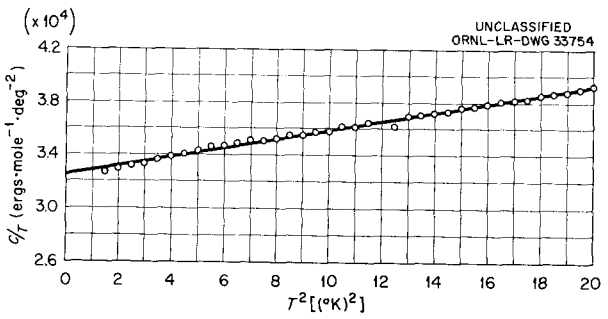

Fig. 12. Specific Heat of Alpha-Annealed Titanium from 1 to 4.5°K.

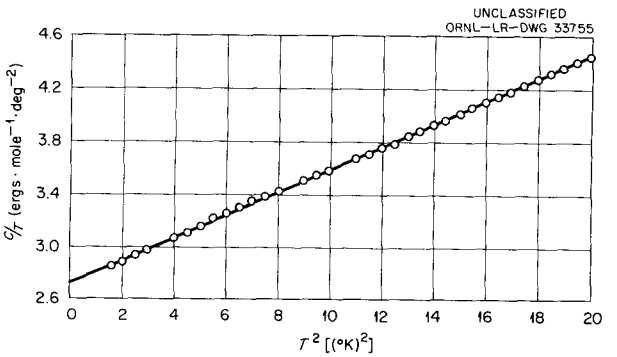

Fig. 13. Specific Heat of Alpha-Annealed Zirconium from 1 to 4.5°K.

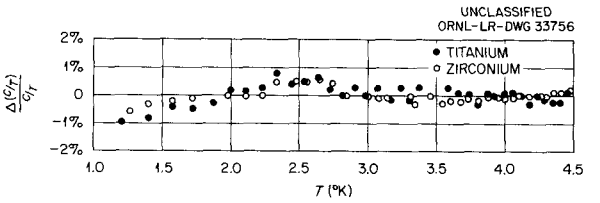

Fig. 14. Per Cent Deviation in Specific Heats of Titanium and Zirconium as a Function of Temperature.

behave as free electrons, in agreement with a narrow d band having a high density of states. Since the coefficients of the electronic terms and the Debye temperatures of the three zirconium specimens are equal within the experimental error, it is concluded that the transformation structure resulting from quenching from the body-centered cubic form and the equilibrium alpha structure differ very little as far as electronic energy is concerned. Furthermore, any increase in the amount of impurities caused by the melting and annealing treatments has no measurable effect on the specific heats.

Table 3. Electronic Coefficients and Debye Temperatures for Titanium and Zirconium

	γ (ergs·mole^{-1}·deg^{-2})	θ_D (°K)
	$\times 10^4$	
Titanium		
Alpha-annealed	3.254 ± 0.015*	385.8 ± 4.4
Zirconium		
Alpha-annealed	2.728 ± 0.009	282.3 ± 1.1
Beta-annealed	2.736 ± 0.013	281.7 ± 1.1
Cast, alpha-annealed	2.751 ± 0.011	283.0 ± 1.0

*Random error estimated from least-squares fit of C/T vs T^2 at 99% confidence level.

The ratio of the Debye temperatures for titanium and zirconium is very nearly equal to the ratio

$$\left(\frac{M_{Ti}}{M_{Zr}}\right)^{1/3}\left(\frac{\rho_{Ti}}{\rho_{Zr}}\right)^{1/6},$$

where M is the atomic mass and ρ the density, suggesting a similarity in the vibrational spectra and elastic constants of the two elements, in agreement with their positions in the periodic table.

The specific heats as a function of temperature for part of a series of zirconium-indium alloys are shown in Fig. 15. Again the data are linearly related when plotted in the form C/T vs T^2, indicating a constant Debye temperature over the range 1.2 to 4.5°K. No indication of a superconducting transition is found in any of these alloys.

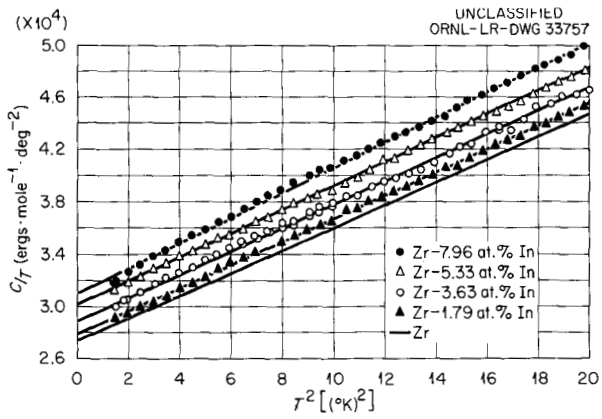

Fig. 15. Specific Heats of Zirconium-Indium Alloys from 1.2 to 4.5°K.

The coefficients of the electronic terms and the Debye temperatures are shown in Fig. 16 and in Table 4. The addition of indium to zirconium increases the coefficient of the linear term and hence the density of states at the Fermi surface quite rapidly. For hexagonal metals the electronic energies are expected to overlap the first energy zone across the {100} and probably also across the {001} faces at nearly two electrons per atom, according to the simple Brillouin zone theory. Additions of indium, then, should have the effect of increasing the density of states, assuming the band structure of zirconium to be rigid and zirconium to be divalent.[17] The observed expansion of the axial ratio with electron additions independently suggests the same {001} face overlap.

[17] J. O. Betterton, Jr., and J. H. Frye, Jr., *Acta Met.* 6, 205 (1958).

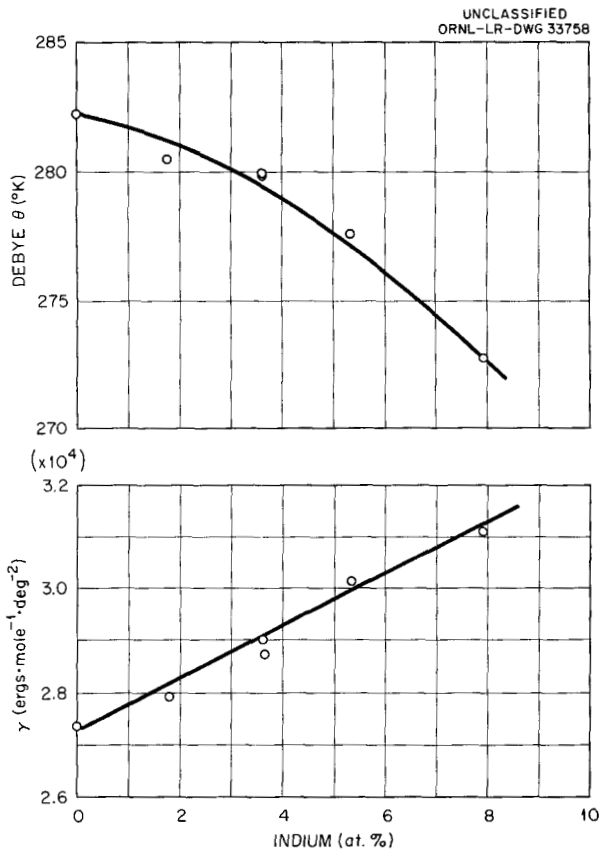

Fig. 16. Electronic Specific Heat and Debye Temperature as a Function of Composition for Zirconium-Indium Alloys.

Table 4. Electronic Coefficients and Debye Temperatures for Zirconium-Indium Alloys

	γ (ergs·mole^{-1}·deg^{-2})	θ_D (°K)
	$\times 10^4$	
Zirconium	2.738 ± 0.011*	282.3 ± 1.0
Zr–1.79 at. % In	2.786 ± 0.012	280.5 ± 1.1
Zr–3.63 at. % In	2.875 ± 0.023	280.0 ± 2.1
	2.900 ± 0.016	279.9 ± 1.3
Zr–5.33 at. % In	3.012 ± 0.012	277.6 ± 1.0
Zr–7.96 at. % In	3.108 ± 0.020	272.7 ± 1.6

*Random error estimated from least-squares fit of C/T vs T^2 at 99% confidence level.

When further information is available on the effects of other solutes, such as silver, cadmium, and tin, on the electronic specific heat of zirconium, it will be possible to use the results as a test of the validity of the various theories of alloying. At the present time, however, rapid increase of the density of states with indium additions does not appear to agree with the hypothesis of Friedel as well as it does with the rigid-band concept.

The Zirconium-Gallium System

D. S. Easton J. O. Betterton, Jr.

The zirconium-gallium system is important in the study of zirconium alloys because, as a group IIIB element, gallium would be expected to behave like aluminum and indium in forming a reasonably concentrated, alpha solid solution and, in this case, with fairly low nuclear absorption cross section. If the size distortion effects are not so great as to be unfavorable to the alpha phase, the α/β phase boundaries might be expected to rise with gallium. In addition, information about the effect of the presence or absence of the complete d shell in the solute atom may be provided. The first intermediate phase also is of interest, since in the zirconium-indium system a face-centered disordered phase occurs at Zr_3In; in the zirconium-aluminum system the corresponding face-centered cubic phase is ordered in the manner of Cu_3Au, which is believed to result from the difference in the size of the atoms being greater in the latter system. The zirconium-gallium alloys will help to show whether this factor alone is important.

The investigation was started at the zirconium-rich end of the system. The methods employed were described earlier in connection with other zirconium systems.[18] It was found that gallium, in spite of its low melting point, has a sufficiently low vapor pressure that alloys up to 16 at. % Ga do not lose gallium appreciably in casting. The distribution and proportion of phases in cast microstructures showed that a eutectic, liquid ($\sim$21 at. % Ga) $\rightleftarrows$ β ($\sim$8 at. % Ga) + δ ($\sim$37 at. % Ga), occurs in this system. A typical microstructure illustrating the reaction is given in Fig. 17. The eutectic is in good agreement with the eutectic reported by Anderko[19] in cast alloys between 25 and 40 at. % Ga, who found the composition Zr_5Ga_3 to be a homogeneous phase with an ordered hexagonal $D8_8$-type structure after annealing at 1000°C. Anderko also observed an incomplete reaction in alloys containing 25 and 33 at. % Ga, which he attributed to a pertectoid reaction between β-zirconium and Zr_5Ga_3 at some temperature above 1000°C that caused an intermediate phase of approximate composition Zr_3Ga to form.

The same intermediate phase was also indicated in the present experiments when alloys from 0 to to 16 at. % Ga were annealed for two weeks at 1095°C. A lineal analysis of the proportion of phases in the ($\beta + \gamma$) region between 5 and 16 at. % Ga indicated that β-zirconium containing 4.5 at. % Ga was in equilibrium with a second phase containing about 27 at. % Ga. The same phase was observed to be in equilibrium with β-zirconium containing 2.5 at. % Ga at 920°C. X-ray studies of the alloy containing 16 at. % Ga were made by spectrometric and Debye-Scherrer techniques. Although not conclusive, the measurements indicate that a Cu_3Au ($L1_2$) structure, which would be analogous to Zr_3Al, is improbable but that a hexagonal $D0_{19}$ structure is possible within the considerable uncertainty of the present results. Anderko, who examined extra lines in a three-phase powder sample, was unable to index these lines with the $D0_{19}$ or $L1_2$ structures.

[18] J. O. Betterton, Jr., J. H. Frye, Jr., and D. S. Easton, *Phase Diagram Studies of Zirconium with Silver, Indium, and Antimony*, ORNL-2344, p 2 (Aug. 12, 1957).

[19] K. Anderko, *Z. Metallk.* 49, 165 (1958).

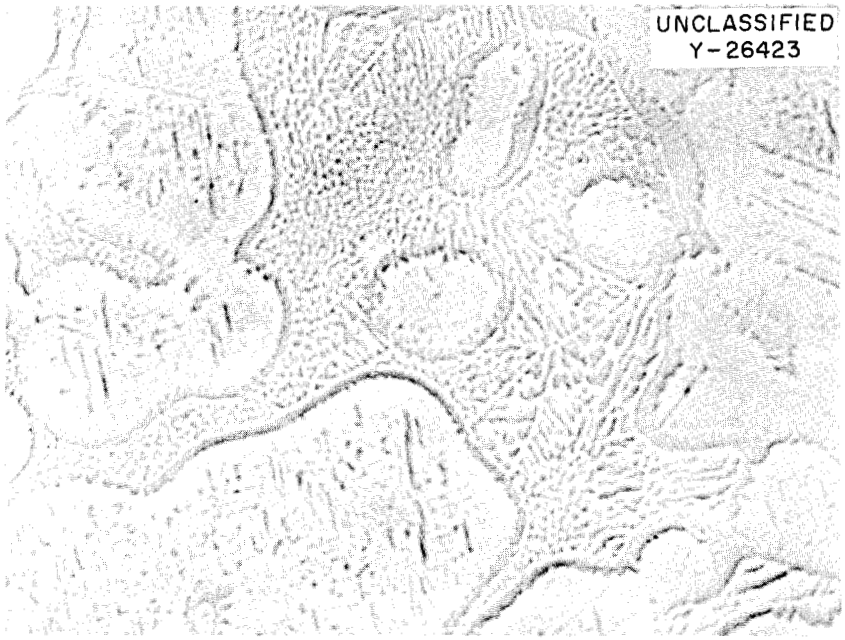

Fig. 17. Cast Structure, Zr + 12 at. % Ga. Unetched. 2000X.

The DO_{19} structure occurs in many titanium systems in the electron concentration 2.3 to 2.6, the titanium being assumed to be divalent. McQuillan[20] has pointed out that this type of structure represents an ordered extension of the alpha phase with the same factors which cause the axial ratio of the α-titanium to expand when group IIIB and IVB solutes are alloyed apparently contributing to the stability of this phase. It would, of course, be interesting if Zr_3Ga should assume this structure, as a zirconium phase has not been previously found of this type.

A significant characteristic of the zirconium-gallium system is the unusually low solubility of the gallium in β-zirconium, which is only about one-third that observed for other group IIIB solutes, aluminum and indium. This could be explained by atomic size factor if the minimum interatomic distance, 2.44 Å, of just two of the atoms in the complicated gallium element structure were adopted. The size factor on this basis is nearly −21%. An alternative method for a solute of irregular crystal structure is the use of the apparent atomic diameter extrapolated from solid solutions of other alloys in which gallium has been used. With this method, the zirconium-gallium size factor is about −9% and would therefore be insufficient to account for the reduced solubility. The hardnesses of the alloys, however, tend to support the presence of a large size factor; that is, the numerical increases in Vickers hardness numbers for 1 at. % solute are approximately: silver, 33; cadmium, 8; indium, 12; gallium, 37; lead, 20; and antimony, 28. An unusually large effect evidently occurs with gallium additions. The hardness numbers for β-zirconium–gallium alloys, quenched from 1095 and 920°C, are shown in Fig. 18.

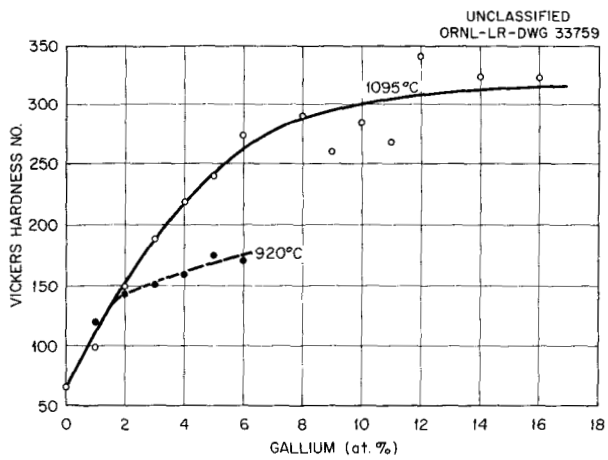

Fig. 18. Vickers Hardness of Zr-Ga Alloys Heat Treated at 920 and 1095°C. Load – 10 kg.

[20] A. D. McQuillen, *J. Inst. Metals* 83, 181 (1954).

Vapor Pressures of Zirconium-Cadmium Alloys

J. O. Betterton, Jr. J. H. Frye, Jr.
D. S. Easton

The zirconium-cadmium system[21] (Fig. 19) shows an appreciable cadmium solubility in both allotropic modifications of zirconium with a slowly rising phase boundary between them. Arguments can be made that this indicates cadmium and zirconium to be about equal in valence, and, from this viewpoint, the alloys are suitable for the study of other factors without the complication of valence differences. Some indication of this may be seen in the two intermediate phases, Zr_2Cd and $ZrCd_2$. Both are disordered face-centered cubic phases of the composition AB_2 in which the zirconium and cadmium assume either proportion without disturbing the phase stability. The same property is also present in the corresponding, ordered face-centered cubic phases $TiZn_3$, Ti_3Hg, and $ZrHg_3$. Measurements of cadmium pressures have been started in this system to determine the heat, entropy, and free energy of the zirconium-rich phases with the hope of obtaining a greater understanding of the allotropic boundaries.

A modified form of the Hargreaves method[22] was adapted for this investigation. The principal features of the apparatus are illustrated in Fig. 20,

[21] D. S. Easton and J. O. Betterton, Jr., *Met. Ann. Prog. Rep. Oct. 10, 1957*, ORNL-2422, p 218.

[22] R. Hargreaves, *J. Inst. Metals* 64, 115 (1939).

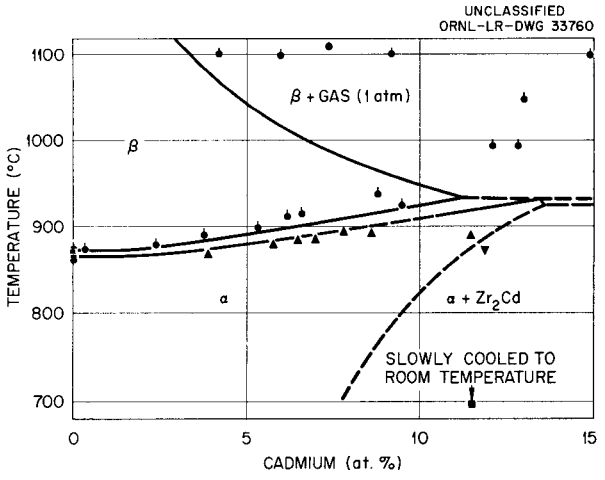

Fig. 19. The Zirconium-Rich Portion of the Zr-Cd System.

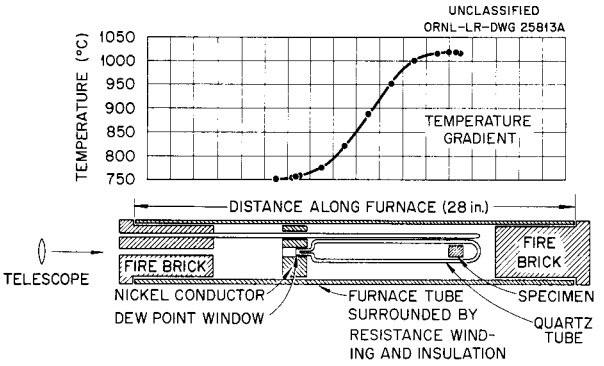

Fig. 20. Vapor Pressure Apparatus.

which also shows the nature of the temperature distribution in the furnace throughout the experiment. Improved features include a small window at the end of a short, 1-mm-bore quartz capillary which is kept at the minimum temperature of the capsule. A period of time is used to establish equilibrium between the cadmium gas and the alloy held at a higher temperature at the other end of the capsule. Then the window is cooled until a drop of liquid appears. The vapor pressures of liquid cadmium are well known, and the formula being used was obtained from Lumsden:[23]

$$\log_{10} P\ (\text{mm}) = 11.7750 - \frac{5709}{T} - 1.1283 \log_{10} T\ .$$

The capillary type of window makes the area available for condensing liquid smaller than usual in the Hargreaves apparatus, increases the sensitivity, and, since the window is placed within a closely fitting nickel block, allows the measurement to be made with known and reproducible heat flows from a temperature gradient along the axis of the furnace (3°C/in.). The apparatus was calibrated by use of a high-purity cadmium bath, care being taken to reproduce the gradient conditions, in the vicinity of the window, that were used in the alloy experiments. This calibration is shown in Fig. 21. The temperature of the observation window at the time when a liquid drop first formed or last disappeared is plotted against the rate of change of the window. The zero of the graph is the temperature of a large bath of pure liquid cadmium held isothermally at the opposite end of

[23] J. Lumsden, *Thermodynamics of Alloys*, p 134, Institute of Metals, London, 1952.

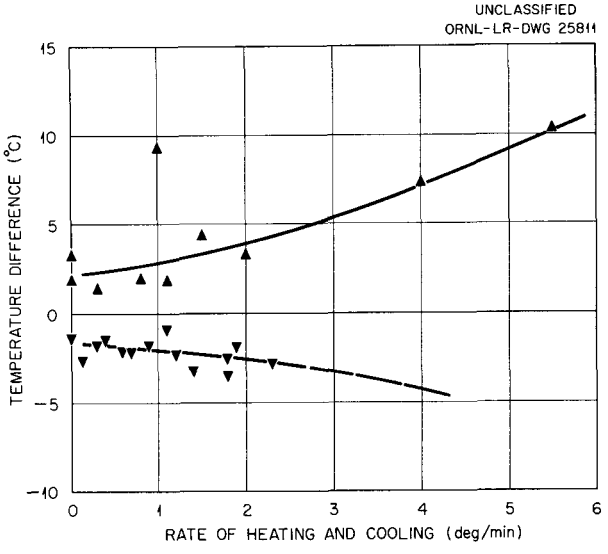

Fig. 21. Comparison of Condensation and Evaporation Temperatures with Temperature of a High-Purity Cadmium Bath.

the quartz tube. Agreement to within 1°C was obtained with rates less than 0.8°C/min and by averaging condensation and evaporation observations.

The alloys were prepared with iodide zirconium of 99.95% purity.[24] The zirconium was outgassed at 1100°C in a vacuum of 10^{-6} mm Hg for hydrogen removal, and then arc-cast into buttons and rolled into 0.011-in. foil. The foil was wound into a coil weighing ~20 g, with small strips of zirconium used as spacers, and then wrapped with a protective tantalum foil. All parts were cleaned chemically, assembled with minimum contamination, and baked out at 1000°C. Finally, 99.99% Cd (Asarco research grade) was freshly distilled into the evacuated tube from a side arm and the evacuated capsule sealed.

It was found that the initial diffusion occurred quickly in the beta region above 950°C. The equilibrium times for this and other temperatures were determined by noting the time required for constancy in the observed pressure. At the end of the experiments the specimen was cooled by breaking the capsule under water and the composition determined by chemical analysis. Small corrections to the composition of the alloy, necessary because of the different cadmium contents of the vapor phase at various temperatures, were made by use of the following equation, which applies in the case of a sinusoidal gradient:

$$N_g = \frac{PV}{R\sqrt{T_s T_w}},$$

where N_g is the number of moles of cadmium in the gas, T_s is the specimen temperature, and T_w is the window temperature.

The vapor pressures of several zirconium-cadmium alloys are shown in Fig. 22. The dotted line represents the approximate location of the allotropic phase change, with the beta phase on the left and the alpha phase on the right. The cadmium pressures increase with temperature and composition in the usual way. Only a limited number of points are shown for the 3.2% alloy, as this experiment is unfinished; the results for the 10.5% alloy are less accurate than later measurements since they were done in an earlier, less sensitive apparatus.

These data can be replotted, in a more informative and sensitive manner, as activities with respect to solid cadmium. For this purpose, the

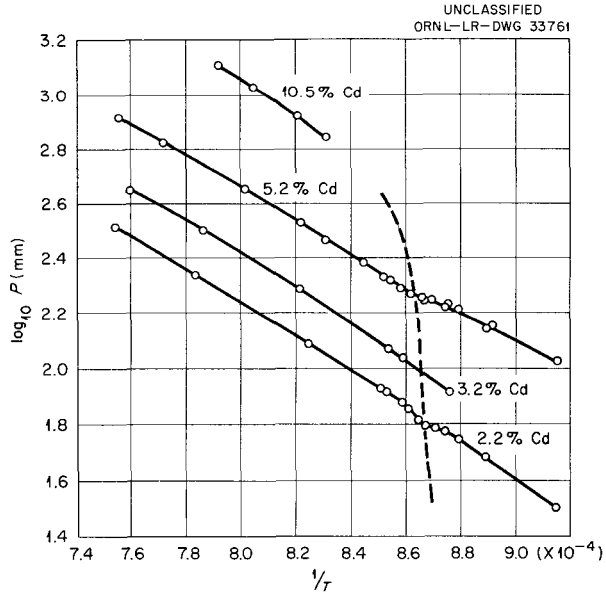

Fig. 22. Cadmium Pressures over Zr-Cd Alloys (Uncorrected for Slight Variations in Alloy Composition with Temperature).

[24] A detailed analysis can be found as batch No. 6 in ref 18.

vapor pressure of solid cadmium was taken as

$$\log_{10} P^0 \text{ (mm)} = 9.7822 - \frac{5915}{T} - $$

$$- 0.2214 \log_{10} T - 3.212 \times 10^{4} T \ .$$

The above formula is based on the specific heat[25] for solid cadmium,

$$C_p = 5.31 + 2.94 \times 10^{-3} T \ ,$$

and recent values for the heat of vaporization and the entropy of the solid metal.[26]

Cadmium vapor is assumed to be an ideal monatomic gas when it is in equilibrium with both the alloy and the solid cadmium at elevated temperatures. (Spectral investigations, which have been reviewed by Herzberg,[27] have shown the presence of weak Cd_2 molecules of the van der Waals type in cadmium gas, but the binding energy is only 0.09 ev/molecule, and it is not thought likely that such weak forces would lead to a large deviation from ideality of the gas.) Then the free energy of the cadmium in the alloy can be written relative to the solid in terms of the free-energy–pressure relations appropriate to the gas phase:

$$F^M_{Cd} = \left(\frac{\partial F}{\partial n} - F^0_{Cd} \right)$$

$$= RT \ln P - RT \ln P^0 = RT \ln A_{Cd} \ .$$

The logarithms of such activities for the zirconium-cadmium alloys are shown in Fig. 23. The horizontal scale is reciprocal temperature. The free energies of the cadmium in the alloys are indicated by the relative positions of the curves, while the slopes when divided by R are the relative partial molar heats. These heats are negative for cadmium in the beta phase, indicating a release of heat when the pure elements are mixed, whereas in the alpha phase (to the right) the slope changes from negative for the 2.2% alloy to positive for the 5.2% alloy. The positive heat in the latter may result

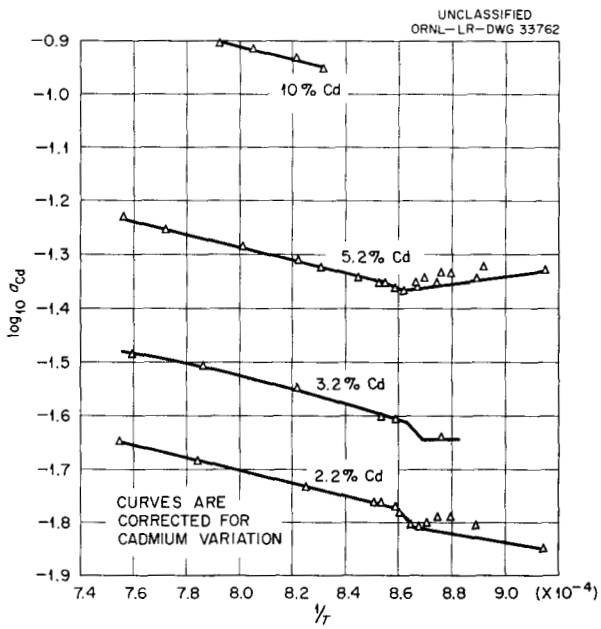

Fig. 23. Activities of Zr-Cd Alloys Relative to Solid Cadmium at the Same Temperature.

from imperfect equilibrium, as will be discussed below, or perhaps this effect results from the surprising behavior of a solute which is exothermic in one allotropic form and endothermic in the other form.

The manner of drawing the activity curves in the alpha region requires explanation. In cooling into this region, the equilibrium times assumed necessary were 50 to 150 hr, such as had been required for the beta phase. The high points indicated for the 5.2% alloy, for example, were obtained in this way. As the work progressed, the annealing times were increased to 800 to 1100 hr. The measurement at 820°C and subsequent reheating experiments were all done with these longer times and gave the points through which the linear curve was drawn. When the time factor is considered, the agreement between the cooling and heating points is better than would seem to be the case in Fig. 23. This situation is illustrated in Fig. 24 and shows that when temperature averages are taken at equal annealing times, the results agree quite well with the final temperature observed in the heating experiment. In the absence of a reheating experiment on the 2.2% Cd alloy, only a provisional line was drawn from the single 1100-hr point at $1/T = 9.15 \times 10^{-4}$ to the minimum in the curve, in analogy with the interpretation above for 5.2% Cd.

---

[25] K. K. Kelley, *U.S. Bur. Mines, Bull. No. 476* (1949).

[26] R. Hultgren, *Selected Values of the Thermodynamic Properties of Metals and Alloys*, Mineral Research Laboratory, Univ. of Calif. (1956).

[27] G. Herzberg, *Molecular Spectra and Molecular Structure. I. Spectra of Diatomic Molecules*, 2d ed., p 516, tr by J. W. T. Spinks, Van Nostrand, Princeton, N. J., 1950.

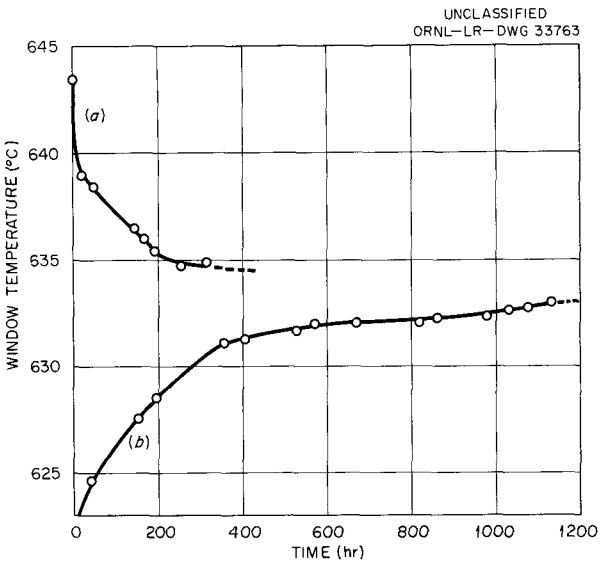

Fig. 24. Variation of the Mean Evaporation and Condensation Temperatures with Time for 5.2% Cd Alloy. (*a*) Cooled to 850°C; (*b*) heated to 850°C.

In the above experiments the diffusion rate of cadmium is clearly greater in β-zirconium than in α-zirconium. This was particularly emphasized by the 5.2% alloy, which, after a total of 4600 hr in the alpha region, was returned to the beta region and in less than 50 hr reproduced the pressure previously measured to within 0.8 mm, or 0.4%. The latter result also confirms the absence of important contamination of the zirconium-cadmium alloy during the long period of the experiment. Similar results have been found by spectroscopic analysis for silicon, whereas in neutron activation analysis 2.2 and 5.2% Cd alloys revealed only slight contaminations of silicon and tantalum. The average silicon content was 42 ppm, with a range of 4 to 91 ppm, and the average tantalum content was 23 ppm, with a range of 0.3 to 98 ppm.

It is by no means certain that 800- to 1100-hr anneals were sufficient to eliminate entirely the cadmium composition fluctuations which would be expected upon passing the alloys slowly through the $(\alpha + \beta)$ region, as was the case in the experiments with the 2.2 and 5.2% alloys. The present experiment with the 3.2% Cd alloy is being made with thinner (0.004-in.) foil, and recently this experiment was moved rapidly through the $(\alpha + \beta)$ region and into the alpha-phase region. The first point, shown in Fig. 23, has not changed in the time period 700 to 1000 hr. It is hoped to increase the time of annealing in the alpha-phase investigations by another type of experiment,[28] in which many alloys will be prepared simultaneously at constant pressure.

A convenient way to discuss the vapor-pressure data is in the form of activity coefficients. These coefficients are obtained by dividing the activities by the composition of the alloys. When this is done, the excess partial molar free energy is obtained as shown below:

$$RT \ln \gamma = RT \ln a - RT \ln X = F^M_{Cd} - \downarrow - F^M_{Cd}\ (\text{ideal}) = F^E_{Cd} .$$

These excess free energies are therefore the experimental free energies less the free-energy term which would be expected from perfectly random configurational entropy. The negative of the first derivative of $RT \ln \gamma$ is the excess of the measured entropy over that expected from perfectly random mixing.

The excess free energies are shown for the zirconium-cadmium alloys in Fig. 25 plotted against

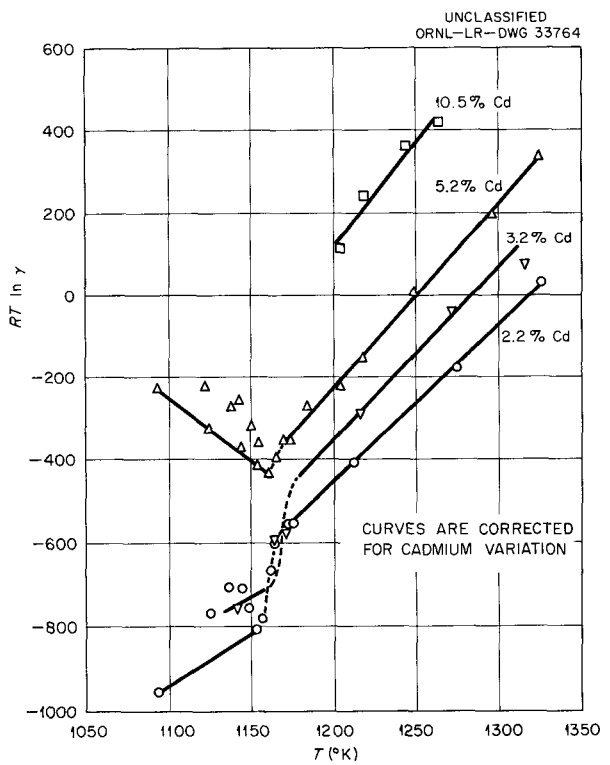

Fig. 25. Excess Free Energies of the Cadmium Component in Zirconium-Cadmium.

[28] P. Herasymenko, *Acta Met.* 4, 1 (1956).

absolute temperature. The data in the beta-phase region above 1170°K fall along fairly straight lines of approximately the same slope. The slopes of these lines were plotted, after change of sign, in Fig. 26 to show the variation of the excess entropy with composition X. Similarly, the almost linear dependence of the excess free energy with composition for the temperature 1225°K is shown in the upper part of this figure. The beta-phase excess free energies are represented to a fair degree of accuracy by

$$RT \ln \gamma_\beta \cong -4775 - 10{,}584X + 3.5T + \\ + 14.28\,TX \text{ (cal/mole)} .$$

The intercept at $T = 0$ represents the relative partial molar heat of cadmium in β-zirconium:

$$H^M_{Cd} \cong -4775 - 10{,}584X \text{ (cal/mole)} ,$$

which, of course, refers to the alloy at temperatures above 1170°K. When this is differentiated with respect to temperature, the near absence of a relative partial molar specific heat of cadmium at these temperatures is indicated: $C^M_{Cd} = 0$.

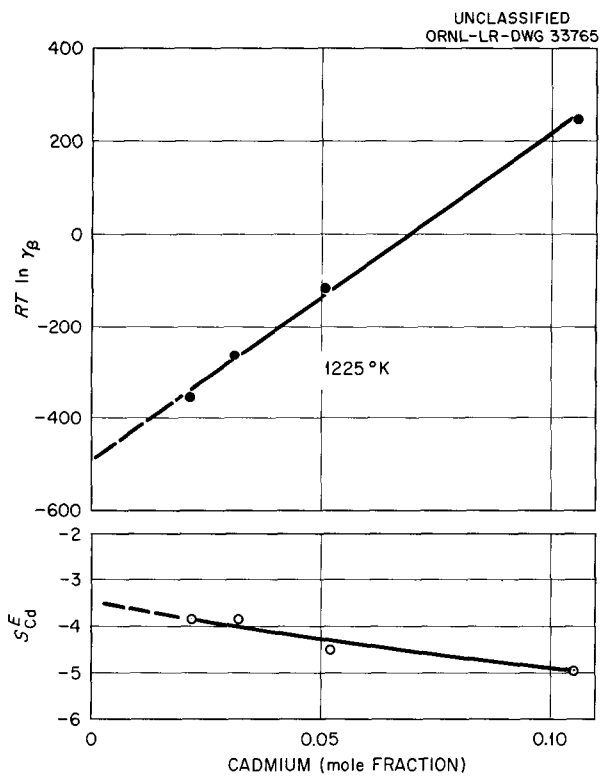

Fig. 26. Excess Free Energy and Entropy of β-Zirconium as a Function of Cadmium Content.

On the other hand, the significant negative excess entropies show that C^M_{Cd} is not necessarily negligible in β-zirconium at lower temperatures. The excess entropy (S^E) may, of course, be due to configurational entropy deviations at 0°K such as would arise from ordering effects. Since its value varies only slowly with composition, it would seem more likely to arise from the thermal entropy, given by the integral

$$\int_0^T C^M_{Cd} \frac{dT}{T} .$$

Nonzero values for C^M_{Cd} would therefore be implied at some lower temperature. The slow variation in S^E_{Cd} suggests some nearly linear process in which the entropy defect involves only a localized region about each cadmium atom.

The excess free energies for the alpha phase are shown in Fig. 25 at temperatures below 1160°K. The lines drawn are provisional and are based on the interpretation of equilibrium times which was given for the activities. The slopes of these curves as they are drawn here would indicate a very rapid change in excess entropy from a negative value for 2.2% Cd to a positive value for 5.2% Cd. It might be possible to relate such rapid changes to the interesting electronic properties of α-zirconium, but the slopes of these curves are not sufficiently well established at the present time for there to be confidence in even the sign of the excess entropy.

The above partial molar properties of the beta phase of zirconium-cadmium can be integrated by the Gibbs-Duhem procedure to determine the integral thermodynamic properties. The integral excess free energy of formation is

$$F^E = (1 - X)\int_0^X \frac{RT \ln \gamma_\beta}{(1 - X)^2} dX ,$$

and it is convenient before integrating to divide $RT \ln \gamma_\beta$ by $(1 - X)^2$ and replot the result in the form $a + bX$. A slight difference ($\sim$3% at $X = 0.10$) compared with the results from the earlier linear formula for $RT \ln \gamma_\beta$ will occur but will still be within the experimental accuracy of the data involved and will give to the integrated expression the property of equaling zero at $X = 1$. The resulting expression is shown below and is valid for

temperatures between 1175 and 1325°K and for $0 < X < 0.1$:

$$F^E \simeq (-4825X - 8275X^2 + 13{,}100X^3) - $$
$$- T(-3.5X - 10.5X^2 + 14X^3) \text{ (cal/mole)} .$$

An approximate form more appropriate to the accuracy of the data is as follows:

$$F^M_\beta \simeq X(-2780)\ R +$$
$$+ RT[X \ln X + (1 - X) \ln (1 - X) + 2.22X] ,$$

where the free energy of mixing has been included and the result is the free energy of formation of the beta phase. The integral properties are plotted in Fig. 27 for the particular temperature 1200°K. Although these curves are preliminary, they show that the free energy of the beta phase of zirconium-cadmium is nearly ideal. The effect is evidently fortuitous, since a significant negative heat of mixing exists which just balances the effect of these alloys having less than ideal entropy.

Work is continuing with Hargreaves-type experiments in which thinner foil will be used and with new experiments of the constant-pressure type. It is hoped, in this way, to provide more information about the negative excess entropy in the beta phase of zirconium-cadmium and to measure the properties of the alpha phase.

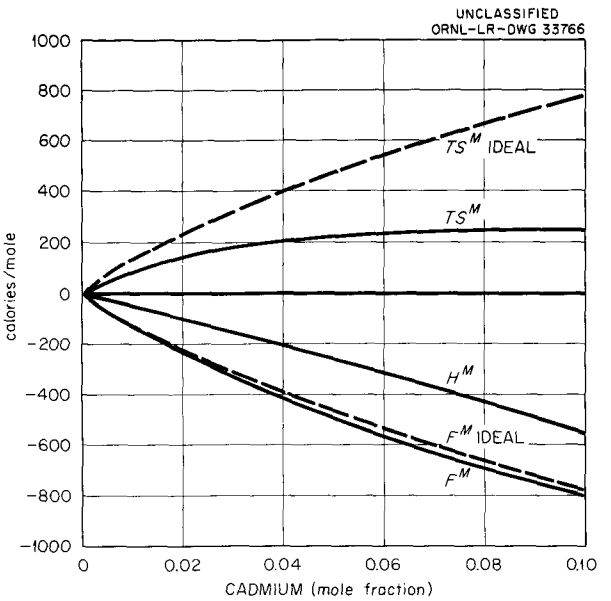

Fig. 27. Results of a Preliminary Calculation of the Integral Thermodynamic Properties of the Beta Phase at 1200°K.

X-RAY DIFFRACTION

H. L. Yakel, Jr.
O. B. Cavin R. M. Steele

X-Ray Diffraction Service Problems

H. L. Yakel, Jr. J. C. Richter
R. M. Steele O. B. Cavin

Approximately 600 x-ray diffraction patterns have been recorded in the service operations of the X-Ray Laboratory during the period covered by this report. The number is below our totals in recent years, due partly to the elimination of slurry particle-size measurements for the Chemical Technology Division. The number reflects, however, an increased attention to the selection of significant samples for diffraction experiments. This has been achieved by increased cooperation between those submitting problems and the staff of the X-Ray Laboratory.

As in the past, the majority of service problems received by this laboratory can be sorted into the categories of phase identification, verification of purity and structure (including the measurement of precise lattice parameters), semiquantitative analysis of mixtures, measurement of crystal orientations, and determination of new crystal structures.

Examples of phase-identification studies carried out this year range from corrosion products formed on metals exposed to molten salts (submitted by the General Corrosion Group of the Metallurgy Division) to the intermetallic phases which occur in the binary zirconium-lead and zirconium-gallium systems (submitted by the Theory of Alloying Group). A previously unreported phase, apparently giving a simple cubic pattern with $a_0 = 5.65$ Å, has been found in equilibrium with α-zirconium in several zirconium-rich zirconium-lead alloys. A new phase near 25 at. % Ga in the zirconium-gallium system was found to give a pattern compatible with a hexagonal unit cell, but further investigations must be made with compound-rich alloys before a final indexing and structure assignment can be given.

The Physics Division submitted a variety of materials for identification, verification of purity, and parameter measurement, prior to their study by neutron diffraction. These included some trifluorides and trichlorides of 3*d* and 4*d* transition elements, the diiodide, dihydroxide, deuteroxide, and sesquioxide of manganese, and miscellaneous compounds (MoF_5, CrTe, etc.). Results in agreement with the literature were obtained for all the compounds except MoF_3, which has been reported by Gutmann and Jack[1] as having the cubic ReO_3 structure. Preparations of this compound have thus far shown the cubic pattern, a rhombohedral pattern ($a_0 = 5.636$ Å, $\alpha = 55° 24'$) suggestive of the VF_3-type structure,[2] and a mixture of both. Further study of these patterns is continuing.

Among the samples received from the Melting and Casting Group for identification and purity verifications were products from U-Si, U-Al, U-C, U-Al-C, U-Al-C-Si, U-N, and UC_2-Al reactions. A number of samples resulting from the reactions of UO_2-Al and U_3O_8-Al at elevated temperatures were analyzed semiquantitatively. Preparations of pure UAl_2, UAl_3, and UAl_4 were obtained for standardization of these quantitative measurements.

At the request of the Fuel Chemistry Group of the Chemistry Division, L. A. Harris and G. D. White of the Ceramics Group have attempted to grow and microscopically observe single crystals of several mixed lithium and thorium (or uranium) fluorides. In the course of their investigation, Harris and White submitted for x-ray analysis several crystals of compounds supposed to be $7LiF{\cdot}6ThF_4$ and $7LiF{\cdot}6UF_4$. From single-crystal Weissenberg and precession data, these compounds have been identified as probably $3LiF{\cdot}ThF_4$ and $LiF{\cdot}4UF_4$, respectively. The unit cell data are given in Table 5.

[1] V. Gutmann and K. H. Jack, *Acta Cryst.* 4, 244 (1951).

[2] M. A. Hepworth *et al.*, *Acta Cryst.* 10, 63 (1957).

Table 5. Unit Cell Data

Cu $K\alpha = 1.5418$

Compound*	Lattice Symmetry	Lattice Parameters (Å)
$3LiF{\cdot}ThF_4$	Tetragonal	$a_0 = 6.218$ $c_0 = 6.487$
$LiF{\cdot}4UF_4$	Tetragonal	$a_0 = 7.931$ $c_0 = 6.390$

*Likely compositions; densities have not been determined.

Since these materials, while not the desired 7:6 compounds, do have atypical structures, the analyses of their diffraction patterns will continue. Crystals of the 7:6 compounds, when available, will be studied by similar methods.

Transitions in Group IVA Metal Hydrides

H. L. Yakel, Jr.

While no further experimental work on the group IVA metal hydrides was performed during the past year, the recent extension of the ligand field theory by Dunitz and Orgel[3] may shed light on the theoretical interpretation of their transitions. In order to make this application, it may be assumed that the hydrogen atoms carry small negative charges, that the eightfold coordination field about each metal atom is a combination of two tetrahedral fields, and that four $3d$ electrons are bound to each metal atom. Under these conditions the ligand field theory predicts the lattice distortion (tetragonal, $c_0/a_0 < 1$) observed. The weakness in this theory is the large number of $3d$ electrons that must be associated with the metal atoms, which would seem to leave few electrons for bonding beyond those attached to the hydrogen atom.

In an alternative approach, it may be assumed that the hydrogen atoms carry small positive charges, that the fields are tetrahedral, and that three $3d$ electrons are bound to each metal atom. This again leads to the prediction of the observed distortion, but has the advantage that now one or two electrons may be considered as bonding electrons.

High-Temperature Diffraction Experiments

H. L. Yakel, Jr.

A major effort has been made during the past year to obtain optimum vacuums in the Unicam S.150 high-temperature camera. The mechanical Wilson seals have been replaced with the more permanent Kovar seals, and the original specimen-rotation mechanism was discarded in favor of a magnetic drive. While the apparatus is now externally leak-tight, considerable problems still arise due to virtual leaks caused by the many internal metal and ceramic surfaces which outgas. A vacuum of approximately 10^{-5} mm Hg is obtainable at temperatures up to 700°C, but the pressure is likely to rise to 10^{-4} mm Hg during the initial heating.

The problem of temperature measurement in the Unicam has received further study. Frequent calibrations of the Pt, Pt–10% Rh thermocouple against the known thermal expansion of silver[4] remains the most suitable method for accurate temperature measurements for a variety of experiments. Instances arise, however, where techniques involving the incorporation of a secondary temperature standard in the diffraction specimen may be applicable. One such instance was the previously reported[5] study of the thermal behavior of $TiD_{1.98}$ at temperatures up to 450°K, where an actual mixture of the deuteride and copper filings constituted the diffraction sample.

Another instance was our recent study of the thermal expansion of filings of a Cu–15 at. % Al alloy (2-hr anneal at 750°C, cooled to room temperature at 15°C/hr) for M. S. Wechsler of the Solid State Division. Incorporation of a temperature standard in the specimen was desirable; yet at the higher temperatures of the experiment a physical mixture of the alloy and silver filings might give an undesirable diffusion reaction. A solution to the problem was found in the use of a composite double-capillary specimen, with the alloy filings sealed in an evacuated 0.3-mm-dia quartz capillary, which, in turn, was sealed in a second evacuated 0.5-mm-dia quartz capillary containing a small amount of silver filings. By suitable positioning of the sample in the x-ray beam, good diffraction patterns of both alloy and silver were obtained. Extrapolated lattice spacings derived from measurements of these patterns gave specimen temperatures to ±3°C (average) and actual alloy parameters to 1 part in 12,000. The observed thermal expansion curve for the Cu–15 at. % Al alloy is shown in Fig. 28.

Other experiments performed with the Unicam apparatus during the past year included a study of $ErMnO_3$ and of the low-temperature aging of Zircaloy-2. In the former, no transition from the hexagonal structure reported earlier[6] to a more usual ABO_3-type structure was found on heating

[3] J. D. Dunitz and L. E. Orgel, *J. Phys. Chem. Solids* 3, 20 (1957).

[4] W. Hume-Rothery and P. W. Reynolds, *Proc. Roy. Soc. (London)* A167, 25 (1938).

[5] H. L. Yakel, Jr., *Acta Cryst.* 11, 46 (1958).

[6] H. L. Yakel, Jr., *Met Ann. Prog. Rep. Oct. 10, 1957*, ORNL-2422, p 228.

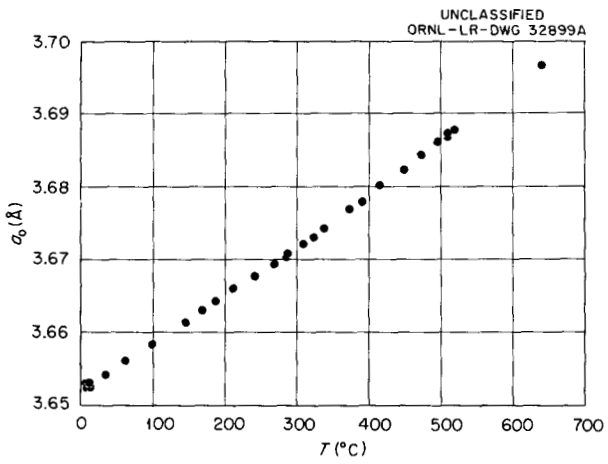

Fig. 28. Lattice Parameter of a Cu–15 at. % Al Alloy Annealed 2 hr at 750°C as a Function of Temperature up to 635°C.

to 1000°K. The latter experiment showed no obvious change, other than normal thermal expansion, in the hexagonal alpha lattice of a swaged wire of Zircaloy-2 (air-quenched from 750°C) after 100 hr at 300 and 400°C. The lattice parameter and mean thermal expansion data are given in Table 6. Corresponding values for pure zirconium are also listed for comparison.

X-Ray Scattering Factors of Transition Metals

H. L. Yakel, Jr.

Weiss and DeMarco recently reported[7] the results of an experiment in which the number of localized $3d$ electrons in metallic Cr, Fe, Co, Ni, and Cu was estimated by extrapolation of careful

[7] R. J. Weiss and J. J. DeMarco, *Revs. Modern Phys.* 30, 59 (1958).

Table 6. Lattice Parameters and Mean Thermal Expansion Coefficients of Zircaloy-2 and Zirconium

	T (°C)	Lattice Parameters			
		a_0 (Å)	c_0 (Å)	c_0/a_0	V (Å^3)
Zircaloy-2	22 ± 3	3.2279 ± 0.0004	5.1459 ± 0.0004	1.5942 ± 0.0003	46.434 ± 0.014
	305 ± 4	3.2322 ± 0.0004	5.1569 ± 0.0008	1.5955 ± 0.0004	46.657 ± 0.017
	390 ± 4	3.2348 ± 0.0003	5.1632 ± 0.0005	1.5961 ± 0.0003	46.789 ± 0.012
	493 ± 4	3.2373 ± 0.0003	5.1707 ± 0.0004	1.5972 ± 0.0003	46.930 ± 0.011
Zirconium	23 ± 2	3.2324 ± 0.0001	5.1476 ± 0.0002	1.59250 ± 0.00005	46.579 ± 0.005
	321.0*	3.23693	5.15885	1.5937	46.811
	381.8*	3.23756	5.16144	1.5942	46.853
	503.8*	3.24000	5.16826	1.5951	46.986

	T_2 (°C)	T_1 (°C)	Mean Thermal Expansion Coefficients			
			$\alpha_{ma} \times 10^6$	$\alpha_{mc} \times 10^6$	$\bar{\alpha}_m \times 10^6$	$\alpha_{mv} \times 10^{6**}$
Zircaloy-2	305	22	4.7 ± 0.4	7.6 ± 0.5	5.7 ± 0.4	17.0 ± 1.4
	390	22	5.8 ± 0.4	9.1 ± 0.6	6.9 ± 0.5	20.8 ± 1.6
	493	22	6.2 ± 0.5	10.2 ± 0.7	7.5 ± 0.5	22.6 ± 1.7
Zirconium*	300	25	5.84	7.88	6.52	19.56
	400	25	5.89	8.50	6.76	20.29
	500	25	5.95	9.13	7.01	21.03

*R. B. Russell, *The Coefficients of Thermal Expansion for Zirconium*, MIT-1073 (Oct. 19, 1951).

**$\alpha_{ma} = \frac{1}{a_0(T_1)} \cdot \frac{a_0(T_2) - a_0(T_1)}{T_2 - T_1}$, etc.

$\bar{\alpha}_m = \frac{2\alpha_{ma} - \alpha_{mc}}{3}$.

measurements of the x-ray scattering factors from which theoretical contributions of a corrected argon core were subtracted. While the number of $3d$ electrons they obtained for the close-packed metals cobalt, nickel, and copper is apparently normal, the numbers similarly derived for body-centered cubic iron and chromium are unexpectedly low (2.3 and 0.2 electrons, respectively). Since this low result for iron and chromium will, if correct, have far-reaching effects in many theoretical fields,[8] it should be verified both by a duplication of Weiss and DeMarco's original experiment and by independent methods, if possible.[9]

At the suggestion of E. O. Wollan of the Physics Division we have undertaken a series of relatively crude experiments in which the scattering power of a supposedly normal transition metal (say Ni or Cu) is directly compared with that of an abnormal metal (Fe or Cr). This is accomplished through a study of the relative intensities of diffractions from a mixture of fine, strain-free particles of the two metals. These relative intensities can be converted into relative scattering powers, with the usual corrections assumed, and then compared with the predictions of Weiss and DeMarco.

One such experiment has been performed with equal-weight mixtures of 10- and 20-μ carbonyl iron and 30- to 40-μ carbonyl nickel. The results of this experiment, which must be regarded as preliminary, suggest that the scattering factors of metallic α-iron are indeed lower than the Thomas-Fermi values,[10] but not as low as those predicted by Weiss and DeMarco. The data are summarized in Table 7, where the scattering factor of iron has been calculated relative to the Thomas-Fermi scattering factor of nickel. The exact number of $3d$ electrons in iron is, of course, a function of the assumed nickel-scattering factor and the extrapolation method used. Using an extrapolation procedure similar to that of Weiss and DeMarco, we may infer, from this preliminary experiment, that there are some four or five $3d$ electrons for iron rather than 2.3.

[8] N. F. Mott and K. W. H. Stevens, *Phil. Mag.* [8]2, 1364 (1957).

[9] R. D. Deslattes, *Phys. Rev.* 110, 1471 (1958).

[10] *International Tables for the Determination of Crystal Structures*, vol 2, p 572, Gebrüder Borntraeger, Berlin, 1935.

Table 7. Scattering Factors of α-Iron Relative to the Thomas-Fermi Values for Nickel[a]

Experimental conditions: Intensities calculated from planimetered areas on diffractometer traces using filtered, nonmonochromatic, Mo $K\alpha$ radiation

	f_{Fe}^{110}[b]	f_{Fe}^{200}	f_{Fe}^{211}
International Tables[c]	17.1	14.3	12.8
Experiment 1		12.7	
2		13.3	
3	15.7	13.4	11.3
4	16.0	13.3	11.6
5	15.4	13.9	12.3
Average	15.7 ± 0.2	13.3 ± 0.3	11.7 ± 0.4
Δf	−1.4 ± 0.2	−1.0 ± 0.3	−1.1 ± 0.4

[a] Based on assumed values for nickel of $f_{Ni}^{111} = 19.1$, $f_{Ni}^{200} = 17.8$, $f_{Ni}^{220} = 14.5$; Weiss and DeMarco (ref 7) give $f_{Ni}^{111} = 19.3$ and $f_{Fe}^{110} = 13.8$ for Mo $K\alpha$ radiation.

[b] The Fe{110} and Ni{111} reflections overlap, but an intensity for the Ni{111} calculated from the other nickel reflections in the pattern may be subtracted, leaving the Fe{110} intensity. Since this method is inherently inaccurate, the values of f_{Fe}^{110} should be given less weight.

[c] See ref 10.

In further experiments, mixtures of differently prepared iron and nickel powders, mixtures of iron powders with other elements (Cu), and refined experimental methods will be used in order to establish these scattering factors more firmly.

X-Ray Diffraction Study of Aging in Zirconium-Columbium Alloys[11]

H. L. Yakel, Jr.

Preliminary diffraction analyses utilizing the Debye-Scherrer technique in the study of aging phenomena in zirconium-columbium binary alloys[12] have been supplemented by a series of single-crystal experiments. Most of these experiments have been performed with a Zr–15 wt % Cb (nominal) hypoeutectoid alloy aged at 250, 400, and 500°C for varying periods. Some data have also been collected for the hypereutectoid alloys Zr–25 wt % Cb and Zr–33 wt % Cb aged above and below the eutectoid temperature. Weissenberg and precession techniques were used with Cu $K\alpha$ radiation ($\lambda = 1.5418$ Å).

Plates containing large grains (~3–4 mm dia) were obtained for each alloy composition by a strain-annealing technique. All samples were quenched from 1200°C, well within the beta field. Orientations of selected grains were determined by the back-reflection Laue method, and thin wire-shaped samples were prepared with the [100] direction of the selected grain parallel to the wire axis. Chemical polishing of the wires was performed with a nitric acid–lactic acid–hydrofluoric acid–water reagent.

Data on the mechanical properties and transformation kinetics of these alloys are given in "HRP Metallurgy – Zirconium Alloy Development," this report.

Results. – Typical rotation patterns of single crystals of the 15 wt % Cb alloy in the as-quenched condition showed strong diffractions associated with the retained-beta phase, very weak and diffuse diffractions associated with the omega phase, and weak diffractions associated with the Widmanstätten precipitate noted metallographically.[13] Such a pattern is shown in Fig. 29*A*. In similar photographs of the 25 and 33 wt % Cb alloys in the as-quenched condition, an absence of the omega reflections and an enhancement of the Widmanstätten reflections were observed.

On aging at 250°C for progressively longer times up to one week, the following diffraction effects were observed for the Zr–15 wt % Cb alloy:

1. The omega reflections became sharper and increased in intensity, with no apparent shift in their Bragg spacing.
2. The retained-beta reflections showed corresponding decrease in intensity but remained quite sharp. Again, within the limits of error of the measurement, the spacings of these reflections remained constant, and were equal to those of the as-quenched alloy, as aging progressed. The lattice parameter of the retained-beta phase was 3.551 ± 0.003 Å (value measured from Debye-Scherrer film was 3.546 ± 0.001 Å).
3. The diffractions associated with the Widmanstätten precipitate gradually disappeared (completely after 24 hr).

A pattern of the alloy after aging for one week at 250°C is shown in Fig. 29*B*. As the omega-phase reflections sharpened and grew more intense, it became obvious that the structure of this phase could not be of the γ-brass type suggested by Parris, Schwartz, and Frost[14] but must have the hexagonal structure proposed by Silcock, Davies, and Hardy.[15] This structure and its relation to the beta structure are shown for a Ti–16% V alloy in Fig. 30. The normal orientation relationships $[0001] \parallel [111]_\beta$, $(1\bar{2}10) \parallel (\bar{1}10)_\beta$ were observed, as well as the equal concentration of the four possible omega orientations in a single beta lattice. The lattice parameters of the omega phase, after one week of aging at 250°C, were as follows:

$$a_0 = 5.029 \pm 0.007 \text{ Å}$$
$$c_0 = 3.080 \pm 0.007 \text{ Å}$$
$$c_0/a_0 = 0.6124$$
$$\text{Volume/atom} = 22.5 \pm 0.2 \text{ Å}^3$$

---

[11] This program is being carried out in cooperation with the HRP Metallurgy Group. Crystals were prepared and heat-treated by M. L. Picklesimer and P. L. Rittenhouse of that Group.

[12] H. L. Yakel, Jr., and R. M. Steel, *Met. Ann. Prog. Rep. Oct. 10, 1957*, ORNL-2422, p 231.

[13] M. L. Picklesimer, P. L. Rittenhouse, and R. L. Stephenson, *Met. Ann. Prog. Rep. Oct. 10, 1957*, ORNL-2422, p 117.

[14] W. M. Parris, C. M. Schwartz, and P. D. Frost, *Precipitation Hardening and Embrittlement of High-Strength Titanium Alloys*, WADC-TR-54-355(Pt. II) (June 1955).

[15] J. M. Silcock, M. H. Davies, and K. H. Hardy, p 93 in *A Symposium on the Mechanism of Phase Transformations in Solids*, Monograph and Report Series No. 18, Institute of Metals, London, 1956.

UNCLASSIFIED
Y-27003

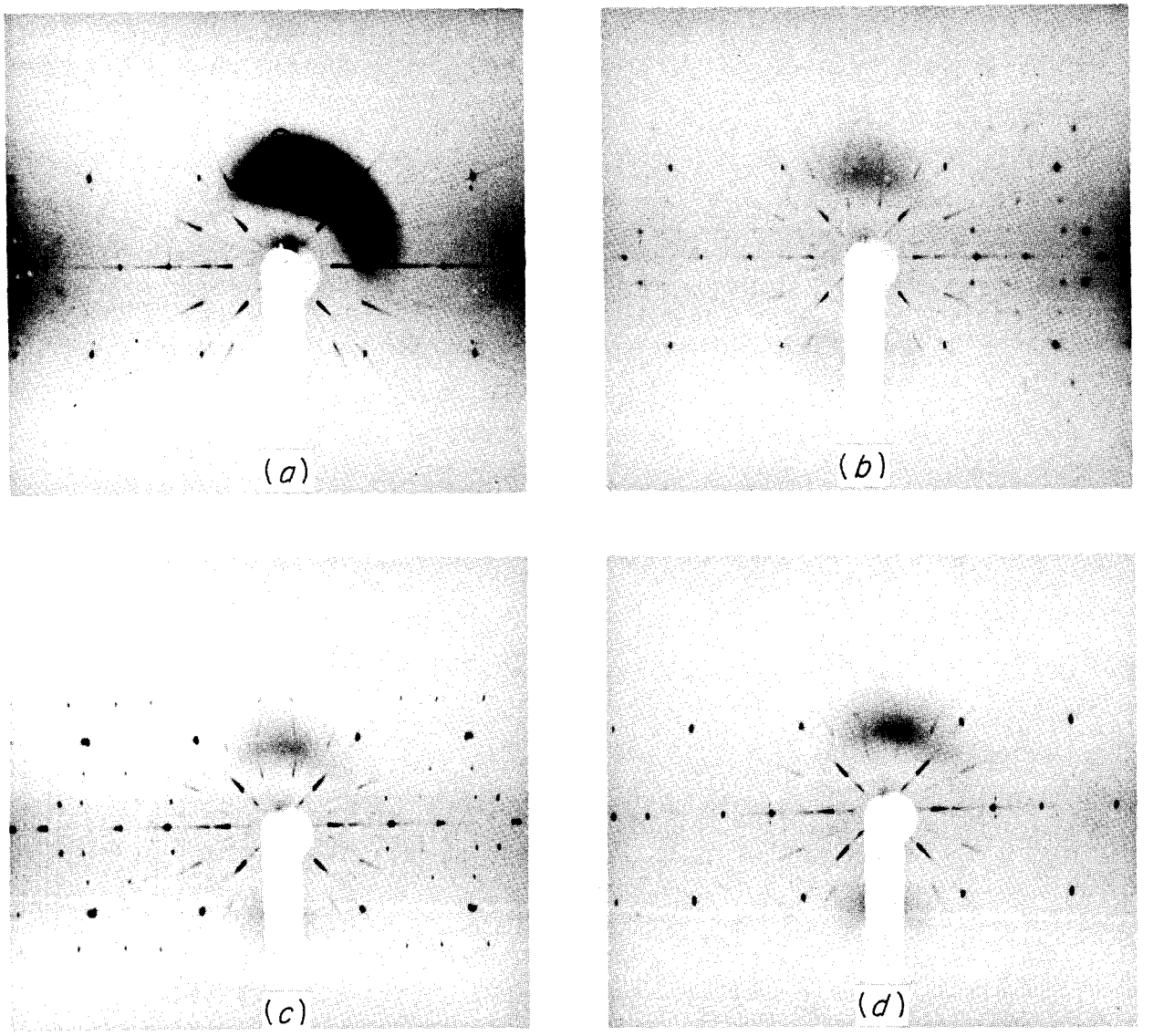

Fig. 29. Rotation Photographs of a Zr–15 wt % Cb Crystal. (*A*) As-quenched from 1200°C; (*B*) after aging one week at 250°C; (*C*) after an additional aging of 24 hr at 400°C; (*D*) after an additional aging of 1 hr at 500°C. $R = 90/\pi$ mm, $\lambda = 1.5418$ Å (Cu $K\alpha$).

On a plot of volume per atom vs columbium concentration, the observed volume of the omega phase is seen to agree with the nominal 15% alloy content, within the experimental error.

To date, a single-crystal specimen of a Zr–25 wt % Cb alloy has been aged for one week at 250°C, and only at the end of this period did a weak, diffuse omega pattern emerge. Reflections associated with the Widmanstätten phase have again virtually disappeared.

On aging the Zr–15 wt % Cb crystal (previously aged for one week at 250°C) at 400°C for times up to two weeks, the following changes in the diffraction pattern were noted:

1. Reflections from the retained-beta phase completely disappeared.

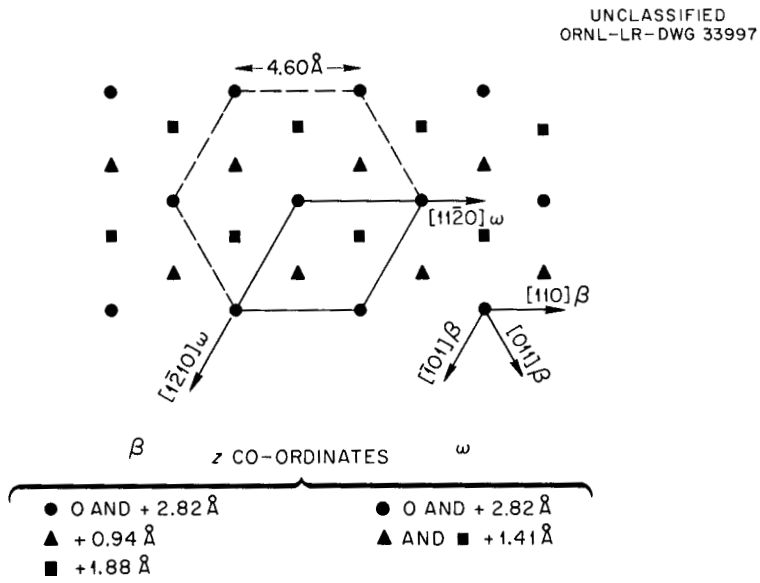

PROJECTION OF ATOMIC POSITION ON THE $(111)_\beta$ AND $(0001)_\omega$ PLANES
THE PARAMETERS OF ω ARE $a = 4.60$ AND $c = 2.82$ Å.

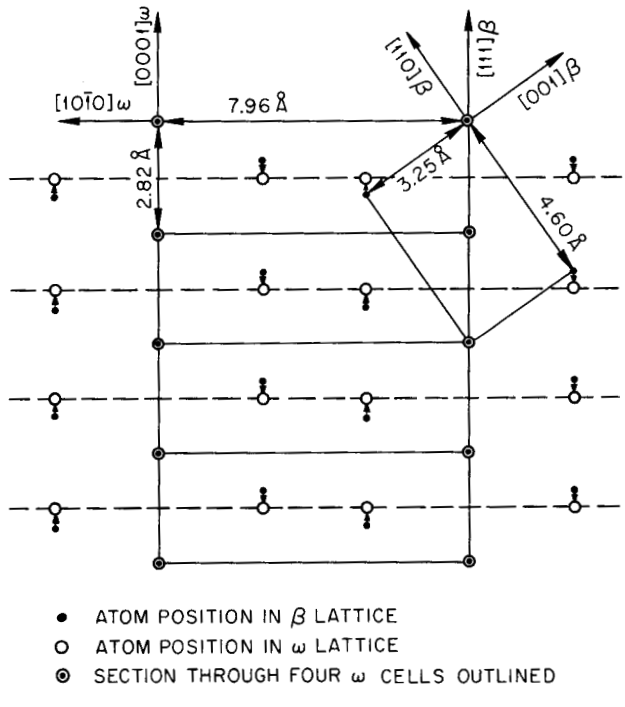

ATOMIC POSITION ACROSS THE POSSIBLE PLANE OF COHERENCE $(1\bar{1}0)_\beta$ AND $(1\bar{2}10)_\omega$.

Fig. 30. Some Relationships Between the β and ω Lattices in a Ti–16% V Alloy (See Ref 15).

2. The omega reflections continued to be sharp and intense. Their spacings were changed somewhat toward higher values. Best average lattice parameters for the omega structure in a Zr–15 wt % Cb alloy after ½ hr of aging at 400°C were as follows:

$$a_0 = 5.047 \pm 0.004 \text{ Å}$$
$$c_0 = 3.131 \pm 0.003 \text{ Å}$$
$$c_0/a_0 = 0.6204$$
$$\text{Volume/atom} = 23.02 \pm 0.07 \text{ Å}^3$$

3. Diffuse, rather weak reflections appeared which were characteristic of a body-centered cubic phase with a parameter of 3.525 ± 0.006 Å (21.9 Å^3 per atom) after ½ hr of aging at 400°C. The lattice parameter of this phase decreased slightly as aging at 400°C proceeded.

A pattern of the alloy after it was aged for 24 hr at 400°C is shown in Fig. 29*C*. The volume of the omega phase of the alloy in this condition indicates that it is considerably more zirconium-rich than it was after one week of aging at 250°C. The diffuse reflections of the columbium-rich beta phase, in conjunction with the split omega reflections near each original retained-beta reciprocal lattice point, would simulate "modulated" structure reflections on Debye-Scherrer photographs and account for this mistaken designation in the previous report.[12]

A set of quite similar observations was made from diffraction photographs of a Zr–15 wt % Cb crystal aged at 400°C but not previously aged at 250°C. An exception was the appearance of weak reflections on the low-angle (high-spacing) side of omega reflections which should not split regardless of changes in cell dimensions. These reflections emerged after a 96-hr aging period at 400°C and were attributed to the formation of a hexagonal alpha phase from the omega phase.

During the 500°C-aging of the Zr–15 wt % Cb crystal previously aged at 250 and 400°C, a marked retrogression, or reversion, of the omega structure was observed. After 1 hr at 500°C, the diffraction pattern of this sample was predominantly that of a body-centered cubic phase (a_0 = 3.543 ± 0.005 Å), with some weak indications of the hexagonal alpha (see Fig. 29*D*). After 5 hr of aging at 500°C, followed by a heavy etch, the pattern was similar to that of the as-quenched sample; that is, the reflections associated with the Widmanstätten phase had reappeared and diffuse omega reflections were noted. Some alpha reflections were again present.

After 24 hr of aging at 500°C, in an unetched condition, the transformation of beta to alpha had apparently progressed. There was evidence of the oriented formation of alpha according to the Burgers mechanism,[16] but some random nucleation could not be ruled out. The beta-phase reflections were quite diffuse and their spacings could not be measured with any accuracy.

Again a similar set of observations was made from photographs of the second Zr–15 wt % Cb crystal (previously aged at 400°C, but not at 250°C) aged at 500°C.

The aging behavior of a Zr–25 wt % Cb alloy at 650°C has also been examined. After a ½-hr aging period, the reflections associated with the Widmanstätten phase were considerably diminished in intensity and the lattice parameter of the retained-beta phase had decreased somewhat, relative to the quenched state. No indication of the dissociation of the alloy was seen, although the beta-phase reflections were broadened, as compared with those in the as-quenched condition.

After a 24-hr aging period at 650°C, the dissociation of the Zr–25 wt % Cb alloy was virtually complete. The lattice parameters of the two body-centered cubic phases were a_0 (β_1 Zr-rich) = 3.534 ± 0.002 Å (20 wt % Cb) and a_0 (β_2 Nb-rich) = 3.333 ± 0.002 Å (85 wt % Cb). Approximate compositions were estimated from a lattice parameter vs composition curve for beta-quenched alloys. They agree well with compositions predicted from the equilibrium diagram.

The observed diffuseness of the reflections of both beta phases was probably indicative of strain rather than of small grain size. The β_1 (Zr-rich) phase was evidently not stable on quenching to room-temperature, as shown by the appearance of weak alpha reflections.

Discussion. – The structure of the omega phase and the aging properties observed are entirely in agreement with Silcock's recent study[17] of the analogous phase in several titanium alloys. The possible formation of alpha from omega was observed in one instance (for the Zr–15 wt % Cb alloy aged for 96 hr at 400°C), but this should be checked rigorously.

---

[16] W. G. Burgers, *Physica* **1**, 561 (1934).

[17] J. M. Silcock, *Acta Met.* **6**, 481 (1958).

The single-crystal data for the Zr–15 wt % Cb alloy are also in reasonably good agreement with the previously reported Debye-Scherrer data, if the erroneous identification of a "modulated" structure is eliminated. That this identification is so clearly shown in error illustrates the advantages of the single-crystal experiments.

The Widmanstätten platelet phase remains somewhat of an enigma. In a series of experiments with crystals of the 25 and 33 wt % Cb alloys, the samples were heated at 250°C and examined in the etched and unetched conditions. The etching treatments had to be varied (duration, acid content, etc.), but in each case it was possible to obtain the Widmanstätten phase after suitable etching and to eliminate it by heat treatment. We interpret this as indicating that the phase may be a hydride, probably rich in columbium, since its disappearance is usually accompanied by a shrinkage of the matrix lattice. Ample evidence exists that such hydrides may be formed, particularly in titanium alloys, through etching with certain reagents.[14,17,18] The diffraction pattern of the Widmanstätten phase is deceptively simple and was at first thought to be due to a tetragonal structure with the same a_0 axis as that of the beta phase and with a c_0 axis some 12% longer. Since, however, electron micrographs of the platelets showed considerable internal structure, suggestive of twinning, this simple tetragonal structure cannot be correct. A rhombohedral structure similar to that of $NbH_{0.7}$ may give better agreement with both x-ray and microscopic data.

Future Work. – Additional single-crystal specimens of Zr–15 wt % Cb will be prepared in order to extend the 400°C-aging studies to longer times and those at 500°C to shorter times. Experiments at 450°C may further define the upper limit of thermal stability of the omega phase.

Low-temperature aging studies on Zr–25 wt % Cb and Zr–33 wt % Cb will be continued in order to follow the behavior of the metastable omega phase to higher columbium concentrations. High-temperature aging studies (just above the eutectoid temperature) will be made at more closely spaced time intervals in order to examine the initial stages of the dissociation, $\beta \rightarrow \beta_1 + \beta_2$.

Careful vacuum annealing experiments should be performed to obtain further information concerning the Widmanstätten phase.

---

[18] D. N. Williams, *Hydrogen in Titanium and Titanium Alloys*, TML-100 (May 16, 1958).

MICROSTRESSES IN CRYSTALS

B. S. Borie C. J. Sparks

A Diffraction Measurement of the Structure of Cu_2O Films Grown on Copper

B. S. Borie J. V. Cathcart

With the hope of contributing to the understanding of the growth mechanism and the structure of oxide films formed on metal surfaces, a series of diffraction experiments has been undertaken to determine whether it is possible, during the very early stages of the life of such films, to detect their presence by means of x rays and, if so, to attempt to interpret the shape of the diffraction maxima associated with the oxide film in terms of the particle size of the oxide and the deviations from crystalline perfection it may experience as it grows. The experiments have been performed with cuprous oxide grown on flat surfaces of copper single crystals. To date, attention has been confined to the (100) and (110) faces of the metal crystal.

Experimental Arrangement. – Figure 31 illustrates schematically the arrangement of the diffractometer. X rays from essentially a point source (the focal spot of the x-ray tube is, in projection, 1 mm square) impinge on a doubly bent LiF monochromator. The radii of bending are chosen so that Cu $K\alpha$ radiation is diffracted over the angular range α and so that, vertically, the diffracted beam converges at the specimen, which is a flat copper single crystal appropriately oxidized. The scattered radiation must pass through the slit S, approximately 1 cm long and 0.5 mm wide, before striking the face of a scintillation counter. The specimen and detector are mounted on a conventional G-E diffractometer so that parafocusing geometry is maintained as the counter scans through 2θ.

With this arrangement the diffraction maxima of the Cu_2O film were found to be clearly detectable for films as thin as 188 Å. On the basis of the work done to date, it is estimated that films as thin as 75 Å should still be measurable by this technique. The success of the method depends on the use of strictly monochromatic radiation, which ensures a very low background. The Bragg peaks of the surface film are so weak as compared with the background obtained with the usual nickel-filtered copper radiation that they would not be visible. It is probably necessary also that the film be substantially a single crystal, so that its whole irradiated volume may contribute to the diffracted beam to be measured.

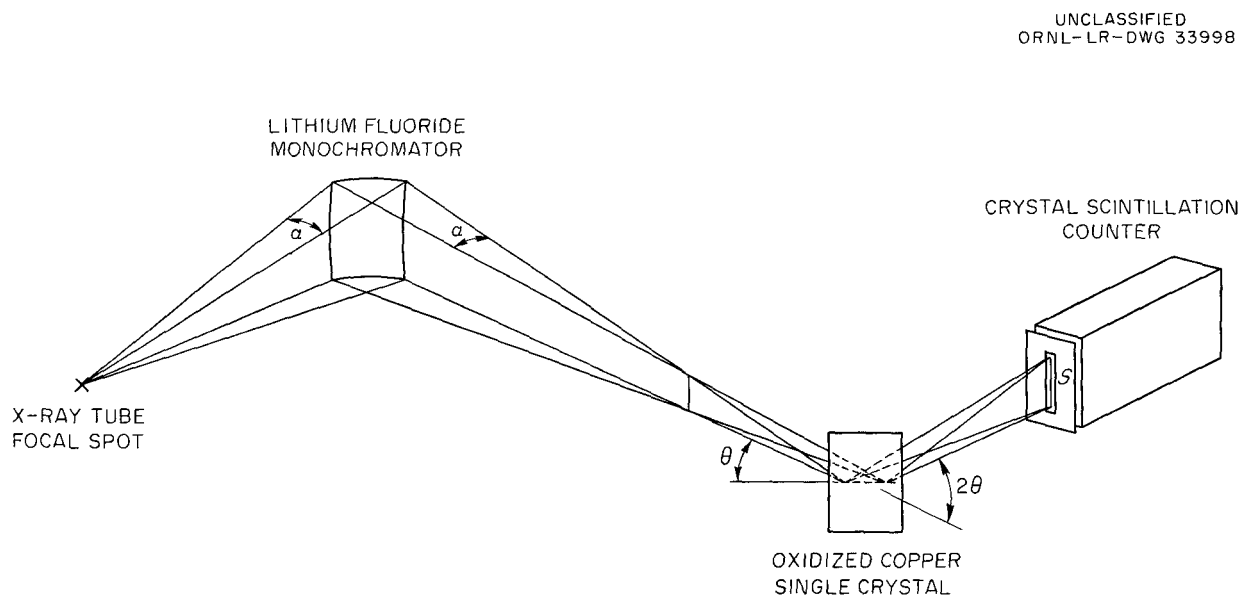

Fig. 31. Arrangement of Diffractometer for the Measurement of Thin, Surface Oxide Films.

Diffraction Theory. – Warren and Averbach[1] have shown that if the shape of a Bragg maximum $00l$, broadened because of strain and small particle size, is represented by the Fourier series

$$I(h_3) = \sum_n C_n e^{2\pi i n h_3} ,$$

then the coefficients C_n may be related directly to the particle size and strain distribution present in the sample. The continuous variable h_3 is related to the Bragg angle θ by

$$h_3 = 2|a_3|\frac{\sin\theta}{\lambda} ,$$

where $\vec{a}_3$ is a vector along a unit cell edge (the cell is assumed to be orthogonal). At the center of the diffraction peak, h_3 takes on the value l. Warren showed that

$$(1) \qquad C_n = \frac{N_n}{N}\left\langle e^{2\pi i l Z_n} \right\rangle ,$$

where N is the total number of unit cells in the crystal and N_n is the number of unit cell pairs which may be formed in such a manner that the vector between the cells is $n\vec{a}_3$. If the crystal is strained, then the vector between cells is given by $n\vec{a}_3 + Z_n\vec{a}_3$. The average indicated in Eq. 1 is taken over all such pairs which may be formed in the crystal. The area under the Bragg peaks is normalized so that C_0 is unity.

To specialize the Warren result to the case of an oxide single-crystal film adherent to a metal surface, we assume that the film is of uniform thickness and that the strain in the film is uniform in a plane parallel to the metal surface and varies only in a direction normal to the surface. In such a case, the average of Eq. 1 need be taken only over a single column of unit cells parallel to the diffraction vector, the direction of which is the film normal. Let the film be $M + 1$ unit cells thick, and let them be labeled from zero to M. Then Eq. 1 may be written

$$(2) \qquad (M+1)C_n = \sum_{m=0}^{m=M-n} e^{2\pi i l(Z_{n+m} - Z_m)} .$$

We consider the variation of Z_n as a function of n. We may take Z_0 to be zero, and if $\vec{a}_3$ is chosen to correspond to the center of gravity of the diffraction peak, we have that $Z_M = 0$. With these boundary conditions, we may write Z_n as a power series in n:

$$(3) \qquad Z_n = A_0 n(M-n)(1 + A_1 n + A_2 n^2 + \ldots) .$$

We discuss the simplest case, that for which all the A's are zero except A_0. Then

$$Z_{n+m} - Z_m = A_0 n(M-n) - 2A_0 mn ,$$

and Eq. 2 may be written

$$(4) \qquad (M+1)C_n = e^{2\pi i l A_0 n(M-n)} \sum_{m=0}^{m=M-n} e^{-4\pi i l A_0 nm} = \frac{\sin 2\pi l A_0 n(M-n+1)}{\sin 2\pi l A_0 n} .$$

In general, $2\pi l A_0 n$ is a very small angle, and so the denominator in Eq. 4 may be replaced by the angle. Let $B = A_0/|a_3|^2$, the distance $L = n|a_3|$, and the oxide film thickness $T = (M+1)|a_3|$. We may then write the Fourier coefficient of Eq. 4 in terms of T and the variable L:

$$(5) \qquad TC_L = \frac{\sin 2\pi l B L(T-L)}{2\pi l B L} .$$

Since the Fourier coefficients given by Eq. 4 or Eq. 5 are real numbers, it follows that the diffraction-line contour which they represent must be symmetrical. This restriction is a consequence of the assumption that all A_n of Eq. 3 except A_0 are zero. Any other less simple assumption would make the summation of Eq. 2 extremely difficult to perform, though, as we have seen, some such more general representation of Z_n is necessary to account for any asymmetry in the shape of the Bragg maxima.

Comparison of Theory with Experiment. – For the present, we confine our attention to those oxide films having Bragg maxima which are symmetrical and hence may possibly be described by the simple theory discussed above. Of the two orientations on which we made measurements, this was the case

[1] B. E. Warren and B. L. Averbach, *J. Appl. Phys.* 21, 595 (1950).

only for oxide grown on a (110) face of the copper single crystal.

Two films of different thicknesses on the (110) face have been examined. In the first experiment the crystal was oxidized in purified oxygen for 30 min at 250°C, and in the second, for 3 hr at 250°C. The resulting oxide film thicknesses, as measured with a polarizing spectrometer, were 188 and 538 Å, respectively. The details of the oxidation procedure have been described previously.[2]

As determined by Lawless and Gwathmey,[3] the epitaxial relation between the oxide and copper for this orientation is such that their cube axes are parallel. Hence, only reflections of the type $hh0$ may be observed without tilting the specimen so that its normal no longer lies in the plane of the diffractometer. Though other reflections may be observed by such a tilt, the geometry of our instrument becomes so distorted by tilting that little meaning may be assigned to the observed line shapes.

Measurements of the weak 110 and rather intense 220 Bragg maxima were made on the two oxide specimens. The contours of these symmetrical diffraction peaks were corrected for instrumental contributions by the method of Stokes,[4] and the resultant shapes were resolved into Fourier coefficients. A new orthorhombic unit cell for the oxide was chosen so that the two useful reflections could be indexed 001 and 002 (in order to obtain reflections of the type $00l$, as assumed by the theory).

In attempting to fit the theory, it is useful to consider the function LC_L, which, from Eq. 5, is given by

$$LC_L = \frac{\sin 2\pi lBL(T - L)}{2\pi lBT} . \tag{6}$$

As L increases, this function increases from zero and passes through a maximum. The maximum may be of two kinds, depending on the magnitudes of the parameters lB and T. If these parameters are such that $lBL(T - L) = 1$ for some L, then this point corresponds to the maximum, and $LC_L(\max) = 1/2\pi lBT$. The function then decreases slowly, and it is not symmetrical about its maximum. On the other hand, if lB and T are such that $lBL(T - L) < 1$ for all L, then the maximum value of LC_L occurs at $L = T/2$, and the function is symmetrical about its maximum.

Figure 32 is a plot of the experimentally measured values of LC_L as a function of L for $00l = 001$ and 002 as determined from the 188-Å oxide layer. It is clear from the shapes of these curves that 002 has a maximum of the first kind, from which may be determined BT, while 001 is symmetrical about its maximum, thus determining the thickness T of the film. The experimental measurements are compared in Fig. 32 with values of LC_L computed from Eq. 6 by using values of B and T as determined from the maxima. Figure 33 is a similar comparison of theory and experiment for the 538-Å layer.

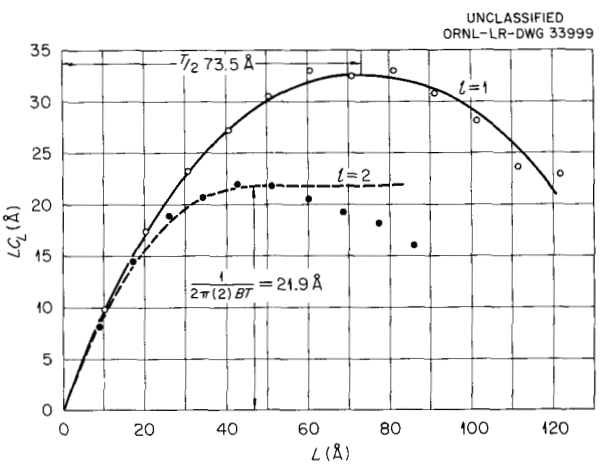

Fig. 32. Comparison of the Experimental Values of LC_L with Theory for the 188-Å Oxide Film.

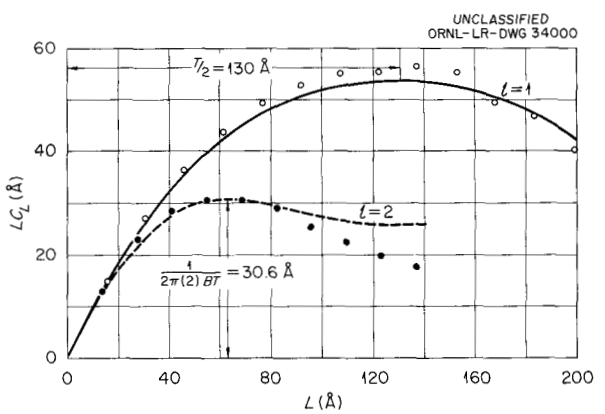

Fig. 33. Comparison of the Experimental Values of LC_L with Theory for the 538-Å Oxide Film.

[2] J. V. Cathcart, *Met. Ann. Prog. Rep. Oct. 10, 1957*, ORNL-2422, p 93.

[3] K. R. Lawless and A. T. Gwathmey, *Acta Met.* 4, 153 (1956).

[4] A. R. Stokes, *Proc. Phys. Soc. (London)* 61, 382 (1948).

Discussion. – To interpret the meaning of the parameters B and T, let the interplanar spacing at the nth unit cell be given by $d_n = d(1 + \epsilon_n)$, where d is the average interplanar spacing as determined from the Bragg angle corresponding to the peak center. Then from the definition of Z_n,

$$\epsilon_n = Z_n - Z_{n-1} = A_0 n(M - n) - $$

$$- A_0(n - 1)(M - n + 1) = A_0(M + 1) - 2A_0 n \ ,$$

or with $B = A_0/|a_3|^2$, $L = n|a_3|$, $T = (M + 1)|a_3|$, and $d = |a_3|/l$,

$$\epsilon_L = BlTd - 2BlLd \ . \tag{7}$$

For the 188-Å oxide layer, $dl = 3.065$ Å, $2\pi BT = (43.8 \text{ Å})^{-1}$, and $T = 147$ Å, from which one may compute that $d_n = 3.031$ Å at $n = 0$ and $d_n = 3.099$ Å at $n = M + 1$. The interplanar spacing varies linearly between these values across the film thickness of 147 Å. Corresponding values for the 538-Å film are $T = 260$ Å, $d_0 = 3.033$ Å, and $d_{M+1} = 3.081$ Å. This variation of the interplanar spacing as a function of position in the two films is illustrated in Fig. 34. All d's referred to here are those of the planes 110 (cubic indexing).

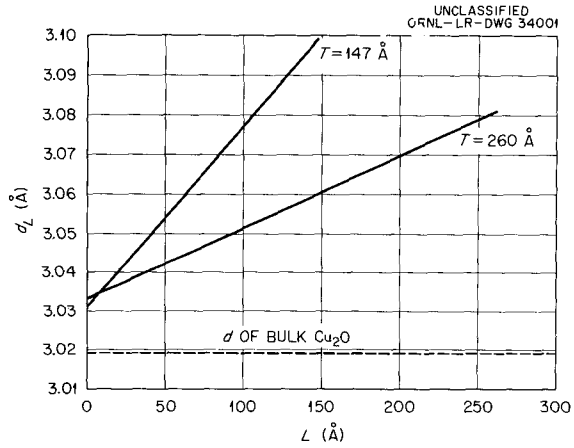

Fig. 34. Variation of the Interplanar Spacing as a Function of Position in the Oxide Films.

From this figure, it is clear that, as compared with the lattice parameters of the bulk oxide, there is in both films a significant lattice expansion normal to the surface of the oxide. In the thicker film, the average interplanar spacing is closer to that of the bulk oxide, and the gradient of this lattice expansion is less extreme than that for the thinner film.

Unfortunately, the direction of the lattice-expansion gradient in the oxide film cannot be fixed on the basis of the x-ray data presented here; therefore, no unambiguous conclusions can be drawn concerning the relationship between this lattice expansion and the epitaxial strain or the type of lattice defect existing in the film. If the defects were cation vacancies, a higher concentration of vacancies would be expected at the gas-oxide interface, suggesting that the larger interplanar spacings occur at this interface. It is not impossible, however, that some other type of defect (e.g., interstitial cations) may predominate in these relatively thin films even though it has been shown that the defects in much thicker Cu_2O films are, in the main, cation vacancies.[5] It may be possible to resolve this question through the careful measurement of the integrated intensities in absolute units of the two reflections studied, since their structure factors should be very sensitive to concentrations of vacancies or interstitial ions. Measurements of this sort are planned.

There is a significant discrepancy between the film thickness as measured by x rays and that determined by the polarizing spectrometer. Indeed, for the thicker film, the polarizing spectrometer value is about twice that obtained from the diffraction experiment. Presumably, the reason for this is that the spectrometer measures the *total* film thickness, while the diffraction line contour is sensitive only to that portion of the film which is a single crystal throughout its thickness. At present, it is not clear what the part of the film which is not a single crystal may be. It may be a polycrystalline layer of Cu_2O, though this possibility does not appear to be consistent with electron diffraction photographs of similar films stripped from the metal single crystal. An extra, very broad, very weak line was observed from the thicker film which presumably is to be associated with the discrepancy discussed here. It is hoped that further work will clarify this point.

Though the data of Figs. 32 and 33 appear to fit the theory reasonably well, the measurements at larger values of L deviate somewhat from the predictions of the theory. Since these points are

[5] J. Bardeen, W. H. Brattain, and W. Shockley, *J. Chem. Phys.* 14, 714 (1946).

associated with small, high-order Fourier coefficients, they undoubtedly suffer most from experimental error. They are also the points most affected by deviations from the assumption that the film is of uniform thickness.

The Fourier coefficients are also sensitive to the choice of background, which in this case is primarily made up of temperature diffuse scattering from the metal substrate. For the measurements here discussed, background was rather arbitrarily chosen to be a straight line connecting the tails of the Bragg peak. This is probably fairly inaccurate and unnecessary. Future experiments will be corrected for background simply by subtracting the scattering observed from an unoxidized copper crystal.

Short-Range Structure of the Alloy Cu–16 at. % Al

B. S. Borie C. J. Sparks

Radiation damage experiments by Wechsler and Kernohan[6] have shown that the electrical resistivity of the face-centered cubic alloy Cu–16 at. % Al decreases as a function of time in the reactor, passes through a minimum, and then increases continuously. Since pure metals do not exhibit such a decrease, it has been suggested that the resistivity change may be associated with a radiation-induced change in the short-range order present in the alloy. To determine whether or not this is the case, diffuse x-ray scattering measurements before and after exposure of the alloy to reactor irradiation have been made. This report is concerned only with the interpretation of such measurements before irradiation.

Diffraction Theory. – The theory developed by Warren, Averbach, and Roberts[7] has been used. They have shown that for a solid solution containing short-range order in which the atoms do not lie exactly on their lattice sites because of a difference in their size, or perhaps because of some other difference in the atomic properties of the two kinds of atoms, the diffuse x-ray scattering may be written

$$(8)\qquad \frac{I}{Nm_A m_B (f_A - f_B)^2} = \sum_{lmn} \alpha_{lmn} \cos 2\pi(h_1 l + h_2 m + h_3 n) - \sum_{lmn} \beta_{lmn}\, 2\pi(h_1 l + h_2 m + h_3 n)\sin 2\pi(h_1 l + h_2 m + h_3 n) \ .$$

Here, I/N is the diffuse x-ray intensity in electron units per atom, m_A is the fraction of the total number of atoms in the crystal which have atomic scattering factor f_A, and m_B and f_B are similar quantities for B atoms. The integers l, m, and n define a particular coordination shell. The quantity α_{lmn} is the short-range-order parameter associated with the lmn shell. The continuous variables h_1, h_2, h_3 define a particular position in reciprocal space. At the Bragg maxima, they take on values equal to half the Miller indices hkl.

The parameter β_{lmn} is associated with the fact that the equilibrium positions of the atoms do not correspond precisely to lattice sites. If the atomic positions do correspond to sites in the lattice, then all β_{lmn} are zero. The derivation of Eq. 8 is dependent on the assumption that the displacement $\vec{\delta}$ of an atom from its ideal site is sufficiently small that

$$\exp\left[2\pi i\left(\frac{\vec{s} - \vec{s}_0}{\lambda}\right)\cdot\vec{\delta}\right]$$

may be well approximated by

$$1 + 2\pi i\left(\frac{\vec{s} - \vec{s}_0}{\lambda}\right)\cdot\vec{\delta} \ .$$

The unit vectors $\vec{s}_0$ and $\vec{s}$ define the directions of the incident and scattered beams.

If data are gathered only in the plane $h_3 = 0$ in reciprocal space, as was done here, then Eq. 8 may be written

$$(9)\qquad I'(h_1 h_2) = \sum_{lm} A_{lm} \cos 2\pi(h_1 l + h_2 m) - \sum_{lm} B_{lm} 2\pi(h_1 l + h_2 m)\sin 2\pi(h_1 l + h_2 m) \ ,$$

where

$$I'(h_1 h_2) = \frac{I(h_1 h_2 0)}{Nm_A m_B (f_A - f_B)^2} \ ,$$

$$A_{lm} = \sum_n \alpha_{lmn} \ ,$$

[6] M. S. Wechsler and R. H. Kernohan, *Solid State Ann. Prog. Rep. Aug. 31, 1958*, ORNL-2614 (in press).

[7] B. E. Warren, B. L. Averbach, and B. W. Roberts, *J. Appl. Phys.* 22, 1493 (1951).

and

$$B_{lm} = \sum_n \beta_{lm} \ .$$

Separation of the Size-Effect Modulations from the Short-Range-Order Diffuse Scattering. – Figure 35 shows a contour map of the diffuse intensity distribution in absolute units in the h_1h_20 plane of reciprocal space after division by the atomic form factor for copper and after correction for Compton scattering. It is apparent that this intensity distribution may not be explained simply by the short-range-order cosine series of Eq. 9. For example, the points $h_1h_2 = \frac{1}{2}, \frac{1}{2}$ and $h_1h_2 = \frac{3}{2}, \frac{1}{2}$ should be symmetry centers if this were the case, and they quite clearly are not. The diffuse scattering map shows significant diffraction effects associated with the fact that the atoms do not lie precisely on the sites of a lattice.

Before a Fourier transform may be performed on the diffuse scattering to obtain short-range-order parameters, a correction for the size-effect modulations is necessary. This was done in the following way: The function $Q(h_1h_2) = I'(h_1h_2) - I'(h_1, h_2 + 1)$ was formed. From Eq. 9 it is clear that

$$Q(h_1h_2) = \sum_{lm} B_{lm}\, 2\pi m \sin 2\pi(h_1 l + h_2 m) \ .$$

From this expression may be obtained

$$(10)\quad P(h_1h_2) = h_2 Q(h_1h_2) + h_1 Q(h_2h_1)$$

$$= \sum_{lm} B_{lm} 2\pi(h_1 l + h_2 m)\sin 2\pi(h_1 l + h_2 m) \ .$$

From Eqs. 9 and 10 there results

$$(11)\quad I'(h_1h_2) + P(h_1h_2) = \sum_{lm} A_{lm} \cos 2\pi(h_1 l + h_2 m) \ .$$

The size-effect series is thus eliminated from the data without the determination of the parameters

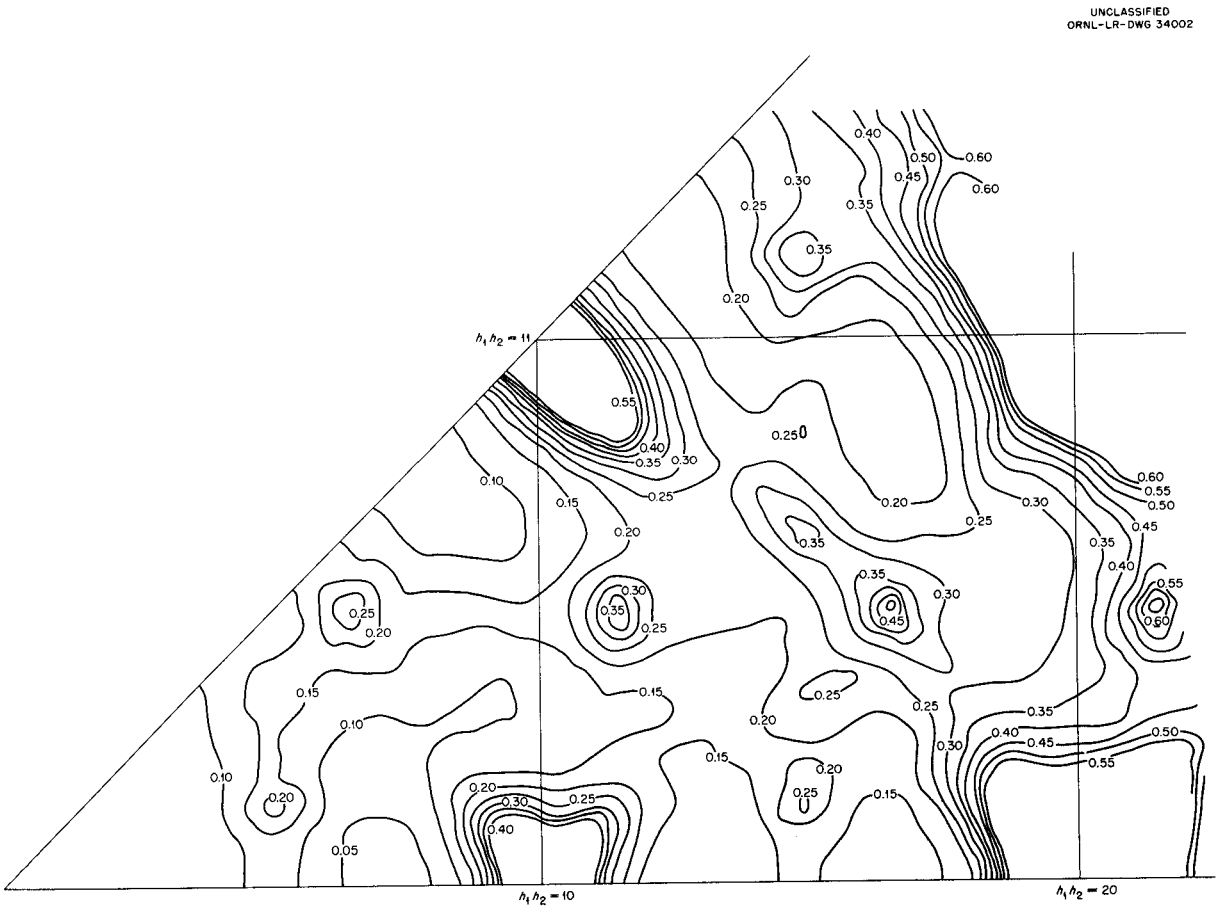

Fig. 35. Diffuse Intensity Distribution in the h_1h_20 Plane of Reciprocal Space for Cu–16% Al. Units are I/Nf^2_{Cu}.

B_{lm} and without any assumptions concerning their relative magnitudes. Since the assumptions required for the derivation of Eq. 9 are best near the origin of reciprocal space and since the effect of thermal motion on the short-range-order diffuse scattering is smallest in this region, the above-described separation was performed in the area defined by $h_1, h_2 < 1$. The resultant map is shown in Fig. 36. Its distribution has all of the required symmetry properties of the cosine series of Eq. 11.

Interpretation of the Diffuse Scattering. – The map of Fig. 36 shows diffuse maxima at the points $h_1h_2 = 0.5, 0.15$; $h_1h_2 = 0.5, 0.35$; $h_1h_2 = 0.65, 0.5$; and $h_1h_2 = 0.85, 0.5$. A similar intensity distribution for Cu_3Au, quenched from high temperature and then heat-treated for a short time below the critical temperature, has been reported by Guinier and Griffoul.[8] They interpret such an array of

[8] A. Guinier and R. Griffoul, *Rev. met.* **45**, 387 (1948).

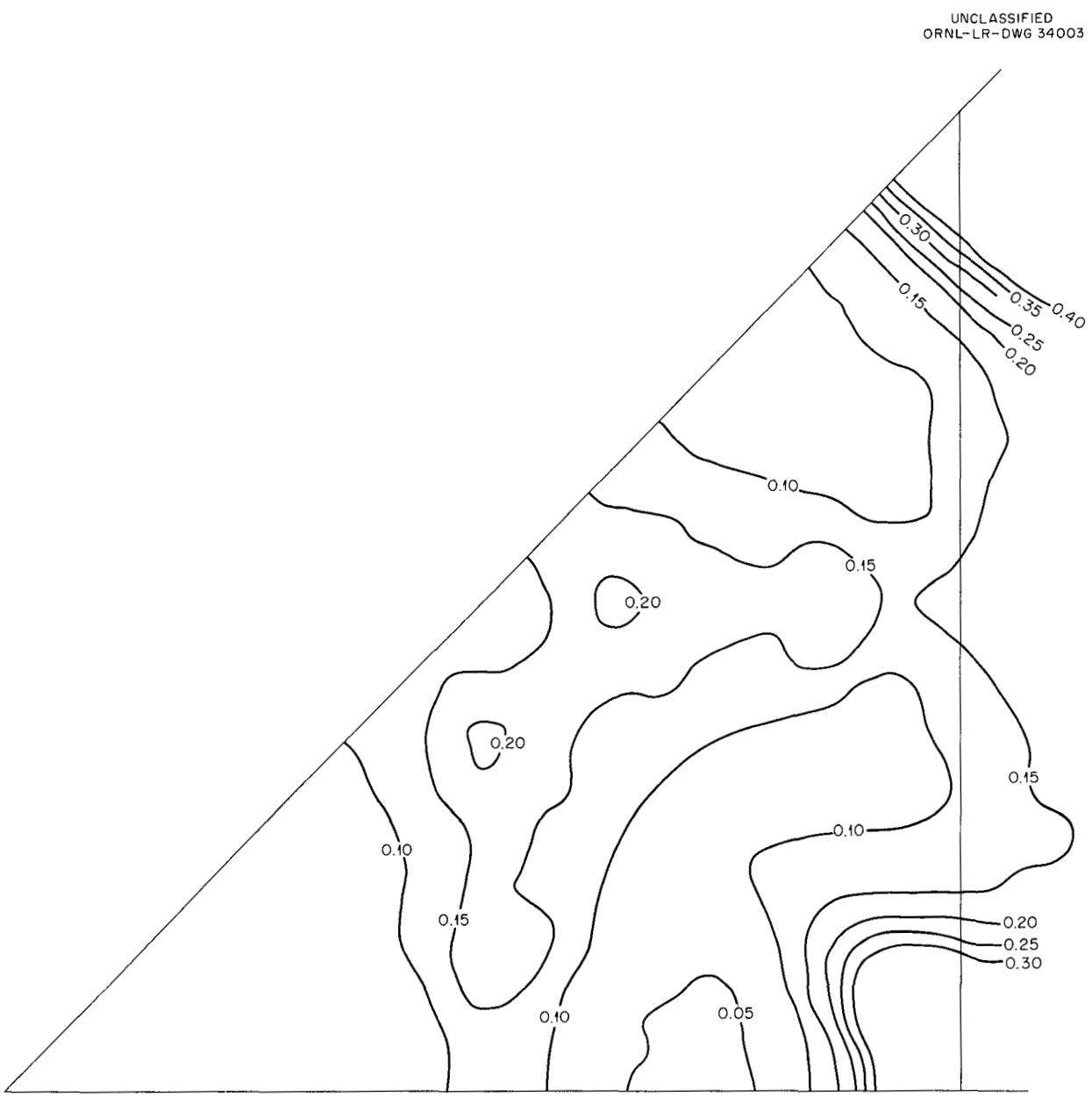

Fig. 36. Diffuse Intensity Distribution After Size-Effect Correction.

satellites about the normal superstructure positions with the aid of a theory developed by Wilson.[9] It is assumed that the crystal is composed of highly ordered antiphase domains, the domains being bounded by faults on the (100) planes in such a way that gold atoms have only copper nearest neighbors. The average domain size is determined by the distance from a normal superstructure position to a diffuse maximum. If the domains are infinitely large, the maxima occur at the superstructure positions. If, on the other hand, the domains are as small as possible (one unit cell), the maxima occur halfway between the normal superstructure positions.

If a similar interpretation of the diffuse intensity discussed here is attempted, it is concluded that the probability of faulting on (100) planes in a way similar to that found by Guinier and Griffoul is greater than the probability that no such fault occurs. This must be so since the diffuse maxima are farther from the normal superstructure positions than they are from a point halfway between the superstructure positions. This leads to a model for the short-range structure in this alloy in which aluminum atoms form distorted tetrahedra with their second and third nearest neighbors as illustrated in Fig. 37. All the nearest neighbors of an aluminum atom are presumed to be copper. One may imagine small islands of clusters of such tetrahedra embedded in a copper matrix, more or less randomly oriented relative to each other, their density in the alloy being determined by its composition.

[9] A. J. C. Wilson, *X-Ray Optics. The Diffraction of X-Rays by Finite and Imperfect Crystals*, p 97, Methuen, London, 1949.

UNCLASSIFIED
ORNL-LR-DWG 34004

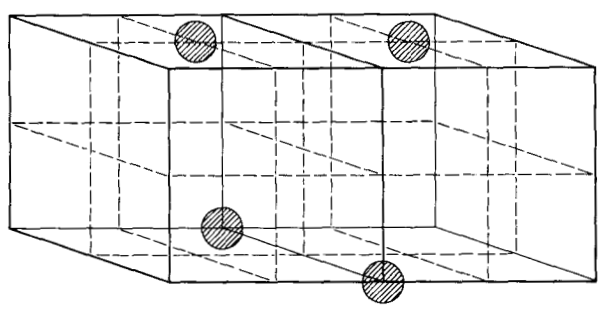

Fig. 37. Two Face-Centered Cubic Unit Cells Showing the Proposed Distorted Tetrahedral Aluminum Array. The face centers are marked by intersections of the dashed lines. Other atomic sites in the vicinity of the four aluminum atoms are presumed to be occupied by copper.

Fourier coefficients A_{lm} of the diffuse scattering distribution of Fig. 36 have been determined with the aid of the Oracle. First efforts to match them with coefficients computed from the model discussed above appear promising. An attempt has been made to reproduce the experimentally determined size-effect modulations as given by Eq. 10 by assuming that the aluminum atoms are distorted from their ideal face-centered cubic sites in such a way that the tetrahedra become more regular; these results also indicate the correctness of this model for the short-range structure of the alloy.

It is hoped that a similar treatment of the diffuse scattering measured from an irradiated specimen will show how reactor radiation rearranges the atoms in this alloy.

Refinement of the Diffraction Theory for the Atomic Size Effect in Alloys

B. S. Borie

In a recent paper[10] (referred to here as Part I), the writer developed a theory for the diffraction effects to be observed because of atomic size from a binary substitutional solid solution. The theory is an extension of the ideas of Huang[11] and Warren, Averbach, and Roberts.[7] It was shown that, in general, both the Huang diffuse scattering and the Warren modulations of the diffuse scattering are to be observed, and that the Bragg maxima, though still sharp, are reduced in intensity by a factor similar to the Debye factor for thermal motion. All three effects were expressed in terms of a single parameter, C_A, which is a measure of the degree to which the sizes of the two kinds of atoms differ from the average atomic size as determined by the lattice constants of the alloy.

It was necessary to evaluate the lattice sum associated with the Huang diffuse scattering by means of an integral approximation. The resultant expression for the total diffuse scattering was rather complicated and certainly very approximate. It is the object of this paper to show that, for a solid solution with no order, the diffuse scattering may be expressed in a much simpler and more

[10] B. S. Borie, *Acta Cryst.* 10, 89 (1957).

[11] K. Huang, *Proc. Roy. Soc. (London)* A190, 102 (1947).

accurate form, in terms of a single lattice sum which may be readily evaluated numerically.

Diffraction Theory. – It is convenient to begin this modification of the size-effect theory with Eq. 14 of Part I, which may be written:

$$(12)\quad \frac{I}{N} = (m_A f_A + m_B f_B)^2 (1 - 2M') \sum_{n \neq m} \exp\left(i\vec{k}\cdot\vec{r}_{mn}\right) + (m_A f_A^2 + m_B f_B^2) +$$

$$+ 2m_A C_A (m_A f_A + m_B f_B)(f_A - f_B) \sum_{n \neq m} \frac{i\vec{k}\cdot\vec{r}_{mn}}{|\vec{r}_{mn}|^3} \exp\left(i\vec{k}\cdot\vec{r}_{mn}\right) +$$

$$+ (m_A f_A + m_B f_B)^2 \sum_{n \neq m} H_{mn} \exp\left(i\vec{k}\cdot\vec{r}_{mn}\right) .$$

The notation is that of Part I: I/N is the scattered x-ray intensity in electron units per atom; $\vec{k}$ is defined by

$$\vec{k} = \frac{2\pi}{\lambda}\left(\vec{s} - \vec{s}_0\right) ,$$

where $\vec{s}$ and $\vec{s}_0$ are unit vectors in the directions of the scattered and incident beams; and $\vec{r}_{mn}$ is the vector between atomic sites m and n in the undistorted lattice. The crystal is composed of A and B atoms, a fraction m_A of which are A atoms of atomic scattering factor f_A. Associated with the size difference of the two kinds of atoms are distortion constants C_A and C_B, which are related by the expression $m_A C_A + m_B C_B = 0$. Both $2M'$ and H_{mn} are lattice sums:

$$(13)\quad 2M' = \frac{m_A}{m_B} C_A^2 \sum_{j \neq m} \frac{\left(\vec{k}\cdot\vec{r}_{mj}\right)^2}{|\vec{r}_{mj}|^6} ,$$

$$(14)\quad H_{mn} = \frac{m_A}{m_B} C_A^2 \sum_{j \neq m,n} \frac{\vec{k}\cdot\vec{r}_{mj}}{|\vec{r}_{mj}|^3} \frac{\vec{k}\cdot\vec{r}_{nj}}{|\vec{r}_{nj}|^3} .$$

To the first term of Eq. 12 we add

$$(m_A f_A + m_B f_B)^2 (1 - 2M')$$

to complete the sum for $n = m$, and we subtract it from the remaining terms:

$$(15)\ \frac{I}{N} = (m_A f_A + m_B f_B)^2 (1 - 2M') \sum_n \exp\left(i\vec{k}\cdot\vec{r}_{mn}\right) + m_A m_B (f_A - f_B)^2 +$$

$$+ 2m_A C_A (m_A f_A + m_B f_B)(f_A - f_B) \sum_{n\neq m} \frac{i\vec{k}\cdot\vec{r}_{mn}}{|\vec{r}_{mn}|^3} \exp\left(i\vec{k}\cdot\vec{r}_{mn}\right) +$$

$$+ (m_A f_A + m_B f_B)^2 \left[2M' + \sum_{n\neq m} H_{mn} \exp\left(i\vec{k}\cdot\vec{r}_{mn}\right)\right] .$$

The first part of Eq. 15 corresponds to the sharp crystalline reflections reduced in intensity by a factor $(1 - 2M')$. The remaining terms give the diffuse scattering, which, with the aid of Eqs. 13 and 14, may be written

$$(16)\ \frac{I_D}{m_A m_B N} = (f_A - f_B)^2 + 2(f_A - f_B)(m_A f_A + m_B f_B) \frac{C_A}{m_B} \sum_{n\neq m} \frac{i\vec{k}\cdot\vec{r}_{mn}}{|\vec{r}_{mn}|^3} \exp\left(i\vec{k}\cdot\vec{r}_{mn}\right) +$$

$$+ (m_A f_A + m_B f_B)^2 \frac{C_A^2}{m_B^2} \left[\sum_{j\neq m} \frac{\left(\vec{k}\cdot\vec{r}_{mj}\right)^2}{|\vec{r}_{mj}|^6} + \sum_{n\neq m} \sum_{j\neq m,n} \frac{\vec{k}\cdot\vec{r}_{mj}}{|\vec{r}_{mj}|^3} \frac{\vec{k}\cdot\vec{r}_{nj}}{|\vec{r}_{nj}|^3} \exp\left(i\vec{k}\cdot\vec{r}_{mn}\right) \right] .$$

Equation 16 is a perfect square if the square of the summation in the second term gives the two lattice sums of the last term. With the notation

$$G(k,n) = \frac{i\vec{k}\cdot\vec{r}_{mn}}{|\vec{r}_{mn}|^3} \exp\left(i\vec{k}\cdot\vec{r}_{mn}\right) ,$$

we may write

$$(17)\ \left| \sum_{n\neq m} G(k,n) \right|^2 = \sum_{n\neq m} \frac{i\vec{k}\cdot\vec{r}_{mn}}{|\vec{r}_{mn}|^3} \exp\left(i\vec{k}\cdot\vec{r}_{mn}\right) \sum_{j\neq m} \frac{\left(-i\vec{k}\cdot\vec{r}_{mj}\right)}{|\vec{r}_{mj}|^3} \exp\left(-i\vec{k}\cdot\vec{r}_{mj}\right)$$

$$= \sum_{j\neq m} \frac{\left(\vec{k}\cdot\vec{r}_{mj}\right)^2}{|\vec{r}_{mj}|^6} + \sum_{n\neq m} \sum_{j\neq m,n} \frac{\vec{k}\cdot\vec{r}_{mn}}{|\vec{r}_{mn}|^3} \frac{\vec{k}\cdot\vec{r}_{mj}}{|\vec{r}_{mj}|^3} \exp\left[i\vec{k}\cdot\left(\vec{r}_{mn} - \vec{r}_{mj}\right)\right] .$$

The first summation of Eq. 17 is identical with the first sum of the last term of Eq. 16. Since $\vec{r}_{mn} - \vec{r}_{mj} = \vec{r}_{jn}$, and since for a large crystal the sum over any two of the three indices m, n, j is equivalent to the sum over any other two, the second sum of Eq. 17 may be written

$$\sum\sum \frac{\vec{k}\cdot\vec{r}_{mn}}{|\vec{r}_{mn}|^3}\,\frac{\vec{k}\cdot\vec{r}_{mj}}{|\vec{r}_{mj}|^3}\exp\left(i\vec{k}\cdot\vec{r}_{jn}\right) .$$

The double sum is taken over any two of the three indices m, n, j with the restriction that no two of them may equal each other. This is clearly equivalent to the second sum of the last term of Eq. 16. Since $G^*(\vec{k},n) = G(\vec{k},-n)$, $\sum_{n\neq m} G(\vec{k},n)$ is real, and Eq. 16 may be written

$$(18)\qquad \frac{I_D}{m_A m_B N} = \left[(f_A - f_B) + (m_A f_A + m_B f_B)\frac{C_A}{m_B}\sum_{n\neq m} G(\vec{k},n)\right]^2 .$$

Comparison of the Theory with Experiment. – We specialize the result of Eq. 18 for a close-packed cubic crystal, and we compare the diffuse scattering distribution thus obtained with that experimentally measured for Cu_3Au. The vector $\vec{r}_{mn}$ may be written $\vec{r}_{mn} = l_1\vec{a}_1' + l_2\vec{a}_2' + l_3\vec{a}_3'$, where $\vec{a}_1'$, $\vec{a}_2'$, and $\vec{a}_3'$ are half the usual cubic cell vectors. For a close-packed cubic cell, l_1, l_2, and l_3 are integers whose sum is even. With $\vec{b}_1'$, $\vec{b}_2'$, $\vec{b}_3'$ reciprocal to $\vec{a}_1'$, $\vec{a}_2'$, $\vec{a}_3'$, the vector $\vec{k}$ may be written

$$\vec{k} = 2\pi(h_1\vec{b}_1' + h_2\vec{b}_2' + h_3\vec{b}_3') .$$

The continuous variables h_1, h_2, and h_3 are equal to half the Miller indices at a reciprocal lattice point. Since the summation of Eq. 18 over the imaginary part of $G(\vec{k},n)$ vanishes, this equation may be written

$$(19)\qquad \frac{I_D}{m_A m_B N} = \left[(f_A - f_B) - (m_A f_A + m_B f_B)\frac{8C_A}{m_B a_0^3}\sum_{l_1 l_2 l_3}\frac{2\pi(l_1h_1 + l_2h_2 + l_3h_3)}{(l_1^2 + l_2^2 + l_3^2)^{3/2}}\sin 2\pi(l_1h_1 + l_2h_2 + l_3h_3)\right]^2 ,$$

where a_0 is the cubic unit cell size.

The size-effect lattice sum of Eq. 19 is readily evaluated numerically. Its distribution in the h_1h_20 plane of reciprocal space is shown in Fig. 38. There are singularities at each reciprocal lattice point, and in the vicinity of each point the function is negative on the side of the point nearest the origin, and positive on the far side. In general, the function is large near lattice points and increases in magnitude with distance from the origin.

With $C_A = -0.072$ Å^3 for disordered Cu_3Au (copper atoms are called A), as determined in Part I from the decreased integrated intensities of the Bragg maxima, and with $a_0 = 3.74$ Å, the diffuse scattering in the vicinity of $h_1h_2h_3 = 100$ ($hkl = 200$) in the h_1h_20 plane was computed by means of Eq. 19 and the size-effect function of Fig. 38. It is compared with the experimentally measured distribution in Fig. 39. The experimental data are those shown in Fig. 4 of Part I.

Discussion. – By a rearrangement of the expression for the diffuse intensity associated with the atomic size effect, it has been shown that Huang's integral approximation is unnecessary and that the diffuse scattering may be expressed in a very simple form. In spite of the fact that the Cu_3Au specimen used contained a significant degree of short-range order, agreement between observed and calculated intensity distributions in the vicinity of the Bragg maxima is quite good. It is interesting that the Laue monotonic diffuse scattering, the second term of Eq. 15, here completes a square, while in the case of short-range order with no size effect it is the leading term of a Fourier series.

Equation 19 has been arranged so that the size-effect function shown in Fig. 38 is quite general and may be used to compute the diffuse scattering for any close-packed cubic solid solution.

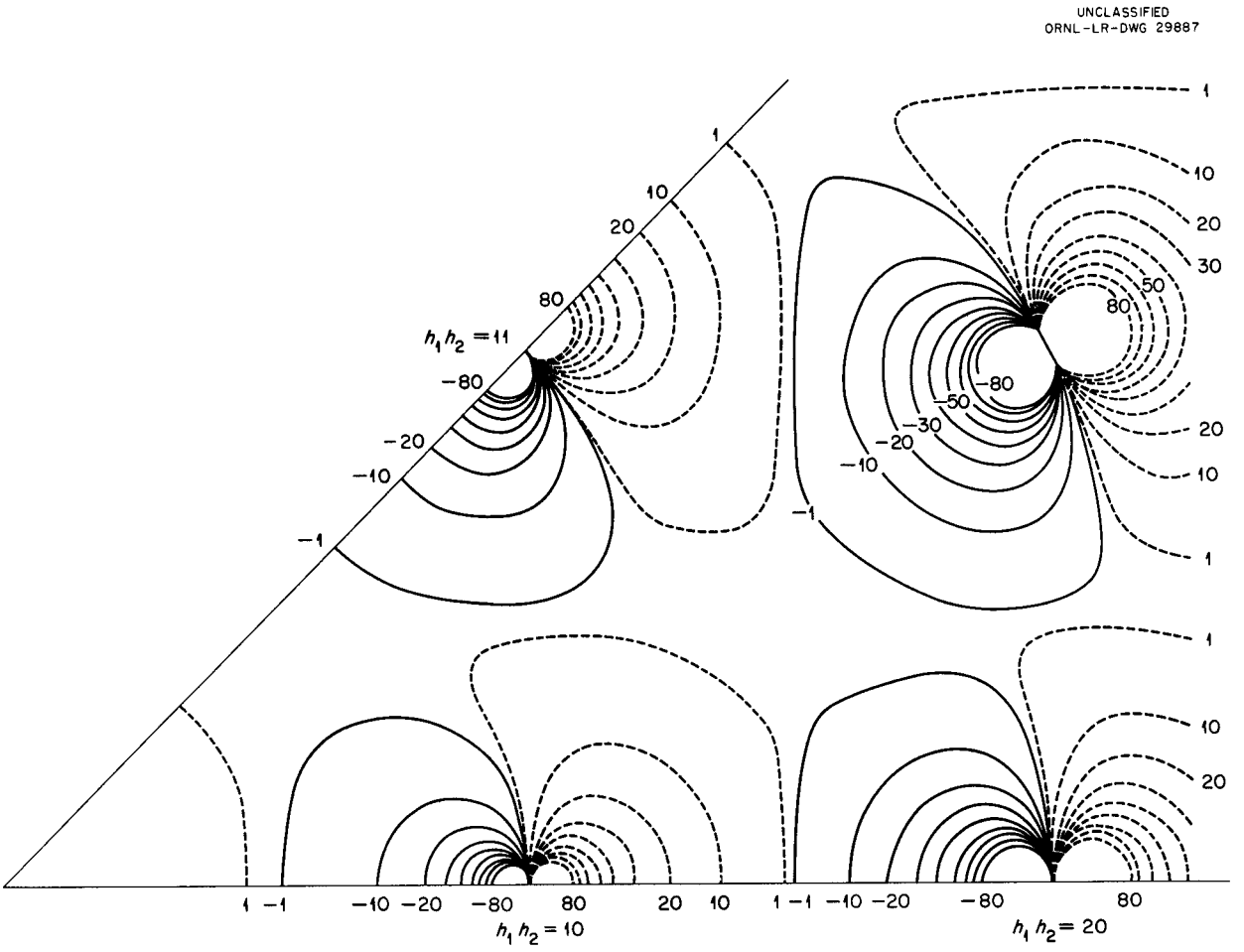

Fig. 38. Closed-Packed Cubic Size-Effect Lattice Sum,

$$\sum_{l_1 l_2 l_3} \frac{2\pi(l_1 b_1 + l_2 b_2 + l_3 b_3)}{(l_1^2 + l_2^2 + l_3^2)^{3/2}} \sin 2\pi(l_1 b_1 + l_2 b_2 + l_3 b_3) \ ,$$

in the $b_1 b_2 0$ Plane of the Reciprocal Space. Contours greater than 80 have been omitted.

UNCLASSIFIED
ORNL-LR-DWG 29886

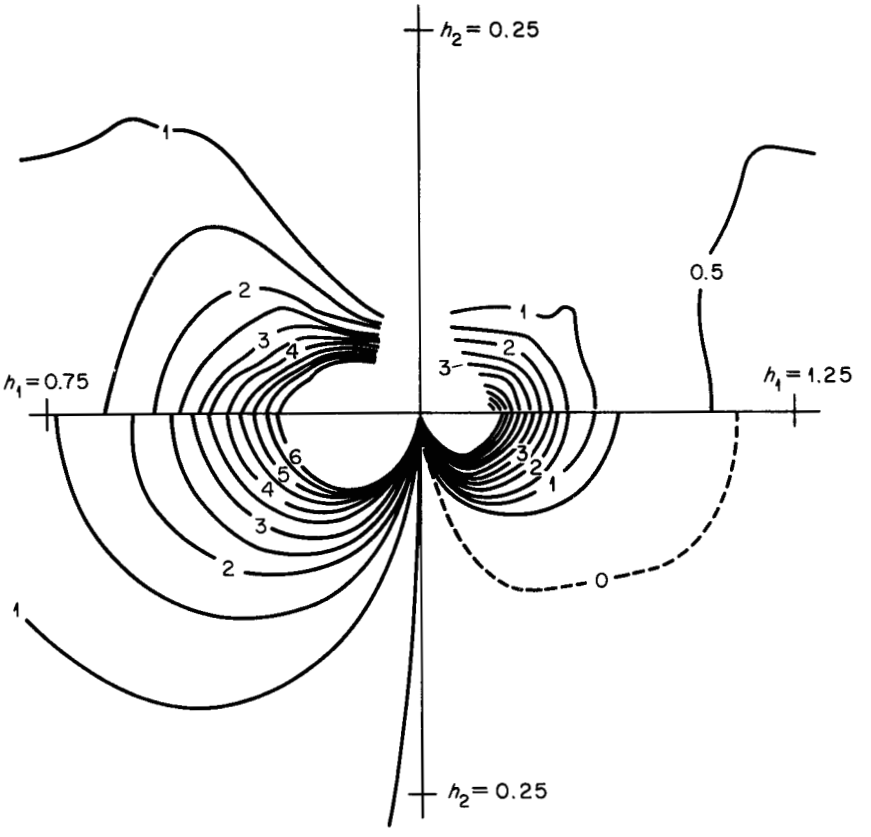

Fig. 39. Comparison of the Observed (Above) and Computed (Below) I_D/Nf_A^2 in the Vicinity of $h_1 h_2 h_3 = 100$ for Cu_3Au. Contours greater than six have been omitted.

HIGH-TEMPERATURE REACTIONS

G. P. Smith, Jr.

C. R. Boston
J. V. Cathcart
G. W. Clark
J. J. McBride
G. F. Petersen

Near-Ultraviolet Absorption Spectrum of the Nitrate Ion in Fused Salt Media

G. P. Smith C. R. Boston

Measurements have been made of the near-ultraviolet absorption spectrum of the nitrate ion in the presence of a variety of cations and anions in fused salts. These measurements are a part of a study of the effect which neighbor ions and temperature level have on electronic transitions in ionic systems. The absorption spectra of ions of the transition metals are of special importance here because of the applicability of crystal-field theory. However, for initial study, the nitrate ion has certain advantages, among which is the fact that it is known precisely what entity is absorbing the light. Infrared and Raman spectra of fused nitrates have shown that the nitrate ion in fused salts is essentially the same entity which is familiar in aqueous solutions and crystalline salts.

The intrinsic importance of fused salts as special cases of ionic systems lies in the enormously enhanced mutual solubilities of salt mixtures as compared with crystalline salts. This, of course, greatly facilitates the study of compositional variables.

The electronic spectrum of the nitrate ion down to the vacuum ultraviolet consists of two bands, a very low-intensity band at about 300 mμ (referred to here as the first band) and a high-intensity band at about 200 mμ (referred to here as the second band). Our measurements cut off at 250 to 260 mμ and hence show the first band together with a part of the absorption edge of the second band. This first band has been assigned to the forbidden $n \rightarrow \pi^*$ transition.

The current state of progress for this investigation can be briefly summarized as follows. Experimental measurements on high-temperature systems are almost complete. Semiquantitative examination of the results shows that changes in both cation and anion composition of the melts have a strong effect on both the intensity and the mean energy of the first band. These changes can be correlated with the ionic potentials of these ions and with existing information on the effect of neighbor ions on the stability of the nitrate ion. The influence of changes in temperature on the nitrate-ion spectrum is quite small by comparison with the influence of changes in neighbor ions over the temperature ranges currently investigated. A quantitative Gaussian analysis of the spectral profiles has been undertaken with a substantial degree of success. The techniques developed are the first which will quantitatively analyze a system of overlapping bands. They have been tested on a few representative spectra. Their application to the remainder of the spectra represents the major uncompleted task of the current investigation.

Experimental Procedures and Preliminary Treatment of Data. – Measurements were made according to techniques previously described.[1] Figure 40 shows representative results traced from

[1] C. R. Boston and G. P. Smith, *J. Phys. Chem.* 62, 409 (1958).

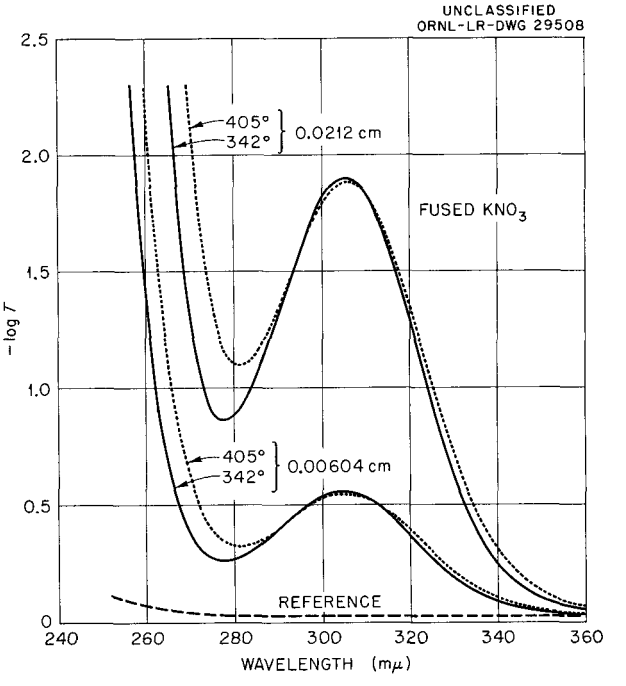

Fig. 40. Absorption Spectra of Pure Fused KNO_3 at Two Temperatures for Each of Two Path Lengths.

chart recordings. Four spectra for fused KNO_3 are shown. The two upper spectra were measured with a path length of 0.0212 cm; they give the more accurate information on the profile of the first band. The two lower spectra were measured with a path length of 0.00604 cm; they include data to shorter wavelengths and hence include more of the absorption edge of the second band. Numerical results, to be discussed later, were obtained by splicing onto the long-path-length spectra the absorption edges from the short-path-length spectra. The length of a splice was 10 mμ.

The path lengths employed here are exceptionally short for a cell-insert system. Consequently, a considerable effort was devoted to the precise determination of these path lengths by several methods.

In order to obtain the absolute absorbance, it was necessary to correct the $-\log T$ curves for light loss due to reflections at interfaces and to absorption by the cell and insert. The following expression was derived for the absorbance A_i of the two layers of fluid contained in a cell with insert:

$$A_i = -\log T - (A_i)_s - 2 \log \frac{1}{1 - R_a} - 4 \log \frac{1}{1 - R_f} + \log M \ ,$$

where T is the transmittance of the entire system, $(A_i)_s$ is the combined absorbance of the two silica cell walls and the silica insert, R_a and R_f are the reflectances of the air-silica and fluid-silica interfaces, respectively, and M is a correction for multiple reflections. Each of these terms is, of course, a function of wavelength. The reflectance terms were computed from Beer's formula,

$$R = \frac{(n - n')^2 + 0.0336(\lambda a_i)^2}{(n + n')^2 + 0.0336(\lambda a_i)^2} \ ,$$

where n and n' are the refractive indices of the phases forming the interface in question, a_i is the absorbance index of the absorbing phase, and λ is the wavelength in centimeters. The multiple reflection term M is quite involved. However, it may easily be shown that the only terms of significance for the specific systems considered here are given by

$$M = 1 + \sum_n R_a^{2n} 10^{-2n(A_i)^*} \ ,$$

where $(A_i)^*$ is the absorbance of the system consisting of cell plus insert plus fluid. All the above-mentioned quantities were either computed or measured as was appropriate; it was found that all the terms involving the properties of the fluid were negligible for the specific systems considered here, and so the reference function B, defined as the difference between $-\log T$ and A_i, could be obtained from the expression

$$B = (A_i)_s + 2 \log \frac{1}{1 - R_a} - \log M \ .$$

It may be shown that, for the spectra discussed here, the reference function $B(\lambda,t)$ at the wavelength λ and temperature t may be taken as:

for $250 \leqq \lambda \leqq 280$ mμ ,

$$B(\lambda,t) = -\frac{l}{l_p} \log T_p(\lambda,t) - \left(l - \frac{l}{l_p}\right) \log T_p(280 \text{ m}\mu,t) \ ,$$

and for $280 \leqq \lambda \leqq 360$ mμ ,

$$B(\lambda,t) = -\frac{l}{l_p} \log T_p(\lambda,t) \ ,$$

where $T_p(\lambda,t)$ is the transmittance at wavelength λ and temperature t of a silica plate of thickness l_p, and l is a thickness equal to the sum of the thicknesses of the two silica cell walls and the silica insert used in the measurements on the fused salts.

It was thus possible to determine the reference function entirely from measurements on a silica plate. Such a reference function is shown at the bottom of Fig. 40. This reference function, when subtracted from the $-\log T$ curves, gives the absorbance function A_i. Then, with the aid of the measured path length and the density and composition of the fused salt, the molar absorbance index function a_M was computed. For numerical computation on spectral profiles, values of a_M were read at 2-mμ intervals.

Special attention was given to the possibility of spectral interference from the nitrite ion, since this substance, a product of the thermal decomposition of the nitrate ion, absorbs significantly in the near ultraviolet. The nitrite ion in fused nitrate solution was found to have an absorption minimum in the neighborhood of the lowest-energy nitrate band and

an absorption maximum at ~360 mμ, where the fused nitrates are generally transparent. Thus, inasmuch as all spectral measurements included the 360-mμ region, it was possible to detect the presence of the nitrite ions before they became concentrated enough to affect appreciably the nitrate spectrum. For measurements reported here, there was no spectral evidence of nitrite contamination. This conclusion was supported by colorimetric determinations of nitrite content by the formation of an aminoazo complex.

Spectra. – Representative spectra for the pure fused alkali-metal nitrates are shown in Figs. 41 and 42. These are also fairly representative of the mixtures, except for a few instances where the first band was overlapped by the absorption edge of the second band. This latter situation is illustrated by Fig. 43, which shows spectra for different compositions of KNO_3-$AgNO_3$ mixtures.

Figure 41 gives spectra for $LiNO_3$ and $NaNO_3$, each at two temperatures. It will be seen that semiquantitatively the replacement of Li^+ ions by Na^+ ions lowers the first band maximum by a factor of about ½ and shifts it toward lower energies by about 0.2 ev. The latter is about twice the energy of a ground-state vibrational quantum for the nitrate ion and about four times the thermal energy. In Fig. 42 it will be seen that the first band maximum continues to drop with increasing atomic number of the cation through Rb^+ and then this trend is reversed. The energy of the band maximum progressively shifts toward lower energies (red shift) throughout the series. Changes among the last three members of the series are small.

The effect of a change in temperature on the band maximum, by contrast with the effect of a change in cation, was quite small. This may be seen for $LiNO_3$ and $NaNO_3$ in Fig. 41 and for KNO_3 in Fig. 40. It was also true for the other members of the series and for the mixtures. On the other hand, a decrease in temperature had a substantial influence on the absorption edge of the second band. Inasmuch as this band overlaps the first band, very little of a quantitative nature can be said about the effect of temperature on the first band until overlap is removed. This subject is considered further in the discussion of profile analysis.

The effect of mixed monovalent cations on the nitrate band was determined from spectra of the following mixtures: $LiNO_3$-$NaNO_3$, $LiNO_3$-KNO_3, $LiNO_3$-$CsNO_3$, and KNO_3-$RbNO_3$. A nonlinear relationship between $(a_M)_{max}$ and composition was observed. An example is shown in Fig. 44, in which $(a_M)_{max}$ is plotted against composition for the $LiNO_3$-$CsNO_3$ system. It can be seen that the observed $(a_M)_{max}$ values are lower than would be expected if the system behaved "ideally." The largest deviations (~10%) occurred in the $LiNO_3$-$CsNO_3$ system, where the cations differ greatly in size; the smallest deviations were found in the KNO_3-$RbNO_3$ system, in which the cations are of similar size. This nonlinearity in $(a_M)_{max}$ may be due to a nonlinear relationship between the extent of anion-anion contact and composition.

From the above measurements on alkali-metal nitrates, it can be seen that the light-absorption characteristics of the nitrate ion are strongly influenced by the nature of its surrounding cations. It would be interesting to extend this work to include another series of pure nitrates, such as the group II metal nitrates. However, the nitrate ion is usually unstable in the presence of divalent cations. The group II metal nitrates are no exception, since they decompose rapidly at their melting points. On the other hand, mixtures of the type KNO_3-$M(NO_3)_2$, where M represents Ca, Sr, Ba, or Cd, were found to be quite stable up to 30 to 40 mole % $M(NO_3)_2$. Thus, by measuring spectra at several points in this stable composition range, an approximate value of $(a_M)_{max}$ for pure $M(NO_3)_2$ was obtained by extrapolation. The latter procedure should be fairly reliable since $(a_M)_{max}$ varies linearly with composition, as shown in Fig. 45. A similar procedure was used to obtain E_{max} values, and these, together with $(a_M)_{max}$ values, are shown in Fig. 46.

The cation effect on the nitrate band is summarized in Fig. 46, where $(a_M)_{max}$ and E_{max} values for the nitrate band in the presence of the various cations studied are plotted against the ratio of charge to radius, or ionic potential, of the cation. It can be seen that a very good correlation exists for cations having the inert gas electronic configuration. Cadmium does not have the latter configuration and, in turn, deviates considerably from the $(a_M)_{max}$ line and slightly from the E_{max} line.

Foreign anions were found to have a pronounced effect on the nitrate absorption when the cation was small enough to permit anion-anion contact, as, for example, in the $LiNO_3$-LiCl system. With larger cations, as, for example, in the KNO_3-KCl system,

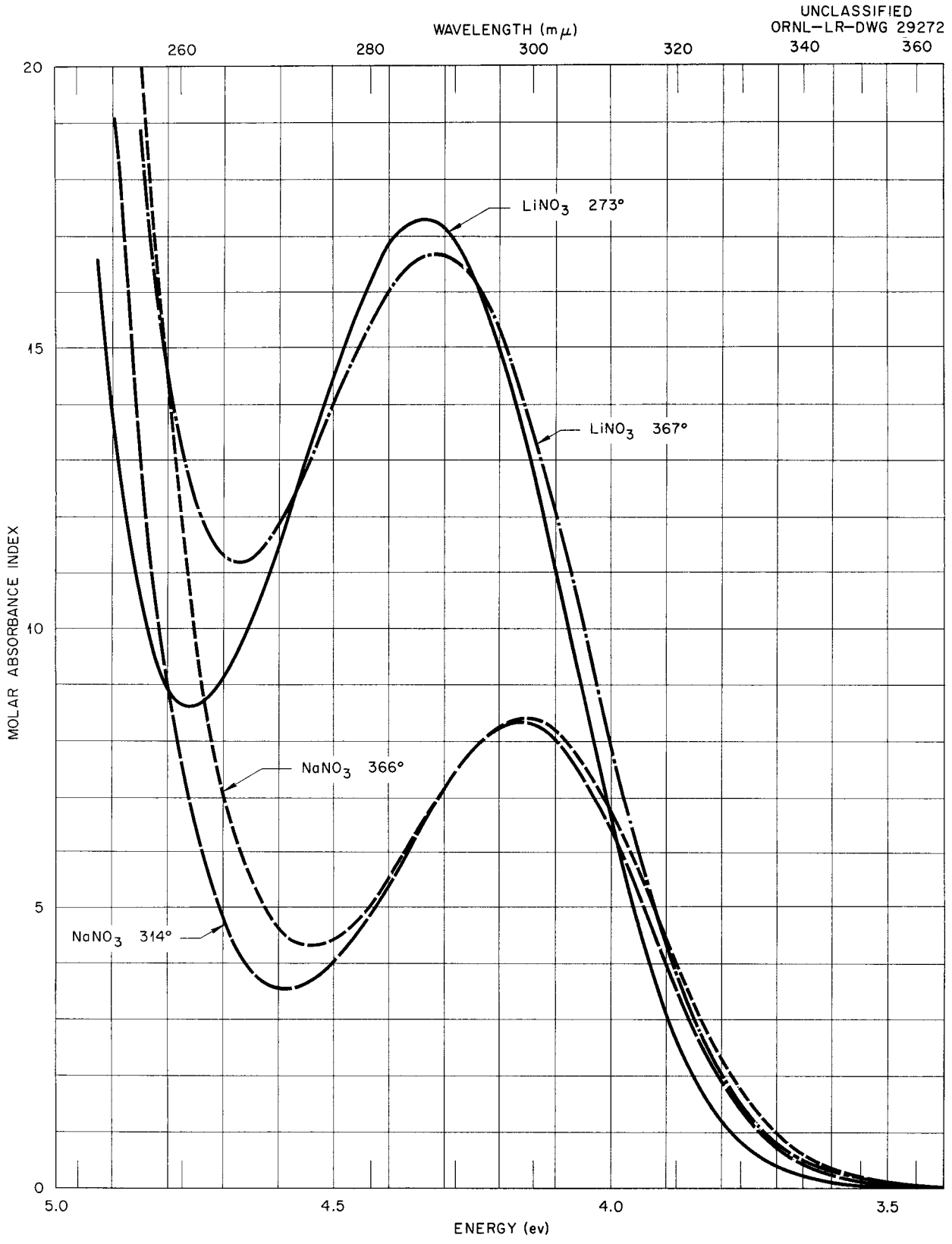

Fig. 41. Absorption Spectra for $LiNO_3$ and $NaNO_3$, Each at Two Temperatures.

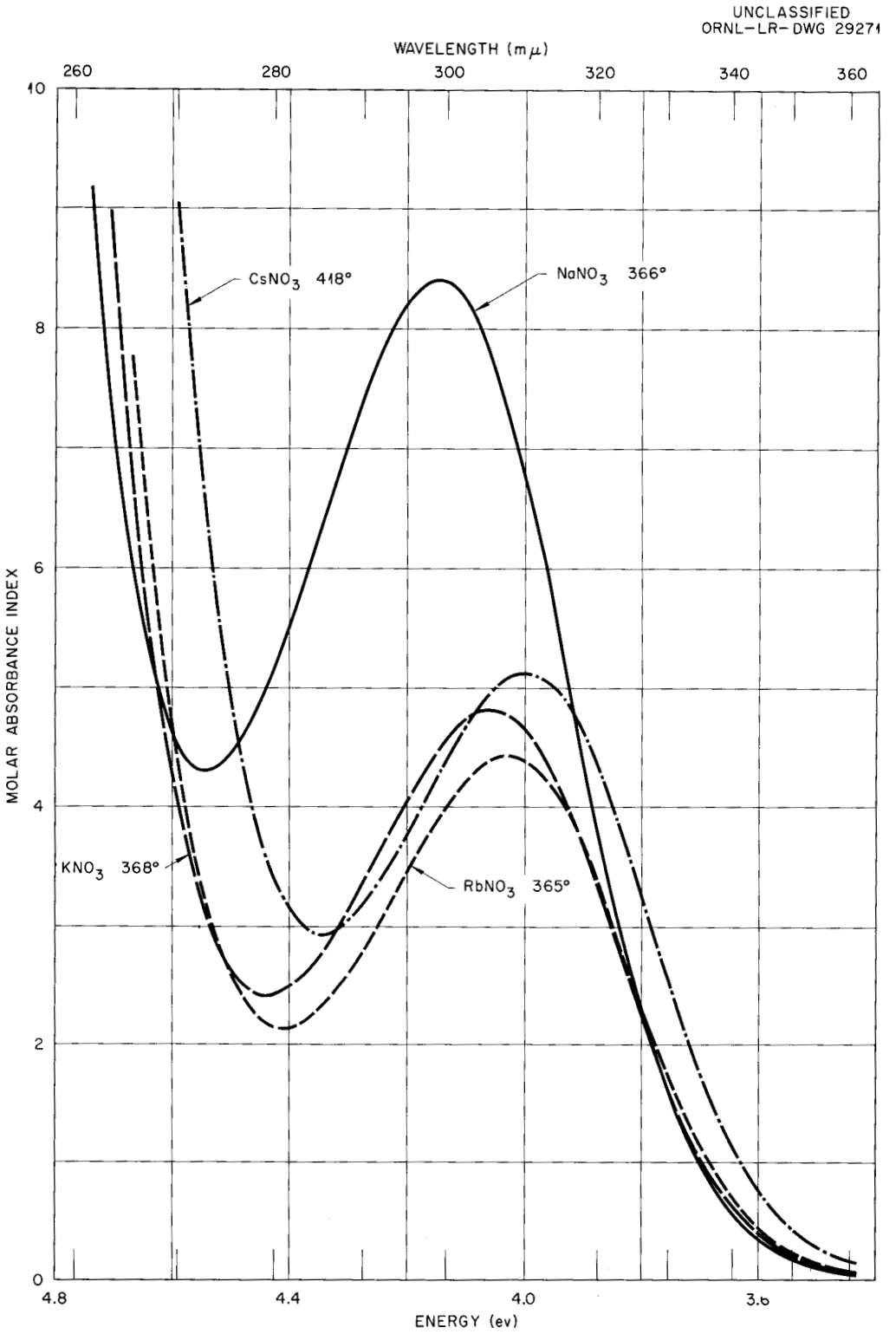

Fig. 42. Representative Absorption Spectra for the Fused Nitrates of Sodium, Potassium, Rubidium, and Cesium.

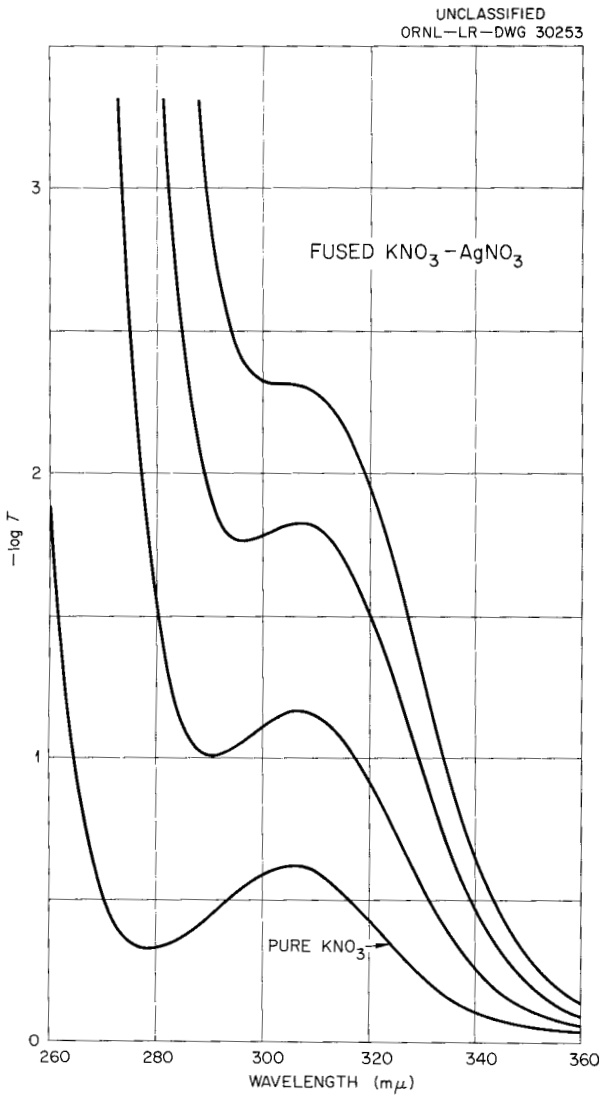

Fig. 43. Absorption Spectra for Three Fused Mixtures of Potassium and Silver Nitrates Together with the Spectrum of Pure Potassium Nitrate, All at the Same Temperature.

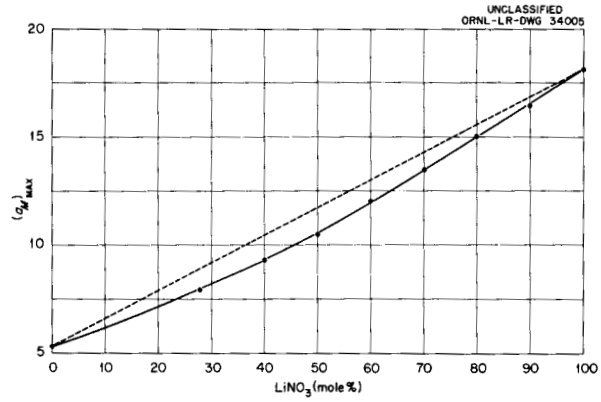

Fig. 44. Effect of Mixed Cations on Nitrate Absorption in $LiNO_3$-$CsNO_3$ Systems.

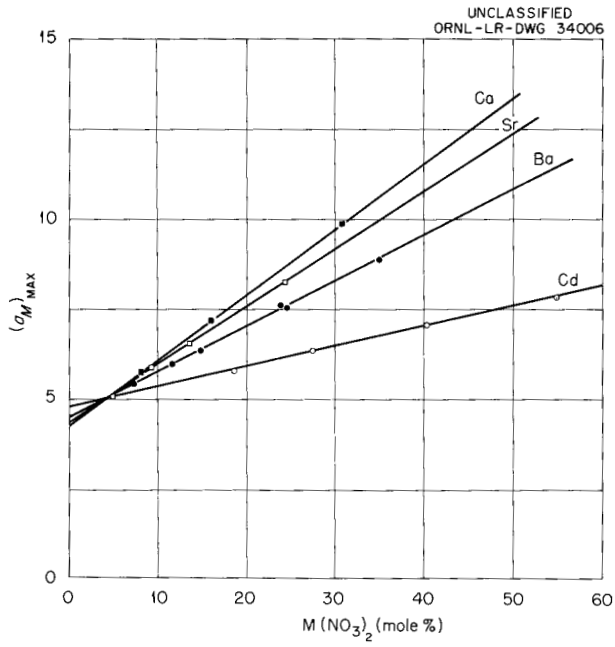

Fig. 45. Effect of Group II Cations on Nitrate Absorption in KNO_3-$M(NO_3)_2$ Systems.

the influence of the foreign anion was greatly reduced. Figure 47 shows the effect of Cl^- on the nitrate absorption in the reciprocal salt system composed of the nitrates and chlorides of lithium and potassium. The shaded areas of the diagram were inaccessible in these measurements because of the high melting points of these mixtures relative to the decomposition temperature of the nitrates. The circles represent compositions at which spectra were determined, and the numbers by some of the circles are the $(a_M)_{max}$ values at these compositions. The systems $LiNO_3$-$LiClO_4$ and $LiNO_3$-LiBr were also measured to further explore this "anion effect." Both Cl^- and ClO_4^- enhance the nitrate absorption, with Cl^- doing so to a slightly greater extent than ClO_4^-. Considerable band overlap occurred in the $LiNO_3$-LiBr spectra, preventing a direct comparison of the Br^- ion with Cl^- and ClO_4^- at this time.

Profile Analysis. – Techniques were developed for a quantitative analysis of the spectral profiles with two distinct purposes in mind: first, the precise representation of the experimental data by

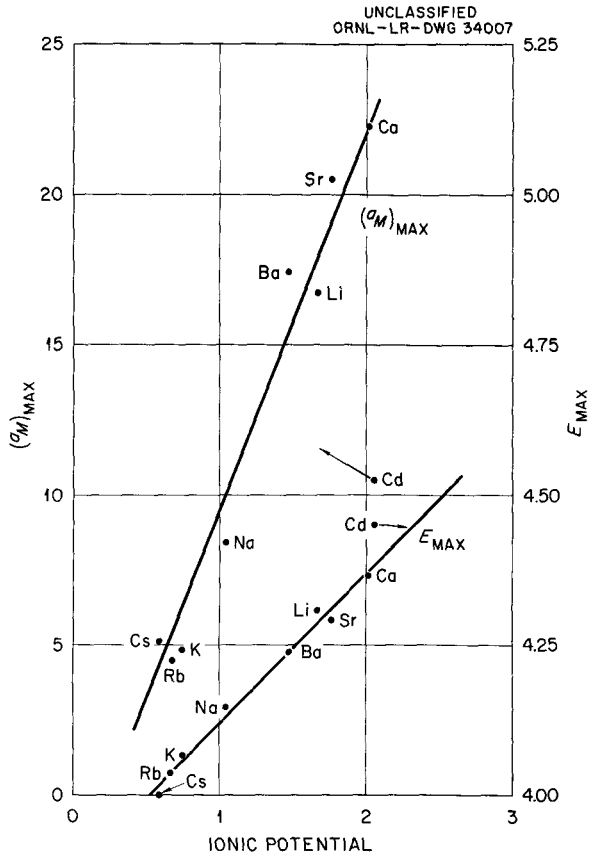

Fig. 46. Correlation of E_{max} and $(a_M)_{max}$ of Nitrate Band with Cation Potential.

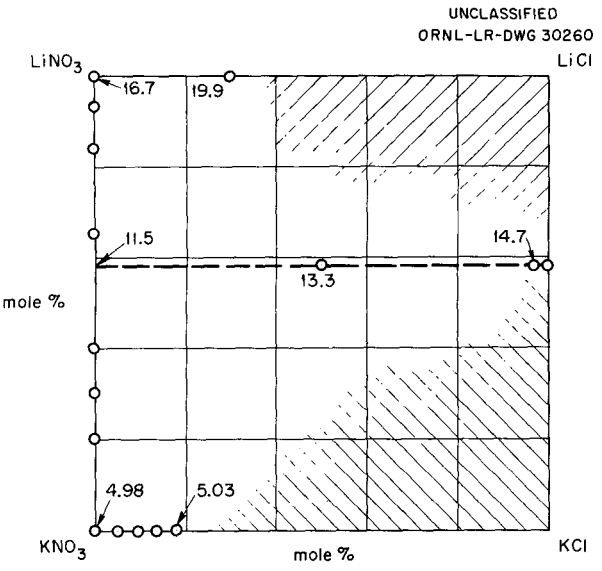

Fig. 47. Effect of Chloride Ion on Nitrate Absorption.

means of a few parameters, and second, the separation of the first band from overlap by the second band so that the spectral parameters of the first transition could be specified with an accuracy commensurate with that of the composite spectrum.

Preliminary tests of the data showed that possible non-Gaussian terms such as the contribution of the Lorentzian function to the Voigt function were not significant. Next, the spectral profile was broken down into its three absorption edges, namely, the low-energy absorption edge of the first band, denoted 1, l; the high-energy edge of the first band, denoted 1, h; and the low-energy edge of the second band. It was shown that the latter was best represented by a simple exponential taken as an approximation to a Gaussian function, while each of the two edges of the first band was properly represented by the unsymmetrical Gaussian $a \exp(-u|E - E_1|^n)$. Hence the function for the profile of the composite spectrum may be written as

$$a_M = a_1 \exp(-u_{1,j}|E - E_1|^{n_{1,j}}) + a_2 \exp(qE) \quad ,$$

where $j = l$ for $E \leqq E_1$, $j = h$ for $E \geqq E_1$, a_M is the molar absorbance index of the composite spectrum, E is the photon energy, a_1 and E_1 are the coordinates of the first band maximum, $u_{1,l}$ and $u_{1,h}$ are constants which implicitly specify the width at half-maximum and, in part, the asymmetry of the first band, $n_{1,l}$ and $n_{1,h}$ are constants which specify the degree to which the band is diffuse or sharp, and a_2 and q are constants defining the absorption edge of the second band.

An iterative procedure was developed whereby the above equation could be fitted to the experimental data with the aid of a desk calculator.

Fittings were carried out for six spectra, including one for each of the pure fused alkali-metal nitrates except $LiNO_3$, for which fittings were made for spectra at two temperatures. Results of the third iteration for $RbNO_3$ at 341°C are shown in Fig. 48; these results are typical of all six fittings. The smooth, solid curve represents the profile function fitted to the experimental data represented by dots. At the bottom of the figure, the difference between the computed and experimental values, Δ, is plotted on an expanded scale. The standard deviation between the experimental and computed values is 0.024, or about 0.3% of the band maximum. The maximum deviation for a single point is about 1% of the band maximum. These deviations are within the experimental error.

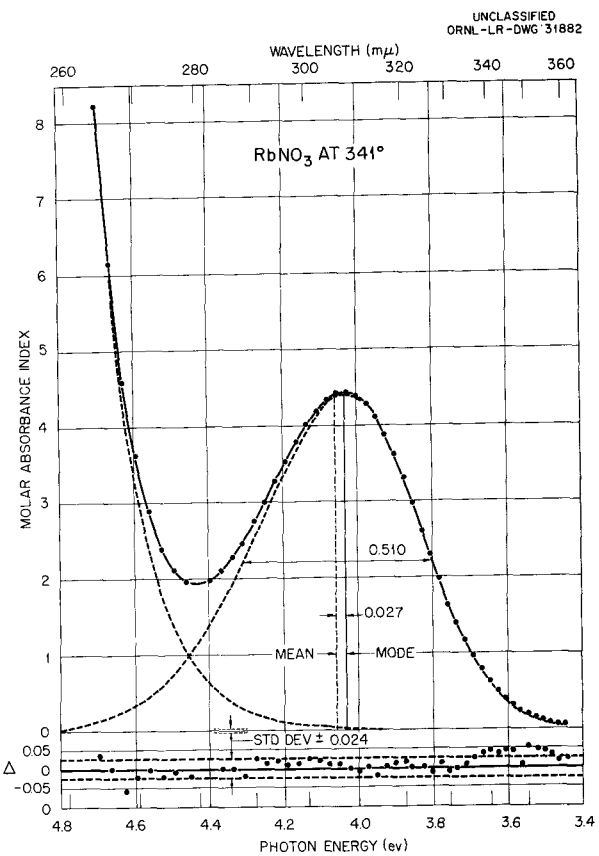

Fig. 48. The Profile Equation (Solid and Dashed Curves) Fitted to an Experimentally Measured Spectrum (Dots).

The components of the spectrum are shown as dashed lines. The absorption edge of the second band falls off rapidly. The first band is mildly skewed toward higher energies. Both these results are typical of all six spectra which were examined.

The computing procedure is being coded for the Oracle and will be applied to all the nitrate spectra. These computations will include the transition probabilities and the oscillator strengths.

An interesting result of applying the profile equation to the data for $LiNO_3$ at 273 and 367°C is shown in Fig. 49. The solid curve is the profile of the first band for $LiNO_3$ at 273°C; the dashed curve is the profile at 367°C. Although the change in temperature reduces the band maximum, this is compensated by an increase in band width so that the net change in integrated cross section for the transition is measured to be about 0.4%, which, to within the experimental error, is virtually nil. This means that at both temperatures $LiNO_3$ absorbs the same fraction of the total energy from a "white" radiation source by means of the $n \rightarrow \pi^*$ transition but that this energy is distributed over a wider range of vibrational jumps at the higher energy.

A preliminary investigation has been made of another type of profile function which consists of two symmetric Gaussian functions to represent the first band. Satisfactory computing procedures have not been developed, but preliminary results are shown in Fig. 50 for the case of fused $NaNO_3$ at 366°C. The solid curve represents the experimental data, while the absorption edge of the second band and the two components of the first band are shown as dashed lines. There are possible physical interpretations of the very weak component.

D. A. Gardiner of the Mathematics Panel has developed an Oracle procedure for obtaining a least-squares fit between our data and the very simple function consisting of a single symmetrical Gaussian and an exponential. Results are available at the moment only for a single $RbNO_3$ spectrum. These results show that, although the symmetrical Gaussian is not so good a fit as the skewed form, nevertheless, the fit is surprisingly good and would be quite satisfactory for obtaining the integrated optical cross section.

Density Measurements on Fused Nitrate Mixtures

G. F. Petersen

Measurements of the densities of various fused nitrate mixtures were made by the Archimedean method. Twenty-seven compositions were studied, each over a substantial temperature range. The results were fitted by the method of least squares to the equation

$$\rho = a - bt \quad ,$$

where

ρ is the density, g/cm^3,

t is the temperature, °C,

a and b are empirical constants.

The results of these measurements are given in Table 8.

Nuclear Magnetic Resonance Measurements on Fused Fluorides

J. J. McBride

The research on the use of nuclear magnetic resonance (NMR) techniques for investigating the

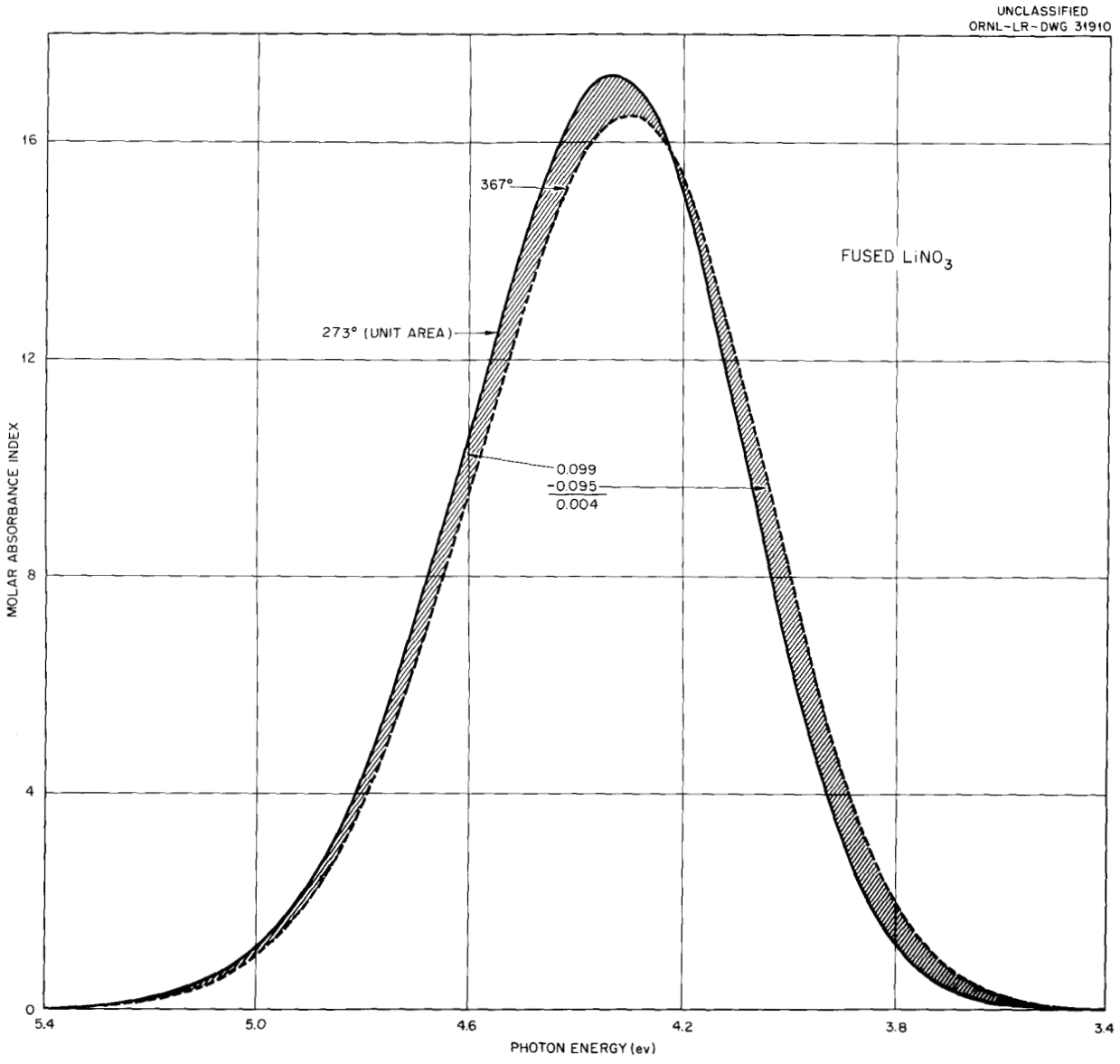

Fig. 49. Profiles of the Lowest-Energy Electronic Band of $LiNO_3$ at Two Temperatures.

structure of fused electrolytes has been extended. This work has had the continuing invaluable assistance of R. Livingston's group of the Chemistry Division.

During the past year, modification of the original Livingston group NMR apparatus has been completed to the point where it may now justifiably be termed a high-temperature (room temperature to about 900°C) spectrometer of moderately high resolution and sensitivity.

With the completion of an operating (although by no means completely satisfactory) apparatus, the emphasis in the program has shifted from equipment development to a search for, and an investigation of, fused electrolyte systems about which NMR may give useful and significant results.

Some preliminary measurements were made on the Na^{23} and the H^1 resonances in fused NaOH under various conditions, but further examination showed that this is not likely to be a fruitful avenue for research at present. The principal interest now is in fluoride melts. The F^{19} resonance has been studied in molten SnF_2, in molten Flinak (the triple eutectic of LiF, NaF, and KF), and in molten

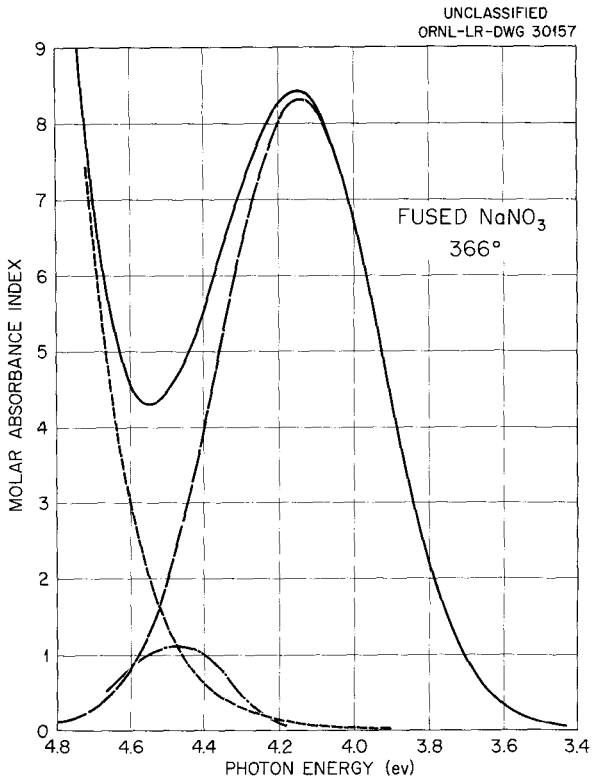

Fig. 50. Results of a Profile Analysis in Which the First Electronic Band Is Represented by Two Symmetrical Gaussian Functions.

ZrF_4-KF mixtures. Interpretations of the F^{19} line observed in SnF_2 melts were confused by the rapid chemical decomposition which takes place just above the melting point. The F^{19} resonance in molten Flinak is a single sharp line, typical of simple ions in liquids; studies were made of line width and signal-to-noise ratio as functions of temperature and of r-f power level.

In addition to the observations on fused electrolytes, some apparatus development, aimed principally at increasing high-temperature stability and sensitivity of the instrument, is continuing.

Growth of MgO Single Crystals[2]

G. W. Clark

The Arc-Conduction Scheme. – The idea here was to use a high-current, low-voltage arc just over the surface of a polycrystalline charge of MgO to raise its temperature sufficiently for the MgO to become electrically conducting. At such an elevated temperature, the arc was to be quenched and the necessary thermal energy was to be developed by passing a high current through the charge. Thus, by supplying enough electrical power to overcome the losses, it was expected to obtain a melt of MgO contained in its own crucible.

Such a system was constructed and shallow melts were obtained, but this experiment was not successful because spurious arcs developed after the quenching of the initial arc. Such surface arcing greatly reduced the thermal effectiveness of the system. Although this method in principle appears to be a feasible one for producing MgO crystals, it was apparent that the developmental research required to overcome these experimental difficulties was beyond the scope of the present contract.

Arc-Modified Flame Fusion (Verneuil) System. – The arc-modified flame fusion scheme was simple in concept, but presented engineering design and technique problems. Argon was forced past a rod-shaped cathode and through a nearby, axially symmetric, water-cooled copper anode. Upon the establishment of a high-current arc between these two electrodes, the argon flowing through the arc was excited. When the physical system, voltage, current, and gas flow were properly adjusted, a stable excited-gas "flame" projected axially beyond the anode. Fine MgO powder was intermittently injected, with some difficulty, into this flame just below the anode.

A few very small magnesia boules were grown by this method. Based upon this experience, the system was redesigned to permit the more efficient introduction of the MgO powder and to allow the use of oxygen in place of argon. However, it has not yet been possible to eliminate all the experimental difficulties in the system.

The Hydrothermal Technique. – A study of the $MgO\text{-}H_2O$ phase diagram[3] indicated the possibility that MgO could be grown hydrothermally. A simple system, similar to those for growing quartz[4] and corundum[5] single crystals, was constructed. Several runs were made in an effort to determine conditions favorable for transporting MgO nutrient down a temperature gradient to a suspended seed crystal. The conditions necessary for significant material transport were not found.

[2] Final report on subcontract with Virginia Institute of Scientific Research, Richmond, Virginia.

[3] D. M. Roy, R. Roy, and E. F. Osborn, *Am. J. Sci.* 251, 344 (1953).

[4] E. Buehler and A. C. Walker, *Sci. Monthly* 69, 148 (1949).

[5] R. A. Landise and A. A. Ballman, *J. Am. Chem. Soc.* 80, 2655 (1958).

Table 8. Coefficients in the Density Equations for Fused Nitrate Mixtures*

Composition (mole %)	a	b	Standard Deviation (g/cc)	Temperature Range (°C)
		$\times 10^{-3}$	$\times 10^{-4}$	
100 $NaNO_3$	2.1248	0.701	5	320–455
100 KNO_3	2.1101	0.733	8	345–505
100 $LiNO_3$	1.9221	0.555_7	6	295–420
100 $CsNO_3$	3.2784	1.135	4	420–560
89.33 KNO_3–10.67 $LiNO_3$	2.1017	0.735_2	3	320–430
75.5 KNO_3–24.5 $LiNO_3$	2.0830	0.729	5	275–450
62.6 KNO_3–37.4 $LiNO_3$	2.0553	0.696_4	4	190–450
49.6 KNO_3–50.4 $LiNO_3$	2.0334	0.683	7	170–470
37.5 KNO_3–62.5 $LiNO_3$	2.0100	0.657_2	4	250–475
32.0 KNO_3–68.0 $LiNO_3$	1.9965	0.637_6	8	220–450
20.3 KNO_3–79.7 $LiNO_3$	1.9742	0.623_3	2	240–420
12.5 KNO_3–87.5 $LiNO_3$	1.9540	0.598_8	4	275–450
29.77 KCl–70.23 KNO_3	2.0691	0.680_4	15	485–635
20.46 KCl–79.54 KNO_3	2.0898	0.712	12	420–590
8.71 KCl–91.29 KNO_3	2.1013	0.727_5	7	345–550
30 LiCl–70 $LiNO_3$	1.8891	0.524_3	3	375–500
20.05 LiCl–79.95 $LiNO_3$	1.9026	0.538	2	340–500
10 LiCl–90 $LiNO_3$	1.9113	0.537_4	4	270–450
89.98 KNO_3–10.02 $Ba(NO_3)_2$	2.3047	0.772_7	4	320–520
80.01 KNO_3–19.99 $Ba(NO_3)_2$	2.4749	0.794_6	8	375–520
70.08 KNO_3–29.92 $Ba(NO_3)_2$	2.6289	0.804_8	4	435–520
90.00 KNO_3–10.00 $Sr(NO_3)_2$	2.2175	0.740	11	360–510
79.96 KNO_3–20.04 $Sr(NO_3)_2$	2.3162	0.737	14	345–500
70.09 KNO_3–29.91 $Sr(NO_3)_2$	2.4025	0.721	2	420–455
89.98 KNO_3–10.02 $Ca(NO_3)_2$	2.1319	0.709	4	395–495
80.00 KNO_3–20.00 $Ca(NO_3)_2$	2.1715	0.735	11	300–470
70.09 KNO_3–29.91 $Ca(NO_3)_2$	2.1924	0.713	4	225–475

* $\rho = a - bt$.

METAL SURFACE STUDIES

J. V. Cathcart

Reactions at Metal Surfaces

An investigation of certain aspects of the oxidation of metals is in progress. One aim of this work is the achievement of an understanding of the factors which determine the degree of protectiveness of oxide films formed on metals. Previous research to this end has included studies of the oxidation of the alkali metals[6] and of several structurally important metals in groups IV and V of the periodic table. The work done on columbium and tantalum indicated the possible importance of the mode of diffusion through the oxide film in determining the protectiveness of the oxide film.[7] The investigation has now been extended to include a brief survey of some of the oxidation characteristics of titanium and vanadium. A study of the oxidation of copper[8] was also undertaken since the oxidation of copper proceeds via cation diffusion, in contrast with the oxidation of columbium and tantalum, where anion diffusion prevails.

A second goal of the research is the investigation of the effect of radiation on the oxidation of metals.[9] This work is especially appropriate at this time in view of the trend toward higher temperatures and higher radiation levels in new reactor designs. This phase of the research has been initiated with a study of the effect of radiation on the oxidation of columbium.

Surface Topography of Oxide Films on Vanadium and Titanium. – Studies of the surface topographies of oxide films formed on polycrystalline specimens of columbium, tantalum, and zirconium have been described previously.[7] The main purpose of this work was the investigation of the influence of anion diffusion on the degree of protectiveness of oxide films. It was concluded that, for metal-oxygen systems in which the oxidation process is maintained predominantly by anion diffusion, the oxidation process itself is responsible for the continual generation of stresses in the oxide film and that in such systems there is a tendency for cracks to form in the oxide film.

In order to complete this survey, polycrystalline samples of two other metals from groups IV and V of the periodic table, titanium and vanadium, were studied. For neither metal is there much information available concerning the mode of diffusion prevailing during oxidation, although for the oxidation of titanium[10] there is evidence that, at least under certain conditions, both anion and cation diffusion occur.

The topography of oxide films formed on vanadium was investigated at temperatures ranging from 300 to 600°C. At the higher temperatures the oxide consisted of arrays of geometrically shaped crystallites. Figure 51 shows an electron micrograph of a vanadium specimen oxidized for 33 hr at 500°C. At 400°C the faceting of the oxide surface was less pronounced, and at even lower temperatures, for example, 300°C, the oxidized vanadium surfaces were essentially smooth and featureless.

The surface texture of vanadium oxide films can be accounted for in part by the fact that the melting point of V_2O_5 is only 690°C. Thus at 500°C, V_2O_5 should possess a high degree of surface mobility, permitting a rearrangement of the oxide surface which exposes energetically more favorable surfaces.

---

[6] J. V. Cathcart, *Met. Semiann. Prog. Rep. Oct 10, 1956*, ORNL-2217, p 145.

[7] J. V. Cathcart, *Met. Ann. Prog. Rep. Oct. 10, 1957*, ORNL-2422, p 76–90; J. V. Cathcart, J. J. Cambell, and G. P. Smith, *J. Electrochem. Soc.* **105**, 442–46 (1958).

[8] J. V. Cathcart, *Met. Ann. Prog. Rep. Oct. 10, 1957*, ORNL-2422, p 91–102.

[9] The contribution of the Metallurgy Division to a project sponsored jointly by the Metallurgy and Solid State Divisions.

[10] Tor Hurlen *et al.*, *Oxidation of Titanium*, WADC-TR-58-296 (April 1958).

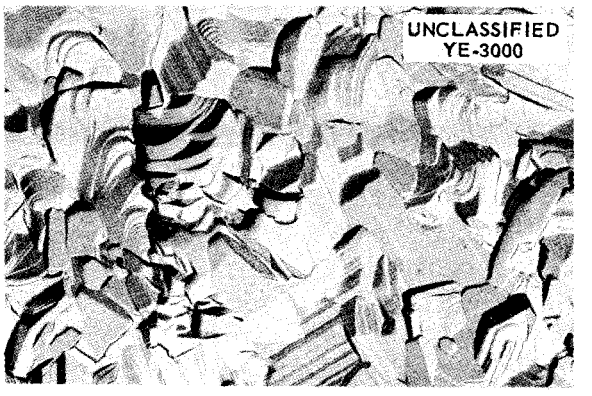

Fig. 51. Carbon Replica, Preshadowed with Gold-Manganin, of Vanadium Specimen Oxidized 33 hr at 500°C. 12,000X.

It is not known whether this marked surface mobility of V_2O_5 also implies movement of both cations and anions within the bulk of the oxide, but it has been observed that small pieces of V_2O_5 will creep under their own weight at 600°C. Such a high degree of plasticity should permit the relief of stresses produced in the oxide during oxidation, and, therefore, no crack formation in the vanadium oxide is to be expected.

Similar studies of oxide films formed on titanium at temperatures ranging from 400 to 800°C revealed a variety of surface topographies. At 400°C, many small nodular protuberances were observed on the oxide films (Fig. 52). These features were thought to represent the beginnings of whisker growth since, at 500°C (Fig. 53), whiskers were clearly visible. In addition, an irregular, wrinkled texture began to develop in the oxide. As may be seen in Fig. 54, at 600°C whiskers several thousand angstroms in length were observed (note the long, slender shadows cast by the whiskers), and the topography of the oxide film itself suggested that the onset of faceting had occurred. Finally at 750 and 800°C (Fig. 55), all signs of whisker growth disappeared, and the oxide developed a heavily faceted texture.

Other investigators[10] have reported similar results in studies of the oxidation of titanium. It has been suggested that some of the surface features described above may be related to the plastic deformation of the oxide and that the faceting of the oxide at high temperatures is attributable, as in the case of V_2O_5, to enhanced surface diffusion. However, no suitable explanation has yet been advanced for the majority of the topographic features reported.

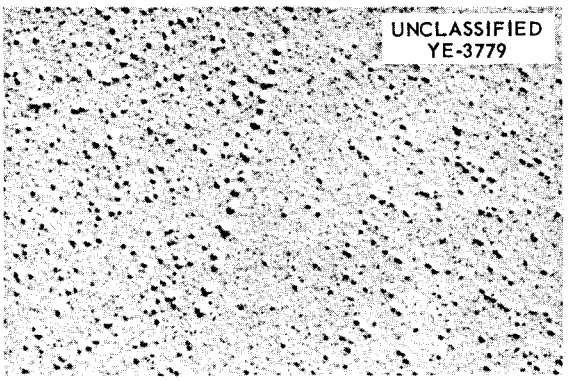

Fig. 52. Carbon Replica, Preshadowed with Gold-Manganin, of Titanium Specimen Oxidized 2 hr at 400°C. 12,000X.

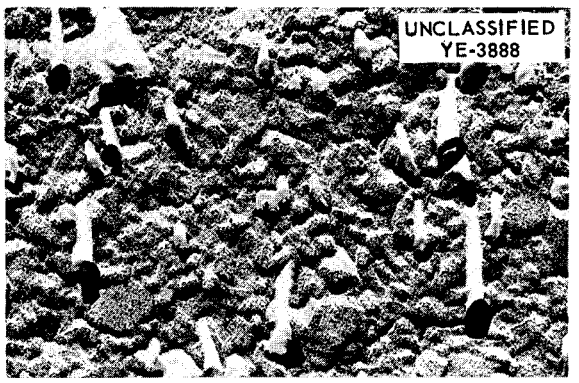

Fig. 54. Carbon Replica, Preshadowed with Gold-Manganin, of Titanium Specimen Oxidized 4 hr at 600°C. 34,000X.

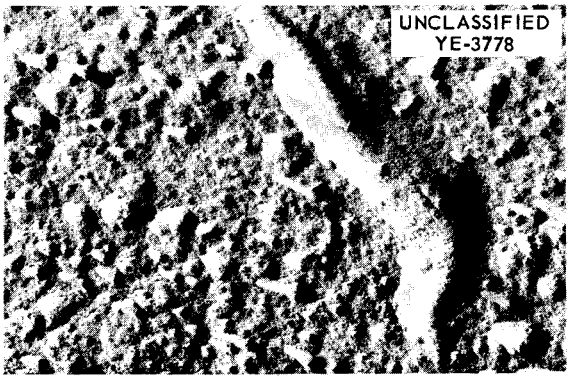

Fig. 53. Carbon Replica, Preshadowed with Gold-Manganin, of Titanium Specimen Oxidized 8 hr at 500°C. 34,000X.

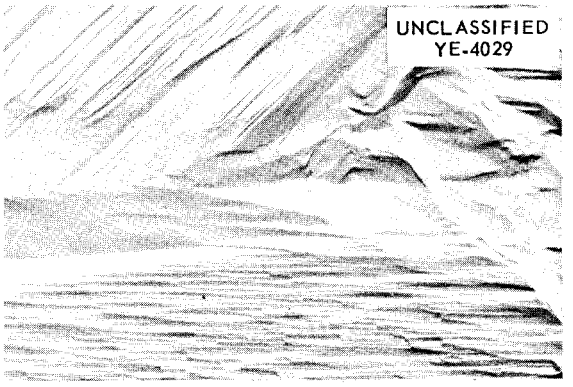

Fig. 55. Carbon Replica, Preshadowed with Gold-Manganin, of Titanium Specimen Oxidized 6 hr at 750°C. 8400X.

The Oxidation of Copper.[8] – An effort is being made to characterize thin oxide films formed on various crystallographic planes of copper single crystals. This investigation was undertaken for several reasons: (1) the results obtained will serve as a standard in a projected study of the effect of radiation on the oxidation of copper; (2) the oxidation of copper proceeds via a cation diffusion mechanism, and therefore this work serves to complement the investigation, previously described,[7] of the oxidation of columbium and other metals where anion diffusion prevails; (3) it is possible to examine extremely thin oxide films on copper, thus providing needed information concerning the important but experimentally neglected early stages of the oxidation of metals.

Method of Study. – Four general experimental techniques – electron microscopy, film thickness measurements, and electron and x-ray diffraction – have been utilized in this research. Primary emphasis has been placed on electron-optical examinations of cuprous oxide films. Both carbon replicas of the oxide films and the films themselves (stripped electrolytically from the copper crystals) have been studied. The oxide-gas or the oxide-metal interfaces of some of these stripped films were shadowed lightly with a gold-Manganin alloy in order to reveal more clearly the topography of these interfaces.

The thickness of the oxide films was determined with a polarizing spectrometer, thus permitting the electron-optical studies to be correlated with existing kinetic data for the oxidation of copper.[11]

The preferred orientation of the oxide films has been investigated, and the epitaxial relationships between the oxide and the substrate metal have already been reported.[8]

A study, by special x-ray diffraction techniques, of the lattice distortions in very thin cuprous oxide films is also in progress. This work is being performed jointly with the Microstresses in Crystals Group of the Metallurgy Division and is described elsewhere in this report.

Method of Stripping Oxide Films. – Oxide films were stripped electrolytically from copper specimens in a bath consisting of a saturated aqueous solution of KCl. The apparatus used was a modification of that described by Gulbransen *et al.*[12] It was found that the use of relatively high stripping currents (e.g., a current density of about 10 ma/cm^2) in general led to spurious results. High currents favored the formation of a difficultly soluble copper-potassium chloride complex, produced a thickening of the oxide film, and, in some cases, caused the formation of large, thick, geometrically shaped features on the oxide.

These difficulties were largely overcome by lowering the current density to 2 ma/cm^2 and by stirring the bath during stripping. These conditions for stripping were judged to give valid results for the following reasons:

1. No oxide lines were observed in diffraction patterns from thin Cu_2S films stripped in this manner.
2. As the oxide films thickened, qn increase in the roughness of the oxide-gas interface occurred. Topographic features on this surface which were resolvable in carbon replicas of the surface made before the stripping of the oxide were also visible in the stripped film. It was concluded, therefore, that the stripping process did not alter the topography of the oxide-gas interface of the oxide.
3. Significant thickness inhomogeneities were observed in the thinnest oxide films studied, and these thickness irregularities appeared to occur primarily at the oxide-metal interface. With increasing time and temperature of oxidation, it was found that these irregularities developed in a logical and systematic manner. Thus, the internal consistency of the experimental data also supported the validity of the stripping procedure.

It is recognized that none of these criteria alone represents positive proof that the oxide films were unchanged during stripping, but taken as a whole they provide convincing evidence of the validity of the stripping procedure.

Results. – Studies have been made of oxide films on the (100), (111), (110), and (311) of copper crystals. These planes were selected because the (100) and the (311) exhibited the fastest and slowest oxidation rates, respectively, of all the crystallographic planes of copper. The (111) and (110) were included because, in addition to being major crystallographic planes, they exhibit intermediate and slow oxidation rates.

The oxidation characteristics of the planes were studied from room temperature to about 300°C and

---

[11] F. W. Young, Jr., J. V. Cathcart, and A. T. Gwathmey, *Acta Met.* 4, 145–52 (1956).

[12] R. T. Phelps, E. A. Gulbransen, and J. W. Hickman, *Ind. Eng. Chem. Anal. Ed.* 18, 391–400 (1946).

for times ranging from less than 1 min to 48 hr. Typical stages in the development of oxide films on the (311) at various times and temperatures are illustrated in Fig. 56*a* to 56*g*. Films formed in 10 min at 70°C (Fig. 56*b*) consisted of a very thin layer of oxide on which was superimposed a network of very irregular patches of slightly thicker oxide. Shadowing of the gas-oxide and oxide-metal interfaces of these stripped films indicated that the thicker patches of oxide apparently extended into the metal, since the oxide-metal interface was generally rougher than the gas-oxide interface. This result was confirmed by replicas taken of the gas-oxide interface before stripping (Fig. 56*a*) and of the oxide-metal interface after stripping (Fig. 57*a*).

An increase in the temperature of oxidation to 130°C resulted in the lateral and somewhat limited vertical growth of the thicker patches of oxide described above (see Fig. 56*c*); at 150°C, pronounced vertical as well as lateral growth of these patches was observed. As illustrated in Fig. 56*d* and 56*e*, this vertical growth appeared to be associated with a nucleation phenomenon which resulted in the formation of triangular areas containing the thickened oxide patches. With increasing time, these triangular areas coalesced, producing a relatively dense and uniform film (Fig. 56*f*).

Up to this point the gas-oxide interface remained relatively smooth, but when the temperature of oxidation was increased to 250°C, pronounced roughnesses developed on this interface (Fig. 56*g*). Many nodular protuberances were formed whose heights ranged from 200 to 700 Å. In addition, substantial whisker growth occurred on the oxide, as was evidence by the many long, slender shadows, also visible in the replica.

This phenomenological description of the growth of an oxide film on the (311) of a copper crystal as a function of time and temperature may be summarized as follows: The initial oxide film was characterized by marked thickness inhomogeneities. The film developed at first primarily through the lateral growth of the thicker patches of oxide. A second growth stage then occurred involving both lateral and vertical growth of the film in triangular patches whose symmetry reflected that of the substrate metal. The coalescence of these triangular regions led to the formation of a relatively compact and smooth oxide film. Further growth was reflected in a pronounced increase in the roughness of the oxide-gas interface of the film.

Special comment is required for oxide films formed on the (311) at 70°C. Almost without exception these films contained, in addition to the features described above, many large, thick, irregular particles (Fig. 57*b*). Through replication of the gas-oxide and oxide-metal (see Fig. 57*a*) interfaces of the oxide and through studies of stripped oxide films which had been shadowed on one or the other of these interfaces, it was determined that these particles extended in some cases as much as 1000 Å below the bottom of the oxide film but did not protrude above the oxide-gas interface. Electron diffraction work showed these particles to be copper, a result which was supported by the fact that the particles, in contrast with the surrounding oxide, were insoluble in hydrochloric acid.

These copper particles were rarely observed on oxide films formed at temperatures other than 70°C. They were found on oxide films stripped from the (311), (111), and (110), but they were not observed on films from the (100). Variations in neither the time nor the current density during the stripping of the oxide films served to eliminate the particles. The mechanism of their formation is still unsolved; however, a coalescence of the thicker patches of oxide was observed to have taken place immediately adjacent to the particles (and, presumably, over them as well) (see Fig. 57*b*). No such localized "densification" of the oxide film occurred at temperatures other than 70°C. It was assumed therefore that the formation of the particles was dependent on the particular oxide topography formed at 70°C and that their presence was indicative of incomplete stripping of the oxide film. Since the particles were not oxide and appeared to be related to an anomaly in the stripping procedure, they were omitted from consideration in the description given above for the development of an oxide film.

Thickness inhomogeneities were also observed in very thin oxide films formed on the (100) of copper (Fig. 58*a*), but the patches of thicker oxide were smaller and more numerous and regular than those formed on films on the (311). Increasing the temperature of oxidation to 130 or 150°C resulted in both lateral and vertical growth of these thicker patches of oxide to produce rather smooth, closely

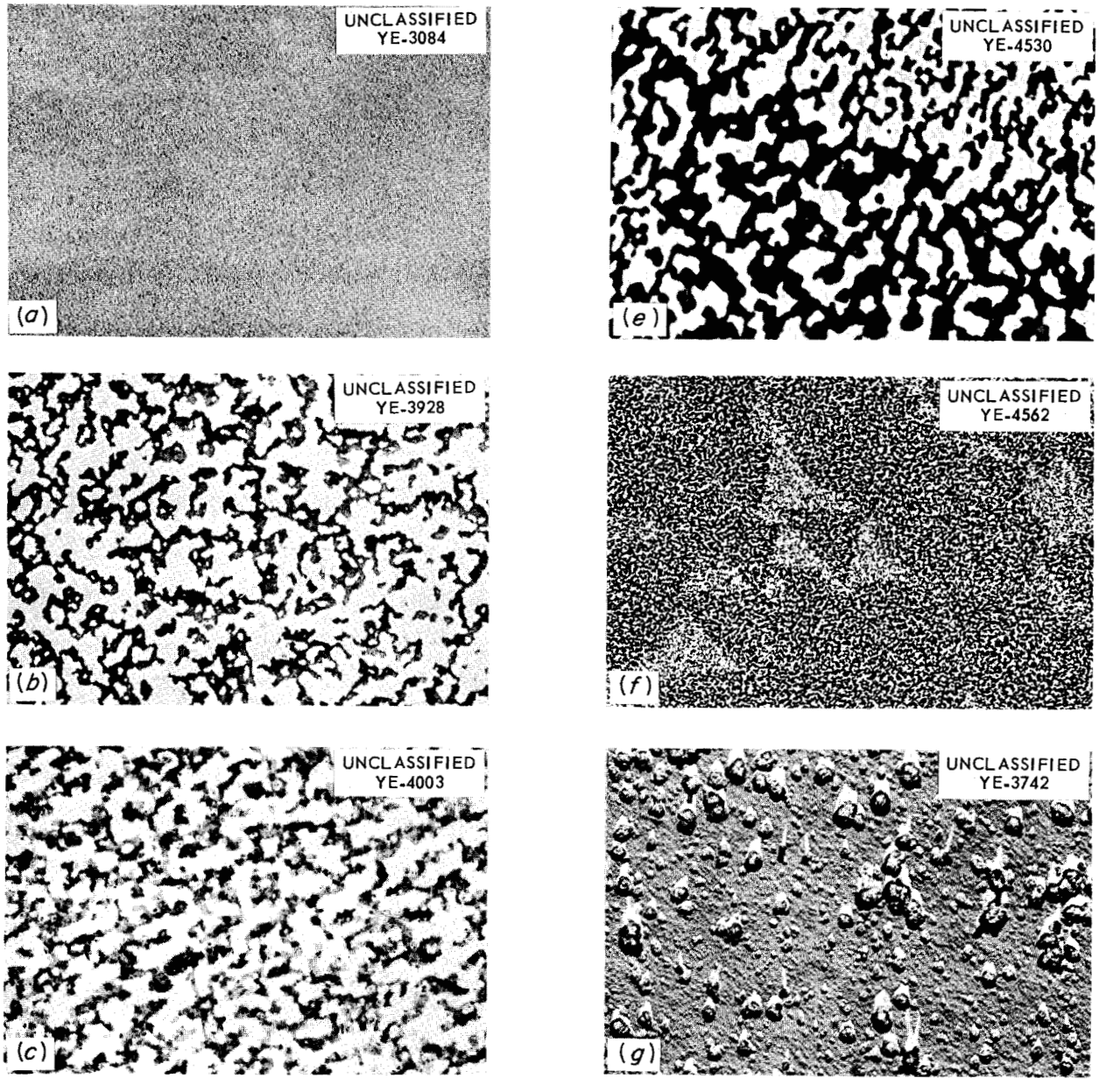

Fig. 56. Cuprous Oxide Films from the (311) Plane of a Copper Crystal. (*a*) Carbon replica, preshadowed with gold-Manganin, made before stripping of film; crystal oxidized 22 min at 70°C; average film thickness, 18 Å; 12,000X. (*b*) Film stripped from crystal oxidized 10 min at 70°C; average thickness, 17 Å; 34,000X. (*c*) Film stripped from crystal oxidized 15 min at 130°C; average thickness, 40 Å; 34,000X. (*d*) Film stripped from crystal oxidized 17 min at 150°C; average thickness, 60 Å; 10,000X. (*e*) Film stripped from crystal oxidized 17 min at 150°C; average thickness, 60 Å; 36,000X. (*f*) Film stripped from crystal oxidized 30 min at 150°C; average thickness, 66 Å; 10,000X. (*g*) Film stripped from crystal oxidized 24 hr at 250°C; average thickness, 195 Å; 12,000X.

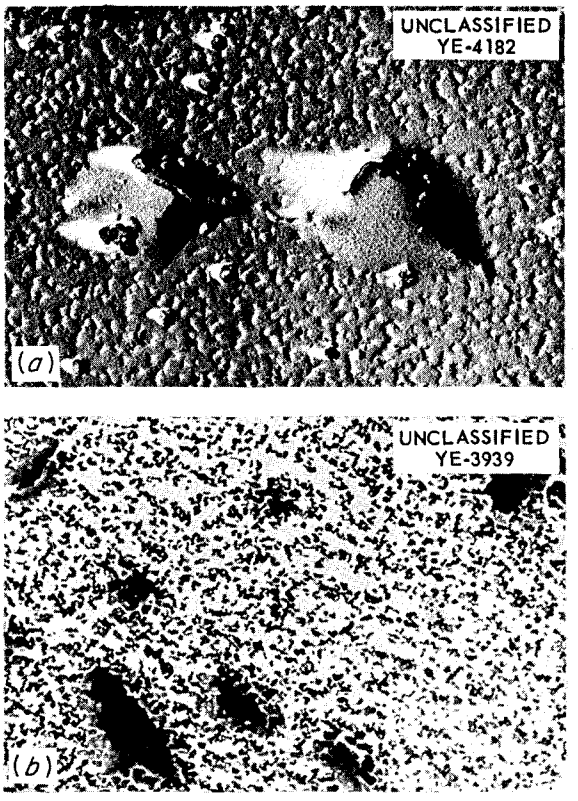

Fig. 57. (*a*) Carbon Replica, Preshadowed with Gold-Manganin, of the Bottom Side (Oxide-Metal Interface) of a Cu_2O Film Stripped from the (311) Plane of a Copper Crystal Oxidized 10 min at 70°C. Average film thickness, 18 Å; 10,000X. (*b*) Cu_2O Film Stripped from the Copper Crystal. Average film thickness, 18 Å; 12,000X.

packed films (Fig. 58*b* and 58*c*). At 250°C, the oxide-gas interface was covered with nodular protuberances (Fig. 58*d*) similar in many respects to those observed on thick films on the (311).

The oxidation characteristics of the (311) and (100) have been investigated more extensively than those of the (111) and (110). However, the early development of oxide films on the latter two planes was quite similar to that described above for the (311). At 250°C, where oxide films of considerable thickness were formed, the oxide-gas interface on the (111) and (110) exhibited surface topographies almost identical with those shown for the (311) and (100).

In summary, the development of oxide films on the (100), (111), (110), and (311) of copper single crystals has been studied. At low temperatures the films formed on all these planes exhibited pronounced thickness inhomogeneities. The gas-oxide interface of these thin films was relatively smooth compared with the oxide-metal interface. Continued oxidation at higher temperatures involved both lateral and vertical growth of the thicker regions of the oxide until, at about 150°C, rather compact and relatively smooth oxide films developed. At even higher temperatures, the oxide-gas interface of the films became quite rough due to the formation of nodular protuberances several hundred angstroms high.

The Effect of Radiation on the Oxidation of Columbium. – An investigation of the effect of radiation on the oxidation of columbium is in progress.[13] Polycrystalline columbium specimens in the form of coupons $1 \times 2 \times 0.04$ cm were vacuum-annealed for 4 hr at 1100°C and then mechanically polished through 0.3-μ alumina and electropolished. The electropolished samples were placed in small quartz capsules which were filled with purified oxygen at room temperature to a pressure of 270 mm Hg. The capsules were sealed and placed in a small furnace contained in an aluminum can, and the entire assembly was lowered into the ORNL Graphite Reactor, with the furnace cold. Approximately 3 to 5 min were required to bring the furnace to the desired oxidation temperature. During oxidation, the specimens were subjected to a neutron flux of about 6×10^{11} *nv*.

This procedure was tested several times out-of-pile, and the results obtained were found to be in good agreement with the results of previous studies of the oxidation of columbium in the absence of radiation.

Several in-pile experiments have been performed at temperatures in the vicinity of 400°C. It has been concluded tentatively that the radiation produced little effect on the oxidation of columbium. However, because of difficulties in determining accurately the temperature of the specimens, final judgment is withheld pending the outcome of additional work.

---

[13]This research is being conducted jointly by the Metallurgy and Solid State Divisions.

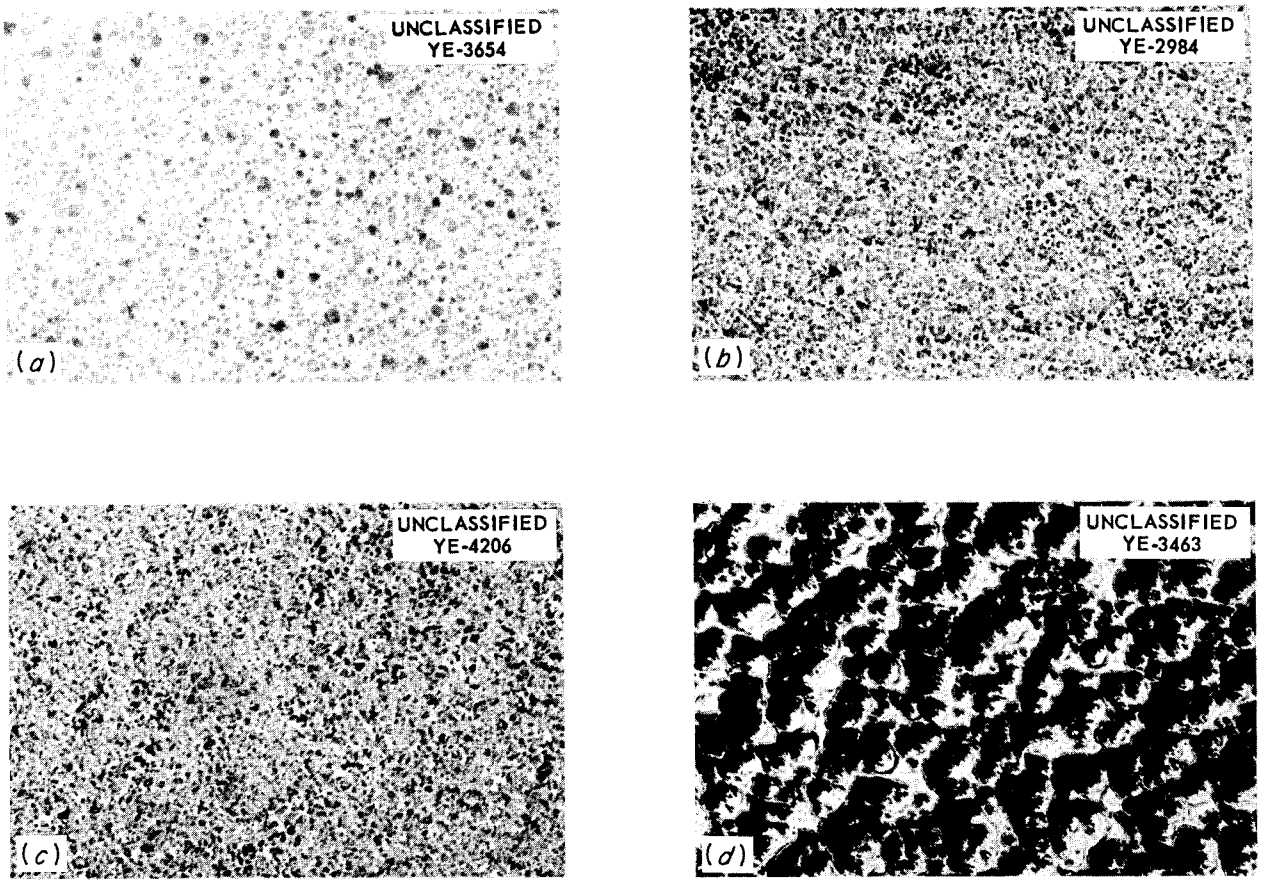

Fig. 58. Cuprous Oxide Film Stripped from the (100) Plane of a Copper Crystal. (*a*) Crystal oxidized 10 min at 70°C; average film thickness, 22 Å; 34,000X. (*b*) Crystal oxidized 30 min at 130°C; average film thickness, 145 Å; 34,000X. (*c*) Crystal oxidized 5 min at 150°C; average film thickness, 163 Å; 36,000X. (*d*) Crystal oxidized 1 hr at 250°C; average film thickness, about 7000 Å; 34,000X.

HRP METALLURGY

G. M. Adamson, Jr.

HRP METALLURGY

G. M. Adamson, Jr.

M. L. Picklesimer
S. G. Nelson
P. L. Rittenhouse
R. L. Stephenson
E. S. Bomar, Jr.
F. W. Cooke
W. J. Leonard
J. J. Prislinger
C. H. Wodtke

PHYSICAL METALLURGY

Zirconium Alloy Development

M. L. Picklesimer
S. G. Nelson
P. L. Rittenhouse
R. L. Stephenson

Zirconium-columbium and zirconium-columbium-X ternary alloys have shown promise in having an in-pile corrosion resistance superior to that of Zircaloy-2 to aqueous uranyl sulfate fuel solutions. An alloy development study has been under way for the past two years with the major objective of developing such a zirconium-base alloy as an engineering material suitable for the construction of the core tank of a reactor vessel. The study has required the determination of the physical metallurgy of the alloy systems, since these have not been studied previously. The early work was discussed in the last metallurgy report[1] and in HRP reports.[2]

In summary, Zr-Cb alloys with 5, 7.5, 10, 15, 20, and 25 wt % Cb; Zr–15 wt % Cb–X alloys with X (in wt %) as 1 and 2 Al, ½ and 1 Cu, 3 V, 1 Cr, 1 Fe, 1 Ni, 2 and 5 Mo, 2 and 5 Pd, 1 and 2 Sn, 5 Ta, 2 and 5 Pt, and 2 Th; Zr–20 wt % Cb–X alloys with X as 2 Mo and 2 Pd; and Zr-Pd and Zr-Pt binary alloys with 1, 2, 5, 10, and 15 wt % alloying element have been studied in more or less detail by beta-quench and reheat transformations, with metallography and hardness measurements as the methods of evaluation. The transformation kinetics have been determined for most of the alloys at 300, 400, 500, and 600°C and are being determined at 350, 450, and 550°C. The standard metallographic methods of determining transformation kinetics are of little avail in these alloys series, and therefore the primary method has been by microhardness measurements. A transformation machine for determining the transformation kinetics by resistance measurements at temperature has been designed, built, and tested. Such determinations for both the isothermal and the beta-quench and reheat transformations are now in progress with the apparatus.

The transformation mechanisms and products are being studied by single-crystal x-ray diffraction techniques and by using the methods of rotating wire specimens, oscillating cameras, and layer-line studies. (The principal data are given in "An X-Ray Diffraction Study of Aging in Zirconium-Columbium Alloys," this report.)

In the last report[1] the hardening transformation for the zirconium-columbium alloys was reported as being by the mechanism of the formation of two body-centered cubic phases from the retained-beta phase. The single-crystal layer-line diffraction studies of the past year have shown that actually the mechanism is that of the formation of an omega phase, a metastable hexagonal structure poor in columbium, from the retained-beta phase. This is similar to the structure and mechanism of formation of the omega phase found in the titanium-vanadium and titanium-molybdenum systems as reported by Silcock *et al.*[3,4] Overaging occurs with the formation of the alpha phase in the temperature range in which the omega phase forms. It is not yet definitely known whether or not the alpha phase is formed from the metastable omega phase or from the retained-beta phase which is enriched in columbium.

---

[1] M. L. Picklesimer, P. L. Rittenhouse, and R. L. Stephenson, *Met. Ann. Prog. Rep. Oct. 10, 1957*, ORNL-2422, p 117 ff.

[2] G. M. Adamson *et al.*, *HRP Quar. Prog. Reps., Oct. 31, 1956*, ORNL-2222, p 114–16; *Jan. 31, 1957*, ORNL-2272, p 119–23; *April 30, 1957*, ORNL-2331, p 124–28; *July 31, 1957*, ORNL-2379, p 122–26; *Oct. 31, 1957*, ORNL-2432, p 131–33; *Jan. 31, 1958*, ORNL-2493, p 141–43.

[3] J. M. Silcock, *Acta Met.* 6, 481 (1958).

[4] J. M. Silcock, M. H. Davies, and K. H. Hardy, p 93 in *A Symposium on the Mechanism of Phase Transformations in Solids*, Monograph and Report Series No. 18, Institute of Metals, London, 1956.

Studies have shown that the omega phase formed by aging at 400°C regresses to re-form the retained-beta phase on reheating to 550°C. The regression can be completed in less than 2 min of reheating at 550°C, as shown in Fig. 59. Other evidence indicates that such regression can also occur on reheating a 400°C-aged specimen to 500°C, with the specimen then transforming and re-forming the omega phase as though it had not been aged at 400°C.

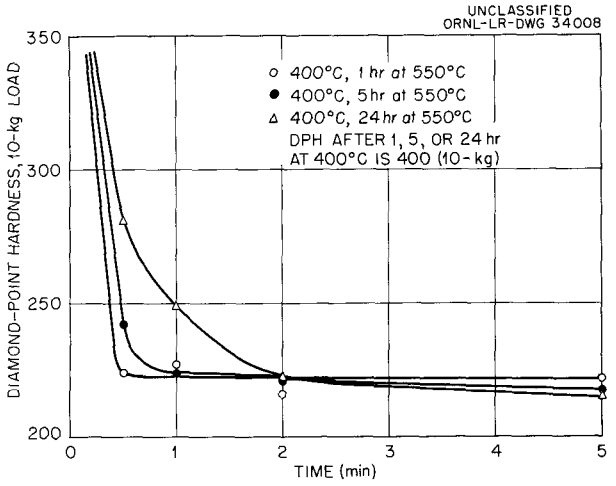

Fig. 59. Change in Hardness of Zr–15% Cb Alloy Aged at 550°C After Prior Aging at 400°C. Shows rapid regression of omega phase and resulting softening.

The Widmanstätten platelet phase, observed in the beta-quenched specimens, has been identified as having a body-centered tetragonal (bct) structure. The phase occurs only on the (100) type of planes of the body-centered cubic matrix. The bct phase forms martensitically on quenching, but only if the amount of omega phase formed during quenching is small. Although the bct phase forms as sheets on the (100) type of planes of the matrix, the phase contains a finer structure, as shown in Fig. 60; this indicates that the structure relationship to the matrix is not that of the *C* axis of the bct cell lying in a [100] matrix direction indicated by the x-ray diffraction patterns obtained on single-crystal specimens. As shown by either microstructural or x-ray diffraction examination, the bct phase dissolves in the beta matrix on reheating to 250°C or above without any detectable decomposition.

The transformation kinetics studies have shown that the hardening reaction of the formation of omega phase on the beta-quench and reheat transformations is delayed by increasing columbium content and by adding small amounts of ternary alloying elements. The minimum incubation time for the Zr-Cb-X alloys occurs in the neighborhood of 400°C for all the alloys studied. Hardness-time curves for five representative alloys, Zr–15% Cb, Zr–15% Cb–2% Pd, Zr–15% Cb–5% Pd, Zr–15% Cb–2% Mo, and Zr–15% Cb–5% Mo, determined after beta-quenching and aging at 400°C are presented in Fig. 61. The most potent ternary alloying addition investigated has been molybdenum. The hardening reaction can be delayed sufficiently by increasing the columbium content to 20 wt % or by adding 5% Pd or 2% Mo to permit multipass welding on beta-quenched material for constructional purposes. Preliminary time-temperature-transformation diagrams have been constructed, but the data are not sufficiently complete to justify presentation.

A number of the experimental zirconium-base alloys have been oxidized in air at 600 and 700°C, with iodide zirconium and Zircaloy-2 as controls. The data are reported in Tables 9 and 10. Five alloys tested at 600°C and four tested at 700°C had better oxidation resistance to air than Zircaloy-2. However, for the times investigated, none had better oxidation resistance to air than did iodide zirconium. The alloys which showed the lower oxidation rates had glassy-appearing oxides which remained adherent, except for some edge cracking, for the entire test period. Those alloys with poor oxidation resistance in air showed early spalling and cracking of the oxide films.

Mechanical properties have been determined to date on only a few specimens of the Zr–15% Cb binary alloy which had been beta-quenched and aged at 400 or 500°C. Aging at 400°C for 24 hr produced a tensile strength of over 200,000 psi at room temperature with less than 1% elongation. Aging at 500°C for two weeks produced, at room temperature, an ultimate tensile strength of 150,000 psi, a yield strength of 135,000 psi, and an elongation of 10% in 1 in. Tests at 300°C for the same aging condition showed a yield strength of 90,000 psi, an ultimate tensile strength of 105,000 psi, and an elongation of 16% in 1 in.

In-pile loop corrosion tests of many of the Zr-Cb-X alloys in several heat-treated conditions have been conducted in uranyl sulfate fuel solutions in a

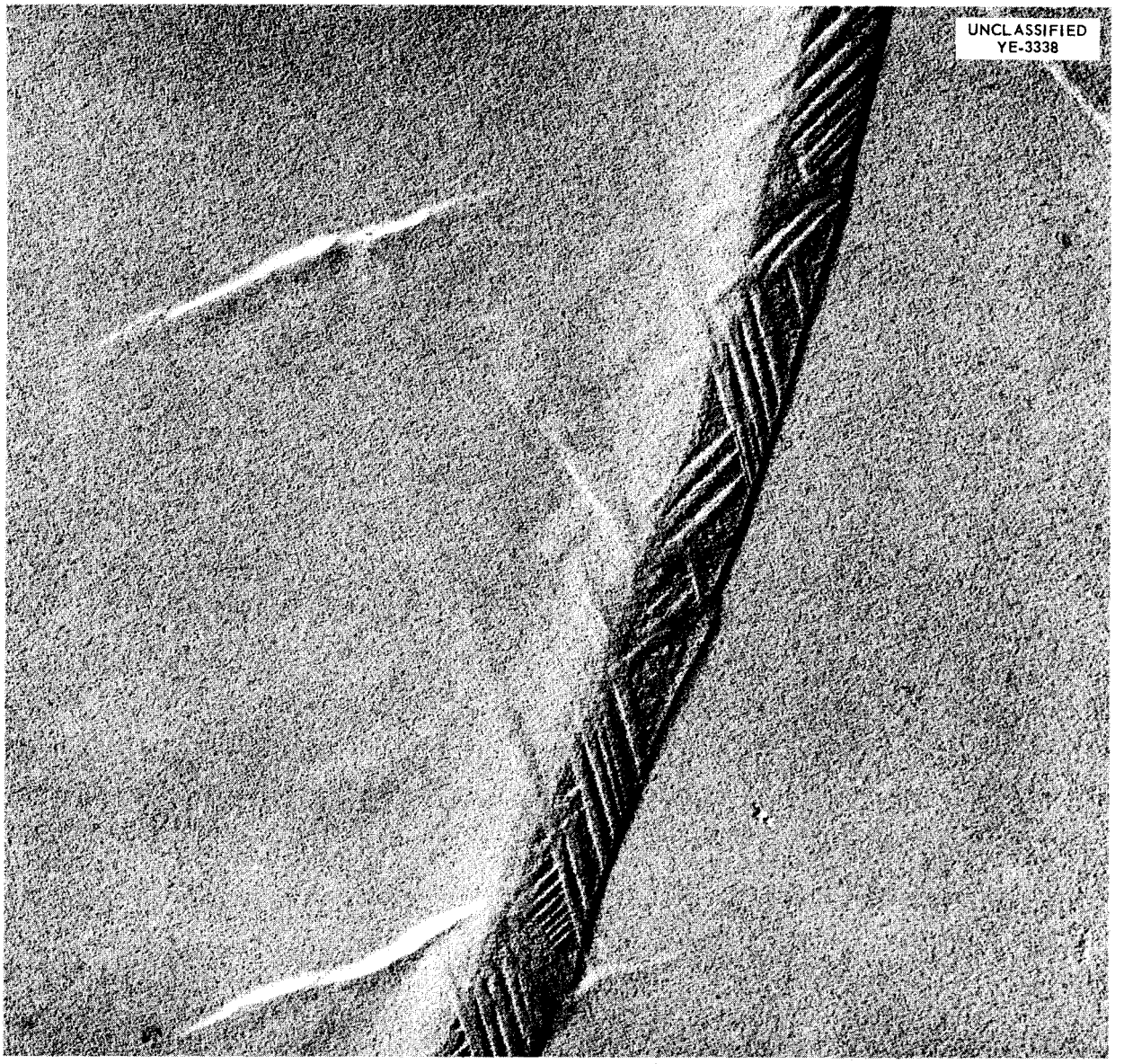

Fig. 60. Electron Micrograph of Zr–15% Cb Alloy. Shows fine structure of Widmanstätten platelets in alloy water-quenched from 900°C; chemical etch, carbon replica, palladium-shadowed. 23,000X.

joint effort with the HRP Corrosion Group.[5] The specimens were prepared, heat-treated, and chemically polished by the HRP Physical Metallurgy Group. Weight losses after in-pile exposure were determined by the HRP Corrosion Group. Metallographic and surface examinations of all specimens were conducted by the HRP Physical Metallurgy Group with the aid of the Metallography Group of the Solid State Division.

In general, the Zr–15% Cb–X alloys showed the best corrosion resistance in the beta-quenched condition (actually aged at loop operating temperatures of 250 to 280°C) and decreasing corrosion resistance in the order of heat treatments: beta-quenched and aged at 400°C for 24 hr, beta-quenched and aged at 400°C for two weeks, beta-quenched and aged at 500°C for two weeks, and beta-quenched

[5] G. H. Jenks *et al.*, *HRP Quar. Prog. Reps., Oct. 31, 1956*, ORNL-2222, p 100; *Jan. 31, 1957*, ORNL-2272, p 102; *April 30, 1957*, ORNL-2331, p 112; *July 31, 1957*, ORNL-2379, p 99; *Oct. 31, 1957*, ORNL-2432, p 106; *Jan. 31, 1958*, ORNL-2493, p 117.

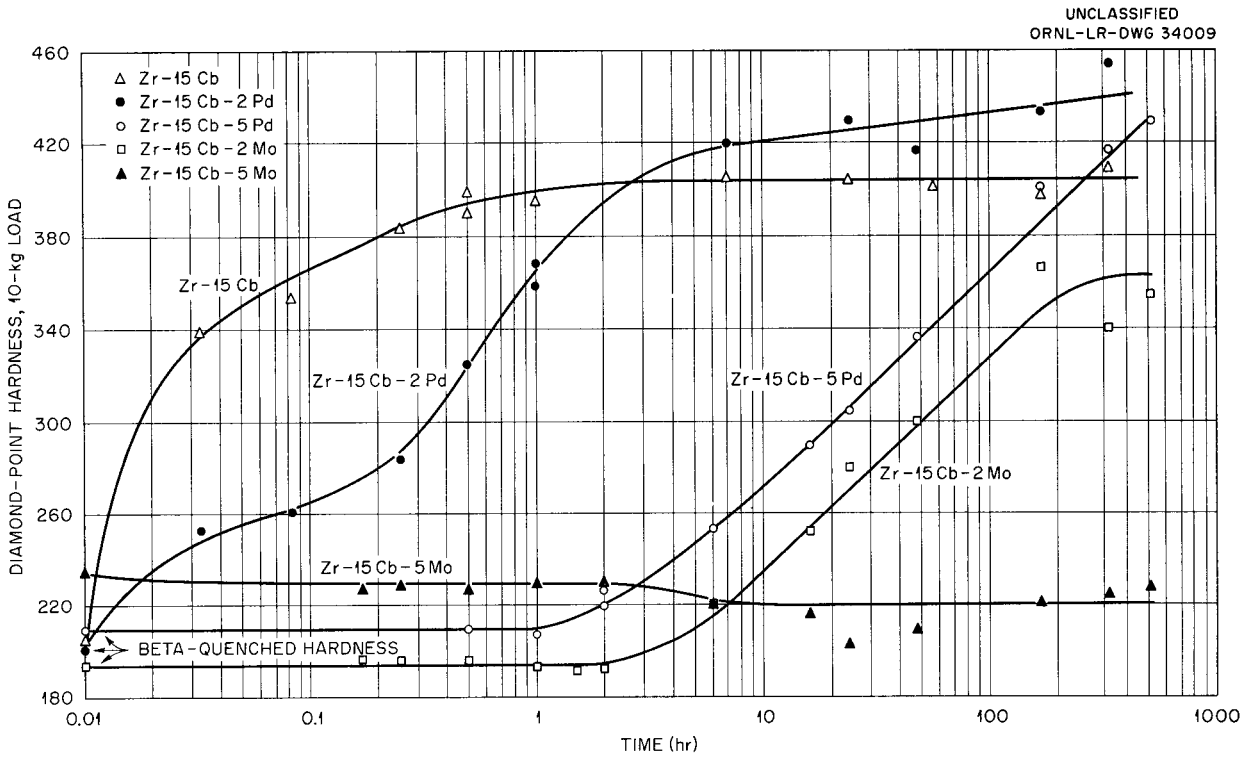

Fig. 61. Hardening of Beta-Quenched and Reheated Zr-Cb-X Alloys Aged at 400°C.

and aged at 600°C for 24 hr. It should be emphasized that all the specimens received a second and variable aging of several hundred hours at 250 to 300°C during pretreatment and testing before the loop was placed in the reactor. Most of the Zr–15% Cb–X alloys had a corrosion resistance slightly less than that of Zircaloy-2 when they were beta-quenched and aged at 500°C for two weeks, a heat treatment which provides relatively high tensile strength with moderate ductility.

The ternary additions improved the corrosion resistance of the Zr–15% Cb base for each heat treatment in the order: ½ wt % Cu (most improvement); 5% Pd; 2% Pd, 2% Th, 2% Mo, and 5% Mo; 2% Pt; 1% Fe, 1% Cr, and 1% Ni; and 3% V. Variations of columbium content showed that the optimum content was 15% Cb, with both 10 and 20% Cb having poorer corrosion resistance.

Direct comparison of the corrosion rates of all the alloys studied cannot be made because the specimens had to be exposed in several loops. Only comparisons relative to the Zircaloy-2 control specimens in each loop can be made. Comparisons between data for the several loops require the assumption that the corrosion rates for the Zircaloy-2 specimen for the several loops can be correlated. Such an assumption seems to be valid but has not been rigorously proved. All in-pile corrosion data obtained to date indicate that the corrosion rate of the zirconium-base alloys increases with increasing fission power density[5] at the surface of the specimens.

Physical Metallurgy of Zircaloy-2

M. L. Picklesimer

The temperature limits of the $\alpha + \beta$ field in Zircaloy-2 have been determined by using resistance measurements. An apparatus designed for determining the transformation kinetics by resistance changes during transformation at 200 to 1000°C was used. Both isothermal transformations and beta-quench and reheat transformations can be studied, and for Zircaloy-2 the time required to reach equilibrium at various temperatures in the α, $\alpha + \beta$, and β fields can be determined for various starting microstructures including those with partitioned alloying elements.

Table 9. Weight Gain for Zirconium-Base Alloys Oxidized in Air at 600°C

Alloy (wt %)	Weight Gain (mg/cm^2)			
	1 hr	16 hr	32 hr	64 hr
Iodide Zr	0.23	0.85	1.16	1.50
Zr–15Cb–5Mo	1.80	3.93	5.06	6.82
Zr–15Pt	0.64	2.66	4.31	7.56
Zr–15Cb–5Pd	1.14	2.56	3.75	7.82
Zr–15Cb–½Cu	1.08	2.78	4.53	8.46
Zr–15Cb–2Pt	0.81	2.52	3.77	8.60
Zircaloy-2	0.21	2.96	5.26	9.38
Zr–15Cb–2Mo	1.68	4.02	7.04	10.50
Zr–15Cb–2Pd	0.98	4.18	7.85	15.12
Sponge Zr–15Cb	1.15	4.54	8.81	16.50
Zr–15Cb–3V	0.74	2.35	6.12	21.76
Zr–15Cb	1.15	5.71	12.60	22.00*
Zr–15Cb–1Cr	1.09	4.57	10.50	23.40
Zr–15Cb–2Th	0.68	5.22	12.76	23.75
Zr–15Pd	1.28	7.14	19.70	37.22
Zr–15Cb–1Al	2.71	6.96	8.70	**

*Some oxide was lost, so the weight gain was probably 25 mg/cm^2 or greater.

**Scaling resulting in weight loss at 64 hr.

Table 10. Weight Gain of Zirconium-Base Alloys Oxidized in Air at 700°C

Alloy (wt %)	Weight Gain (mg/cm^2)			
	2 hr	8 hr	16 hr	32 hr
Zr–15Cb–5Pd	2.47	4.02	5.43	7.09
Zr–15Cb–½Cu	2.58	4.77	7.21	13.50
Zr–15Cb–5Mo	3.35	6.65	9.35	13.53
Zr–15Cb–2Mo–2Pd	3.48	7.54	11.06	15.00
Zircaloy-2	2.27	6.22	12.83	28.37
Zr–15Cb–2Pt	2.30	6.25	12.37	28.70

The resistance-temperature curves for Zircaloy-2 were determined by holding the specimen at the desired temperature point for 20 to 30 min and reading the resistance of the specimen from a multirange resistance recorder permitting readings of ±0.00002 ohm for specimen resistances from 0.02000 to 0.04000 ohm. Several check determinations were made by holding the specimen for times up to 24 hr at temperatures both in the alpha-phase field and in the $\alpha + \beta$ field. No changes in resistance occurred within the determination accuracy after 15 min at temperature. Successive runs were made on the same specimen to determine the effects of holding the specimen for various times at 1030 to 1040°C in the high vacuum of the equipment (always less than 5×10^{-5} mm Hg). The data determined from several specimens show that the normal content of hydrogen in Zircaloy-2 (approximately 40 to 50 ppm H_2) causes the $\alpha/(\alpha + \beta)$ temperature to be 815 ± 1°C, confirming earlier metallographic work,[6] while that for a content of less than 5 ppm H_2 is 832 ± 1°C. The $\beta/(\alpha + \beta)$ temperature is 985 ± 5°C for the particular material studied and was not appreciably affected by hydrogen contents from less than 5 to approximately 50 ppm H_2.

The resistance-temperature curves determined also show that the resistance of Zircaloy-2 approximately doubles in heating from room temperature to about 700°C, changes only a small amount in heating from 700 to 815–832°C, decreases rapidly as small amounts of beta phase are formed, and remains almost constant with increasing temperature from 975 to 1040°C. The data for several successive runs on the same specimen are presented in Fig. 62. The specimen was in the as-received condition for the first run, plotted as run 4 in Fig. 62, and the data show the $\alpha/(\alpha + \beta)$ temperature as 815°C. The run was continued to 1040°C and the specimen held at the temperature for 3 hr for vacuum-annealing to reduce the hydrogen content. The specimen was then helium-quenched to 500°C and the $\alpha/(\alpha + \beta)$ temperature redetermined as 832°C. Successive determinations of the resistance-temperature curves up to 1040°C duplicated the second run. No differences in the resistance-temperature curves were found below 815°C for either hydrogen content. No change in the room-temperature resistance occurred for any of the runs on the same specimen, showing that no

[6] M. L. Picklesimer and G. M. Adamson, *Development of a Fabrication Procedure for Zircaloy-2*, ORNL CF-56-11-115 (Nov. 21, 1956).

preferential vaporization of alloying elements or changes in diameter were occurring in the specimen.

Development of Fabrication Procedures for Zircaloy-2

M. L. Picklesimer P. L. Rittenhouse

The usual commercial fabrication procedures for Zircaloy-2, with the major and final amount of reduction occurring at rolling temperatures and anneals of 1550°F, produce intermetallic stringers and a considerable degree of preferred orientation, resulting in appreciable anisotropy of mechanical properties in the fabricated material. A fabrication schedule which prevents the formation of the intermetallic stringers and considerably reduces the anisotropy of mechanical properties has been reported;[6] the schedule has been tested commercially but has not been shown to produce optimum properties in fabricated material.

A study of the fabrication variables has been under way this year to determine their effects on the preferred orientation, the mechanical anisotropy, the mechanical properties, and the morphology of Zircaloy-2. The variables being studied are the number of beta quenches, the location of beta

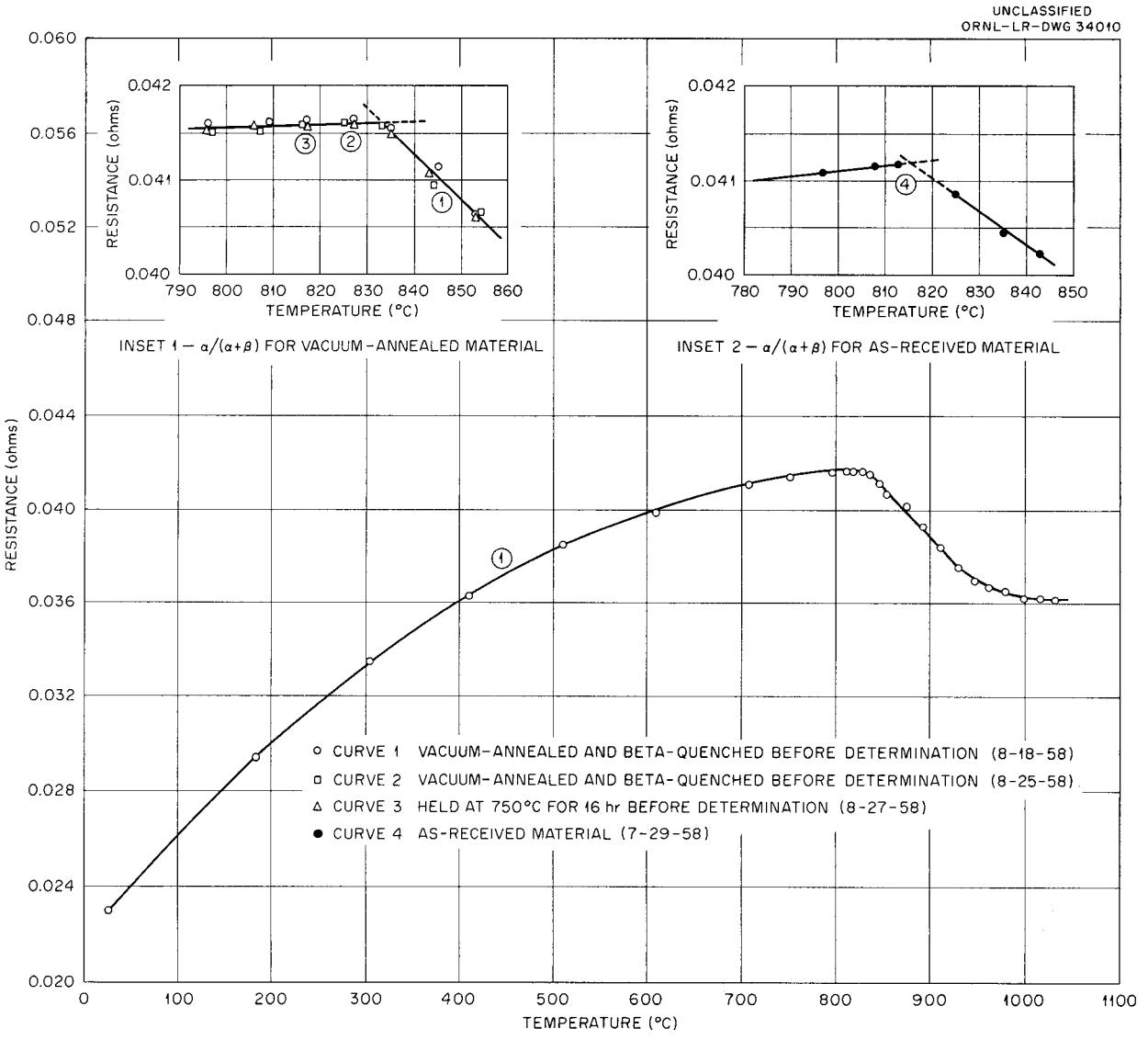

Fig. 62. Changes in Resistance with Temperature for Zircaloy-2. Shows the effect of hydrogen content on the $\alpha/(\alpha+\beta)$ temperature.

quenches in the schedule, rolling temperatures, reductions per pass, reductions per anneal, annealing temperatures, amount of cross rolling, location of cross rolling in the schedule, and amount and direction of reduction after the final beta quench. The evaluations of the fabrication variables are being made by determining stress-strain tensile curves for round specimens cut for different directions in the plane of rolling and subsize Izod notch-impact curves for different notch orientations, by determining the preferred orientations by x-ray diffraction and inverse pole figures, and by making a detailed analysis of the sizes and shapes of cross sections from the fracture to the shoulder of fractured tensile specimens.

The data determined to date on 12 different schedules are by no means complete but do permit the following conclusions to be drawn:

1. The usual mechanical-property determinations such as tensile and yield strengths, etc., do not provide sufficient separation of the fabrication variables to determine their effects.
2. The tensile strengths, elongation, and reductions of area are not appreciably affected by the fabrication variables under study.
3. The yield strength is increased by increased randomization of the texture.
4. The cross sections of fractured round tensile specimens become elliptical wherever flow occurs in anisotropic material.
5. The major axis of the elliptical cross section always lies in the direction normal to the rolling plane.
6. Analyses of the ellipticity of the cross sections from the fracture to the shoulder of the tensile specimen do provide a means of separating the effects of the fabrication variables.
7. Cross rolling in the final stages of fabrication, such as the reduction after the last beta quench, produces considerable anisotropy in material that otherwise would be randomized.
8. Cross rolling in the early stages of ingot breakdown and before the final beta-quench step has little effect on the final anisotropy.

No data have thus far been obtained which would justify major modifications of the presently used HRP fabrication schedule,[6] whose major features are (1) performing the later stages of fabrication at temperatures below 1475°F, (2) heating to 1000°C and water-quenching or rapidly cooling in a forced draft of air at a thickness of 130 to 150% of final thickness, (3) making a final reduction of 20 to 50% at 500°C, and (4) annealing at 1400 to 1450°F for 30 min at temperature.

Zirconium-Hydrogen Studies

R. L. Stephenson S. G. Nelson

It has been postulated that a thin layer of hydride exists immediately under the water-corrosion layer of zirconium alloys which may cause the breakaway phenomenon observed in the corrosion rate determination. During the past year an attempt was made to develop a technique for protecting the edge of mounted zirconium alloy specimens from rounding during polishing and etching so that the hydride layer could be examined metallographically if it exists. Specimens have been hydrided in a modified Sievert's type of gas apparatus to produce thin hydride layers on the surfaces of zirconium alloys.

It has been observed that at above 400°C the hydride layer is formed uniformly over the surface of the specimen but that at 400°C and below, the hydride occurs as large patches and "blisters" scattered essentially at random over the surface, with no hydride layer connecting them.

Metallographic examination of a series of hydrided specimens containing various amounts of hydrogen has shown that a surface layer, produced by adding a total content of 200 ppm H_2 at 500°C to the specimen, can be detected and examined. Total additions of 100 ppm H_2 could not be detected as a hydride surface layer; if present, the layer may have been obscured by the small amount of edge rounding that occurred.

Slant polishing of specimens prepared with a rather heavy hydride layer has shown that the hydride needles reported by several investigators to be in the center of grains of Zircaloy-2 immediately under the hydride layer are actually deformation twins formed by the deformation occurring in the conversion of the surface layer to hydride. Photomicrographs in both bright field and polarized light are presented in Fig. 63. The plane of polish for the photomicrographs in Fig. 63*a* and 63*b* is at an angle of about 10° to the hydrided surface layer, while that for Fig. 63*c* and 63*d* is 90°. The lens-shaped twins found in the slant-polished specimen show rather conclusively that the lines or hydride needles observed in the 90° polished specimen are the traces of such thin twins.

On a lightly oxidized specimen, anodized to produce an oxide about 10,000 Å thick, some

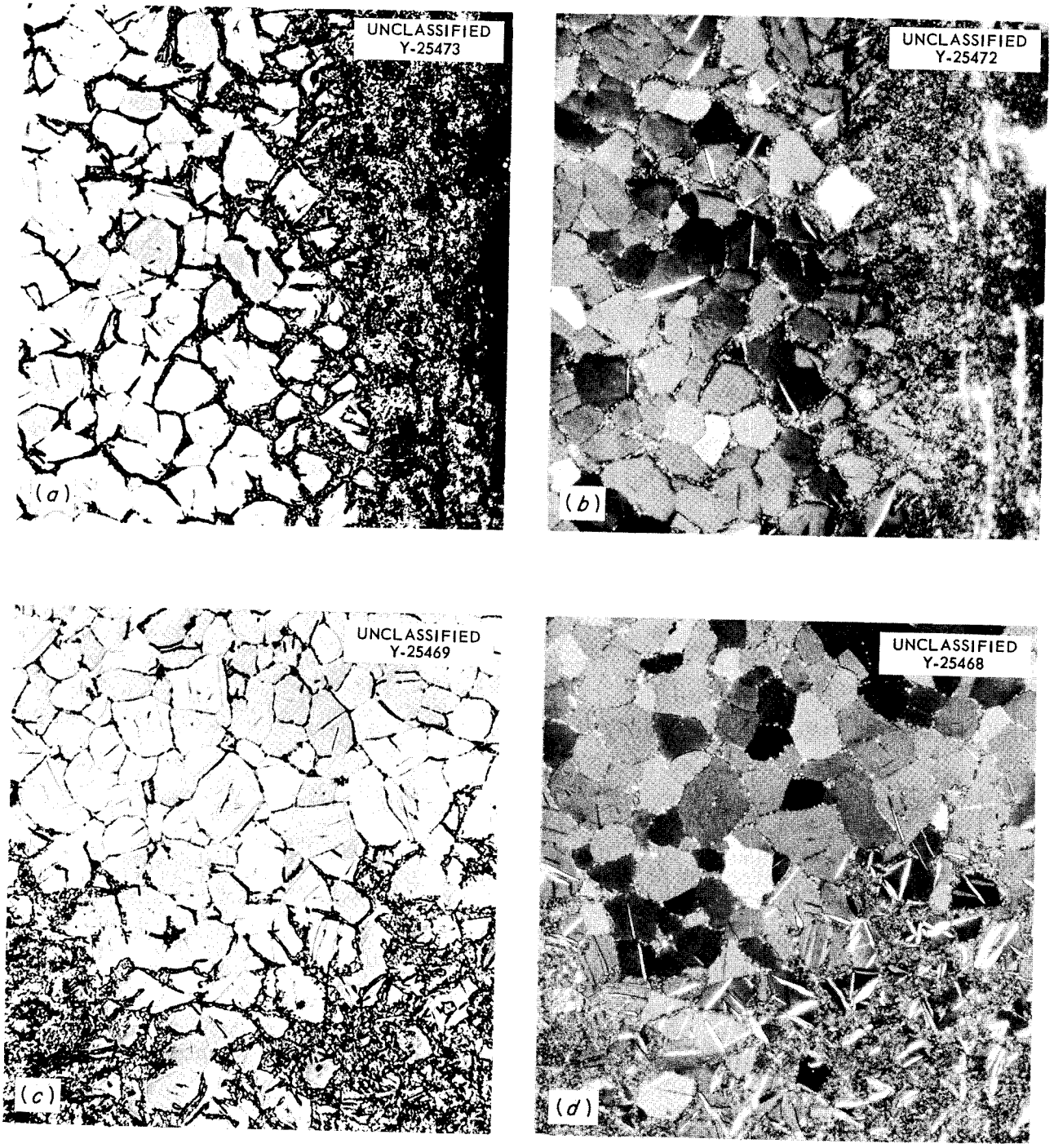

Fig. 63. Surface Layer of Zirconium Hydride on Zircaloy-2. (*a*) Bright field; slant-polished 10°; shows lens-shaped twins. (*b*) Polarized light; slant-polished 10°; shows lens-shaped twins. (*c*) Bright field; slant-polished 90°; shows traces of twins. (*d*) Polarized light; slant-polished 90°; shows traces of twins. Shows that so-called "needles" under hydride layer are actually deformation twins. Anodized. 200X.

success has been obtained in depositing nickel from a Kanigan bath for protection of the edge of the specimen during polishing. However, no success has been obtained in depositing nickel on a specimen that was oxidized in air or on one that had a water-corrosion oxide layer on it.

Special Zirconium Alloys – Mechanical Properties

M. L. Picklesimer

The Armour Research Foundation of the Illinois Institute of Technology has compled an investigation,[7] under a research contract, of weldable β- and α-zirconium–base alloys for applications under stress at temperatures up to approximately 300°C. The tensile strengths, ductilities, and tensile impact strengths were studied as functions of aging time at temperature and of heat treatment.

Tensile properties and tensile impact strengths were determined for four α-zirconium materials, iodide Zr and sponge Zr and 1.5% Sn alloys of both materials. Sheet-type specimens, both welded and unwelded, were tested. Test temperatures were room temperature and 300°C for the tensile tests and –100 to 300°C for the tensile impact tests. The alpha materials generally exhibited a lack of heat treatability, little or no deterioration of properties due to welding, and essentially no indication of impact transition temperature (hydrogen contents of 14 ppm and less and notched tensile impact tests, not notched bar or beam impact tests).

Tensile strength and tensile impact behavior were established for alloys based on iodide zirconium containing 15% Cb, 15% Cb–2% Pd, 15% Cb–2% Pt, and 15% Cb–1% Fe and for a binary sponge Zr–15% Cb alloy. High strength levels could be established by heat-treating beta-quenched specimens at 300 to 500°C. Tensile strengths of 200,000 psi were obtained on some alloys by certain heat treatments.

Temperature-time-resistivity data were obtained for the Zr-Cb-X alloys to establish the transformation kinetics by means of resistivity changes for comparison with the studies made by hardness changes. In general, the resistivity curves showed several plateaus during transformation that were not observed in the hardness curves, indicating that the transformation is probably more complex than would be established by the hardness data alone.

[7] Armour Research Foundation, *Special Zirconium Alloys*, Report No. 18, ARF Project B100, Subcontract No. 903, W-7405-Eng-26, Oct. 15, 1957.

ENGINEERING METALLURGY

Mechanical Metallurgy

J. J. Prislinger

Zircaloy-2. – To enable the design and development engineers to more efficiently use Zircaloy-2, a study is being made of its mechanical properties. This study includes the application and interpretation of various mechanical-property testing methods, with special emphasis on evaluating the sensitivity of the tests to the anisotropic behavior of this hexagonal metal.

As a supplement to the work described in "Development of Fabrication Procedures for Zircaloy-2," this report, this study has made use of several plates of Zircaloy-2. Plate 1 was the usual commercial material that had been fabricated in the $\alpha + \beta$ field with only straight rolling. Plate 2 was fabricated commercially but to the ORNL-developed schedule.[8] Some data were also obtained on scrap material left from the fabrication of the HRT core tank. This material had been fabricated in the $\alpha + \beta$ field but had received 50% cross rolling. It was only $\frac{1}{4}$-in. thick and could not be used for all phases of the study.

Impact energy curves obtained from full-size Charpy V-type specimens cut from the commercial plate are presented in Fig. 64*a*. It is evident that a wide variation in properties may be obtained, depending upon sample and notch orientation, with the latter being the more critical of the two. In addition to having higher impact energies, the specimens with the vertical notch had less lateral contraction in the area below the notch. In spite of their lower fracture energies the fractured surfaces from specimens with horizontal notches contained shear lips, normally considered an indication of ductility, while those with vertical notches had an S-shaped surface. In neither case was there a sudden change in fracture appearance with decreasing temperature.

The set of impact curves in Fig. 64*b* was obtained from subsize Izod-type impact tests of the same plate used for the Charpy tests. The anisotropy of the material may be noted from the spread in these curves. Both types of tests yielded similar curves for specimens with horizontal notches; however, in

[8] M. L. Picklesimer and G. M. Adamson, *Development of a Fabrication Procedure for Zircaloy-2*, ORNL CF-56-11-115 (Nov. 21, 1956).

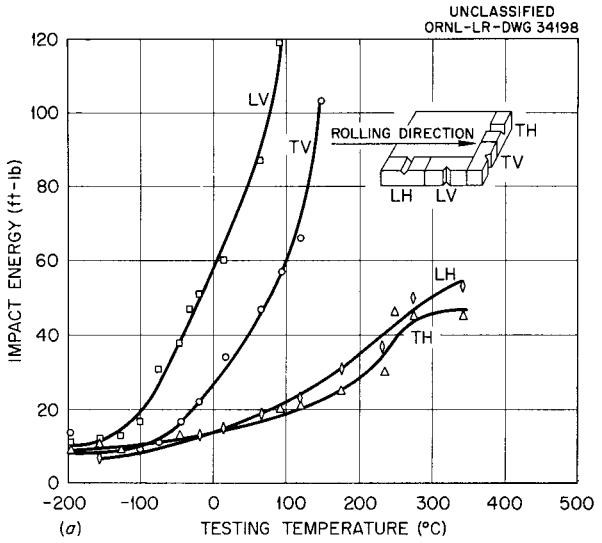

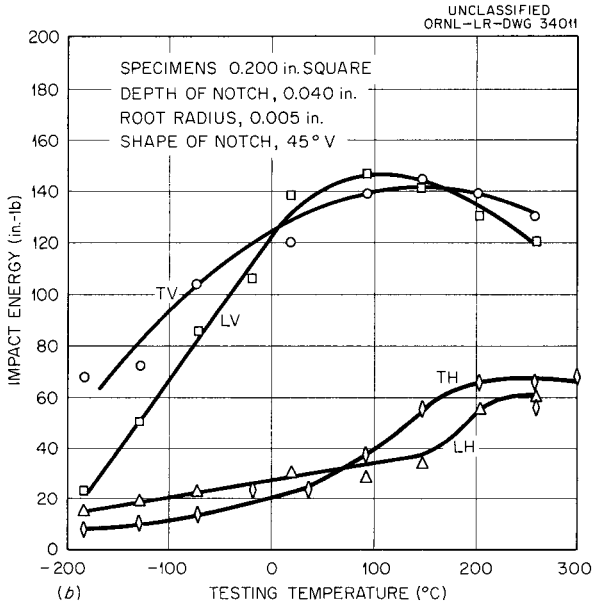

Fig. 64. Impact Energy Curves for Commercial Zircaloy-2. (*a*) Full-size Charpy V-notch; (*b*) subsize Izod type. Shows considerable anisotropy in the properties.

the subsize specimens the curves from specimens with vertical notches were of similar shape but were displaced about 100°C downward. It is not yet known whether the difference for specimens with vertical notches resulted from a size effect or from the basic differences in the two tests.

Zircaloy-2 fabricated to the ORNL-developed schedule is a more nearly isotropic material, as is evident by comparison of the impact curves in Fig. 65 with those in Fig. 64. While differences are still apparent, these four curves fall within a much narrower band. When received, this material was above tolerance in hydrogen, ~60 ppm. To minimize the effects of this embrittling variable, the impact samples were heated to 400°C and quenched before being broken. A few samples which were vacuum-annealed to remove the hydrogen produced curves similar to those of samples quenched from 400°C. After treatment, samples from all four orientations showed fibrous, ductile-appearing fractures at all temperatures. When the samples were broken without minimizing the effects of hydrogen, similar behavior was noted at temperatures above 100°C, but below 100°C, brittle-appearing fractures with very low energies were found.

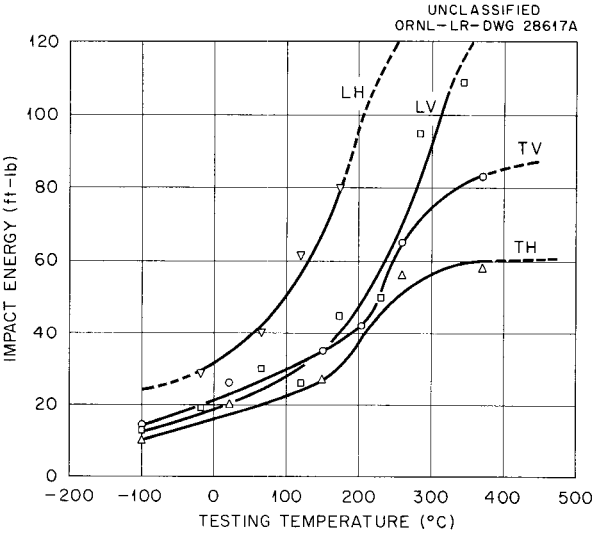

Fig. 65. Impact Energy Curves from Full-Size Charpy V Specimen of ORNL-Fabricated Zircaloy-2. Shows a nearly isotropic material.

It is possible to obtain Zircaloy-2 material which has almost identical mechanical properties, as shown by transverse and longitudinal tensile specimens, but yet varies in the thickness direction, as shown by impact tests or by a study of the shapes

of the fractured tensile specimens. With Zircaloy-2, many of the rules of thumb usually used in impact testing no longer apply. The location of the notch is more critical than the sample orientation, and the presence or absence of shear-lip seems to be more dependent on preferred orientation than on ductility or temperature.

Subsize multiple-break tensile specimens were also used for studying the anisotropy of Zircaloy-2; data from four plates of Zircaloy-2 are given in Table 11. Plates 1 and 2 were the same as those used in the impact property study. Plate 3, of the same material as plate 2, was given a second but identical fabrication schedule under more carefully controlled laboratory conditions. Plate 4 was scrap material from the HRT core tank plate. With the exception of plate 1, the differences in ultimate strength, yield strength, elongation, and reduction in area for samples machined from the longitudinal and transverse directions are very small. This is true for the specimens broken at room temperature and those at ~300°C.

Table 11. Tensile Properties of Zircaloy-2[a]

Plate[b] Service	Specimen Orientation in Plate	Ultimate Strength (psi)	Yield Strength, 0.2% Offset (psi)	Elongation in 1 in. (%)	Reduction (%)			Isotropic Ratio of Reduction
					Area	Longitudinal or Transverse Direction[c]	Normal Direction[d]	
Broken at Room Temperature								
Plate 1	Longitudinal	64,900	54,800	31.1	47.7	45.5	4.4	10.4
	Transverse	69,000	58,300	25.8	43.3	40.6	3.3	13.7
Plate 2	Longitudinal	73,200	63,300	31.0	46.4	35.5	16.7	2.1
	Transverse	75,200	59,400	29.1	44.0	28.4	21.6	1.3
Plate 3	Longitudinal	73,800	66,400	32.2	46.0	37.2	14.4	2.6
	Transverse	74,200	58,400	32.7	44.3	25.5	25.5	1.0
Plate 4	Longitudinal	61,400	52,300	30.7	60.6	56.6	10.0	5.7
	Transverse	63,300	59,000	24.5	62.1	57.8	10.0	5.8
Broken at 300°C								
Plate 1	Longitudinal	32,600	25,500	35.5	43.5	38.4	7.8	4.9
	Transverse	29,300	21,200	29.3	68.4	65.5	13.3	4.9
Plate 2	Longitudinal	38,600	31,400	30.4	64.5	52.2	24.4	2.1
	Transverse	37,600	29,000	31.5	61.5	43.8	31.6	1.4
Plate 3	Longitudinal	32,800	27,800	32.9	76.5	63.3	35.5	1.8
	Transverse	35,000	25,100	32.1	68.7	48.3	39.4	1.2
Plate 4	Longitudinal	28,400	22,200	38.8	77.6	68.9	27.2	2.5
	Transverse	32,200	29,600	27.9	76.2	71.1	17.8	4.0

[a] Strain rate = 0.05 in./in./min.

[b] Plate 1, hot-worked commercially in $\alpha + \beta$ field without any cross rolling.
Plate 2, fabricated experimentally according to new fabrication schedule, except inert-gas melted.
Plate 3, same material as used for plate 2 and refabricated to same schedule in laboratory.
Plate 4, core tank scrap material from HRE-2; hot-worked commercially in $\alpha + \beta$ field; also cross-rolled.

[c] Minor axis of elliptical fractured face.

[d] Major axis of elliptical fractured face.

An unusual but sensitive index of anisotropy is shown in Table 11. With these anisotropic materials the fractures had elliptical rather than round cross sections. The table shows the percentage reduction for both the major and minor axes of the ellipse of the fractured faces and also the ratio between them. A statistical study of eight identical specimens showed that these ratios are reproducible.

For the core tank material, plate 4, the percentage reduction is much lower in the normal direction than in the plane of the plate. Similar reductions were obtained for both the longitudinal and transverse specimens.

That cross rolling was beneficial for plate 4 was confirmed by the high isotropic ratios when plate 4 was compared with plate 1. Very little deformation occurred in the normal direction for plate 1. This plate also shows a difference in properties between the longitudinal and transverse specimens.

Titanium. – A mechanical-property study of titanium A-40 has been made to determine its suitability as a reactor structural material. Although not thought to be serious, a reduction in impact properties of unalloyed titanium (yield strength, 45,000 psi) has been found[9] with a minimum in the neighborhood of 250°C. Since this temperature is within the proposed operating-temperature range of the reactor, attempts have been made through mechanical testing to understand this phenomenon. In tensile tests Rosi and Perkins[10] found a decrease in ductility, as measured by percentage elongation, for high-purity titanium in the range of 230 to 450°C with titanium A-100AT, an all-alpha alloy. Makrides and Baldwin[11] also reported a dip in the reduction-in-area vs temperature curve. Increasing the strain rate from 0.05 in./in./min to 100 in./in./min moved the trough in the reduction-in-area curve from 350 to 540°C. These investigators believed this phenomenon to be due to a strain-aging mechanism.

In addition to tensile and creep tests performed on Ti A-40 in the temperature range of interest, a few tests were conducted on specimens aged in the absence of stress. A group of Charpy V-notch impact specimens of Ti A-40 (25 ppm H_2) were aged for 3024 hr at 315°C. The data are plotted in Fig. 66 along with the curve for the as-received specimens. There is very little difference between the two curves, which shows that aging at 315°C has not impaired the impact strength in the temperature range studied. This supports the data obtained with subsize Izod specimens in a previous study on the effect of hydrogen concentration on the aging of titanium.[12]

Creep Studies. – Long-time creep tests conducted between room temperature and 315°C are being carried out on Zircaloy-2 and on titanium A-40 and A-110AT in the vicinity of their 0.2% yield strengths at these temperatures. Design considerations make it desirable to know the creep properties of these materials, especially beyond 1000 hr, for which there are very few data in the open literature. Of special interest are the shapes of the time-deformation curves for determining whether the transition from second- to third-stage creep is gradual or abrupt. Creep tests of 4800 hr for Ti A-40 and Ti A-110AT and 7200 hr for Zircaloy-2 indicate that the transition is gradual.

Radiation Effects on Zirconium and Titanium Alloys

J. J. Prislinger

As a portion of the mechanical-property studies of materials of interest to the HRP, samples have been exposed to high-temperature fissioning uranyl sulfate solutions. Subsize tensile and impact samples were tested in the in-pile loops operated by the Materials Section of the Reactor Experimental Engineering Division.[13] They were exposed directly to the same solution in regions of both high (core samples) and low (in-line) neutron flux. The loops were operated essentially isothermally at 250 to 280°C. Only a limited number of samples may be exposed in this manner and in addition they must be subsize; therefore, reproducibility is poor and many question remain to be answered.

[9] G. M. Adamson *et al.*, *HRP Quar. Prog. Rep. April 30, 1957*, ORNL-2331, p 124–28.

[10] F. D. Rosi and F. C. Perkins, *Trans. Am. Soc. Metals* 45, 972–92 (1953).

[11] N. Makrides and W. M. Baldwin, Jr., *High Temperature Brittleness in Titanium Alloys*, WADC-TR-57-251(Pt. I) (March 1957).

[12] G. M. Adamson *et al.*, *HRP Quar. Prog. Rep. Oct. 31, 1956*, ORNL-2222, p 114–116.

[13] G. H. Jenks *et al.*, *HRP Quar. Prog. Reps., Oct. 31, 1956*, ORNL-2222, p 100; *Jan. 31, 1957*, ORNL-2272, p 102; *April 30, 1957*, ORNL-2331, p 112; *July 31, 1957*, ORNL-2379, p 99; *Oct. 31, 1957*, ORNL-2432, p 106; *Jan. 31, 1958*, ORNL-2493, p 117.

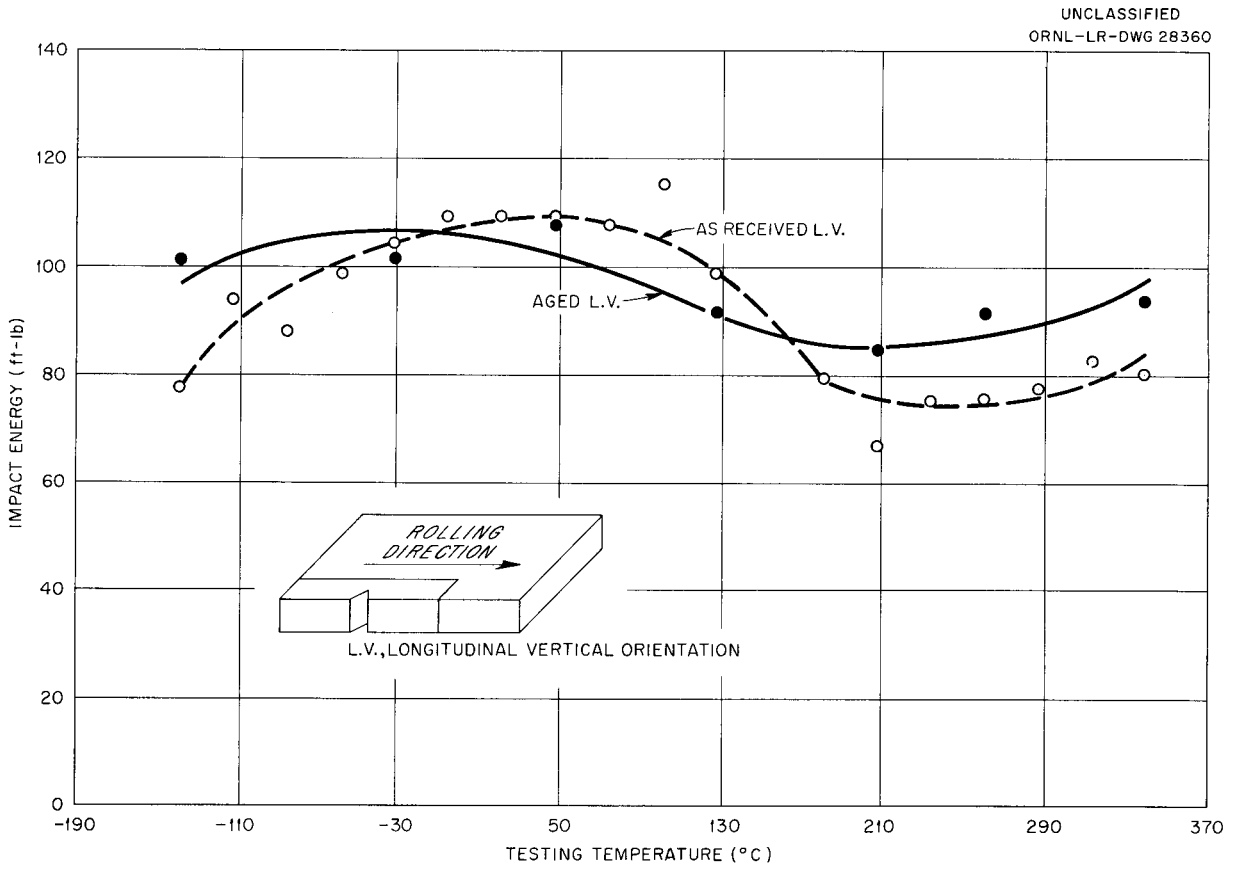

Fig. 66. Charpy V-Notch Impact Strength (L_V) of As-Received and Aged (315°C, 3024 hr) A-40 Titanium.

Subsize tensile and Izod-type impact samples of Zircaloy-2, Zircaloy-3A, and crystal-bar zirconium have been exposed. At the fluxes encountered, no large changes in mechanical properties were found with any of these alloys. Impact curves for Zircaloy-3A and crystal-bar zirconium are presented in Fig. 67*a* and 67*b*, respectively. For both materials a single curve adequately serves for line, core, and control points, showing that no change has occurred due to radiation or loop environment.

Data obtained from the tensile samples contain some inconsistencies, but small trends are evident at fast-neutron doses of the order of 10^{19} *nvt*. In general, small increases were found in the yield points with small decreases in total elongation. The most consistent, but still small, change was a decrease in uniform elongation, as defined by that portion of the stress-strain curve between the proportional limit and the maximum stress value.

In-pile mechanical-property tests of quite a variety of titanium alloys were conducted primarily as screening tests. Again, in each case, data are available from only a few subsize samples. In tensile tests both the unalloyed Ti A-55 and the alpha alloy Ti A-110AT gave similar changes. With specimens broken at either room temperature or 315°C, small radiation-induced increases were noted in both yield and ultimate strength, with corresponding decreases in ductility. Unlike zirconium, the major change in ductility was a decrease in necking elongation rather than in the uniform elongation. Corresponding changes were found with the alpha-beta alloy C-130AM, except that the changes in the specimens broken at 315°C seemed to be smaller than in those broken at room temperature. For all these alloys the results for specimens exposed to the test solution at low fluxes (in-line samples) are different from those for both the control and the high-flux core specimens. More data are required to determine whether these effects are real. However, no logical mechanism has yet been proposed for explaining why there

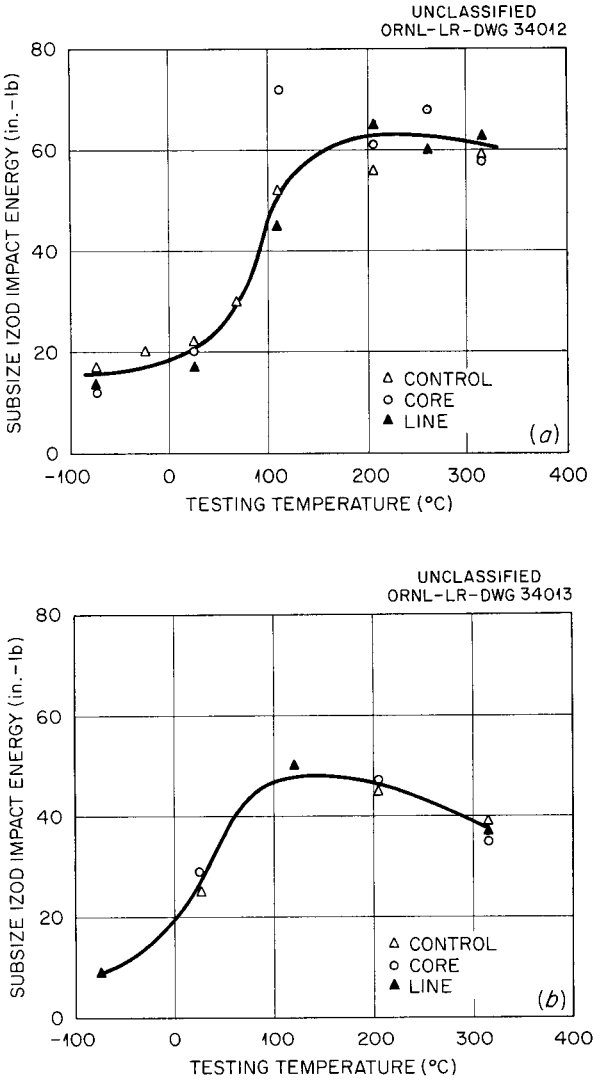

Fig. 67. Subsize Izod Impact Strengths of Irradiated Zirconium Alloys. (*a*) Zircaloy-3A from loop L-14-13 (0.17 *m* UO_2SO_4, 250°C, dose 2 to 5 × 10^{18} *nvt*); (*b*) crystal-bar Zr from loop L-2-15 (0.17 *m* UO_2SO_4, 280°C, fast-neutron dose of 0.7 to 1.4 × 10^{19} *nvt*).

are such changes in a line sample but not in the other two.

Impact energy curves obtained with subsize Izod-type specimens of unalloyed titanium A-40 are shown in Fig. 68. The unusual shape of these curves is caused by a maximum at about −100°C. In this figure, the values for line and core specimens both lie below the control line; however, in samples irradiated to 1 × 10^{19} *nvt* in loop L-2-14, the core sample points were above those for the controls. It may be concluded that no measurable

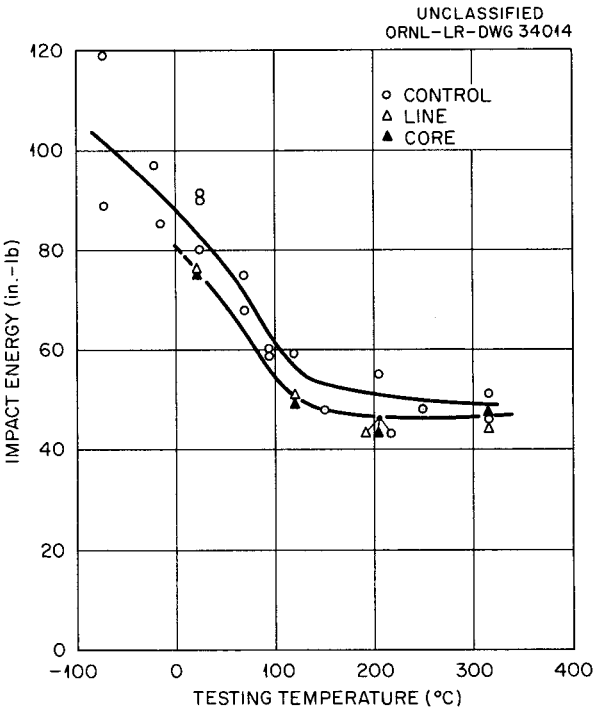

Fig. 68. Subsize Izod Impact Strength of A-40 Titanium Exposed in In-Pile Loop L-4-12 (0.17 *m* UO_2SO_4, 250°C, Estimated Fast-Neutron Dose of 4.9 to 9.5 × 10^{19} *nvt*).

change in impact properties occurred under these conditions.

Impact curves for unalloyed titanium A-55 and alpha-alloy titanium A-110AT are shown in Fig. 69*a* and 69*b*, respectively. In neither case was a radiation or loop-environment-induced change noted. Comparing the shape of the A-55 curve with that for the A-40 material shows the marked effect on impact strength of the addition of small amounts of oxygen and/or nitrogen. The analyses of these alloys are identical within the usual analytical accuracy, with the difference in yield strength being caused by very small differences in the gaseous impurities.

Welding Development

W. J. Leonard

Titanium Alloys. – Air-welding techniques for commercial titanium[14] have been developed and a

[14] G. M. Adamson and W. J. Leonard, *Welding J. (N. Y.)* 37, 673–82 (1958).

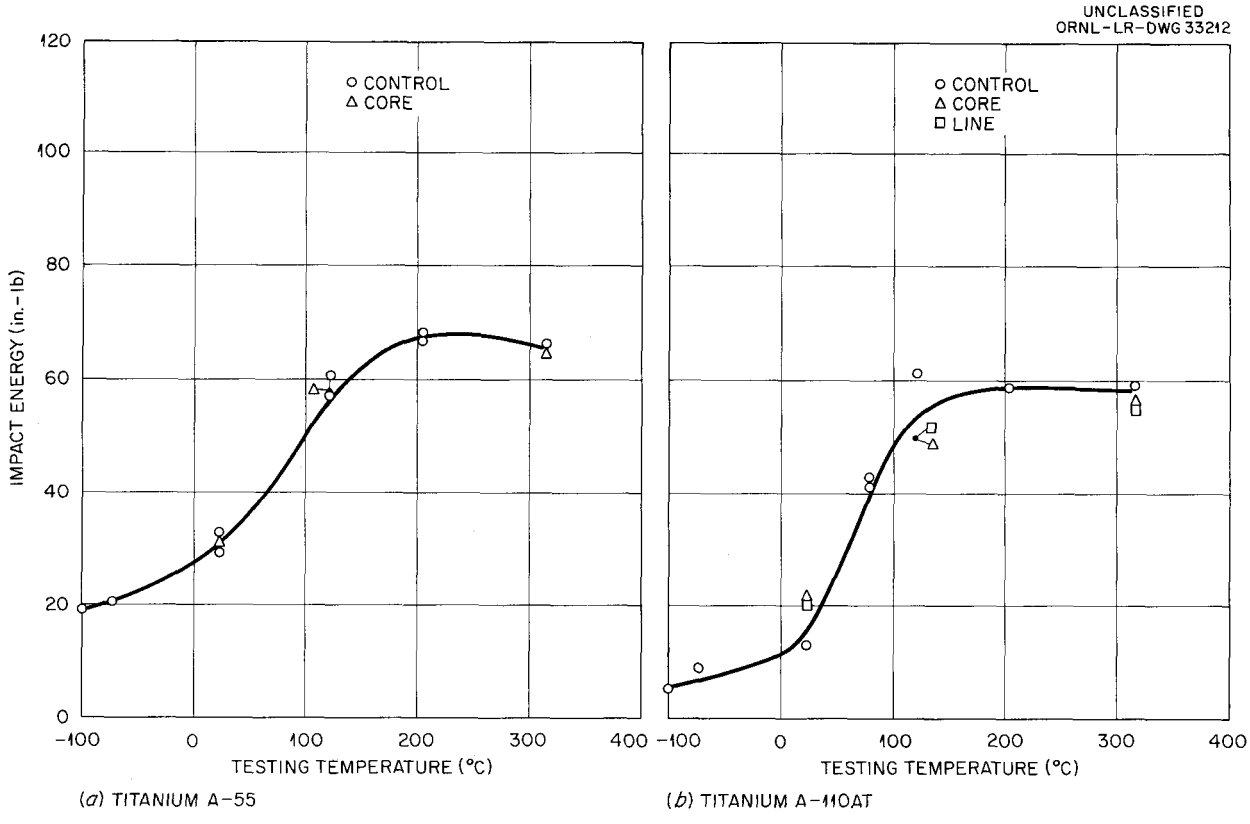

Fig. 69. Subsize Izod Impact Strengths of Irradiated Titanium Alloys. (*a*) A-55; (*b*) A-110AT. Loop L-4-16 (0.04 *m* UO_2SO_4, 280°C, fast-neutron dose of 2.5 to 5.0 × 10^{18} *nvt*).

formal HRP welding procedure and welder-qualification specification[15] written. Although the quality of titanium welds made to this specification is considered entirely satisfactory and evaluations by mechanical test of air welds and dry-box welds gave identical results, it was known that the average hardness of cross sections of multipass air welds fell in the range of 210 to 225 DPH, while those from multipass dry-box welds were in the range of 180 to 190 DPH. Detailed work on air-welding has now revealed some of the reasons for this difference, and air welds having the same hardness as dry-box welds can now be made routinely. To accomplish this, it was found necessary to grind the surface of each weld pass made in air, removing the gold or blue-colored thin surface film before proceeding with the next pass. The diameter of the gas cup on the welding torch must be of adequate size to completely cover the molten metal and any base metal in the heat-affected zone that exceeds approximately 1600°F. The inert-gas-coverage system, including backup, in each welding setup must be carefully inspected prior to welding to ensure its adequacy.

To ensure root passes having the most desirable geometry, the use of preplaced root inserts in making the root pass of a weld is often beneficial. Acceptable root passes using $\frac{1}{16}$- or $\frac{1}{32}$-in. preplaced inserts may be made in titanium. However, the average hardness range was found to be 220 to 230 DPH, which, though not disqualifying, is high. The increase in contamination results from the higher welding-heat input required to secure full-penetration, completely fused root passes. By using an insert of square cross section (0.070-in. sides), welding could be performed at heat inputs equal to or lower than hand-fed wire welding. The welds were equivalent in hardness to hand-fed wire welds but contained excessive porosity. Changing the welding variables and purging conditions yielded

[15] HRP Welding Specification No. 7 – Inert-Gas Shielded-Arc Welding of Commercially Pure Titanium.

no combination which would eliminate this porosity. Figure 70 shows the root face of an insert weld, illustrating the uniform geometry of such a weld. With the welding conditions examined, insert-type root passes of quality equal in all respects to hand-fed wire welds have not yet been obtained.

Titanium A-110AT, an alpha-stabilized high-strength titanium alloy, is a weldable material. Previous work[16] indicated that the developed titanium-welding procedures were applicable to this alloy. Weldments made on this alloy by the procedures used for commercial titanium resulted in weld metal of a hardness only slightly greater than that of the base metal used. During this year, bend tests made on transverse bars from Ti A-110AT weldments from various plates of different thicknesses have given inconsistent results. Some from $\frac{1}{16}$-in. sheet and $\frac{1}{8}$-in. plates were bent successfully on $2T$ ($2 \times$ thickness) radii; others from $\frac{1}{2}$-in. welded plate stock broke on an $8T$ radius. The specifications for the base metal require a 105° bend on an $8T$ radius. The majority of breaks occurred in the heat-affected zone of the base metal. The amount and distribution of the grain-boundary phase present in base metal appear to exert a considerable effect on the ductility possessed by a weldment.[16] It appears to be necessary to make a metallographic examination of each plate of this alloy before its weldability can be determined.

A series of test welds on 4-in.-dia, $\frac{3}{8}$-in.-wall pipe material, for use as a pressurizer in a boiling-water loop-pressurizer mockup, was made. All welds had acceptable mechanical properties as evaluated by tensile test specimens, and successfully passed bend tests on 4 and $5T$ radii. Table 12 gives the tensile data on these pipe weldments. Metallographic examination of the extruded-pipe base metal showed relatively small amounts of the grain-boundary phase. Whether other beneficial effects were derived from an extruded structure

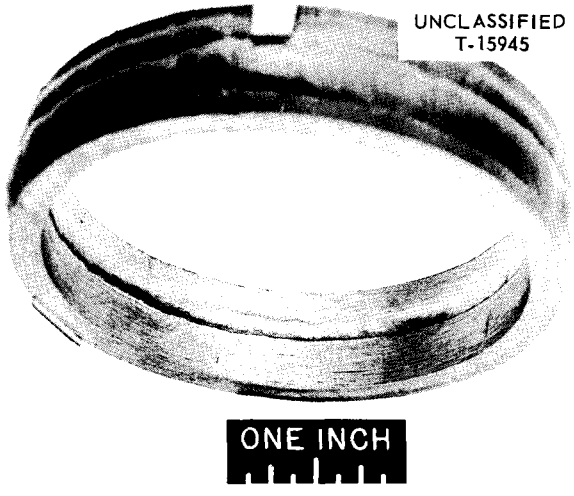

PREPLACED ROUND WIRE INSERT ROOT PASS RC-140 IN 2½-in. SCHED. 40 RC-A55 PIPE

Fig. 70. Root Face of a Titanium Root Insert Weldment.

[16] W. J. Leonard, *Met. Ann. Prog. Rep. Oct. 10, 1957*, ORNL-2422, p 127–29.

Table 12. Mechamical Properties of Specimens from 4-in.-dia $\frac{3}{8}$-in.-wall Ti A-110AT Pipe Weldment

Test Number	Ultimate Tensile Strength (psi)	Yield Strength, 0.2% Offset (psi)	Elongation in 2 in. (%)	Bend Angle (deg)	Radius, T	Remarks
1	133	118	10	5–10	2½	Ruptured
2	135	119	11	5–10	2½	Ruptured
3	132	122	12.5	20–30	2½	Ruptured
4	145	131	10	105	2½	Crack appeared
5	145	128	9	105	5	Sound
6	162	*	18	105	4	Sound

*Extensometer removed before yield point was reached.

compared with a rolled structure was not determined. The welded mockup was successfully fabricated with the use of this alloy.

An investigation of the possibility of torch-brazing titanium in air was conducted.[17] The choice of a filler material, due to the corrosive environment of the homogeneous reactor, was limited to metals such as silver, platinum, or gold. The quest to find a suitable flux, which would not break down before flow of the filler wire, was unsuccessful. The filler metal (silver) was not afforded adequate protection at its flow temperature (1900°F approximately), nor was the titanium surface cleanliness maintained to an extent to permit wetting by the molten silver. The silver flowed unevenly and balled up, while the titanium surface under the flux was covered by a film thought to be oxide. Limited testing with silver and gold filler wire indicates that these metals will flow and wet titanium in a brazing furnace under a high-purity argon atmosphere. Under these conditions the metal is self-fluxing, with the oxides being dissolved in the base metal.

Zirconium Alloys. – Welding development has been concentrated on air welding of Zircaloy-2, a zirconium-tin alloy containing iron, nickel, and chromium as minor alloying elements. The mechanical properties of dry-box and trailer welds of this material have been studied by a number of investigators, and sufficient data exist for establishing basic quality levels for Zircaloy-2 weldments. Dry-box welds made by the tungsten-arc inert-gas welding process result in welds having an average weld-metal hardness in the range of 180 to 190 DPH. Air welds made by use of a trailer shield gave these same results, but air welds made without the use of a trailer gave average hardnesses in the range of 220 to 230 DPH. In a detailed investigation of air welding, techniques were developed in which equal hardnesses could be obtained for all three methods, 180 to 190 DPH.[18] This was accomplished by using larger size gas cups on the welding torch ($\frac{5}{8}$-in. dia), mechanically removing the surface film after each pass, and slightly modifying the joint design to lower the heat input required during welding. Bend-test specimens taken from air welds could be successfully bent on the same radius as dry-box or trailer welds (4*T* radius). Table 13 gives typical mechanical properties of multipass Zircaloy-2 welds. No essential differences in mechanical properties or metallographic structure were noted in these welds made by different techniques.

Combustion of Zirconium and Titanium

G. M. Adamson, Jr.

In work under a subcontract at Stanford Research Institute it has been shown that both titanium and zirconium can react quite rapidly with oxygen under circumstances where ordinary engineering alloys are quite inert. The results of this work have been given in an annual report.[19]

Two types of tests were developed for studying the ignition reactions; in one, a dynamic-atmosphere test, a thin metal disk was fractured by either gas

[17] G. M. Adamson *et al.*, *HRP Quar. Prog. Rep. Oct. 31, 1957*, ORNL-2432, p 131–33.

[18] G. M. Adamson *et al.*, *HRP Prog. Rep. for Quarters Ending April 30 and July 31, 1958*, ORNL-2561 (in press).

[19] F. E. Littman and F. M. Church, *Reactions of Titanium with Water and Aqueous Solutions*, Stanford Research Institute final report, March 15, 1957 – June 15, 1958, SRI Project No. SD-2116.

Table 13. Mechanical Properties of Zircaloy-2 Plate Welds

Type of Weld	Ultimate Tensile Strength (psi)	Yield Strength, 0.2% Offset (psi)	Elongation (%)	Bend (deg) (4*T* Radius)
Dry box	81,000	60,000	8*	180
Trailer	81,000	56,000	16	180
Air	83,000	57,000	18	180

*Fracture initiated in small defect in cover pass.

pressure or by a plunger; while in the other, a static-atmosphere test, either a thin sheet or a $\frac{1}{4}$-in. rod was broken in tension. In either test, composition, pressure, and temperature of the atmosphere could be varied. It proved to be surprisingly easy to initiate combustion of titanium and zirconium in both types of tests. Ignition and complete consumption of both disks and rods occurred when titanium and Zircaloy-2 were ruptured even at room temperature in a high pressure of pure oxygen.

The limiting conditions for ignition of titanium A-55 are shown in Fig. 71. The upper curve was determined under the static conditions of the tensile-type test, while the lower curve was determined by using a disk ruptured mechanically and with high-velocity gas passing through the rupture.

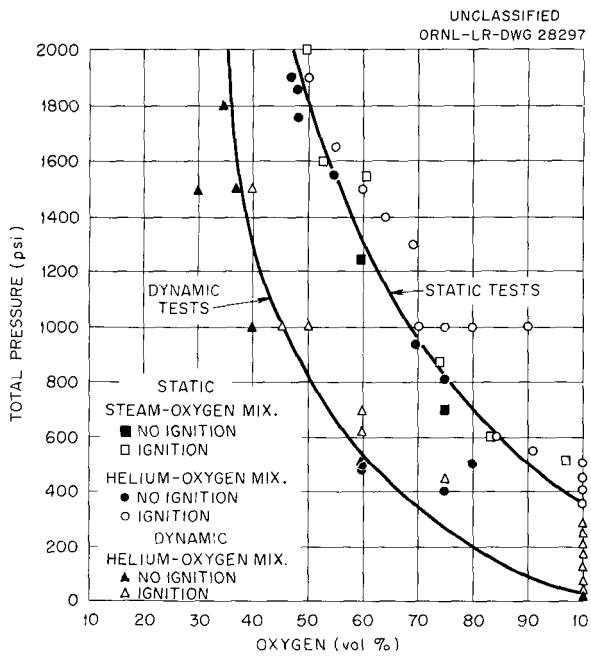

Fig. 71. Limits for Ignition of Titanium in Oxygen-Containing Gases and Vapors.

Reactions occurred under conditions shown by the area above the lines but not under those below.

In a high-velocity stream of pure oxygen, reaction occurred at pressures as low as 50 psi with titanium. The lowest curve in both figures becomes asymptotic with the pressure axis at about 35% oxygen, indicating that no ignition reaction will take place with leaner mixtures at any pressure. It should be pointed out that, with higher velocities than those studied, it is possible that the critical oxygen pressure is even lower than shown.

A point of major interest in the consideration of the use of these metals in aqueous reactors, with their steam pressurization, is that similar curves for ignition resulted when the oxygen was diluted with either helium or steam. The water vapor apparently does not enter into the ignition reactions. As would be predicted from these curves, no reaction takes place when the sample is fractured under water even if the water is saturated with oxygen.

While zirconium is similar to titanium in that autoignition can occur, the critical oxygen pressures appear to be considerably higher. Where, under dynamic conditions, titanium ignited with 50 psi oxygen, a zirconium disk required 500 psi. Under static conditions, a 0.015-in.-thick strip of titanium ignited at a pressure of 350 psi but a similar strip of zirconium required 750 psi. A $\frac{1}{4}$-in. titanium rod ignited under the same conditions as the strip, but a zirconium rod did not ignite at 1500 psi oxygen. On the other hand, stainless steel, aluminum, magnesium, iron, tantalum, columbium, and molybdenum did not ignite at oxygen pressures as high as 2000 psi.

It was also found that much lower oxygen pressures were required to sustain the combustion reactions than to initiate them. This was accomplished by electrically heating a titanium strip to the melting point and determining the oxygen pressure and percentage at which the combustion became self-sustaining. The curves in Fig. 72 show that, even under static conditions, combustion will be sustained at oxygen pressures as low as 1 atm and at higher pressures with helium mixtures containing as low as 15% oxygen. It may also be noted that, for the sustention of combustion, steam does have the effect of lowering the required oxygen percentage. The reaction was not, however, sustained in pure steam.

In a subcontract with Aerojet-General Corporation, the reactions between molten Zircaloy and

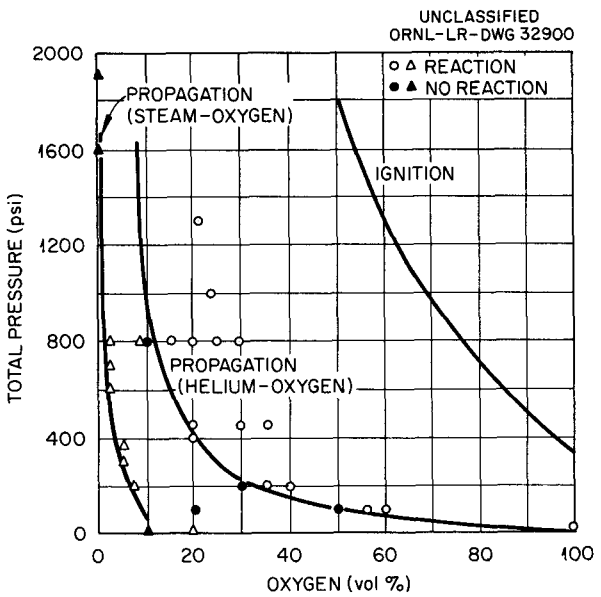

Fig. 72. Limits for the Sustention of Combustion Reactions of Titanium in Oxygen-Containing Gases and Vapors.

water were compared with those with oxygenated uranyl sulfate solutions.[20]

Using their explosion dynamometer, Aerojet showed that comparable reactions were obtained by injecting molten Zircaloy-2 droplets into water and into oxygenated uranyl sulfate. In both cases only about 30% of the energy was released; however, the amount was shown to vary with particle size.

Aerojet also conducted tests by heating Zircaloy-2 and zirconium wires to their melting points. In no case were they able to obtain a self-sustaining reaction in water, oxygenated uranyl sulfate, or steam. If, however, as little as 0.5% oxygen was added to the steam zone above the liquid, the reaction was self-sustaining in that area but was eventually quenched in the liquid.

---

[20]H. M. Higgins, *Reaction of Zircaloy-2 with Water and with Uranyl Sulfate Fuel Solution*, AGC-AE-40.

REACTOR METALLURGY

W. D. Manly

DYNAMIC CORROSION AND INSPECTION

J. H. DeVan

G. M. Tolson A. J. Rosenberg J. R. DiStefano

GCR Materials Compatibility Tests

J. H. DeVan G. M. Tolson
A. J. Rosenberg

Two types of test equipment have been employed in studying the compatibility of various structural metals with graphite and with the gaseous impurities evolved by graphite in a high-temperature helium-cooled reactor system.[1] The first type, a static-pot device, has been used to study the rate of reaction between metals and the impurities evolved from graphite under isothermal test conditions. The second, a thermal-convection loop, is similar to the static pot but includes a side arm which is maintained at a lower temperature than the pot proper in order to induce convective flow and display the effects of the circulation of helium and the gaseous impurities through a temperature gradient. In particular it was desired to study the possible dissociation of CO to form CO_2 and carbon in cold-leg regions. Gas analyses were made on samples taken throughout the tests in order to determine the type of impurities and the levels attained. The extent and type of reactions occurring between the gases and various metals placed in these devices were studied by means of weight-change determinations, metallographic examination, and x-ray and electron diffraction studies. The effects of these reactions on mechanical properties were studied by microhardness tests and by tensile tests at room temperature and 1400°F.

Static-pot tests were operated at 1400°F, and thermal-convection tests were operated with a cold-leg temperature of 500°F and a hot-leg temperature of 1400°F. Two grades of reactor graphite, AGOT and TSF, were used in the tests. Molybdenum, columbium, zirconium, and zirconium-base alloys, as well as several iron-base alloys and one nickel-base alloy, were evaluated in the earlier tests. The more active metals were eliminated in the later tests. This was done so that data on the oxidation rates of type 304 stainless steel, which has become the most probable selection for the GCR-II canning material, and several other types of alloy steels might be obtained in the absence of other materials of greatly different oxiding potentials.

The gas analyses show an initial increase in percentages of H_2, CO_2, N_2, and H_2O on heating to operational temperature, with a gradual leveling off at 1400°F. The maximum amounts of impurities realized in the tests containing AGOT graphite were several times greater than those in the tests containing TSF graphite. However, the degree of attack was not sufficiently different in the AGOT and TSF tests to make possible a definite conclusion as to whether TSF is a markedly superior grade of graphite from a materials compatibility standpoint.

With the notable exception of the zirconium and zirconium-base alloys, most of the metals showed only slight surface attack, with the stainless steels showing especially good resistance. The weight-gain data for type 304 stainless steel are shown in Table 14. Note that all weight changes are less than 1 mg/cm^2. The most common reaction film found on the stainless steel specimens was Fe_3O_4, with Fe_2O_3 and Cr_2O_3 being found in a few cases. Tensile tests and microhardness tests on the stainless steels after compatibility testing showed the specimens to be annealed from the as-rolled condition but showed no other effect on mechanical properties. The tensile data for type 304 stainless steel are presented in Table 15.

Although oxidation occurred on the stainless steel surfaces, there were a few cases where there was evidence of decarburization, carbide formation, and nitride formation on other metals. It is indicated that the outgassing of the graphite, in conjunction with the reaction of impurities with the graphite and metal surfaces, results in the gaseous atmosphere changing its nature during operation, that is, oxidizing to reducing.

Molten-Salt Reactor Program

J. H. DeVan J. R. DiStefano

A molten-salt reactor system requires structural materials which will resist corrosion by the salts. Evaluation tests of various materials in fluoride salt mixtures have indicated that nickel-base

[1] *The ORNL Gas-Cooled Reactor; Materials and Hazards*, ORNL-2505 (Revised) p 12.33–12.42 (1958).

Table 14. Weight Gains by Type 304 Stainless Steel in GCR Tests

Maximum temperature, 1400°F

Test	Grade of Graphite	Total Time (hr)	Weight Gained (mg/cm^2)
SPT No. 1*	TSF	1000	0.74
			0.70
2	AGOT	1000	0.15
			0.23
3	TSF	1000	−0.25
			−0.26
			−0.40
4	TSF	1000	0.006
			0.003
			0.025
NCT No. 1**	TSF	1000	0.032
2	AGOT	1000	0.18
			0.22
			0.59
			0.53
3	TSF	2100	0.084
			0.063
			0.091

*Static-pot test.

**Thermal convection test.

Table 15. Tensile Properties of Type 304 Stainless Steel Exposed in GCR Materials Compatibility Tests

Condition	Extension in 2 in. (%)	Tensile Strength (psi)	2% Offset Yield Strength (psi)
Room-Temperature Tensile Data			
Before testing			
Annealed	63	85,000	34,000
As rolled	18.75	107,905	92,845
After testing			
SPT No. 3	46.00	90,333	36,563
SPT No. 4	41.00	90,270	34,705
NCT No. 3	54.3	86,813	31,170
1400°F Tensile Data			
Before testing			
Annealed	39	28,300	10,500
As rolled	41.00	29,250	
After testing			
SPT No. 3	30.37	24,427	15,365
SPT No. 4	48.5	23,860	15,760
NCT No. 3	59.0	23,950	

alloys are, in general, superior to other commercial alloys for the containment of these salts under flow conditions. Consequently, two structural alloys, INOR-8 and Inconel, were chosen as materials to be studied under molten-salt reactor conditions. A three-phase out-of-pile corrosion program[2] is now in progress to evaluate the compatibility of several fluoride mixtures with these alloys. The first phase, which has been completed, was intended to determine the relative corrosion properties of the different salt mixtures in thermal-convection loops over a 1000-hr test period. Phase 2 tests, which also utilize thermal-convection loops, investigate the phase 1 system over longer times and at two temperature levels – 1250 and 1350°F. The third phase of the out-of-pile tests is being conducted in forced-circulation loops at flow rates and temperature conditions simulating those of the operating reactor.

Inconel Thermal-Convection Loop Tests.[3-6] – All Inconel thermal-convection loops operated to date have shown measurable attack ranging from <1 to 4 mils, as can be seen in Table 16. Although the corrosion rate is higher than observed for INOR-8, the Inconel tests provide a method for evaluating the effects of such parameters as time, temperature, and salt composition on the depth of attack.

[2]J. H. DeVan, J. R. DiStefano, and R. S. Crouse, *MSR Quar. Prog. Rep. Oct. 31, 1957*, ORNL-2431, p 23.

[3]J. H. DeVan, J. R. DiStefano, and R. S. Crouse, *MSR Quar. Prog. Rep. Jan. 31, 1958*, ORNL-2474, p 51.

[4]J. H. DeVan and J. R. DiStefano, *MSR Quar. Prog. Rep. June 30, 1958*, ORNL-2551, p 57.

[5]J. H. DeVan, J. R. DiStefano, and R. S. Crouse, *MSR Quar. Prog. Rep. Oct. 31, 1958*, ORNL-2626 (in press).

[6]*Molten Salt Reactor Program Status Report*, ORNL CF-58-5-3, p 118–19 (May 1, 1958).

Table 16. Operating Conditions and Metallographic Results of Inconel Thermal-Convection Loop Tests

Loop No.	Salt No.	Salt Composition (mole %)	Temperature (°F)	Time Operated (hr)	Depth of Attack (mils)
		Fuel Salts			
1163	123	53 NaF–46 BeF_2–1 UF_4	1250	1000	<1
1170	129	55.3 NaF–40.7 ZrF_4–4 UF_4	1250	1000	2
1161	122	57 NaF–42 ZrF_4–1 UF_4	1250	1000	<1
1171	126	53 LiF–46 BeF_2–1 UF_4	1250	1000	2½
1178	130	62 LIF–37 BeF_2–1 UF_4	1250	1000	1
1222	130	62 LiF–37 BeF_2–1 UF_4	1350	1000	3
1191	131	60 LiF–36 BeF_2–4 UF_4	1250	1000	<1
		Blanket and Breeder Salts			
1174	125	53 NaF–46 BeF_2–0.5 UF_4–0.5 ThF_4	1250	1000	2
1192	125	53 NaF–46 BeF_2–0.5 UF_4–0.5 ThF_4	1250	1000	4
1173	124	58 NaF–35 BeF_2–7 ThF_4	1250	1000	4
1176	127	58 LiF–35 BeF_2–7 ThF_4	1250	1000	<1
1169	128	71 LiF–29 ThF_4	1250	1000	<1
1177	128	71 LiF–29 ThF_4	1250	1000	<1
		Coolant Salts			
1207	12	11.5 NaF–46.5 LiF–42 KF	1050	4360	2
1175	13	11.5 NaF–46.5 LiF–42 KF	1125	1000	<1
1172	84	27 NaF–35 LiF–38 BeF_2	1125	1000	2

The importance of operating temperature is emphasized in Table 16 by comparing loops 1178 and 1222. An increase of 100°F in the operating temperature caused an increase in depth of attack from 1 to 3 mils. Results of previous thermal-convection loop tests operated at 1500°F indicate corrosion rates three to six times higher at 1500°F than at 1250°F.[6]

Corrosion theory[7] states that the depth of attack is dependent upon the UF_4 concentration of the salt. An example of this is illustrated by comparing loops 1163 and 1170, but an anomaly is observed in the case of loops 1178 and 1191.

When a small amount of ThF_4 was substituted for UF_4 in the salt mixture, an increase in attack was observed. This result was contrary to the expected corrosion behavior of these salts, since the ThF_4 component is known to react to a lesser degree with the constituents of Inconel than does the UF_4 component.

INOR-8 Thermal-Convection Loop Tests. – Results of tests operated with INOR-8 indicate that it has excellent corrosion resistance to molten fluoride salts in the temperature range of 1200 to 1300°F. The operating conditions and results of the 13 INOR-8 loops which have been operated are presented in Table 17. Only loop 1162 (ref 7), which operated for 6360 hr, and loop 1220 have shown any measurable attack (in both cases less than 1 mil in extent). The attack in loop 1162, as shown in Fig. 73, was in the form of widely scattered subsurface voids to a depth of 0.75 mil.

Forced-Circulation Loop Tests. – Because the forced-circulation loops are scheduled for long-time operation, results are available for only three

[7] *Ibid.*, p 112–17.

Table 17. Operating Conditions and Metallographic Results of INOR-8 Thermal-Convection Loop Tests

Loop No.	Salt No.	Salt Composition (mole %)	Temperature (°F)	Time Operated (hr)	Depth of Attack (mils)
		Fuel Salts			
1162	123	53 NaF–46 BeF_2–1 UF_4	1250	6360	¼
1205	129	55.3 NaF–40.7 ZrF_4–4 UF_4	1250	1000	No attack
1197	126	53 LiF–46 BeF_2–1 UF_4	1250	1000	No attack
1179	130	62 LiF–37 BeF_2–1 UF_4	1250	1000	No attack
1204	131	60 LiF–36 BeF_2–4 UF_4	1250	1000	No attack
		Blanket and Breeder Salts			
1203	125	53 NaF–46 BeF_2–0.5 UF_4–0.5 ThF_4	1250	1000	No attack
1164	124	58 NaF–35 BeF_2–7 ThF_4	1250	1000	No attack
1220	127	58 LiF–35 BeF_2–7 ThF_4	1250	1000	½
1213	128	71 LiF–29 ThF_4	1250	3114	No attack
1221	128	71 LiF–29 ThF_4	1250	1000	No attack
		Coolant Salts			
1165	12	11.5 NaF–46.5 LiF–42 KF	1250	1340	No attack
1194	12	11.5 NaF–46.5 LiF–42 KF	1125	1000	No attack
1195	84	27 NaF–35 LiF–38 BeF_2	1125	1000	No attack

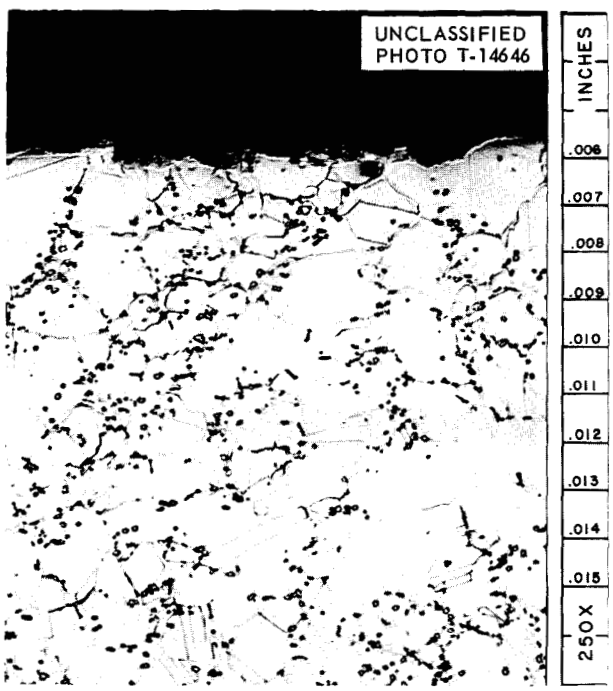

Fig. 73. Photomicrograph of Hot Leg of INOR-8 Thermal Convection Loop 1162, Which Circulated Salt No. 127 for 6360 hr at 1250°F. Etchant: modified aqua regia. (Secret with caption)

Inconel tests. The status of all forced-circulation loops now in operation is shown in Table 18, and the results of the loops which have completed operation are shown in Table 19. Attack varied from 1.5 to 8 mils, and was higher in each forced-circulation loop than in the corresponding thermal loop circulating the same salt for 1000 hr.

Inspection

G. M. Tolson J. H. DeVan

Material Inspection. – The materials inspected during the period are summarized in Table 20. Intended use was the criterion for determining the type of inspection performed and the acceptability of the material. Whenever possible, rejected material was downgraded for less critical applications. Inspection has revealed that INOR-8 material is now of a quality which equals that found in Inconel and stainless steels made to ASTM standards.

Although the rejection rate on INOR-8 tubing was high, it varied with the method of fabrication. The seamless tubing had a very low rejection rate. However, all the as-welded and most of the weld-drawn tubing contained many weld defects, such as

Table 18. Present Status of MSRP Forced-Circulation Loop Tests Now in Operation

Scheduled duration of tests, 1 year

Loop No.	Loop Material	Salt Composition (mole %)	Time Operated (hr)	Maximum Salt-Metal Interface Temperature (°F)	Maximum Bulk Salt Temperature (°F)	ΔT (°F)	Reynolds Number	Flow Rate (gpm)
9344-1	Inconel	53 NaF–46 BeF_2–1 UF_4	7989	1300	1100	200	3250	2
9344-2	Inconel	11.5 NaF–46.5 LiF–42 KF	5862	1200	1100	200	8200	2.5
9377-3	Inconel	60 LiF–36 BeF_2–4 UF_4	4698	1300	1100	200		
9377-4	Inconel	62 LiF–37 BeF_2–1 UF_4	1251	1300	1100	200		
9354-1	INOR-8	53 LiF–46 BeF_2–1 UF_4	4212	1300	1100	200	2000	2.5
9354-3	INOR-8	27 NaF–35 LiF–38 BeF_2	6164	1200	1080	120	3000	2
9354-4	INOR-8	62 LiF–37 BeF_2–1 UF_4	1582	1300	1100	200		
9354-5	INOR-8	62 LiF–37 BeF_2–1 UF_4	3165	1300	1100	200		
MSRP-6	INOR-8	62 LiF–36.5 BeF_2–1 ThF_4–0.5 UF_4	717	1300	1100	200		
MSRP-7	INOR-8	71 LiF–16 BeF_2–13 ThF_4	1197	1300	1100	200		
MSRP-8	INOR-8	58 NaF–35 BeF_2–7 ThF_4–0.5 UF_4	430	1300	1100	200		
MSRP-9	INOR-8	62 LiF–36.5 BeF_2–1 ThF_4	384	1300	1100	200		
MSRP-11	INOR-8	53 NaF–45.5 BeF_2–0.5 UF_4–1 ThF_4	192	1300	1100	200		

Table 19. Operating Conditions and Results of MSRP Forced-Circulation Loop Tests

Loop material, Inconel
Scheduled duration of tests, 1 year
Maximum salt-metal interface temperature, 1300°F
Flow rate, 2 gpm

Loop No.	Salt Composition (mole %)	Time Operated (hr)	Maximum Bulk Salt Temperature (°F)	ΔT (°F)	Reynolds Number	Metallographic Results
CPR	57 NaF–42 ZrF_4–1 UF_4	9148	1085	215	5000	Intergranular penetration to <1.5 mils
9377-1	53 LiF–46 BeF_2–1 UF_4	3073	1105	195	1600	Voids to 5 mils
9377-3	62 LiF–37 BeF_2–1 UF_4	3064	1100	200	3000	Maximum intergranular voids to 8 mils, av 4 mils

Table 20. Material Inspection

Item	Type of Material	Quantity Inspected (ft)	Quantity Rejected (ft)	Per Cent Rejected
Tubing	INOR-8 (seamless)	1262	27	2.1
	INOR-8 (weld drawn)	2622	1334	51
	INOR-8 (as welded)	672	672	100
	INOR-1, -2, -3, -4, -5, and -6	273	95	34.6
	Inconel	8393	1100	13.1
	Type 316 stainless steel	93	1	1.08
	Copper	180	0	0
Duplex tubing	Inconel over stainless steel	483	3	0.6
Pipe	INOR-8	100	5	5
	Inconel	110	1	0.9
	Stainless steel	40	1	2.5
Plate	INOR-8	179 ft^2	3 ft^2	1.7
Bar	INOR-8	162	10	6.2
	Inconel	6	0	0
	Stainless steel	2	1	50

lack of fusion (Fig. 74), a crack (Fig. 75), and porosity (Fig. 76). The latter tubing in every case came from a single heat, SP-16, which showed hot-short properties. Ultrasonic inspection was performed only on a small part of the seamless INOR-8 tubing and was able to locate some cracking (Fig. 77) which was not found by radiographic inspection. Although complete ultrasonic inspection would tend to make the rejection rate higher than is shown in Table 20, it is felt that the tubing was of reactor quality.

Weld Inspection. – Depending on the quality needed, welds have been divided into three general types, "C," "CN," and "S." A "C" type weld is of reactor quality and receives visual, penetrant, and radiographic inspection. The "CN" type weld is just as critical as the "C" type, but it is in such a position that it cannot be radiographed. The third type, "S," is used in noncritical applications and receives only a visual inspection. Specifications are being revised to include two new types of welds, which will be called "B" and "BN." The "B" type weld will be equivalent to an ASME Boiler Code weld which is radiographed. The "BN" type weld will be used where leak-tight

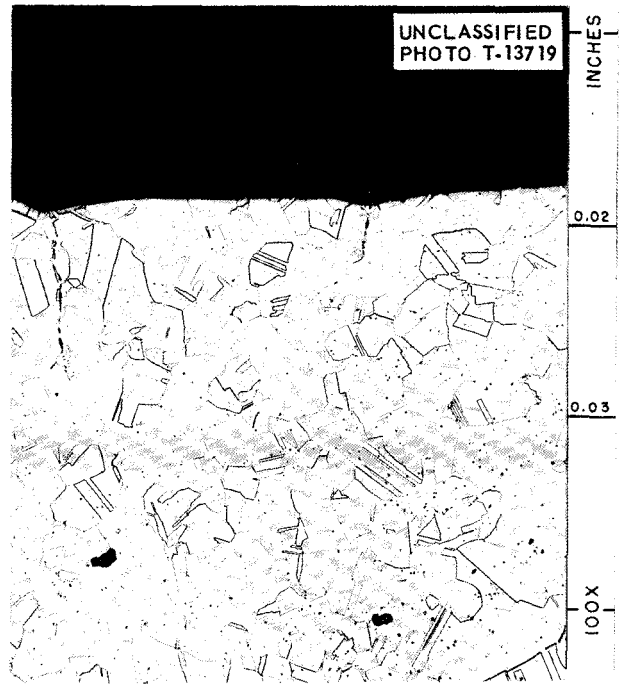

Fig. 74. Lack of Fusion Found in the Weld Area of INOR-8 Tubing. Etchant: aqua regia. (Secret with caption)

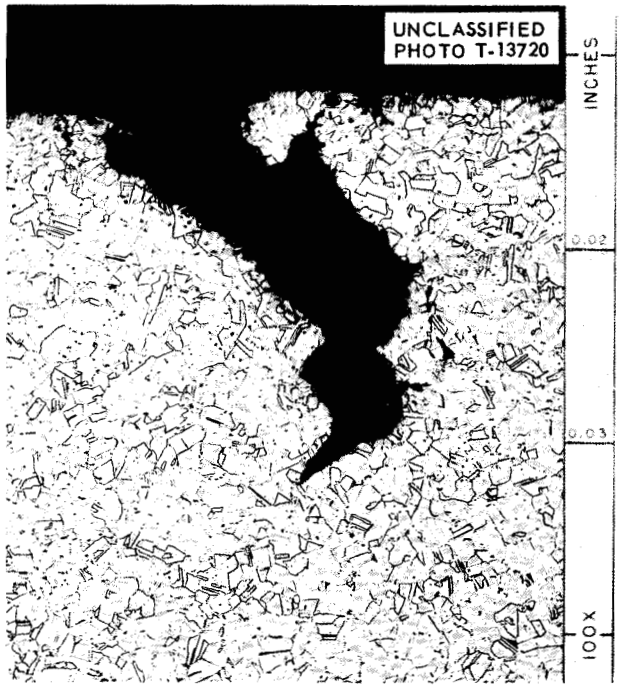

Fig. 75. Crack in the Weld Area of Weld-Drawn INOR-8 Tubing. Etchant: aqua regia. (Secret with caption)

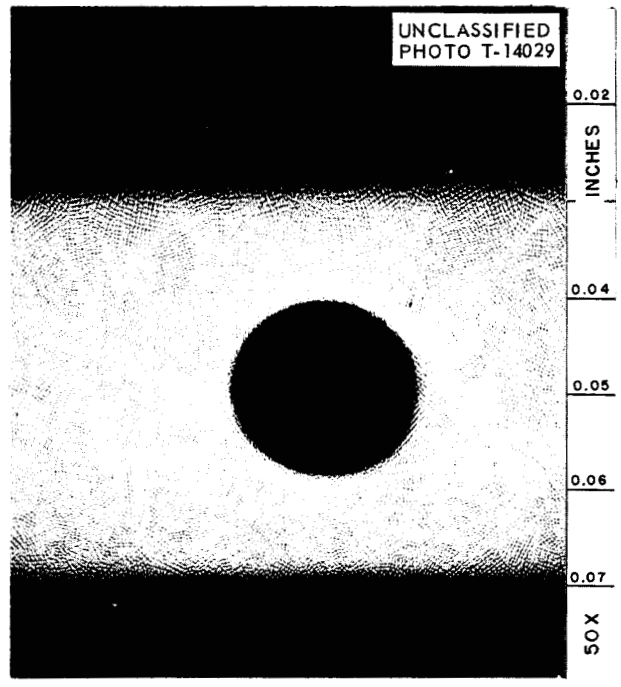

Fig. 76. Porosity in Weld Area of As-Welded INOR-8 Tubing. Etchant: chromic acid and HCl. (Secret with caption)

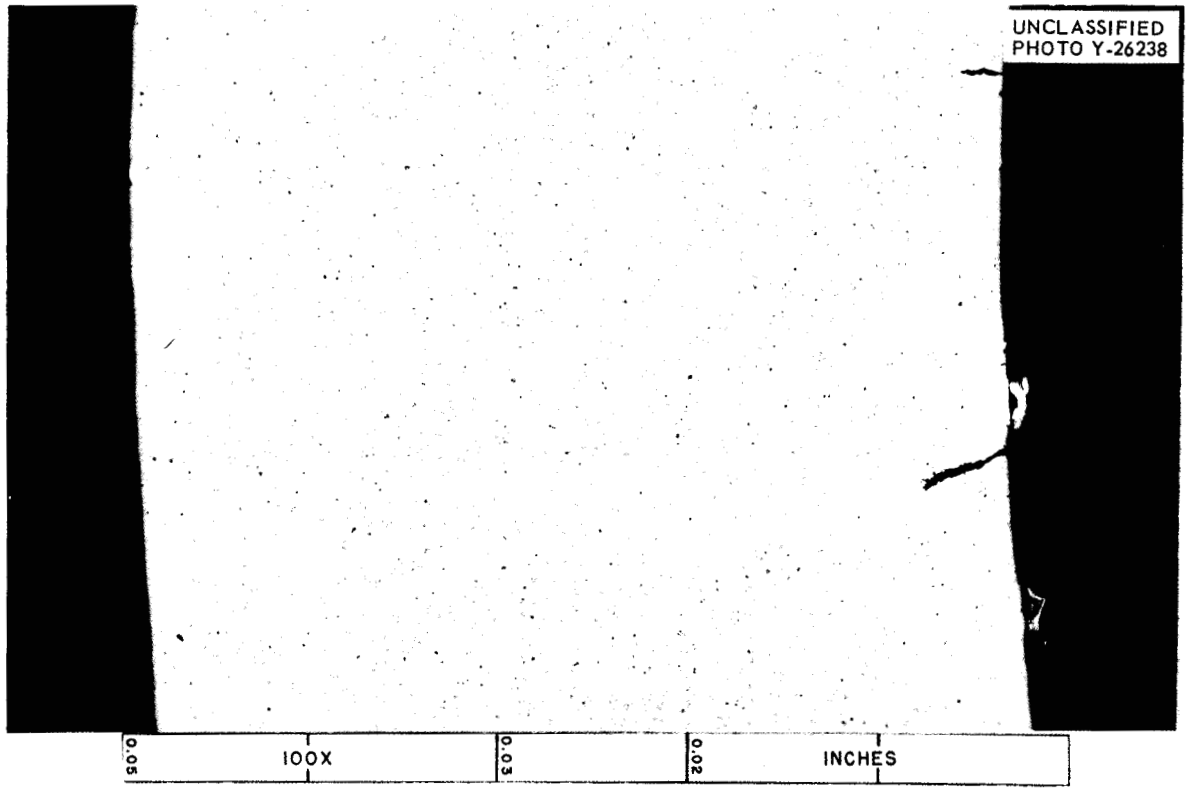

Fig. 77. Multiple Cracks Found by Ultrasonic Inspection of INOR-8 Tubing. (Secret with caption)

joints are required but where certain deviation may be allowed; it will not be radiographed.

A total of 2977 welds were inspected. Twelve per cent of the "C" type welds were rejected, and less than 1% of the "CN" and "S" type welds were rejected; welds made on INOR-8 material showed a 10% rejection rate.

Fabricated Components. – Various fabricated components, such as bellows, valves, heat exchangers, and pump parts, were inspected by visual, penetrant, and radiographic methods for the Experimental Engineering Group in order to evaluate fabrication methods and to locate defective conditions which could result in failure of the components under test. Whenever possible, defective conditions were repaired.

Specifications and Publications. – All welding, material, and inspection specifications have been revised and have been submitted for TID publication.[8] A report has been made on techniques developed for the penetrant inspection of thin-wall tubing.[9]

Design Evaluation. – Engineering drawings and designs made by the Experimental Engineering Group have been evaluated for sound metallurgical practices. Failure analysis work was conducted to determine the cause for component failures.

---

[8] *Reactor Material Specifications*, TID-7017 (to be published).

[9] R. B. Oliver, G. M. Tolson, and A. Taboada, *Am. Soc. Testing Materials, Spec. Tech. Publ. No. 223*, 127 (1958).

GENERAL CORROSION

E. E. Hoffman

W. H. Cook
D. H. Jansen
J. W. Hendricks
L. R. Trotter

Lithium Purification Studies: Methods of Reducing the Nitrogen and Oxygen Content

E. E. Hoffman

L. R. Trotter J. W. Hendricks

Purification studies on lithium by various means, including low-temperature filtration, vacuum distillation, and gettering with active refractory metals, have been conducted.[1,2] Commercially produced lithium usually contains from several hundred to several thousand parts per million of oxygen and nitrogen. The purpose of these investigations is to ascertain which of the several possible purification techniques is most effective in reducing the total oxygen and nitrogen impurity content to less than 50 ppm.

There are two principal reasons for wanting as pure a grade of lithium as is possible and practical to produce. These are as follows: (1) Only by conducting corrosion tests with "pure" lithium can the effect of minor amounts of oxide and/or nitride on the corrosiveness of the lithium be determined. (2) High-purity lithium (especially low-oxygen-content lithium) is needed as a feed material in the production of low-oxygen yttrium metal by the Fabrication Group of the ANP Metallurgy Section.

Results of the lithium purification studies to date have been complicated by the difficult analytical techniques which must be used in order to obtain reliable oxygen analyses on lithium samples. Over a period of many months, lithium samples have been taken from numerous test systems for determining the impurity content of the lithium, particularly oxygen and nitrogen. Because of the uncertainties regarding which is the best of the present methods for determining oxygen in lithium, three samples each were obtained from approximately 25 different purification experiments and were sent for analysis by the following methods:

1. activation analysis[3] (ORNL Analytical Chemistry Division),
2. butyl iodide–iodine method[4,5] (ORNL Analytical Chemistry Division),
3. methyl alcohol–Karl Fischer method[6] (Nuclear Development Corporation of America).

Although the agreement between the various methods is not good by any means, the best agreement was obtained between the butyl iodide–iodine method and activation analysis. Improved sampling and analytical techniques are to be employed in the future to further determine the reliability of these two methods for determining oxygen in lithium.

Attempts to purify lithium by low-temperature (250°C) filtration have been unsuccessful. These results would tend to indicate that the solubility of the oxide and nitride is quite high at temperatures slightly above the melting point of lithium. A limited number of solubility experiments have been conducted, and in these tests lithium samples taken at 250°C, in the presence of either excess lithium oxide or excess lithium nitride, analyzed 1100 to 1400 ppm nitrogen and 1250 to 1350 ppm oxygen. A nitrogen solubility experiment sampled at 300°C gave nitrogen contents of 1760 and 1900 ppm. Additional nitrogen and oxygen solubility experiments will be conducted to verify the results obtained and to check the solubilities at several temperatures.

Attempts to purify lithium by vacuum distillation at temperatures of 600 to 650°C have not been successful. Seven distillations have been performed to date, and the nitrogen and oxygen content of the distillate has been of the same magnitude or higher than that of the lithium charged into the still in all distillations.

Results to date indicate that gettering of the nitrogen and oxygen from lithium with active metals is probably the most efficient and practical method of purification. Titanium and zirconium have been tested as getters for nitrogen in lithium at 1460 and 1500°F. Titanium has been found to be a more

[1] E. E. Hoffman *et al.*, *ANP Quar. Prog. Rep. March 31, 1958*, ORNL-2517, p 9–21.

[2] E. E. Hoffman, *ANP Semiann. Prog. Rep. Sept. 30, 1958*, ORNL-2599 (in press).

[3] L. C. Bate and G. W. Leddicotte, *Anal. Chem. Prog. Rep. Dec. 31, 1957*, ORNL-2453, p 30.

[4] A. S. Meyer, Jr., and R. E. Feathers, *ANP Quar. Prog. Rep. Sept. 30, 1957*, ORNL-2387, p 149–51.

[5] A. S. Meyer, Jr., and R. E. Feathers, *ANP Quar. Prog. Rep. March 31, 1958*, ORNL-2517, p 57.

[6] N. I. Sax and H. Steinmetz, *Determination of Oxygen in Lithium Metal*, ORNL-2570 (Oct. 15, 1958).

effective nitrogen getter than zirconium for purifying lithium. Neither titanium nor zirconium gettered oxygen from lithium, as might be expected, since lithium oxide is thermodynamically more stable than either titanium or zirconium oxide. Extensive dissimilar-metal mass transfer has also been observed in the titanium gettering tests. This transfer, particularly of nickel from the stainless steel container walls to the titanium getter foil, was found to occur quite rapidly when clean titanium specimens were immersed in lithium containing <100 ppm nitrogen. Titanium specimens immersed in lithium containing 100 ppm or more of nitrogen were protected from nickel pickup by a titanium nitride surface layer, which acted as a diffusion barrier.

Calcium and yttrium metal have been tested as possible getters for oxygen in lithium. Calcium was found to be undesirable because of its relatively high solubility in lithium, and in addition it did not reduce the oxygen content of the lithium metal.

Since the primary reason for lowering the oxygen content of lithium is to eliminate possible contamination of yttrium metal during the reduction of the yttrium fluoride salt (see the section "Hydride Moderator Studies," this report), yttrium itself is a promising getter candidate. Yttrium oxide is one of the most stable of the oxides. Two gettering tests have been conducted,[2,7] and in both, the oxygen content of the yttrium increased during the exposure to lithium. Table 21 shows the effect of the exposure to lithium on the oxygen and nitrogen content of the yttrium. Table 22 illustrates the hardness changes which occurred in an yttrium specimen as a result of the oxygen and nitrogen pickup. Lithium samples taken at 1300°F indicate that yttrium is slightly soluble (0.01 wt %) in lithium at this temperature; however, this would not interfere with the use of the lithium in subsequent yttrium reductions.

Static Corrosion Tests of Various Materials in Lithium

Yttrium-Lithium Static Corrosion Test (E. E. Hoffman). – Yttrium has been corrosion tested in contact with static lithium in a columbium container for 100 hr at 1500°F.[7] The yttrium specimen showed a considerable weight loss (0.1 g/in.^{2},

[7]E. E. Hoffman, *ANP Quar. Prog. Rep. March 31, 1958*, ORNL-2517, p 20.

Table 21. Analyses of Yttrium Metal Getter Specimens Before and After Exposure to Lithium at 1500°F

Length of test, 72 hr

Specimen No.	Time Period of Exposure (hr)	Oxygen Content (ppm)			Nitrogen Content (ppm)		
		Before	After	Change	Before	After	Change
1 (Y-3)	0–72	1300	3800	+2500	450	1100	+650
2 (Y-6)	24–72	1400	3900	+2500	570	850	+280
3 (Y-8)	48–72	940	1800	+860	110	170	+60

Table 22. Diamond Pyramid Hardness Tests on an Yttrium Rod Specimen Used in Lithium-Yttrium Gettering Experiment No. 1 as a Function of Distance from Surface Exposed to Lithium

Specimen No.	Treatment	Diamond Pyramid Hardness (500-g Load)				
		Distance from Surface (mils)				
		5 (Edge)	25	65	105	145 (Center)
1 (Y-3)	Exposed to lithium 72 hr at 1500°F	117	95	71	66	59
1 (Y-3)	Same heat treatment as above, but in vacuum rather than lithium	59	60	58	59	59

2.4%) and had an etched appearance following the test. Yttrium mass-transfer crystals were found on the wall of the columbium capsule near the liquid lithium level.

Beryllium-Lithium Static Tests (E. E. Hoffman). Early lithium corrosion tests of beryllium specimens in iron capsules showed very heavy attack on the beryllium.[8] The beryllium from tests conducted at 1830°F for 400 hr showed 127 mils of intergranular attack and a large weight loss. Tests have been conducted recently to recheck the corrosion resistance of beryllium to lithium under several test conditions.[9] The results are listed in Table 23; the results of the earlier test at 1830°F are included for comparison purposes. In the tests conducted in iron capsules at 1830°F, the beryllium specimens suffered extensive attack due to dissimilar-metal mass transfer of beryllium from the specimen to the capsule wall. It may be seen that beryllium has good resistance to attack by lithium at both 1500 and 1800°F when contained in an all-beryllium system.

Columbium-Lithium Static Tests: The Effect of Welding Environment on the Corrosion Resistance of Columbium Welds and Heat-Affected Zones (E. E. Hoffman). – As a result of the heavy attack observed in previous tests of columbium and lithium systems, particularly in weld areas, a series of tests[9] was initiated to study the effect of various Heliarc welding procedures on the subsequent corrosion resistance of arc-cast columbium (analysis: O_2, 380 ppm; N_2, 20 ppm; C, 140 ppm). Two joining techniques and three types of environment were employed in the weld sample preparation. The results of the tests are listed in Table 24 and clearly indicate the difficulty of producing welds or heat-affected zones in unalloyed columbium which are corrosion resistant to lithium at elevated temperatures.

Static Lithium Corrosion of Zirconium-Base Braze-Welding Alloys (E. E. Hoffman). – Two zirconium-base alloys, 85% Zr–15% Cb and 80% Zr–15% Cb–5% Mo, have been exposed to lithium for 100 hr at 1830°F.[10] The binary alloy has also been tested at 1500°F for 100 hr. Neither of the alloys has shown any attack or weight loss in these tests. The binary alloy has been used on a number of occasions as a braze-welding alloy for assembling columbium corrosion test systems. None of the braze-weld joints have failed or been attacked by lithium.

Refractory-Metal-Base Brazing Alloys in Lithium (D. H. Jansen). – Since most commercially available brazing alloys have but limited corrosion resistance to high-temperature lithium, refractory-metal-base alloys are being screened in a lithium bath.[11] Corrosion results on a series of zirconium-base and titanium-base alloys tested for 500 hr are given in Table 25.

These early results indicate that zirconium alloys containing iron are naturally brittle. Cobalt- and vanadium-containing alloys show less corrosion resistance than the ones containing Mo, Cb, Cr, or Be. The titanium-base alloys all showed good

[8] A. deS. Brasunas, *Interim Report on Static Liquid-Metal Corrosion*, ORNL-1647, p 35 (May 11, 1954).

[9] E. E. Hoffman, *ANP Semiann. Prog. Rep. Sept. 30, 1958*, ORNL-2599 (in press).

[10] E. E. Hoffman, *ANP Quar. Prog. Rep. March 31, 1958*, ORNL-2517, p 21.

[11] D. H. Jansen, *ANP Semiann. Prog. Rep. Sept. 30, 1958*, ORNL-2599 (in press).

Table 23. Corrosion of Beryllium Specimens by Lithium in Static Tests

Temperature (°F)	Time (hr)	Container	Specimen Weight Change (mg/cm^2)	Attack (mils)	
				Intergranular	Solution
1830	400	Iron	−101.8	127	30
1500	100	Iron	−3.9	4	0
1500	100	Beryllium	+0.3	2	0
1830	100	Iron	−66.1	5	20
1830	100	Beryllium	+0.3	3	0

Table 24. The Effects of Various Joining Techniques on the Hardness of Columbium and its Corrosion Resistance to Lithium

Corrosion test conditions: Static, 1500°F, 100 hr
Original base material: Arc-cast columbium; O_2, 380 ppm; N_2, 20 ppm; C, 140 ppm; DPH, 137

Joining Technique	Welding Environment	Specimen Weight Change (mg/in.^{2})	Location of Specimen	Results of Metallographic Examination	Diamond Pyramid Hardness (500-g Load)	
					Before Corrosion Test	After Corrosion Test
Braze welding (85 Zr–15 Cb alloy)	Argon + air	–0.7	Braze weld	1 mil attack	361	343
			Heat-affected zone	Complete grain boundary penetration of specimen	360	94
			Base material	4 mils of subsurface voids	129	112
	Argon + 1600 ppm N_2 + 400 ppm O_2	+1.0	Braze weld	No attack	285	246
			Heat-affected zone	15 mils attack	114	98
			Base material	4 mils of subsurface voids	120	104
	Argon + 67 ppm N_2 + 3 ppm O_2	+0.7	Braze weld	No attack	289	242
			Heat-affected zone	6 mils attack	122	98
			Base material	3 mils of subsurface voids	113	105
Fusion welding	Argon + air	–0.4	Weld	Complete and very heavy attack of entire weld	356	128
			Heat-affected zone	15 mils of intergranular attack	127	90
			Base material	3 mils of attack	127	97
	Argon + 1600 ppm N_2 + 400 ppm O_2	+0.6	Weld	Complete attack of grain boundaries but not as concentrated as in weld above	155	105
			Heat-affected zone	9 mils of intergranular attack	116	93
			Base material	3 mils of attack	128	107
	Argon + 67 ppm N_2 + 3 ppm O_2	+0.2	Weld	Complete attack of grain boundaries in a few scattered areas; less attack than either of the welds listed above	131	95
			Heat-affected zone	7 mils of intergranular attack	118	92
			Base material	1 mil of attack	127	93

resistance to lithium at 1700°F under these conditions.

Dynamic Corrosion Tests of Molybdenum and Columbium in Contact with Lithium

Molybdenum-Lithium Seesaw Tests (E. E. Hoffman). – A series of dynamic corrosion tests on molybdenum in contact with lithium have been conducted by use of the seesaw apparatus.[12] The test assembly is shown in Fig. 78. The results of these tests are given in Table 26 and indicate the excellent corrosion resistance of molybdenum to lithium at temperatures as high as 1900°F. The hot-zone- and cold-zone-specimen surfaces are shown in Fig. 79*a* and 79*b*, respectively, and no attack can be detected even at very high magnification. It may be noted that the hot-zone specimen partially recrystallized during the test.

Columbium-Lithium Seesaw Tests (E. E. Hoffman). – A series of columbium-lithium seesaw tests are planned, in which a test configuration similar to that shown in Fig. 78 will be used. In the columbium tests, however, type 316 stainless steel is being used as the outer protective capsule, instead of Inconel. Only one test has been completed to date; this test was terminated after 300 hr by a sodium leak in the stainless steel pipe. The columbium tube did not fail as a result of the failure of the protective capsule. The hot- and cold-zone specimens were at 1600 and 1100°F, respectively. The hot-zone specimen showed a slight weight gain (0.1 mg/in.^{2}), which may be attributed to gettering of nitrogen from the lithium, while the cold-zone specimen showed no weight

[12] E. E. Hoffman, *ANP Semiann. Prog. Rep. Sept. 30, 1958*, ORNL-2599 (in press).

Table 25. Results of Static Corrosion Tests on Refractory-Metal-Base Brazing Alloys in Lithium

Test conditions: 1500 or 1700°F for 500 hr
Each weight change represents one test; buttons weighed about 5 g
All tests employed arc-melted buttons and columbium capsules unless otherwise indicated

Material Composition (wt %)	Weight Change (%)	Metallographic Results and General Condition of Button After Test
95 Zr–5 Be	+0.005 −0.05	Subsurface void formation to a depth of less than 0.5 mil
84 Zr–16 Fe*	−0.573 −0.62	No attack; numerous small cracks in specimen
82 Zr–18 Cr	−1.81	No attack observed
75 Zr–25 Cb	−0.227 −0.11	No attack observed
75 Zr–15 Cr–10 Fe*	−2.5 −1.7	Edge of specimen attacked nonuniformly to 1 mil
70 Zr–30 V	−10.87 −2.04	No attack seen but the second phase is leached to a depth of 9 mils
69 Zr–31 Mo	−1.34 −1.30	No attack observed
80 Co–20 Cb	−2.6	Specimen uniformly depleted ½ mil; spotty attack varying from 0 to 10 mils in places
55 Ti–45 Zr	−0.063 +0.079	No attack observed
72 Ti–28 Co on Cb T-joint		Spotty attack to less than 1 mil

*Tested at 1500°F. All other tests at 1700°F.

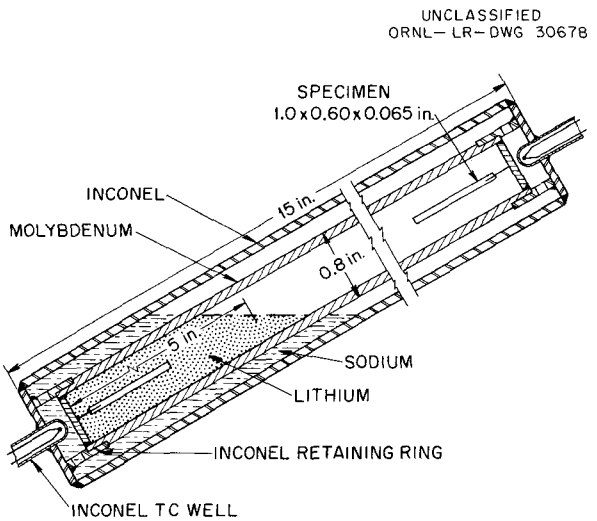

Fig. 78. Seesaw Test Assembly for Evaluating the Corrosion Resistance of Molybdenum in Lithium.

change. Further tests are planned at higher temperatures and for longer test periods.

Columbium-Lithium Thermal Convection Loop Tests (E. E. Hoffman). – Unclad columbium loops filled with lithium have been tested in the stainless steel vacuum chamber.[13] These tests were conducted at hot-leg temperatures of 1500 and 1600°F and failed due to penetration of the longitudinal tube-wall weld of the sintered tubing by the lithium metal. The results of these two tests are summarized in Table 27. The 85% Zr–15% Cb braze-welding alloy used to join various sections of these loops was not attacked by the lithium.

Tests were conducted on the sintered columbium tubing used in these loop tests to determine if the

[13] E. E. Hoffman, *ANP Quar. Prog. Rep. March 31, 1958*, ORNL-2517, p 24.

Table 26. Results of Molybdenum-Lithium Seesaw Test

Test No.*	Temperature (°F)		Length of Test (hr)	Specimen Weight Change ($mg/in.^2$)		Location of Specimen	Metallographic Observations on Specimens
	Hot Zone	Cold Zone		Hot Zone	Cold Zone		
SS-514	1700	1300	500	−25.8	+9.0	Hot zone	Surface pitting to a depth of 0.4 mil
						Cold zone	Metal crystal deposition to a depth of 0.3 mil
SS-525	1700	1000	500	−0.1	+0.4	Hot zone	No attack
						Cold zone	No attack or deposition
SS-523	1800	1000	100	−0.3	−0.7	Hot zone	Surface roughened slightly, less than 0.2 mil
						Cold zone	No attack or deposition
SS-526	1800	1050	500	−0.1	+2.2	Hot zone	No attack
						Cold zone	No attack or deposition
SS-522	1900	1000	100	−0.4	−0.8	Hot zone	Surface roughened slightly, less than 0.2 mil
						Cold zone	No attack
SS-527	1900	1100	150	−0.3	+0.4	Hot zone	No attack
						Cold zone	No attack or deposition

*Analysis (before test) of lithium used in SS-514, SS-523, SS-522: N_2, 284 ppm; O_2, 910 ppm.
Analysis (before test) of lithium used in SS-525, SS-526, SS-527: N_2, 4770 ppm; O_2, 1450 ppm.

test environment (vacuum, 1 to 5 μ) was in any way responsible for the intergranular attack noted in the weld and heat-affected zones of the loops. The results[14] of these static tests, conducted in a variety of gaseous environments, indicated that the attack was not due to contamination (oxygen, nitrogen, etc.) picked up during the test but occurred as a result of the condition of the columbium prior to testing.

Determination of the Solution Rate of Metals in Lithium[15]

E. E. Hoffman

A recently issued report[16] describes a method developed at NDA for measuring the rate at which container metals dissolve in liquid lithium under controlled nonequilibrium conditions. The method consists essentially in immersing a thin test specimen in a comparatively large volume of liquid metal, held at the desired temperature in an inert container. By suitable choice of surface area and immersion time, the specimen can be made to lose about 1 mg in a test period of less than one day. This weight loss does not significantly increase the concentration of test specimen material in the liquid metal, and the loss can be determined with ample accuracy and precision on a semimicro balance.

The solution rates determined in this manner are proportional to the specific solution rate constant α. Based upon experimental evidence from thermal-convection loop tests, it is believed that inhibitors

[14] E. E. Hoffman *et al.*, *ANP Quar. Prog. Rep. March 31, 1958*, ORNL-2517, p 26.

[15] Subcontract with Nuclear Development Corporation of America, July 1, 1957, to July 31, 1958.

[16] B. Minushkin, *Determination of the Solution Rate of Metals in Lithium*, NDA-44 (June 30, 1958).

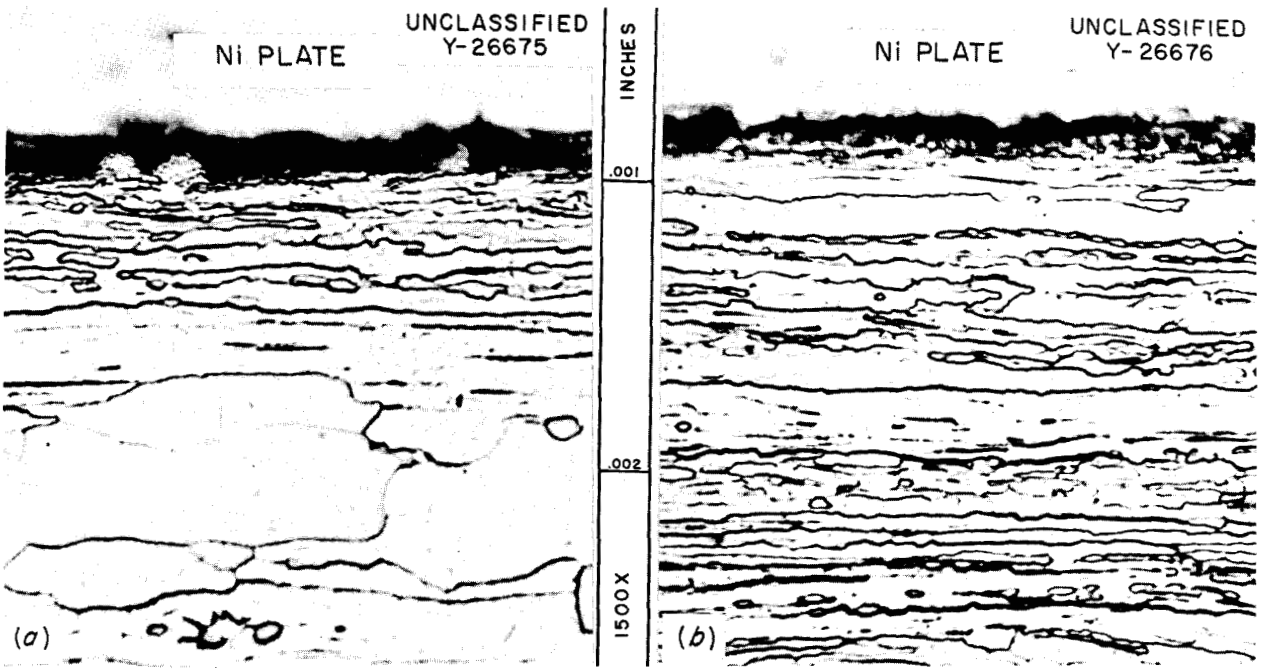

Fig. 79. Surfaces of Molybdenum Specimens from Lithium Seesaw Furnace Tests (SS-522). (*a*) Hot-zone specimen (1900°F); (*b*) cold-zone specimen (1000°F). Specimens nickel-plated to preserve edges during metallographic polishing. Etchant: 50% NH_4OH–50% H_2O_2. (Secret with caption)

and impurities exert their effect on mass-transfer rates by altering the value of the specific solution rate constant. Therefore, the method is suitable for preliminary studies of the effects of additives and impurities on mass transfer.

The data from tests on stainless steel indicate that the method is capable of detecting variables which affect the initial solution rate by about ±20%.

The results indicate that nickel-bearing stainless steel dissolves in lithium at 1600°F at an initially high rate of 3.0 $mg \cdot in.^{-2} \cdot hr^{-1}$ due to the preferential leaching of nickel. Within a relatively few hours, depletion of nickel in the specimen surfaces results in a rapid decrease in solution rate to a value of about 0.3 $mg \cdot in.^{-2} \cdot hr^{-1}$ at solute concentrations of a few hundred parts per million. It was shown that this solution rate accounts for mass-transfer rates observed in thermal-convection loop tests. The solution-rate tests confirm the deleterious effects of nitrogen and oxygen and the beneficial effects of aluminum additions on mass-transfer rates observed in thermal-convection loop tests. In addition, it appears that misch metal and tantalum additions may have beneficial effects.

Solution rate studies of molybdenum in lithium at 1600°F indicate that it is not significantly attacked by lithium. Tests on columbium yielded conflicting results which have not been resolved.

Molten-Salt Reactor Project Studies

Compatibility of Cermet-Metal Joints with Fuel 30 and with Sodium (W. H. Cook). – Several methods were developed by the Welding and Brazing Group for joining cermets to metals.[17] The joints described in Table 28 were corrosion tested for 100 hr in $NaF\text{-}ZrF_4\text{-}UF_4$ (50-46-4 mole %, fuel 30) in a seesaw apparatus with a hot-zone temperature of 1500°F. Specimens of joints 1, 2, and 4 were similarly tested in sodium; joints 3, 5, and 6 were not tested in sodium because it was known that the brazing materials were not corrosion resistant to sodium under the test conditions. On the basis of metallographic examinations of untested and tested specimens, none of the cermet-metal joints tested were attacked[18] with the possible exception of joint 4 exposed to fuel 30.[18]

---

[17] G. M. Slaughter, P. Patriarca, and W. D. Manly, *Welding J. (N. Y.)* 37(6), 249-s (1958).

[18] W. H. Cook, *ANP Quar. Prog. Rep. Dec. 31, 1957*, ORNL-2440, p 170.

Table 27. Results of Columbium-Lithium Thermal-Convection Loop Tests 58 and 59

Loop No.	Test Conditions	Hot-Leg Specimen Weight Change ($mg/in.^2$)	Location of Specimen	Results of Metallographic Examination
58	Hot leg, 1600°F Cold leg, 1300°F Duration, 36 hr	−7.5	Hot leg	
			Arc-cast insert	7 mils attack
			Sintered tube	
			Weld zone	7 mils in most areas, complete penetration in several areas
			Base material	No attack
			Cold leg	
			Sintered tube	
			Weld zone	5 mils attack
			Base material	No attack
59	Hot leg, 1500°F Cold leg, 1300°F Duration, 115 hr	+0.62	Hot leg	
			Arc-cast insert	16 mils attack
			Sintered tube	
			Weld zone	10 mils in most areas, complete penetration in several areas
			Base material	2 to 3 mils attack
			Cold leg	
			Sintered tube	
			Weld zone	11 mils attack
			Base material	No attack

Table 28. Description of Cermet-Metal Joints for Testing in Fuel 30

Joint No.	Cermet	Buffer*	Type of Join
1	K151A (80% TiC–20% Ni)	Nickel	High-temperature fusion
2	K162B (70% TiC–25% Ni–5% Mo)	Nickel	High-temperature fusion
3	K94 (88% WC–12% Co)	Nickel	Brazed with copper
4	K94	Nickel	Brazed with Coast Metals alloy 50 (93% Ni–3.5% Si–2.5% B–1% Fe)
5	K138A (81% TiC–19% Co)	Mallory 1000 (90% W–6% Ni–4% Cu)	Brazed with a 60% Pd–40% Ni alloy
6	KM (89% $WTiC_2$–11% Co)	Mallory 1000	Brazed with a 60% Pd–40% Ni alloy

*In actual application the buffer is joined to the structural metal by conventional brazing practice; it buffers the stresses developed by differences in thermal expansion between the structural metal, Inconel, and the cermet.

Postoperation Examination of Prototype ART Control Rod (W. H. Cook). – The ART prototype control rod, composed of rare-earth oxides, sodium, and Inconel, was disassembled and examined after a 3000-hr test of the control rod and its drive system.[19] On the basis of the materials compatibility exhibited in the 3000-hr test, it was concluded that the control rod was satisfactory for the operating conditions expected for the ART.

The rod consisted of 23 cylinders of rare-earth oxides (45 to 49.5% Sm_2O_3, 22.5 to 27% Gd_2O_3, balance primarily other rare-earth oxides; apparent porosity, 46.3%) contained in an Inconel thimble. The rare-earth oxide cylinders were, nominally, $1\frac{1}{4}$ in. OD, $\frac{3}{4}$ in. ID, and 1 in. long. For the test, the heat had to be applied externally rather than developed internally, as it would be in the ART.

The test results indicated that the rare-earth oxide cylinders can withstand 20-min thermal cycles of 550 ± 50°F from a maximum of 1650 ± 30°F; however, 20-min cycles of 750 ± 50°F from the same maximum broke the cylinders. The quantity of rare earths found in the sodium and the examination of the cylinders indicated that corrosion of the cylinders was negligible during the 3000-hr test. The performance of the control rod material was satisfactory, even though the test operating conditions were somewhat more severe than those expected in the ART.

Inconel–Graphite–Fuel 30 Systems at 1300 and 1500°F (W. H. Cook). – In preliminary carburization tests, systems consisting of Inconel, graphite, and $NaF\text{-}ZrF_4\text{-}UF_4$ (50-46-4 mole %, fuel 30) were tested in a seesaw furnace with a hot zone at 1500°F for 100 hr and in two thermal-convection loops with hot zones at 1300°F for 700 and 1000 hr, respectively. In these tests, the Inconel was not detectably carburized and there was only negligible attack on the graphite specimens.[20] A thin (0 to 0.0005 in.), metallic-appearing film on the graphite from the hot leg of the thermal-convection loop which was operated for 1000 hr was identified as Cr_3C_2. Two thermal-convection loops, one of Inconel and one of INOR-8, each with a graphite insert in its hot leg (1300°F), are in operation with $LiF\text{-}BeF_2\text{-}UF_4$ (62-37-1 mole %, fuel 130). At the end of 4000 hr, the inserts will be examined primarily for deposition of chromium as Cr_3C_2. The purpose is to determine (1) whether fuel 130 transports chromium to the graphite as fuel 30 did and (2) whether the different quantities of chromium in the Inconel and INOR-8 will govern the quantity of chromium, if any, that is transferred. Additional information will also be sought concerning the compatibility of the graphite with the fuel and the carburization of the two alloys.

Carburization of Inconel and INOR-8 by Sodium-Graphite Systems (D. H. Jansen). – As outlined previously,[20] the sodium-graphite system is an effective carburizing medium for Inconel and Hastelloy. This medium has been used to carburize Inconel and INOR-8 to determine the effect of carburization on their mechanical properties. In general, the elongation of both materials was decreased; the tensile strength of Inconel was increased, while that of INOR-8 was slightly decreased (Table 29).

Other detailed results, including elevated-temperature tensile tests in air and creep tests in argon, have been reported earlier.[21]

Carburization of INOR-8 by Fuel 130–Graphite Systems (D. H. Jansen). – A comprehensive type of test (fuel 130–INOR-8–graphite) was terminated after 2000-hr operation at 1300°F. The test was designed to determine whether INOR-8 is carburized when exposed to fuel 130 which is in contact with bare graphite. Metallographically, no carburization could be observed, but chemical analyses and mechanical test results indicated that carburization had taken place under these conditions.[21]

UO_2 Precipitation in Compatibility Tests of Fused Fluoride Salts and Graphite (W. H. Cook). Compatibility tests of various grades of graphites with $LiF\text{-}BeF_2\text{-}UF_4$ (62-37-1 mole %, fuel 130) and $NaF\text{-}ZrF_4\text{-}UF_4$ (50-46-4 mole %, fuel 30) at 1300°F are being conducted.[22] The primary interest is in the compatibility of fuel 130 and graphites. It appears that fuel 130 is sensitive to small quantities of contamination of the graphite and will precipitate appreciable quantities of its uranium as UO_2 as a result of these impurities. This is true

[19] W. H. Cook, *ANP Quar. Prog. Rep. Dec. 31, 1957*, ORNL-2440, p 172.

[20] E. E. Hoffman, W. H. Cook, and D. H. Jansen, *MSR Quar. Prog. Rep. Jan. 31, 1958*, ORNL-2474, p 54.

[21] D. H. Jansen, *MSR Quar. Prog. Rep. Oct. 31, 1958*, ORNL-2626 (in press).

[22] W. H. Cook, *MSR Quar. Prog. Rep. Oct. 31, 1958*, ORNL-2626 (in press).

even though relatively rigorous methods are used to degas and protect the graphite. The quantity of uranium precipitated varies with different grades of graphite, which is probably a reflection of their purities.[23]

Precious-Metal-Base Brazing Alloys in Fuel 130 (D. H. Jansen). – In connection with a proposed barren-salt-to-fuel-salt heat exchanger for the Molten-Salt Reactor, silver- and gold-base brazing alloys have been tested in fuel 130 (LiF-BeF_2-UF_4, 62-37-1 mole %). Silver-base alloys, which according to free-energy considerations should show good corrosion resistance to LiF and BeF_2, are quite heavily attacked[21] by fuel 130, while a gold-base alloy (75% Au–20% Cu–5% Ag) showed excellent corrosion resistance to it (Table 30).

[23] R. L. Carter and W. J. Greening, p 142 in *Problems in Nuclear Engineering: Selected Papers from the 1st Nuclear Engineering and Science Congress Held at Cleveland, Ohio* (ed. by D. J. Hughs, S. McLain, and C. Williams), Pergamon Press, New York, 1957.

Table 29. Results of Mechanical Tests Made in Room-Temperature Air on Inconel and INOR-8 Carburized in Sodium-Graphite Systems

Exposure Conditions			Inconel			INOR-8		
Temperature (°F)	Time (hr)	Specimen[a]	Yield Strength (psi)	Tensile Strength (psi)	Elongation in 2 in. (%)	Yield Strength (psi)	Tensile Strength (psi)	Elongation in 2 in. (%)
			× 10^3	× 10^3		× 10^3	× 10^3	
1400[b]	40	Control	23.9	81.3	38.8	53.7	122.0	42.6
		Carburized	27.0	83.9	36.8	53.9	120.5	36.9
1400	400	Control	24.3	81.7	37.9	53.2	120.7	43.0
		Carburized	30.9	92.9	27.0	57.4	103.2	8.8
1600[c]	40	Control	20.9	75.9	47.3	50.5	116.3	50.0
		Carburized	28.5	91.5	25.7	52.8	98.5	7.8
1200	40	Control	24.1	80.8	40.1	53.3	120.3	43.6
		Carburized	27.2	84.2	38.0	53.1	119.6	43.8

[a] Control specimens were exposed to argon at the conditions indicated.
[b] Average of two mechanical tests.
[c] Average of three mechanical tests.

Table 30. Silver- and Gold-Base Brazing Alloys Static Tested in Fuel 130 for 500 hr at 1300°F

Alloy Composition (wt %)	Metallographic Results
Pure silver	Spotty, heavy grain-boundary attack to 50 mils in depth in some places
90 Ag–10 Cu	Attacked rather uniformly and heavily to 16 mils; maximum attack 30 mils
72 Ag–28 Cu	Attacked uniformly to 12 mils
50 Ag–33.3 Au–16.7 Cu	Spotty attack to maximum of 5 mils
42 Ag–40 Au–18 Cu–0.6 Zr	Uniform attack to 15 mils
75 Au–20 Cu–5 Ag	No attack

FABRICATION

J. H. Coobs

H. Inouye
T. K. Roche
D. O. Hobson
W. J. Werner
T. Hikido
J. E. Spruiell[1]

Columbium Research

D. O. Hobson
H. Inouye
T. K. Roche
J. E. Spruiell

Fabrication of Seamless Tubing. – Initial efforts on the fabrication of seamless tubing were directed toward the consolidation of columbium pellets by extrusion.[2] Several tube blanks were prepared by extrusion of pellets canned in mild steel. However, tube reduction of such blanks resulted in failure at the joints between pellets.

As arc-cast columbium became readily available, the extrusion and tube reduction of this material were emphasized. Sixteen extrusions of cast columbium tube blanks and two rod extrusions have been processed.[3,4] The most satisfactory procedure has been to protect the columbium billets during preheating by use of an electroplated copper coating. The billets are heated in argon and extruded at 1500°F with a relatively low extrusion pressure.

Tube reduction of these columbium extrusions at the Superior Tube Company has been relatively successful. The present inventory of columbium tubing consists of ~200 ft of 0.500-in.-ID × 0.030-in.-wall columbium tubing and ~150 ft of columbium which was draw-clad with type 446 stainless steel during reduction.

Contamination Studies. – The oxidation and nitriding rates of pure columbium over the temperature range of 800 to 1600°C and at pressures of 10^{-5} to 10^{-1} mm Hg were studied.[5] It was determined that nitriding in pure nitrogen is insignificant at temperatures up to 1300°C. However, specimens were contaminated with 61 to 5000 ppm of oxygen by heating at 850°C under a partial pressure of 2 μ of oxygen. These specimens are being used to study the effect of oxygen on the corrosion of columbium by lithium.

Purification of Columbium. – The purification of columbium by annealing in a vacuum at very high temperatures has been studied. Specimens were resistance-heated to temperatures ranging up to the melting point. The results of one series of runs at various temperatures show a decreasing level of oxygen and carbon content at intermediate temperatures.[6]

Protection of Columbium from Oxidation. – Considerable interest has been shown in the protection of columbium by coatings which can be applied to irregular shapes. Initial studies were conducted on specimens coated with three nickel-base brazing alloys. These alloys were Wall Colmonoy Nicrobraz, Coast Metals No. 52, and Coast Metals No. 53.[7,8]

The coatings were applied by flame spraying and sintering in purified helium. Oxidation tests on coated samples showed weight gains at 1700°F comparable to those of type 310 stainless steel. However, cracking of the coating may result in rapid oxidation and complete failure of the columbium. Protection of two sealed columbium tubes was unsuccessful because of difficulties in obtaining uniform sintering of the coating.

Effect of Heat Treatment on Arc-Cast Columbium. – Because of the reactivity of columbium with oxygen at high temperatures, the fabrication of powder-metallurgy columbium is customarily performed at room temperature. Arc-cast material, on the other hand, exhibits brittleness when the levels of oxide, nitride, and carbide impurities are quite low. The development of a suitable heat treatment

---

[1] Temporary summer employee.

[2] H. Inouye, D. O. Hobson, and J. H. Coobs, *ANP Quar. Prog. Rep. Dec. 31, 1957*, ORNL-2440 p 177–78.

[3] H. Inouye and D. O. Hobson, *ANP Quar. Prog. Rep. March 31, 1958*, ORNL-2517, p 3.

[4] D. O. Hobson, *ANP Semiann. Prog. Rep. Sept. 30, 1958*, ORNL-2599 (in press).

[5] J. E. Spruiell and H. Inouye, *ANP Semiann. Prog. Rep. Sept. 30, 1958*, ORNL-2599 (in press).

[6] D. O. Hobson, *ANP Semiann. Prog. Rep. Sept. 30, 1958*, ORNL-2599 (in press).

[7] H. Inouye, D. O. Hobson, and J. H. Coobs, *ANP Quar. Prog. Rep. Dec. 31, 1957*, ORNL-2440, p 177.

[8] H. Inouye and D. O. Hobson, *ANP Quar. Prog. Rep. March 31, 1958*, ORNL-2517, p 4.

for altering the chemical form of these impurities has been undertaken.

Notched bend specimens were heat-treated at temperatures from 700 to 1000°C in a vacuum of 2×10^{-6} mm Hg (ref 9). The effect of this heat treatment was evaluated on the basis of microstructure, fracture mode, and ductility. Results show that annealing at an intermediate temperature (850°C) will improve the fabricability. However, the low ductility at lower and higher temperatures indicates that heat treatment of welds would only be temporary and that proper stabilizing elements to neutralize the effects of interstitial elements would be required.

Columbium Alloy Development. – Work has begun on the preparation of columbium alloy specimens to determine their corrosion resistance to molten lithium. Evidence indicates that the mechanism of corrosion of columbium by lithium is related to the presence of oxygen in the "pure" metal. Alloy additions are being selected for their potential for reacting with the oxygen in order to neutralize the effects of the oxygen. Elements currently being considered as alloying additions are beryllium, zirconium, and cerium.

Columbium melting stock has been prepared from sheet material with the following analysis: 0.032% C, 0.0003% H, 0.0084% N, 0.053% O. A 100-g arc melt of unalloyed columbium was prepared and cold-rolled to a thickness of 0.062 in. without difficulty. Nine alloys containing varying amounts of one of the following three elements, Zr (up to 5%), Be (up to 1%), and Ce (up to 0.5%), were prepared as 100-g arc melts. Suitable specimens will be prepared for evaluating corrosion resistance to molten lithium.

Hydride Moderator Studies

T. Hikido W. J. Werner

Yttrium Preparation Research. – Hydrided yttrium has considerable potential as a high-temperature moderator, but before it can be used a number of problems must be solved. These include fabricating the metal into complex shapes, preventing the cracking of the metal during hydriding, achieving and maintaining a bond between hydride and cladding, and preventing the cracking of the hydride when subjected to thermal cycling. It is believed that improvement in the purity of the yttrium metal will alleviate these problems.

During the past year, significant progress was achieved in the yttrium preparation research program being conducted jointly by the Metallurgy and Chemistry Divisions. In this process,[10] Y_2O_3 is converted to YF_3 and mixed with MgF_2 and LiF. The mixture is then purified by the process used in the production of fluoride fuel mixtures. This purified mixture of fluorides is reduced with lithium to yield an yttrium-magnesium alloy, which is then vacuum distilled to remove the magnesium. The sponge resulting from the vacuum distillation step is then arc-melted.

The reduction retort is shown in Fig. 80. Transfer lines for fluoride and lithium are shown attached to the respective transfer cans. Charging of the lithium and fluoride is accomplished by applying gas pressure to the molten liquids in the transfer cans. The yttrium-magnesium alloy produced in the retort is vacuum distilled in the apparatus shown in Fig. 81.

Evaluation of Material. – Yttrium sponge from early runs, after being arc-melted into small castings, could be swaged into rod by using intermediate anneals at 1000°C in vacuum.[11] Additional castings were prepared and were evaluated by chemical analyses, tensile testing, and metallographic examination.[12] The results indicated that the process was capable of achieving the intermediate goal of producing metal with an oxygen impurity of less than 1000 ppm.

Electron-beam melting was investigated as a possible means of purifying the metal with respect to oxygen.[13] Arc-cast material was remelted, and an attempt was made to process the yttrium-magnesium alloy directly to pure metal. No significant improvement in the purity of the metal was shown by this single test.

Yttrium Production Facility. – The results of work with the laboratory-scale equipment were considered as justifying the expansion of the facilities

[9] H. Inouye and D. O. Hobson, *ANP Semiann. Prog. Rep. Sept. 30, 1958*, ORNL-2599 (in press).

[10] T. Hikido and W. J. Werner, *ANP Quar. Prog. Rep. March 31, 1958*, ORNL-2517, p 4–5.

[11] T. Hikido and J. H. Coobs, *ANP Quar. Prog. Rep. Dec. 31, 1957*, ORNL-2440, p 178–79.

[12] T. Hikido and W. J. Werner, *ANP Quar. Prog. Rep. March 31, 1958*, ORNL-2517, p 5–8.

[13] W. J. Werner and T. Hikido, *ANP Semiann. Prog. Rep. Sept. 30, 1958*, ORNL-2599 (in press).

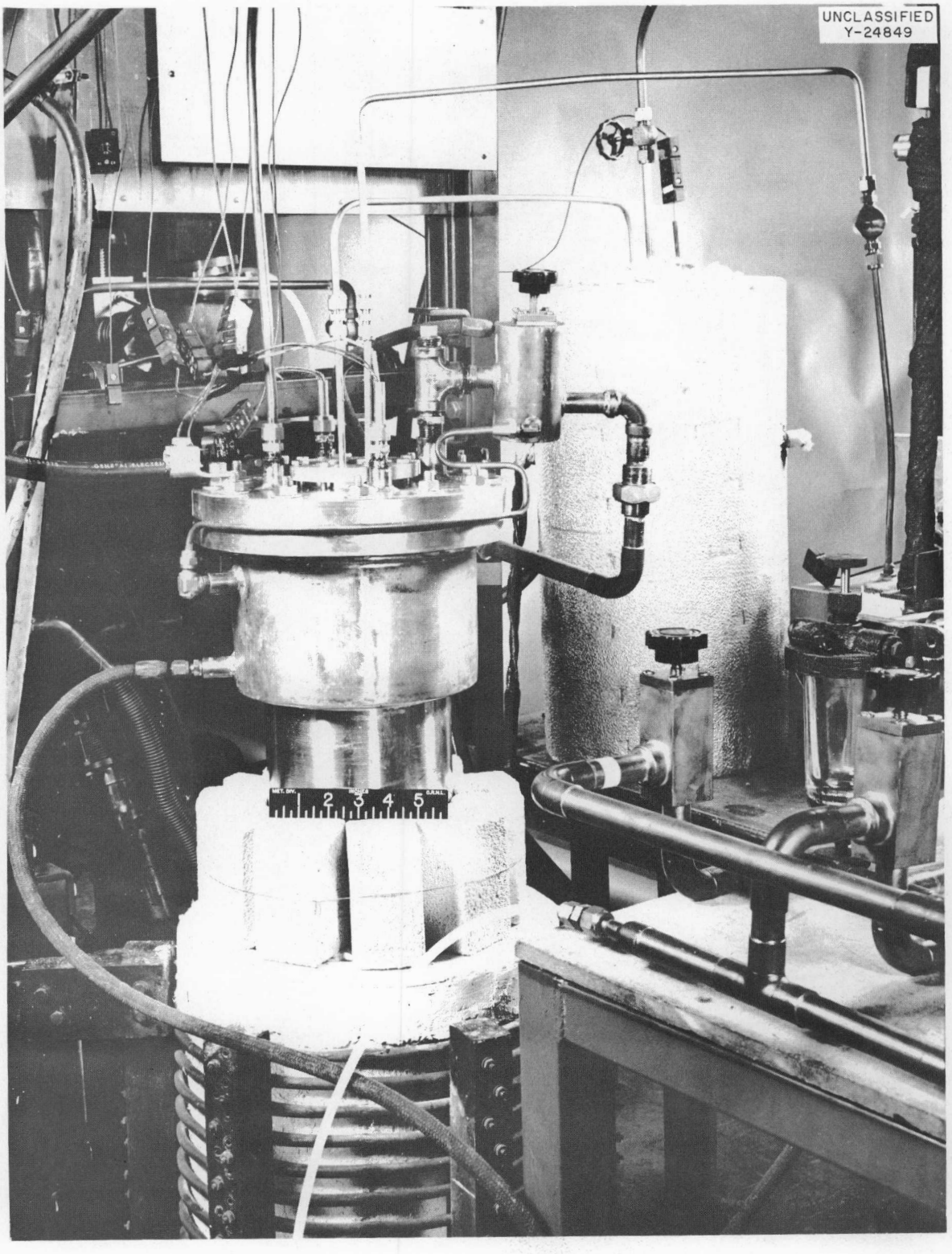

Fig. 80. Laboratory-Scale Reduction Retort with Fluoride and Lithium Transfer Lines Attached.

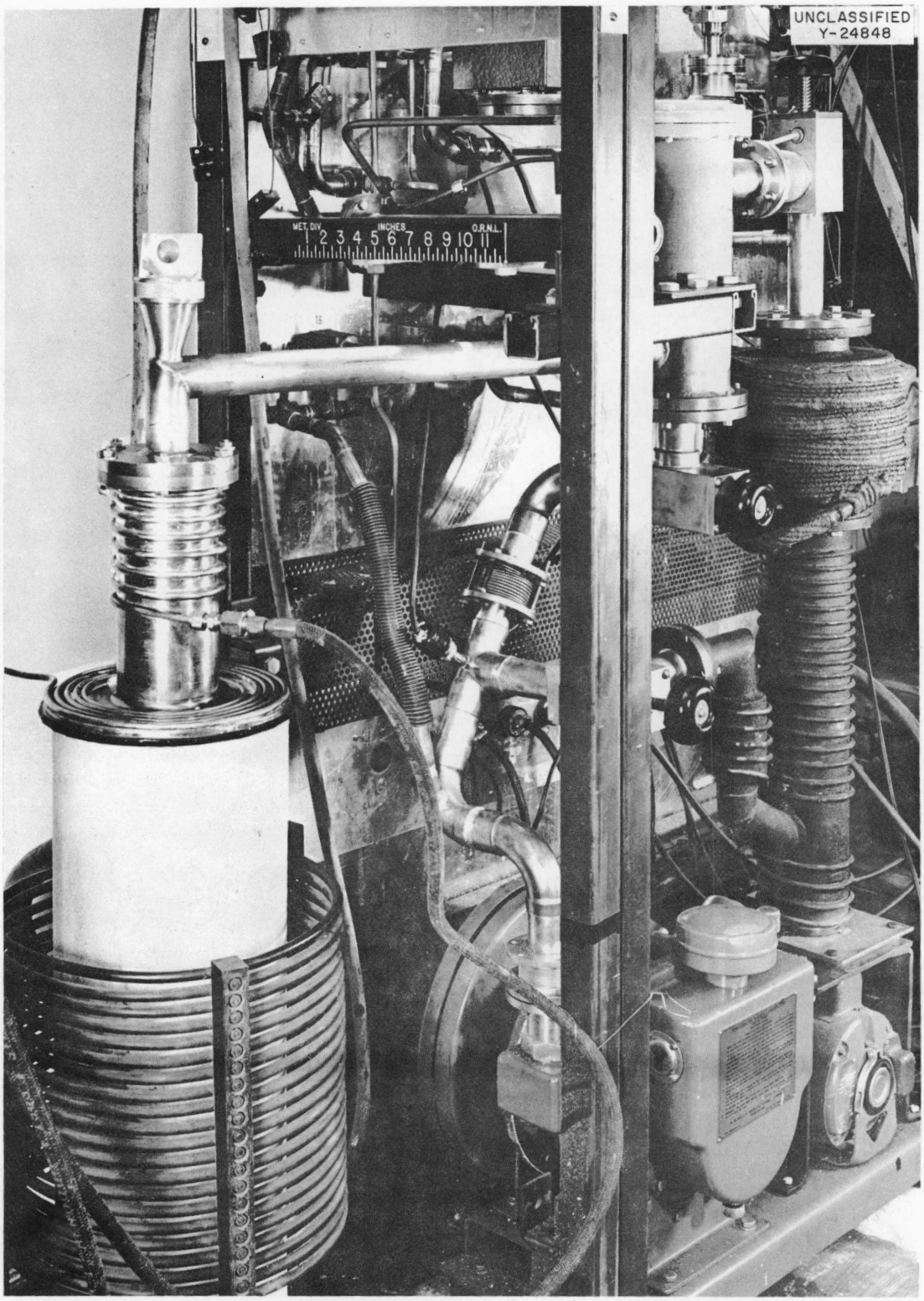

Fig. 81. Laboratory-Scale Vacuum Distillation Equipment for Removing Magnesium from the Y-Mg Alloy.

to prove the feasibility of the process. It was decided that the production of ingots weighing ~20 lb would be satisfactory. Equipment for this production work has been designed and installed,[14] and shakedown operation has begun.

In the first reduction run, an attempt was made to reduce a binary YF_3-LiF mixture directly to yttrium metal. The run was unsuccessful due to a failure of the tantalum crucible used to contain the reacting mixture.

Hydriding Procedures and Dissociation Pressures. – Equipment has been prepared for determining optimum hydriding conditions for high-purity yttrium metal and for studying the dissociation pressure of the hydrided metal.[15]

Fuel Capsule Materials

J. H. Coobs H. Inouye

Selection of Capsule Material for GCR-2. – The operating conditions specified for the helium-cooled reactor led to the selection of austenitic stainless steel for the fuel capsules. Various other materials were considered,[16] but the selection was finally narrowed to AISI type 304 stainless steel because of its fabricability, strength, corrosion resistance, and high-temperature stability.[17]

The Reactions of Type 304 Stainless Steel with Gas Mixtures. – The reactions of stainless steel with CO, CO_2, H_2, H_2O, and CH_4 have been studied from the standpoint that the gases will appear as impurities in a pressurized helium coolant. The objective of this investigation is to determine the effect of the individual gases and, if possible, their effects in combination with each other. It is hoped that the results of this study will show the extent to which purification of the reactor gases is practical. The gas-metal reactions may be detrimental to the stainless steel due to the embrittling effects of oxide penetration, decarburization, or carburization. Embrittlement by oxide penetration will occur when the mode of oxidation is nonuniform, for example, by grain-boundary penetration. Stresses superimposed upon the corrosive effect of the gas aggravate the tendency of the metal to be oxidized nonuniformly. Thus, in thin sections this type of attack is serious.

Embrittlement by decarburization is a special case which may occur with stainless steels of unbalanced composition. In those heats of stainless steel in which chromium is near the maximum and nickel is near the minimum specified content, removal of carbon will set up conditions favorable to the precipitation of the brittle iron-chromium (sigma) compound. Carburization, on the other hand, will cause embrittlement by formation of chromium carbide.

Free-energy calculations for the reactions of the various gases with stainless steel indicate that CO_2, CO, and H_2O are predominantly oxidizing, while methane is carburizing and hydrogen is reducing. In oxidizing gases the principal oxide formed was calculated to be Cr_2O_3. The oxides of iron are also determined to be possible constituents of the films. Oxygen in the helium is not considered as an impurity in the circulating coolant since it will readily react with graphite to form CO or CO_2.

The conditions necessary for carburization are that an oxide film must not form on the metal in the presence of a carburizing gas. The impermeability of this thin film to gases has been demonstrated by other investigators.[18,19] Decarburization may occur via the removal of carbon by hydrogen as CH_4 or by the reduction of an oxide film by the carbon in the steel and removal of the carbon as CO (ref 20).

The Reactions of Type 304 Stainless Steel with CO_2 at 1500°F. – The tests conducted to date have been made in flowing mixtures of argon and CO_2. In concentrations of CO_2 between 0.63 and 0.1%, the oxidation of stainless steel results in the formation of two different mixed-oxide films. A bulk oxide at the gas interface was identified as rhombohedral $3Cr_2O_3 \cdot Fe_2O_3$, greenish in color and magnetic. A very thin film, having a cubic spinel structure and a composition $MnO \cdot Cr_2O_3$, was found between the

---

[14] T. Hikido, *ANP Semiann. Prog. Rep. Sept. 30, 1958*, ORNL-2599 (in press).

[15] W. J. Werner, *ANP Semiann. Prog. Rep. Sept. 30, 1958*, ORNL-2599 (in press).

[16] H. Inouye, *The Selection of Canning Materials for Gas-Cooled Reactors*, ORNL CF-57-11-12 (Nov. 14, 1957).

[17] *The ORNL Gas-Cooled Reactor*, ORNL-2500(Pt. 2), sec 3 (April 1, 1958).

[18] Z. E. Olzak, *Carburizing Effect of Natural Gas Upon High-Alloy Steels at Elevated Temperatures*, EMD-513, Laboratory Report D-90 and Suppl. No. 1, Babcock and Wilcox Tube Co. (December 1942).

[19] J. B. Giacobbe, *Trans. Am. Soc. Metals* 45, 134–50 (1953).

[20] T. N. Rhodin, *J. chim. phys.* 54, 72–89 (1957).

bulk oxide and the substrate metal. Spectrographic analysis of the stripped film indicates that Cr, Fe, and Mn are the major constituents.

The weight gains of the specimens in 100 hr were between 109 and 117 $\mu g/cm^2$. Carbon analyses of the metal for evidence of decarburization were inconclusive.

The Reactions of Magnesium and Magnesium Alloys with CO_2. – Magnesium and uranium are compatible up to the melting point of either metal. In addition, the attractive nuclear properties of magnesium make it an excellent canning material for uranium fuel elements. Its use at elevated temperatures, however, raises the possibility of catastrophic oxidation it the metal is suddenly exposed to excessive temperatures in the reactor atmosphere, or if it is exposed to air as a result of a reactor component failure. In order to assess this potential (fire) hazard, a literature survey was conducted to determine the variables affecting the ignition temperatures of magnesium and its alloys in air and CO_2 (ref 21).

Beginning at about 900°F, the oxidation rate of magnesium in air is linear, resulting in the formation of a porous MgO scale. At higher temperatures, acceleration of the oxidation occurs in such a manner that the rate can be described by two linear intersecting curves. The heat generated by the oxidation reaction will cause the metal to ignite and burn. The ignition temperature of unalloyed magnesium is 1122°F in oxygen at 1 atm.

The ignition temperature of magnesium is slightly sensitive to the oxygen pressure, showing a variation of 100°F between 10 and 0.4 atm of O_2. Alloying lowers the ignition temperature, except in alloys containing Zr, Be, Ce, and La. When the ignition temperature is lowered, the decrease roughly parallels the solidus temperature (melting point) of the alloy. The elements listed inhibit ignition up to temperatures in excess of the melting point of the alloy, due to a protective film rich in the added element.

Fabrication of Iron-Aluminum Alloys. – The excellent resistance of the iron-aluminum alloys to gases at high temperatures, together with their moderate neutron cross section, prompted a study to determine the feasibility of fabricating a modified alloy into tubing for use as fuel-capsule material.

Six cast billets of DB-2, an alloy developed by The Martin Co., were prepared by vacuum-induction melting. In contrast to the previous alloys known as Alfenol and Thermenol, which contain about 15% Al, the present alloy contains a nominal 7% Al and therefore is more ductile without loss of oxidation resistance.

The machined and drilled billets were successfully extruded to tube blanks at an extrusion ratio of 7:1 at 2100°F. The pressure requirements were 50% less than those required for nickel-base alloys. The results of tube-reducing these blanks under the conditions listed in Table 31 were discouraging due to their brittle behavior.

Fabrication of Fueled Graphite Irradiation Specimens at the National Carbon Company (Contract No. AT-(40-1)-2143). – Graphite capsules or fuel dispersions in graphite have a number of advantages for advanced designs of gas-cooled reactors.

[21] H. Inouye, *The Reactions of Magnesium and Magnesium Alloys with Gases at High Temperatures*, ORNL CF-58-1-93 (Jan. 20, 1958).

Table 31. Experimental Tube Reducing of DB-2 Alloy

(8 Al–5 Cr–1 Cb–0.5 Ti–0.07 C–bal Fe)

Extrusion No.	Size (in.)	Temperature (°F)	Results
2A	1.400 OD × 0.160 wall	Room	Failed with no reduction
2B	1.400 OD × 0.160 wall	400	Failed with no reduction
4A	1.400 OD × 0.160 wall	800	Failed at 1.000 in. OD
4B	1.400 OD × 0.160 wall	1200	Failed at 1.000 in. OD
5A			Failed during straightening extrusion

Graphite is highly refractory and resistant to thermal stresses and has a low neutron capture cross section. Samples of fuel in coated and treated capsules, and as dispersions in graphite, are being prepared at the National Carbon Company for irradiation testing at ORNL as part of the study of materials for advanced gas-cooled reactor systems.

Control Rod Material for GCR-2

J. H. Coobs

The design and materials specifications for the control rods for the Gas-Cooled Reactor were developed.[22] The principal considerations for this control rod were low cost, operation at 1100°F, and low residual activity. The relevant properties and important disadvantages of a number of control materials were tabulated, including hafnium, silver, silver alloys, rare earths, and boron steels. After considering the properties of the various materials, the use of a canned silver rod was recommended because of ease of fabrication, compatibility, and thermal stability due to high conductivity.

INOR-8 Development

H. Inouye T. K. Roche

Influence of Composition upon the 1500°F Creep-Rupture Strength and Microstructure of Mo-Cr-Fe-Ni-Base Alloys. – Results of an alloy development program have shown that an alloy having the composition range 15 to 18% Mo, 6 to 8% Cr, 5% (max) Fe, 0.04 to 0.08% C, bal Ni, designated INOR-8, is an attractive structural material for use in a nuclear power reactor fueled with molten uranium-bearing fluoride salts.[23] A study has been completed which enlarges upon the technology of this alloy.[24] In this study, the influence of composition upon the 1500°F creep-rupture strength and the microstructure of alloys encompassed by the range 10 to 20% Mo, 5 to 10% Cr, 4 to 10% Fe, 0.5% Al, 0.5% Mn, 0.06% C, bal Ni was determined. All the alloys were tested in creep rupture at a stress of 10,000 psi, in the annealed condition. The criteria used to evaluate the strength of the alloys were the times required to reach strains between 1 and 10%.

The results of this study could not be explained in simple terms of composition variation, since the principal factors affecting the strength of the alloys were (1) solid-solution elements, (2) carbide and noncarbide aging reactions, (3) the presence of M_6C-type carbides in the microstructures, and (4) grain size. Molybdenum was found to be most effective in strengthening the alloys, due to the combined effects of solid-solution strengthening and an increase in the quantity of dispersed carbides. The influence of chromium was significant when added in amounts of 5 to 10%, while the strengthening effect of iron was interpreted as being insignificant when amounts up to 10% were added to the ternary alloy.

A general consideration of all data obtained from this investigation favorably supports the composition specifications placed upon the alloy INOR-8.

Structural Stability of 18% Mo–Ni Alloys. – The precipitation of intermetallic compounds in Ni-Mo-base alloys is deleterious to the tensile ductility of these materials. An example of this fact is found in the case of Hastelloy B.[25] Inasmuch as the upper composition limit of the alloy INOR-8 has presently been set at 18% Mo, which approaches the solubility limit of molybdenum in nickel, it is important that the structural stability of the alloy be determined. At the same time it is desirable to determine the location of any phase boundary which might exist near the maximum composition of INOR-8.

An investigation of the stability of alloys bordering the maximum compositional limit of the alloy INOR-8 has been initiated.[26] Specimens of 11 compositions are being aged at temperatures varying from 900 to 1800°F and will be evaluated metallographically.

Production of INOR-8 at the Westinghouse Electric Corporation.[27] – Five air-melted heats of INOR-8 consisting of about 5000 lb each were prepared at the Blairsville, Pennsylvania, Metal Plant

---

[22] *The ORNL Gas-Cooled Reactor*, ORNL-2500(Pt. 2), sec 3 (April 1, 1958).

[23] *Molten Salt Reactor Program Status Report*, ORNL CF-58-5-3(Pt. 3), sec 1 (May 1958).

[24] T. K. Roche, *The Influence of Composition upon the 1500°F Creep-Rupture Strength and Microstructure of Molybdenum-Chromium-Iron-Nickel Base Alloys*, ORNL-2524 (June 24, 1958).

[25] R. E. Clausing, P. Patriarca, and W. D. Manly, *Aging Characteristics of Hastelloy B*, ORNL-2314 (July 30, 1957).

[26] T. K. Roche, *MSR Quar. Prog. Rep. Oct. 31, 1958*, ORNL-2626 (in press).

[27] Subcontract No. 1067.

of the Westinghouse Electric Corporation. These heats are being processed to finished products on purchase order where necessary, since the contract has not been renewed. A final report from Westinghouse is being prepared.

Production of Seamless Tubing at the Superior Tube Company.[28] – Reduction of extruded tube shells of INOR-8 to seamless tubing has been carried out at the Superior Tube Company. Good yields of high-quality tubing have been obtained. The services of Superior have also been used in the reduction of extruded columbium tube blanks[29] and the production of special stainless steel tubing for the Gas-Cooled Reactor program.

[28]Subcontract No. 1112.

[29]D. O. Hobson and H. Inouye, *ANP Semiann. Prog. Rep. Sept. 30, 1958*, ORNL-2599 (in press).

Bearing Materials

J. H. Coobs

Flame-sprayed coatings are somewhat porous and were considered worthy of test in the development of salt-lubricated bearings. Two journals made of INOR-8 were flame-sprayed with INOR-8 for use in bearing tests, and a technique was developed for the bonding of flame-sprayed molybdenum to a molybdenum-base material.[30]

[30]J. H. Coobs, *MSR Quar. Prog. Rep. June 30, 1958*, ORNL-2551, p 69.

LIQUID-METAL RESEARCH

J. L. Scott

D. F. Toner
J. W. Prados[1]
D. L. Swift[2]
W. A. Peter, Jr.[2]

The approach taken by the Liquid-Metal Research Group toward the reduction or elimination of mass transfer in systems utilizing liquid metals as coolants has been described previously.[3] Studies initiated this year include theoretical analyses of corrosion test methods in common usage and the measurement and interpretation of diffusion coefficients in liquid metals. A discussion of the results obtained in these areas follows.

Relationship Between the Rate-Controlling Step of the Mass Transfer Process and the Distribution of Corrosive Attack

J. L. Scott J. W. Prados

A study was made for determining the relationship between the distribution of corrosive attack or cold-zone deposits and the rate-controlling step of thermal-gradient mass transfer. The following equations describe the mass transfer process at any point in the loop:[4]

$$(1) \qquad R(Z) = k(Z)\,\rho(X^* - X) = \frac{w}{\pi D}\frac{dX}{dZ} \ ,$$

where

$R(Z)$ = rate of mass transfer at point Z in the loop, $g \cdot cm^{-2} \cdot sec^{-1}$,

$k(Z)$ = local mass transfer coefficient, cm/sec,

ρ = density of the liquid, g/cm^3,

X^* = equilibrium solubility at the interface temperature, expressed as a mass fraction,

X = liquid concentration at Z, expressed as a mass fraction,

w = mass flow rate, g/sec,

D = pipe diameter, cm,

Z = distance coordinate along loop.

The amount of material, Q, per unit area removed or deposited at point Z in a time interval Δt is computed at steady state by the expression

$$(2) \qquad Q = R(Z)\,\Delta t \ ;$$

thus the mass transfer at every point is analytically described.

In operating systems, dX/dZ is very small and is difficult to measure. In this circumstance, however, X may be assumed to be independent of Z and equal to $\overline{X}$, the average loop-liquid composition at steady state. From these assumptions a qualitative measure of the relative lengths of the solution and deposition zones in the loop may be obtained. These results are summarized below for special cases:

Hot-Zone Controlled Mass Transfer

(deposition rate $\gg$ solution rate)

$\overline{X} \cong X^*$ (evaluated at the maximum loop temperature)

$$M \longrightarrow \infty$$

where

$$M = \frac{\text{length of loop in which solution occurs}}{\text{length of loop in which deposition occurs}}$$

Cold-Zone Controlled Mass Transfer

(solution rate $\gg$ deposition rate)

$\overline{X} \cong X^*$ (evaluated at the minimum loop temperature)

$$M \longrightarrow 0$$

Both Zones Control Equally

(solution rate $\cong$ deposition rate)

$$\overline{X} \cong \frac{X^*(\text{maximum}) + X^*(\text{minimum})}{2}$$

$$M \cong 1$$

It should be noted that practical cases will fall between the limits set by the first two situations above.

---

[1] Consultant to the Metallurgy Division.

[2] Student, MIT Engineering Practice School.

[3] J. L. Scott, *Met. Ann. Prog. Rep. Oct. 10, 1957*, ORNL-2422, p 73.

[4] J. L. Scott and J. W. Prados, *Relationship Between the Rate-Controlling Step of the Mass-Transfer Process and Distribution of Corrosion Attack*, ORNL CF-58-7-104 (July 16, 1958).

These considerations lead to an important practical conclusion for systems in which one of the mass transfer steps (solution or deposition) is much slower than the other. Reduction of the rate of this slow, controlling process will lead to a concentration of attack (or deposition) in a smaller region of the system. This could result in more rapid system failure, even though the total rate of mass transfer might decrease. It would be more beneficial, in such systems, to attempt to reduce the rate of the faster, noncontrolling step. This would leave the over-all rate of mass transfer essentially unchanged, but would lead to a more even distribution of attack and deposition, and hence to longer system life.

Factors Affecting Sizes and Shapes of Crystals Formed During Thermal-Gradient Mass Transfer

J. W. Prados J. L. Scott

The formation of crystals in the cold zone of mass transfer loops has not heretofore been studied theoretically to determine the relative importance of the various factors that govern the process. As a first step toward the analysis of crystal formation, calculations were made for determining the stresses at the base of a simple cylindrical rod-shaped crystal model under various fluid-flow conditions. The object of these calculations was to show the conditions that would lead to the breakoff of a crystal, which is subsequently carried along in the fluid stream.

Equations were derived[5] for the maximum stress at the base of the crystal model under static and flow conditions. For the static case, the maximum stress, S, in dynes/cm^2 is

$$S = 4(\rho_s - \rho)\frac{g}{g_c} d\left(\frac{L}{d}\right)^2 , \quad (3)$$

where

ρ_s = density of the solid, g/cm^3,

ρ = density of the liquid, g/cm^3,

g = acceleration of gravity, cm/sec^2,

g_c = force-mass conversion constant, g·cm·dyne^{-1}·sec^{-2}, for Newton's second law of motion,

d = diameter of crystal, cm,

L = length of crystal, cm.

For constant L/d ratios, the stress decreases with diameter; thus long, thin crystals of small diameter are stable in the static case.

Under flow conditions,

$$S = \frac{8C_D\rho V^2}{\pi g_c}\left(\frac{L}{d}\right)^2 , \quad (4)$$

where C_D = drag coefficient for a circular cylinder, and V = mean fluid velocity, cm/sec. Since S is proportional to the square of the fluid velocity, the stress increases rapidly with increases in the flow rate. Thus, crystals of a given L/d ratio, which are stable under static conditions, would be swept away under flow conditions.

These predictions have been found to corroborate qualitatively the experimental observations of crystal sizes and shapes in static, seesaw, thermal-convection-loop, and pump-loop tests. In all cases, crystals that grew under static or viscous flow conditions had large dendritic structures, whereas those crystals deposited in regions of high flow rate were an order of magnitude smaller and were usually equiaxed.

Benzoic Acid Mass Transfer in Water

J. L. Scott D. L. Swift
W. A. Peter, Jr.

In this study, the dissolution and recrystallization of a metal container wall was simulated by the dissolution and recrystallization of benzoic acid in hot water. Since benzoic acid is slightly soluble in water and its solubility increases with temperature, the factors affecting the mass transfer mechanism of the benzoic acid–water system are analogous with those in liquid-metal systems.

The apparatus and the method of analyzing data have been described previously.[6] Results showed that the mass transfer coefficient for dissolution, k_D, was well correlated by the empirical relation

$$\left(\frac{k_D}{V}\right)\left(\frac{\mu}{\rho D}\right)^{0.66} = 0.09\left(\frac{dV\rho}{\mu}\right)^{-0.2} , \quad (5)$$

[5] J. W. Prados and J. L. Scott, *Factors Influencing the Sizes and Shapes of Crystals Formed During Thermal Gradient Mass Transfer*, ORNL CF-58-8-81 (Aug. 22, 1958).

[6] D. L. Swift and W. A. Peter, Jr., *Hot to Cold Zone Mass Transfer*, KT-328 (Feb. 28, 1958).

where

V = the linear velocity of the liquid, cm/sec,

μ = the liquid viscosity, $g \cdot cm^{-1} \cdot sec^{-1}$,

ρ = the liquid density, g/cm^3,

D = the diffusivity of benzoic acid in water, cm^2/sec,

d = the diameter of the sample undergoing dissolution, cm.

Over the temperature range studied, 41.5 to 61.5°C, the solution physical properties did not change markedly, and k_D was almost temperature independent. The effect of flow rate was pronounced, however, with k_D proportional to the 0.8 power of the linear flow velocity. Analysis of composition-time curves for the system, together with observation of crystal formation, indicated that the percentage supersaturation required for crystal nucleation was an inverse function of the fluid velocity. The rates of solution and of deposition for this system appeared to be of comparable magnitude.

Self-Diffusion in Liquid Metals

J. L. Scott

A study was made of the coefficients of self-diffusion of those liquid metals for which data have been reported,[7-13] in order to arrive at a better understanding of the process of liquid-metal diffusion. Upon examination of the data shown in Fig. 82, it is evident that there are striking similarities in the coefficients of self-diffusion, even between metals of widely differing atom sizes, melting points, and crystal structures. In general, two conclusions may be reached:

1. The coefficients of self-diffusion are the same order of magnitude for all of the metals reported, if comparison is made at the same value of T/T_M, where T is the absolute temperature and T_M is the absolute melting temperature.

2. The activation energy for self-diffusion, ΔH_D, increases with the melting point of the metal.

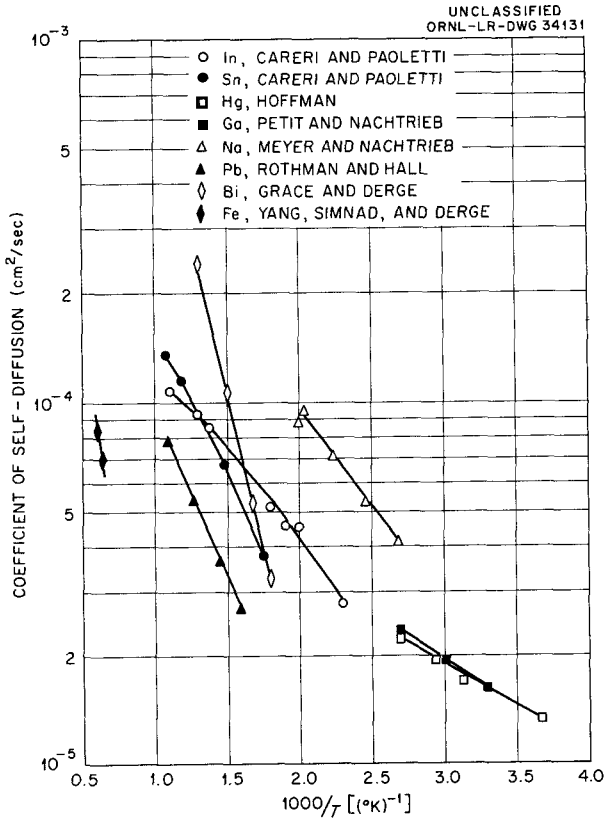

Fig. 82. Coefficient of Self-Diffusion for Liquid Metals as a Function of Temperature.

A closer study of the data showed that ΔH_D varied linearly with T_M according to the equation

$$\Delta H_D = 9.40 T_M - 1340 \quad , \tag{6}$$

and the coefficient of self-diffusion at the melting point, D_M, also varied linearly with the absolute melting temperature according to the relation

$$D_M = 7.02 \times 10^{-8} T_M - 4.00 \times 10^{-6} \quad . \tag{7}$$

Equations 6 and 7 were substituted into the conventional diffusivity relationship,

$$D = D_0 \exp(-\Delta H_D / RT) \quad ,$$

[7] G. Careri and A. Paoletti, *Nuovo cimento* [10]2, 574 (1955).

[8] R. E. Hoffman, *J. Chem. Phys.* 20, 1567 (1952).

[9] J. Petit and N. H. Nachtrieb, *J. Chem. Phys.* 24, 1027 (1956).

[10] R. E. Meyer and N. H. Nachtrieb, *J. Chem. Phys.* 23, 1851 (1955).

[11] S. J. Rothman and L. D. Hall, *Trans. Am. Inst. Mining Met. Petrol. Engrs.* 206, 199 (1956).

[12] R. E. Grace and G. Derge, *Trans. Am. Inst. Mining Met. Engrs.* 203, 839 (1955).

[13] L. Yang, M. T. Simnad, and G. Derge, *Trans. Am. Inst. Mining Met. Petrol. Engrs.* 206, 1577 (1956).

with the following result:

$$(8)\quad D = 7.96 \times 10^{-6}(T_M - 57) \times \times \exp\left\{-\left[\frac{9.40}{R}\frac{T_M}{T} + \frac{1340}{RT_M}\left(1 - \frac{T_M}{T}\right)\right]\right\}.$$

Equation 8 gives a general relationship between the coefficient of self-diffusion of a liquid metal, the temperature, and the melting point of the metal. Computed results agree well with the reported values for all the metals considered except bismuth, many of whose properties are anomalous. In view of the good agreement of this relationship with results for the other metals studied, it is probable that Eq. 8 gives a good estimate of the coefficients of self-diffusion in the liquid state for all metals with normal crystal structures (bcc, fcc, and cph) and with melting temperatures between those of mercury and iron.

[14] J. W. Prados and J. L. Scott, *Proposal for an Experimental Study of Thermal Gradient Mass Transfer in a Thermal Convection Loop*, ORNL CF-58-2-124 (Feb. 18, 1958).

Mass Transfer Experiments in a Thermal-Convection Loop

D. F. Toner

In order to carry out thermal-gradient mass transfer studies under carefully controlled experimental conditions, a thermal-convection loop was designed and was fabricated from quartz. Samples of the material to be tested can be inserted and removed from the system during operation. The basic features of this loop have been previously described,[14] although some modifications in mechanical design have been made. The major advantages over loops previously employed are (1) the use of an inert container material which limits the mass transfer processes to regions in which conditions can be controlled, (2) the ability to measure solution rates from sample weight loss during the course of a run, and (3) the possibility of sampling the liquid metal for analysis during operation.

To date, no experimental data are available.

NONDESTRUCTIVE TEST DEVELOPMENT

J. W. Allen

R. W. McClung E. A. Reed
R. A. Nance J. K. White[1]

Metal Identification Meter

R. A. Nance J. W. Allen

A transistorized model of the metal identification meter[2] has been developed. Although the internal operation has been altered, the new instrument[3] also utilizes induced currents for identification of metals by permeability and conductivity. In developing this instrument, several changes were made which greatly increased its versatility. The changes are:

1. The instrument has been made truly portable by the incorporation of a battery power supply.
2. The range of metals identifiable has been expanded to include all ferromagnetic and non-ferromagnetic metals.
3. The effective depth of penetration of the eddy currents has been decreased by increasing the operating frequency, and thereby the minimum metal thickness necessary for accurate identification has been reduced.
4. The diameter of the probe coil has been decreased to reduce the effect of metal surface curvature.

Cladding Thickness Measurements

R. A. Nance J. W. Allen

The study[4] of eddy-current cladding thickness determinations has been continued. Correlation of metallographic and eddy-current thickness measurements has been satisfactory in many instances. However, in a number of cases involving MTR-type fuel plates, the error of measurements has been excessive. Since the eddy-current measurements are made over an area approximately $\frac{1}{2}$ in. in diameter, the roughness of the interface between the core and cladding will affect the eddy-current thickness measurements. The cladding on several specimens was removed in thin layers by milling, and a contour was plotted of the cladding thickness variation.[5] The eddy-current measurements were within 0.002 in. of the average cladding thickness. However, many small areas as large as $\frac{1}{16}$ in. in diameter were located in which the core material protruded from 0.003 to 0.006 in. into the cladding. In such cases, the minimum cladding thickness was as much as 0.006 in. less than the thickness indicated by eddy currents. Smaller probe coils, capable of measuring the cladding thickness in minute areas, are being investigated.

A technique has been developed for the thickness measurement of the aluminized coating on carbon steel.[5] This technique is capable of measuring coatings of 0.0016 to 0.0005 in. with an uncertainty of ±0.0002 in. The presence of an intermetallic layer approximately 0.0003 in. thick adversely affects measurements below 0.0005 in.

A technique[5] has also been developed in which probe-to-specimen spacing variations of as much as 0.100 in. produce no noticeable effects during the measurement of the thickness of a high-conductivity non-ferromagnetic metal on a ferromagnetic base. This method is particularly well suited to automation because of its independence of lift-off variation.

Eddy-Current Development: GCR Capsule Tubing

R. A. Nance J. W. Allen

The initiation of the GCR program necessitated the development of an inspection method for the $\frac{3}{4}$-in.-OD × 0.020-in.-wall type 304 stainless steel fuel-capsule tubing. The encircling-coil eddy-current method was chosen as the primary inspection method because: (1) eddy-current inspection of tubing can be performed at high speeds; (2) it is very economical, as compared with other methods; and (3) it is easily adapted to inspection in the

---

[1] On loan from HRP Metallurgy.

[2] J. W. Allen, *Met. Ann. Prog. Rep. Oct. 10, 1957*, ORNL-2422, p 38.

[3] R. A. Nance and J. W. Allen, *ANP Semiann. Prog. Rep. Sept. 30, 1958*, ORNL-2599 (in press).

[4] R. B. Oliver, R. A. Nance, and J. W. Allen, *ANP Quar. Prog. Rep. Dec. 31, 1957*, ORNL-2440, p 192.

[5] J. W. Allen and R. A. Nance, *ANP Quar. Prog. Rep. March 31, 1958*, ORNL-2517, p 47.

tubing manufacturer's plant. Many tubing manufacturers currently use eddy-current inspection equipment, whereas almost none are equipped to perform ultrasonic inspection of tubing.

An instrument was developed to study the possibility of detecting small cracklike defects in the capsule tubing. An investigation of the test parameters led to the choice of a closely spaced differential coil system operating at a test frequency of 50 kc which provided sensitivity to small cracklike defects on both the outside and inside of the tubing while being relatively insensitive to gradual dimensional variation along the tube. This equipment has demonstrated its ability to detect manufactured defects 0.001 to 0.002 in. deep on the outside surface of the tube. These defects are machined slots approximately $\frac{1}{8}$ in. long and 0.010 in. wide.

A nonlinear amplifier circuit has been incorporated into this instrument to discriminate against signals produced by inconsequential variations in dimensions, conductivity, and permeability. Figure 83 illustrates the effectiveness of this "noise-rejection" circuitry in improving the interpretability of signal traces. The large signals remaining after the "noise rejection" are produced by machined defects.

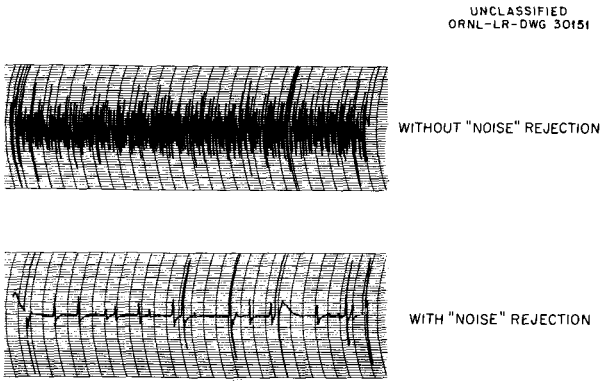

Fig. 83. Differential Coil Eddy-Current Traces of $\frac{3}{4}$ × 0.020 in. Type 304 Stainless Steel. Frequency = 50 kc.

Small, abrupt variations in permeability are frequently encountered in austenitic stainless steel tubing due to localized cold work. It has been found that these signals can be greatly reduced by the use of a strong d-c field in the vicinity of the test coil. This saturation effect is illustrated in Fig. 84.

The results of this research and development effort will facilitate the formulation of improved procedure specifications for use in the eddy-current inspection of tubing in the manufacturer's plant and will assure that high-quality tubing is being supplied to the GCR program.

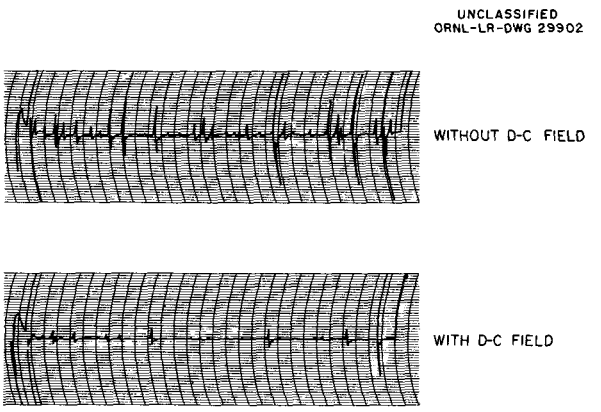

Fig. 84. Differential Coil Eddy-Current Traces of $\frac{3}{4}$ × 0.020 in. Type 304 Stainless Steel Tube. Frequency = 50 kc.

Remote X-Ray Viewing

J. W. Allen R. W. McClung

Studies have been made of the x-ray-sensitive Vidicon[6,7] in a closed-circuit television system for remote, direct x-ray viewing of small, intricate parts and assemblies. The primary advantages of this system (in contrast with those consisting of closed-circuit television applied to fluoroscopy) are the inherent high resolution, which approaches the resolution attainable with a fine-grained radiographic film, and the inherent magnification of images. Although the sensitivity of the present selenium-photoconductor Vidicon system is less than that which can be obtained with existing film techniques, it is sufficient for many applications. This system has considerable development potential.

---

[6] R. B. Oliver and J. W. Allen, *ANP Quar. Prog. Rep. Dec. 31, 1957*, ORNL-2440, p 192.

[7] J. W. Allen and R. W. McClung, *ANP Semiann. Prog. Rep. Sept. 30, 1958*, ORNL-2599 (in press).

Fluid-Flow Rate Measurement

J. W. Allen R. W. McClung

An ultrasonic method for accurately measuring the rate of liquid flow in small-diameter tubes has been investigated, and a prototype instrument was constructed. Preliminary tests indicate that it can be used to measure liquid flow rates effectively and precisely. This work is being accomplished in cooperation with the Chemical Technology Division and was undertaken by the Nondestructive Test Development Group because of its past experience with ultrasonics. The results of this endeavor are reported here because of the possible application of such a system to other flow-measuring problems.

The basic operation of the sonic timer of fluid flow (STOFF) is indicated in the block diagram of Fig. 85. A gas bubble is injected into the liquid stream in such a manner that it completely fills the tube. The bubble is thus carried along with the flowing stream and subsequently interrupts the continual transmission of ultrasound across the stream at each of the two adjacent ultrasonic cells. The monitoring instrument accurately measures the amount of elapsed time between the two interruptions. Since the distance between the two cells is known, the rate of liquid flow can be accurately determined. The only calibration of the system which is necessary is the timing of the movement of a gas bubble under a static fluid condition.

In the prototype system, the ultrasonic cells are 36 in. apart and are attached to $\frac{1}{2}$-in.-dia stainless steel tubing. The chambers to which the $\frac{3}{4}$-in.-dia stainless steel transmitting rods are welded are $\frac{5}{8}$ in.^{2} in cross section and are made of 0.030-in. thick welded stainless steel sheet; the system is completely welded. Both the transmitting and receiving transducers are $\frac{3}{4}$-in.-dia 2.25-Mc *X*-cut quartz crystals, and are acoustically bonded to the transmitting rods with an epoxy resin. The transmitter and receiver chassis are attached to the transmitting rods in such a manner that they form a protective housing for the quartz transducers.

The transmitters shock-excite the 2.25-Mc transducers at a pulse rate of approximately 5000 cps

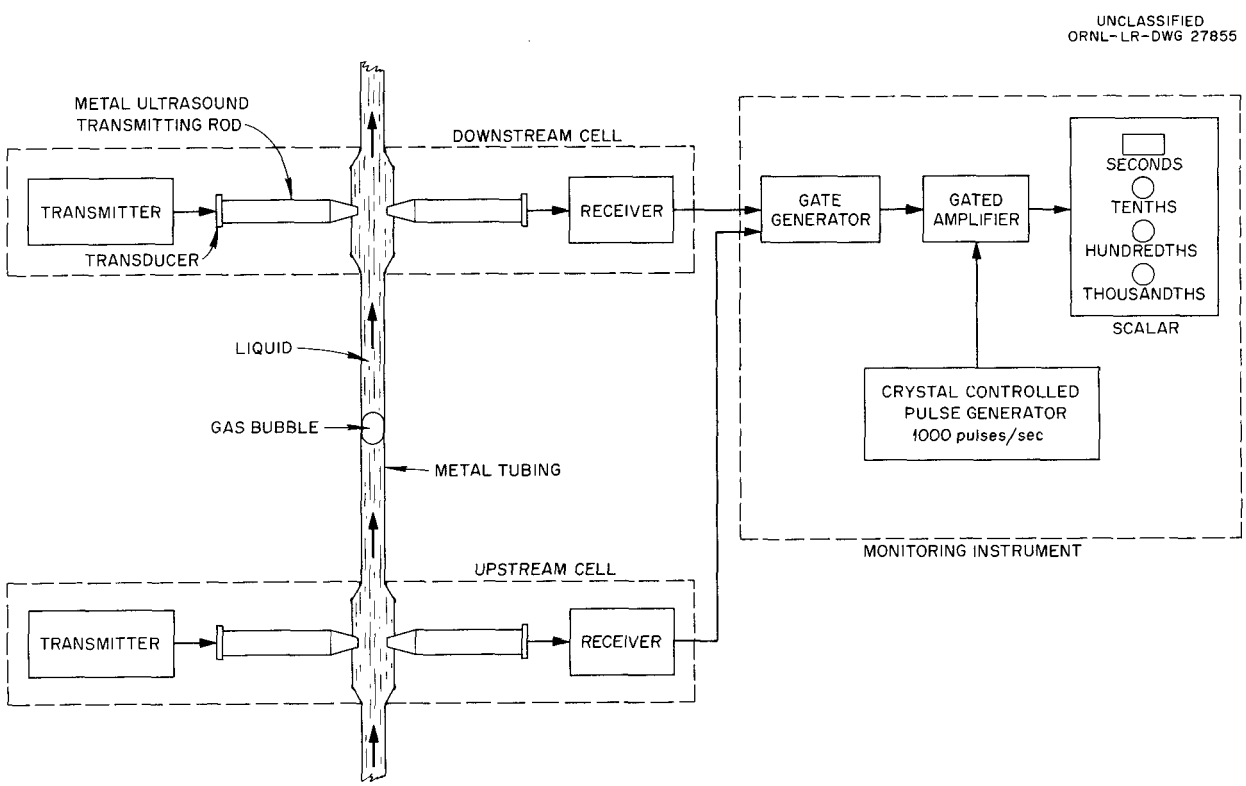

Fig. 85. Block Diagram of Sonic Timer of Fluid Flow.

from a very simple one-tube circuit. This method of excitation was chosen in preference to a continuous excitation in order to eliminate the need for precise and elaborate tuning procedures. Each of the receivers consists of two fixed-tuned 2.25-Mc vacuum-tube amplifiers and a semiconductor diode detector.

The electronic clock for the elapsed-time measurement consists of a crystal-control pulse generator which delivers 1000 PPS to a scaler via a gate circuit. In operation, the interruption of the ultrasonic transmission by the gas bubble at the upstream cell causes the gate to open, and the scaler begins counting the 1000-per-second pulses. When the gas bubble arrives at the second cell, the gate is closed and the counting ceases. The scaler consists of three gas-transfer decade counter tubes and a mechanical register. The elapsed-time interval is thus displayed directly on the scaler to the nearest 0.001 sec. The inaccuracy of the time measurement is thus ±0.001 sec, as imposed by the counter, and could be reduced if necessary.

The construction of this system is relatively simple and inexpensive, and the only operation control is a push-button switch which is used to reset, simultaneously, the scaler and the gate circuitry. The system could be readily adapted to high-temperature operation and can be operated remotely. In the prototype, 50-ft cables connect the cells to the monitoring instruments, and the cable length could be increased considerably without affecting the operation of the system. This system can be adapted to any small-tubing flow system provided a bubble of a gas which is compatible with the liquid and the tubing material can be made to fill the tube.

Ultrasonic Inspection of Welds

R. W. McClung E. A. Reed, Jr.

An important and difficult program has been initiated for the development of ultrasonic inspection techniques for the nondestructive evaluation of weld quality. The primary reason for the emphasis on the use of ultrasonics is the need for a reliable inspection technique which may be adapted for use in very intense radiation fields such as would be encountered in remote reactor maintenance problems.

Some of the early work has been accomplished on test plates of Inconel in which machined grooves have been cut. (These discontinuities are reflection surfaces and aid in gaining information concerning the behavior of ultrasound in metal plates.) One of the plates, which was $8 \times 6 \times \frac{1}{2}$ in., contained a narrow groove across the 6-in. width. This groove varied linearly in depth from the full plate thickness of $\frac{1}{2}$ in. on one side to 0 in. on the other side. With the discontinuity, the effects of the size of the ultrasound beam on the indicated signal were very readily observed. Figure 86 shows the amplitude of the reflected signal plotted against the average depth of the groove on which the sound beam is incident and reveals that for a $\frac{3}{4}$-in. sound beam the signal amplitude is a function of the groove depth up to the full depth of $\frac{1}{2}$ in. When

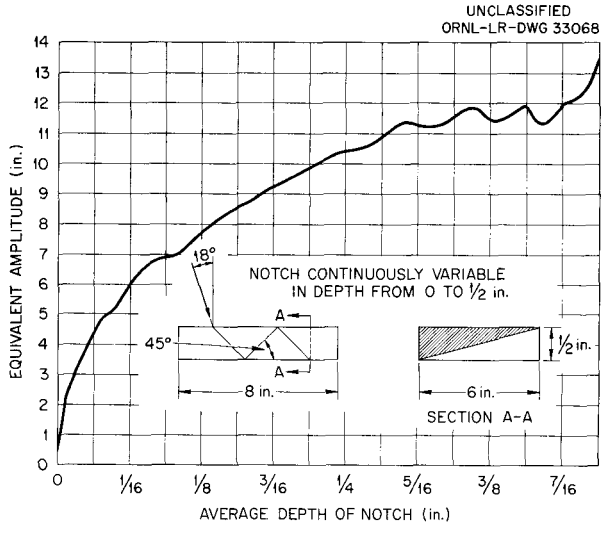

Fig. 86. Signal Amplitude from Varying-Depth Notch.

the ultrasound beam is collimated to $\frac{1}{4}$ in., other conditions being unchanged (Fig. 87), the amplitude rises until a depth of $\frac{3}{32}$ in. is reached; beyond this depth no difference in signal amplitude is noted. These considerations are very important to the proper interpretation of an ultrasonic inspection.

Another of the test plates contained three $\frac{1}{16}$-in.-deep grooves machined across the plate. These grooves intersected the major plate surface at angles of 90, 60, and 45°, respectively. A study was conducted to determine the relative amplitude of the returned signal from each of the grooves as a function of the incident angle when an immersed ultrasonic technique was used. In Fig. 88 a set of curves is shown which was obtained from this study. It may be noticed that the maxima of reflection occurred at slightly different angles for

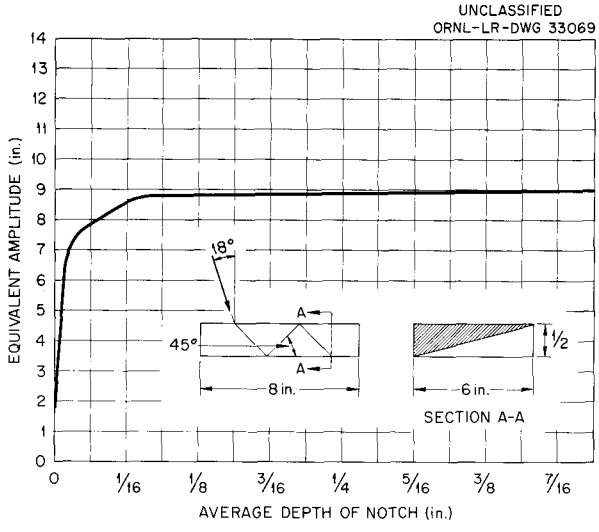

Fig. 87. Effect of Collimation on Signal Amplitude from Varying-Depth Notch.

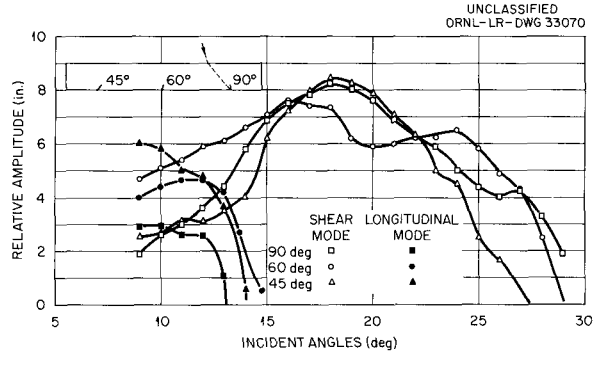

Fig. 88. Ultrasonic Reflections in Notched Plate.

the three grooves. It may be possible that this information could be utilized in an inspection situation to determine the orientation of a discontinuity and, subsequently, more about its identity.

Several welded plates, including both low-carbon steel and austenitic stainless steel materials, have been examined with a pulse-echo shear wave technique. One large 4-in.-thick low-carbon steel weld was evaluated with both longitudinal and shear wave techniques. Many discontinuities were detected by the ultrasonic method and later confirmed by sectioning the weld.

The major problem which was encountered in the austenitic stainless steel materials was the high attenuation of the ultrasound in the weld area. To gain further information about the attenuation differences along the weld bead, a through-transmission technique was used. This consisted in using a transducer to transmit ultrasound into and through the weld and a separate transducer to receive the signal which penetrated. The amplitude of the signal provided a partial evaluation of the attenuating properties of the weld. With this technique, much valuable information is being obtained about attenuation variations and about the effects of surface roughness of the welded specimen.

Ultrasonic Attenuation Studies[8]

J. K. White R. W. McClung
J. W. Allen

Metals which severely attenuate ultrasound represent a difficult testing problem and have been the subject of a recent investigation. Measurements with the Sperry attenuation comparator reveal that all stainless steel welds and castings tested attenuated ultrasound ten times more than the parent wrought metal when attenuation is expressed in decibels per microsecond. A carbon steel weld was found to be a far better transmitter of ultrasound than any of the stainless steel welds. The large losses in stainless steel welds and castings have been attributed to their characteristic large-grained structure. High attenuation in carbon steels can be reduced by a grain-refining heat treatment. In steels of similar grain size, evidence points to an association of low attenuation with hardness.

Probably the most important factor in attenuation at frequencies usually used for testing is Rayleigh scattering. Losses due to this phenomenon vary as the fourth power of frequency and as the cube of grain size. In Zircaloy-2 this seems to be the only important cause of ultrasonic attenuation in the low megacycle range. Steels which were tested showed an increase in attenuation with increasing frequency that was more rapid than the fourth power relation. The relation for steels took the form

$$\alpha = Ae^{\gamma F} ,$$

in which α is attenuation, F is frequency, and A and γ are constants. For HY-80 carbon steel the

[8] J. K. White, R. W. McClung, and J. W. Allen, "Implications of Ultrasonic Attenuation to Nondestructive Testing," *J. Soc. Non-destructive Testing* (to be published).

relationship was

$$\alpha = 0.04e^{0.08F}$$

Ultrasonic Inspection of Thin Sheet and Cladding

R. W. McClung

The detection of laminations in thin ($\frac{1}{4}$ in. or less) metal sections and the nondestructive evaluation of bond quality in clad structures are among the more difficult inspection problems.

A new technique is being developed for the inspection of thin metal sheets for laminar discontinuities and for the evaluation of thin metallic bonded sections such as may be encountered in flat-plate fuel elements. Inspections of this type have been accomplished by a conventional through-transmission technique in which one transducer is used exclusively as a transmitter for beaming ultrasound perpendicularly through the test object. A receiving transducer is mounted on the opposite side of the test plate to monitor the amplitude of the signal which passes through the plate. A loss in signal may then be interpreted as a discontinuity within the scanned plate. Obviously, the mechanical problems are increased by the use of two transducers and, in some instances, a complete installation must be designed for such an inspection. For these reasons, a technique was established for accomplishing the same inspection by using a single transducer and conventional scanning facilities. Figure 89 is a sketch of the inspection configuration. A single transducer is used to transmit an ultrasound beam perpendicularly at the plate. A portion of the sound is reflected at the test-plate surface, but some of it is transmitted through the plate and is reflected by an arbitrary reflecting surface. Part of this signal passes back through the test plate, is received by the single transducer, and is displayed on the CRO. Identification of the proper signal for monitoring may be made readily because of the time of arrival of the signal as displayed on the screen of the CRO. The amplitude variations of the signal are indicative of variations in the transmission properties of the sheet. A lamination will prevent the passage of the ultrasound, and its effect on the monitored signal will be proportional to the cross sectional area of the lamination as compared with the cross section of the ultrasound beam. Bond evaluations by this technique have been conducted with good results on several flat-plate fuel elements and on a 0.050-in.-thick stainless steel plate composed of two 0.025-in. layers bonded with nickel.

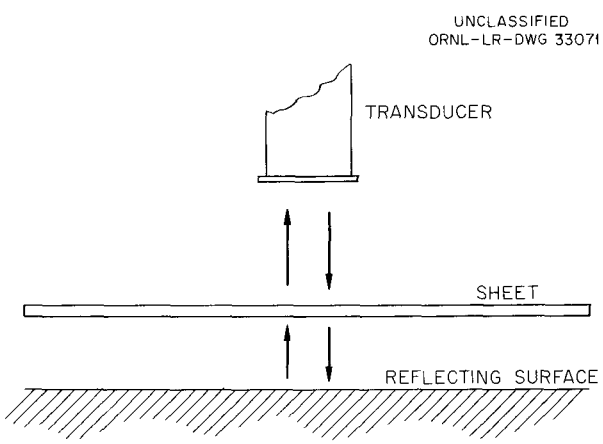

Fig. 89. Single-Transducer Through-Transmission Test.

Optimum transmission conditions are dependent upon the relation between the ultrasonic frequency and the thickness of the plate as a function of the wavelength of the sound in the plate. Calculations based on an optical analogy would predict maximum transmission at thicknesses equal to multiples of a half wavelength. Evidence indicates that this is a good first approximation.

A possible solution to these problems of thin-sheet inspection and non-bond detection in clad structures involves an ultrasonic phenomenon known as Lamb waves,[9] which are characteristic elastic vibrations established in a thin metal plate. The vibration has a frequency in the ultrasonic range, and the frequency, the plate thickness, and the mode of the vibrations are interrelated. Figure 90 is a graph of the possible modes of vibration in aluminum plate in which one coordinate is the product of the frequency and the plate thickness and the other coordinate is the phase velocity of the propagated wave. Both symmetric and asymmetric vibrations are included in this illustration, the symmetric modes consisting of those which have a vibration pattern symmetric about the median plane of the vibrating plate. Since these vibrations are characteristic of the frequency-thickness product and the phase velocity of the propagation, the possibility exists that appropriate modes may be used to make inspections on thin

[9] R. W. McClung, *ANP Quar. Prog. Rep. March 31, 1958*, ORNL-2517, p 49.

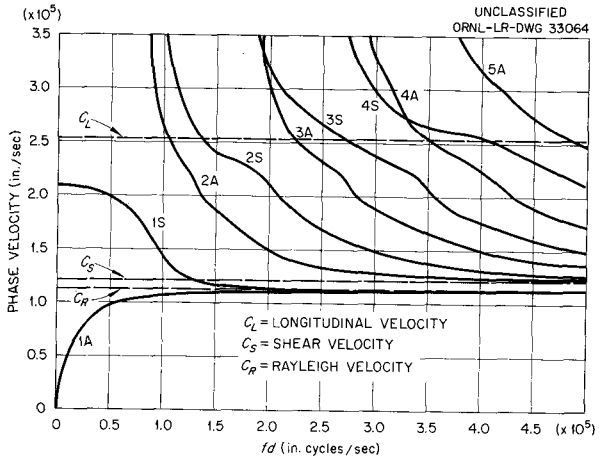

Fig. 90. Calculated Lamb Wave Curves for Aluminum Sheet.

materials wherein the apparent thickness may change due to bonding or lack of bonding or presence of laminations. For utilization of these proposed Lamb waves with an immersed ultrasonic technique, the phase velocity value may be converted to the incident angles of the ultrasonic wave which is exciting the mode of propagation by the relationship $\sin \theta = V_2/V_p$, where θ is the angle of incidence, V_2 is the velocity of propagation of the incident wave, and V_p is the phase velocity of the Lamb wave.

Some work has been accomplished in an attempt to generate and detect these propagated waves. This was done to determine the correlation between experimental data and the curves of Fig. 90, which were calculated from Lamb's original assumptions and equations. Preliminary results on this work appear quite promising, with general agreement being shown between experimental and calculated data. Further work is being done to gain familiarity with this new technique and to explore the avenues of approach for the generation and detection of Lamb waves.

A study of limited scope[10] resulted in the generation of single Lamb waves by use of one ultrasonic transducer for generating the wave, and another transducer was positioned to detect the propagated wave, as shown in Fig. 91. A versatile apparatus has been constructed to generate and detect Lamb waves by this method. The angular relationship of both the transmitter and receiver transducers may be varied independently. With this mechanism a very thorough evaluation of the nature of Lamb waves may be made. Work which has been accomplished with this method by using a single frequency on a thin aluminum sheet and varying the incident angles of the transmitter and receiver transducers demonstrates correlation with calculated data. Figure 92 is a typical curve which illustrates the relationship between the incident angle and received-signal amplitude for a given ultrasonic frequency and metal thickness. The peaks are indicative of the Lamb wave propagation. Some of this work has revealed discrepancies from calculated data which have not yet been explained.

Attempts have been made to transmit and receive these Lamb waves by other techniques so that more

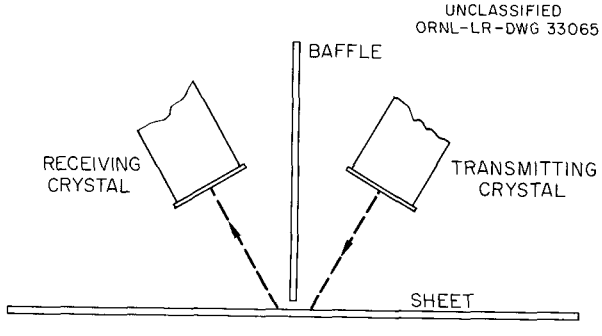

Fig. 91. Dual-Transducer Lamb Wave Propagation.

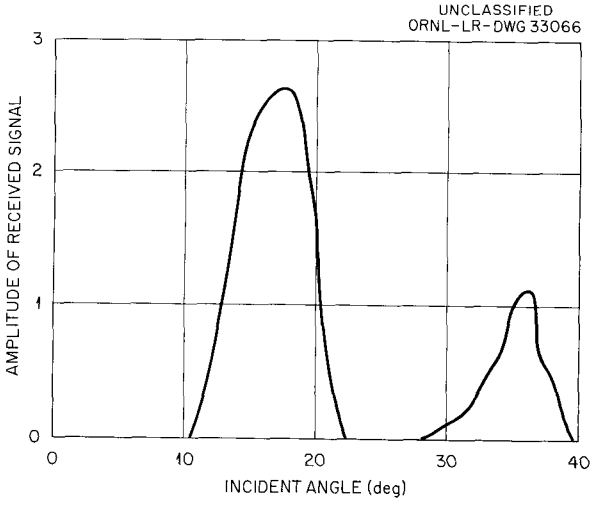

Fig. 92. Generation of Lamb Waves in Aluminum.

[10] D. C. Worlton, *Ultrasonic Testing with Lamb Waves*, HW-45649 (Sept. 25, 1956).

versatility may be available for future inspection techniques and so that more knowledge may be gained concerning the nature of Lamb waves. These different techniques, as shown by Fig. 93, consist in different arrangements of the transmitter and receiver and may involve the use of the same transducer as both generator and detector. Encouraging results have been obtained by these new techniques, but complete evaluation and correlation have not been completed. These new techniques will open new approaches for the resolution of many of the more difficult inspection problems involving thin metal sections.

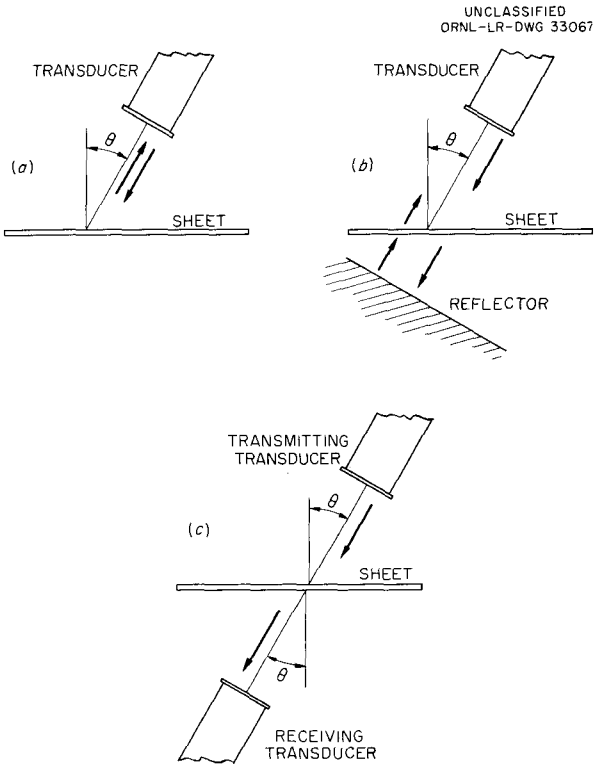

Fig. 93. Alternate Techniques for Lamb Wave Generation.

Bond Inspection of a Finned Heat Exchanger

R. W. McClung

A unique inspection technique was developed for the evaluation of the bond between a corrugated heat exchanger fin and the base channel structure. Figure 94 shows a representative section from the heat exchanger. As seen in the illustration, a finely collimated ultrasound beam was directed perpendicularly at the bonded seam. The heat exchanger section was immersed in water and the ribbed channel was filled with water. Precautions were taken to prevent water from entering the areas under the fin section, which are denoted as *A*. Thus, any nonbonded area would tend to be filled with air rather than water.

As the sound beam impinged upon bonded areas, multiple spiked reflections were obtained and displayed on the CRO as shown in Fig. 95. These signals are produced from the reflecting surface beyond the bonded interface and are detected because of the good transmission properties of the bond. In areas containing a lack of bond, a single, sharp indication from the fin surface was obtained, as illustrated in Fig. 96.

Duplex Tubing[11]

R. W. McClung

A program for developing adequate inspection methods for the evaluation of duplex tubing has been initiated. Of prime importance for heat exchanger application is the quality of the bond interface in each tube. Promising results have been

[11] R. W. McClung, *ANP Semiann. Prog. Rep. Sept. 30, 1958*, ORNL-2599 (in press).

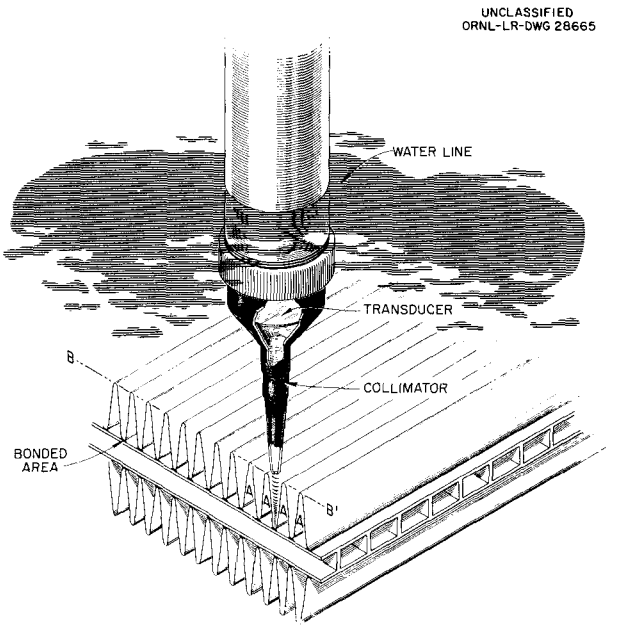

Fig. 94. Ultrasonic Nonbond Inspection of Heat Exchanger.

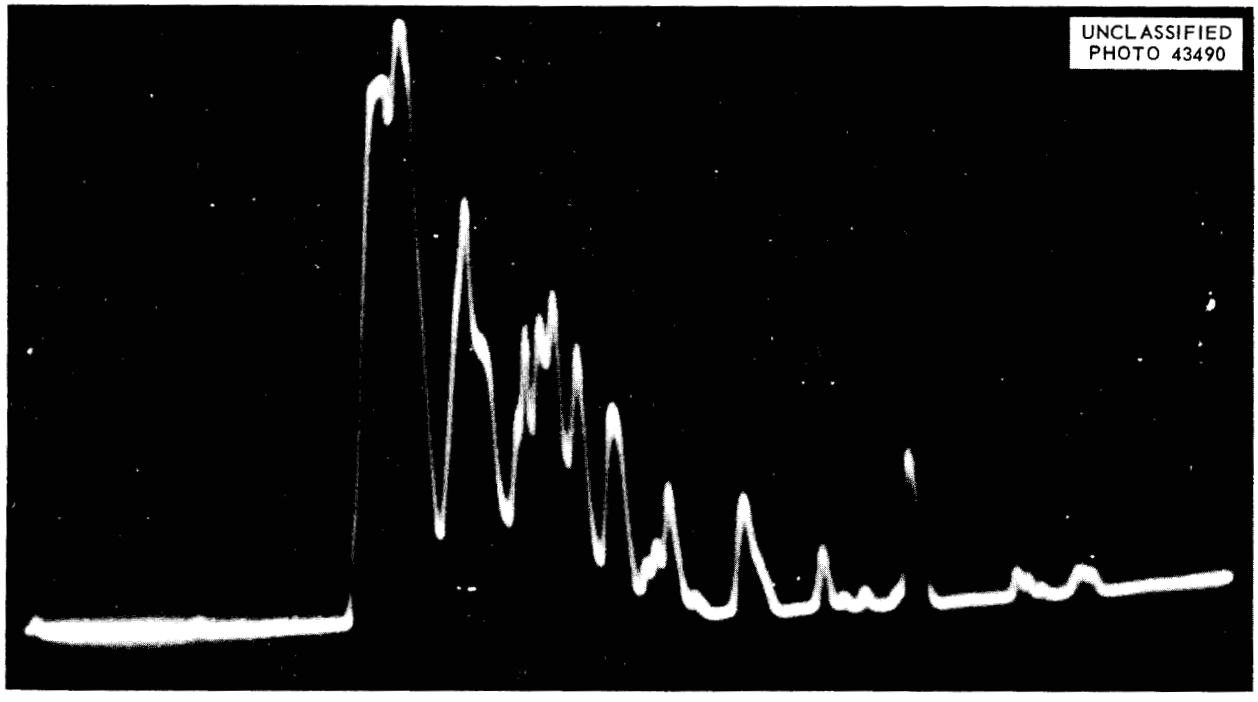

Fig. 95. Ultrasonic Indication from Bonded Area.

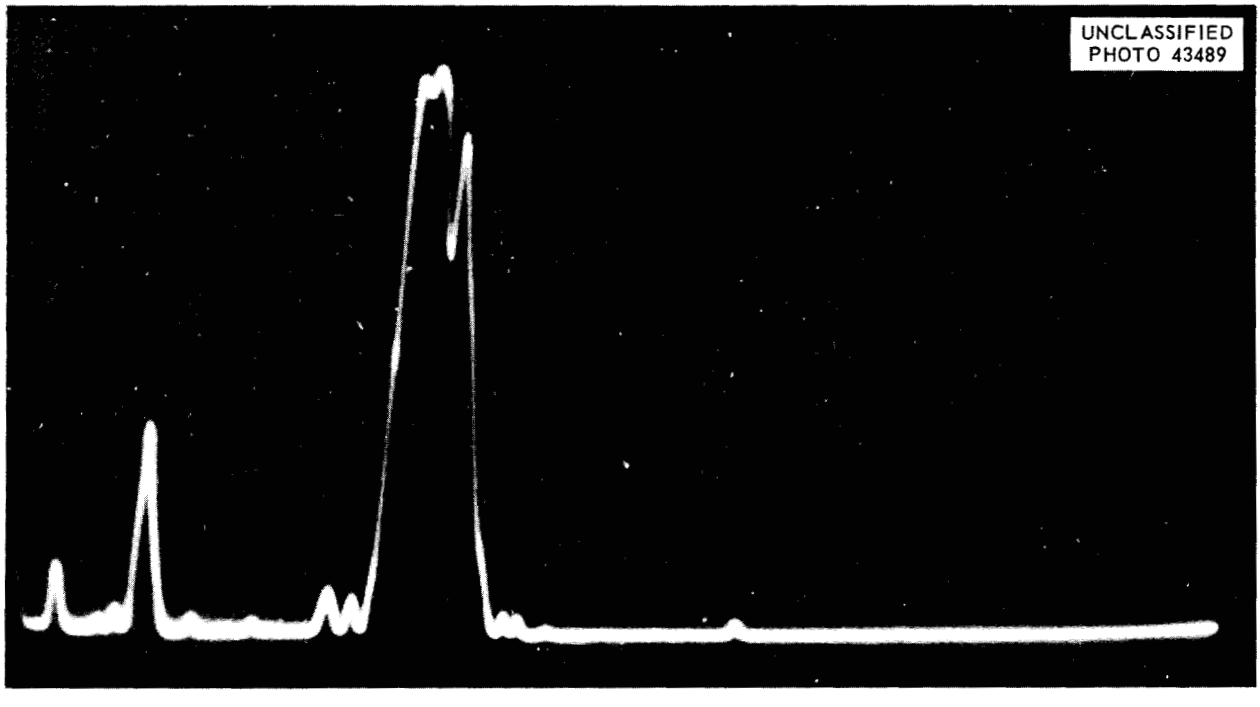

Fig. 96. Ultrasonic Indication from Nonbond Area.

obtained with the pulse-echo resonance ultrasonic techniques for the detection of nonbonded regions.

Material Evaluation

R. W. McClung J. W. Allen

Among the many nondestructive evaluations of material and parts were the following items:

INOR-8 Tubing. – Approximately 600 ft of ¼-in.-OD × 0.025-in.-wall tubing was completely inspected, and approximately 50 discrete discontinuities were detected, among which the most common were laminations.[12] Included in the evaluation of INOR-8 tubing have been several batches of ½-in.-OD × 0.045-in.-wall tubing. Some of this tubing was unique in that the common defect types were cracks on the inner surface.[13] These discontinuities were detected by ultrasonic techniques only.

Type 316 Stainless Steel Tubing. – An ultrasonic and fluorescent-penetrant inspection was conducted for the Nuclear Development Corporation of America on 240 ft of 2.75-in.-OD × 0.065-in.-wall type 316 stainless steel tubing. A few small discontinuities and thin-wall areas were noted by ultrasonics, and a few lap-like indications were noted with the fluorescent-penetrant inspection. These areas were marked, and the tubing was returned to NDA.

Columbium Billets. – Four columbium billets were inspected by immersed ultrasonic techniques. Two small discontinuities, estimated to be between 1/32 and 1/16 in. in diameter, were noted. Large attenuation differences were noted across the billet faces, the attenuation being lowest near the axis and increasing in the radial direction. This was attributed to the large grain size near the outer surface of each of the billets.

Thin-Wall Tubing. – Two short pieces of 1-in.-dia type 304 stainless steel tubing with nominal wall thicknesses of 0.002 in. and 0.004 in., respectively, have been inspected with liquid penetrants, ultrasonics, and radiography. Small clusters of pinholes were detected on the 0.002-in. tube. The most undesirable characteristics noted were the wall thickness variations, as noted in Fig. 97. By the use of special radiographic and densitometric techniques the excursions were measured to be as much as 50% from the nominal thickness.

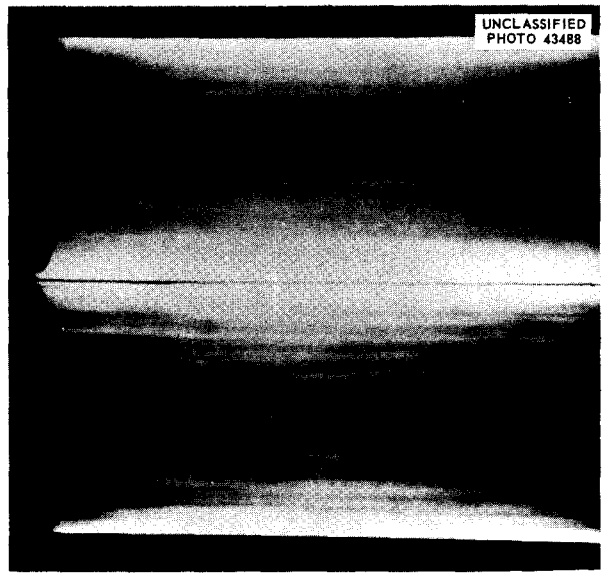

Fig. 97. Radiograph of Thin-Wall Tubing.

GCR-Type Tubing. – An evaluation was conducted on type 304 stainless steel tubing having diameters of 0.750, 0.800, and 1.00 in. and wall thicknesses of 0.005, 0.010, 0.015, and 0.020 in. These tubes had been supplied by four vendors. The fluorescent-penetrant inspection revealed the presence of pinholes in all the tubes. A few small discontinuities were noted by the pulse-echo ultrasonic technique. The major discrepancy was the variation in wall thickness, which exceeded the commercial tolerance of ±10%. Five of the twelve batches examined suffered total or partial rejection because of this. In addition, two of the batches were far in excess of the tolerance on straightness of 1 part in 600.

Columbium Tubing. – Approximately 170 ft of ½-in.-OD × 0.030-in.-wall columbium tubing has been evaluated by the pulse-echo and resonance ultrasonic techniques. Multiple cracking up to 0.001 in. deep was detected over most of the tubing on both inside and outside surfaces. In addition, many larger cracks with depths of 0.003 to 0.004 in. were noted on the outside surface.

Copper Tubing. – Several lengths of commercial-grade ⅜-in.-OD × 0.030-in.-wall and ⅜-in.-OD × 0.060-in.-wall tubing have been evaluated by pulse-echo ultrasonic techniques. Most of the tubing had long folds in the outside surface. Among the deepest were 0.007-in.-deep folds in the 0.060-in.-wall tubing and 0.005-in.-deep folds in the 0.030-in.-wall tubing. The average fold depth was less than 10% of the wall thickness.

[12] R. W. McClung, *Inspection of INOR-8 Tubing from Wallingford Steel Company*, ORNL CF-58-1-27 (Jan. 7, 1958).

[13] J. W. Allen *et al.*, *MSR Quar. Prog. Rep. June, 1958*, ORNL-2551, p 76–77.

MECHANICAL PROPERTIES

D. A. Douglas, Jr.

J. W. Woods
H. E. McCoy, Jr.
R. W. Swindeman
C. R. Kennedy

Most of the work in this group during the past year has been in connection with three reactor projects. In the case of the Gas-Cooled Reactor and the Molten-Salt Reactor, our primary purpose has been to obtain rather specific information to be used in the design of the various component parts. The efforts on the Aircraft Nuclear Propulsion Project, however, were directed toward a fundamental understanding of material behavior under the complex stress states imposed by service operation. The accomplishments in each of these activities are summarized.

Gas-Cooled Reactor

D. A. Douglas, Jr.

J. W. Woods H. E. McCoy, Jr.

One of the major factors influencing the economic feasibility of a gas-cooled reactor system is the fuel element. Therefore very careful consideration must be given to the choice of the fuel and the canning material. As an aid in the selection of the metal for the can, a literature survey was conducted on the strength properties of several alloys in the pertinent temperature range.[1] The ultimate choice of type 304 stainless steel was based on such factors as cost, fabricability, compatibility with the coolant and fuel, and high-temperature strength.

During assembly of the fuel element, pellets of UO_2 are inserted into a cylindrical can. The top of the can is then sealed by the welding of an end cap. This implies, of course, that there is clearance between the pellet and the can wall. The extent of the gap must be a compromise between an economical tolerance for production and the structural stability of the final assembly. This latter consideration is complicated by the fact that certain elements will have hot streaks along their length due to the configuration of the fuel element bundle. Since the primary purpose of the metal can is to contain the fission gases released during operation, the integrity of the can wall under the temperatures and pressures of operation is of the utmost importance. The initial investigation was conducted on cylinders at temperatures of 1600°F and higher.[2,3] The results indicated that the tube would collapse due to creep buckling. From these experiments it was concluded that buckling of the cans would occur at all temperatures where creep of type 304 stainless steel occurs. This prediction has been confirmed by tests at 1300°F which show that a 0.020-in.-wall tube will collapse by creep-buckling in about 2000 hr under a pressure differential of 300 psi.

The solution to this problem appears to lie in either of two directions. Specification of a maximum diametral clearance of 0.005 in. would permit only a uniform collapse of the wall before support by the UO_2 pellets would prevent further deformation. The close tolerance essential to this clearance would be rather difficult and expensive to achieve. In addition, those elements in which hot spots occur may still wrinkle during collapse, since the hot areas will deform more readily than the remainder of the cylinder. An alternate solution is to precollapse fuel elements (produced to commercial tolerances) under conditions of pressure and temperature which result in a uniform collapse. An investigation is currently under way to determine the feasibility of this method.

There are a number of other possible ways in which the container may fail. The most likely of these are summarized below:

1. a buildup of internal pressure in excess of external pressure due to the release of a large volume of fission gas; under this condition, failure can occur by creep in the tangential direction;
2. strain-fatigue failure as a result of thermal cycles;
3. buckling of the can wall in a very restricted area in such a manner that the ductility of the metal is exceeded and fracture occurs; this

[1] J. W. Woods, *Mechanical Properties of Materials for a Civilian Power Advanced-Type Gas-Cooled Reactor*, ORNL CF-57-11-10 (Nov. 14, 1957).

[2] *The ORNL Gas-Cooled Reactor*, ORNL-2500(Pt. 2), p 3.13–3.16 (April 1, 1955).

[3] *The ORNL Gas-Cooled Reactor; Materials and Hazards*, ORNL-2505 (Revised), p 12.9–12.21 (1958).

possibility exists if a portion of a supporting UO_2 pellet crumbles or if a space is left at the top of the element between the end cap and the MgO insulating material;

4. a stress-accelerated corrosion reaction between the impurities in the helium and the stainless steel; it is probable that there will be a variety of oxidizing and reducing conditions present at various stages of the reactor's operation, some of which may produce a grain-boundary attack which would contribute to failure.

Each of the above possibilities is presently being explored to determine how significant it might be in restricting the mechanical life of the fuel element.

Molten-Salt Power Reactor

D. A. Douglas, Jr. R. W. Swindeman

In the design of a power reactor that uses molten salt as a fuel carrier, one of the first problems that must be solved is the selection of an alloy sufficiently resistant to the corrosive action of the salt that a useful life of 20 years for the major components can be anticipated. No commercial alloys were found that possessed adequate fabricability, strength, and corrosion resistance. As a result, an alloy development program was carried out by the Metallurgy Division, and a composition (INOR-8) was found which seemed to possess the desired features.[4]

During the past year, extensive mechanical testing work has been conducted on commercial-size heats of this alloy. Tensile, yield, and moduli values were obtained from ambient temperature to 1600°F. In addition, relaxation and creep data[5,6] were obtained from 1100 to 1600°F.

One of the principal interests of the designer is in the maximum design stress allowable for service life of 10 to 20 years. The prediction of such values, based on the extrapolation of data from short-time tests, is a very necessary responsibility of the Mechanical Properties Laboratory. On the basis of a comprehensive survey of existing data, it appears that a reasonable estimate[7] of the stress which will produce 1.0% creep in 10,000 hr is 9500 psi. A comparable stress for type 316 stainless steel rod tested in air would be about 11,000 psi. It is quite possible that the accumulation of more data and the results of tests of longer duration will permit the predicted stress value for INOR-8 to be revised to one comparable to that for type 316 stainless steel.

Since so few data are available on the mechanical properties of INOR-8, a program is in progress to determine the reproducibility of the creep data both between tests and between heats. The reliability of the data appears to be very good, based on creep rates; however, some variation in rupture life does occur, principally as a result of variations in the elongation for fracture. Correlation of test data between Haynes Stellite and ORNL is excellent.[7] One very important conclusion can be drawn from the results of the test program to date. A comparison of tests in air with similar tests in fused salt indicates that no marked effect on the creep properties of INOR-8 occurs as a result of the fused-salt environment.

Aircraft Nuclear Propulsion

D. A. Douglas, Jr.

R. W. Swindeman C. R. Kennedy

In order to meet power and weight requirements, reactors for aircraft propulsion must operate at extremely high temperatures. All the conventional materials of construction lack adequate strength for operation at these temperatures, and thus attention has been focused on refractory-metal alloys and ceramics. Since very little is known of the mechanical properties of these materials, an investigation of creep and tensile properties is needed. Unfortunately, conventional test devices are unable to perform these tests, so that considerable equipment development is required before the actual testing program can begin. The apparatus currently used for these tests has been described in a recent report.[8]

There is increasing concern as to the accuracy of applying data obtained in the simple laboratory

---

[4] W. D. Manly *et al.*, *Proc. 2d Intern. Conf. Peaceful Uses Atomic Energy, Geneva, 1958*, paper 1990 (to be published).

[5] D. A. Douglas, *MSR Quar. Prog. Rep. June 30, 1958*, ORNL-2551, p 64–66.

[6] *Molten Salt Reactor Program Status Report*, ORNL CF-58-5-3 (May 1, 1958).

[7] R. W. Swindeman, *MSR Quar. Prog. Rep. Sept. 30, 1958*, ORNL-2626 (in press).

[8] D. A. Douglas, *ANP Semiann. Prog. Rep. Sept. 30, 1958*, ORNL-2599 (in press).

test to the complex states of stress and strain induced in service. Thus, one program being pursued in this laboratory is the comparison of creep properties obtained under a wide range of stress distributions. The ultimate goal is to establish creep and failure criteria relating the conventional uniaxial tests to service conditions. The progress in the past year has demonstrated that deformation rates obtained in multiaxial tests can be related to uniaxial rates for a wide range of stress distributions. However, no simple criterion for fracture has been discovered. The details of these experiments are documented in ORNL-2622.[9]

An additional service variable is produced by dynamic load conditions imposed thermally or mechanically. Many of these load reversals occur at relatively low frequencies, so that there is sufficient time for stress relaxation to occur. Therefore the stress state in such a situation is time dependent and does not provide a convenient parameter for study of the materials behavior. However, the strains induced during load reversals can be easily measured and, in general, provide a better concept of the metal's resistance to failure.

The University of Alabama, under subcontract No. 901, has been studying the strain fatigue of Inconel induced by thermal cycles, and at ORNL a similar series of tests using mechanically produced strains was performed.[10,11] In general, on the basis of the strain per cycle and the cycles to failure, thermal and mechanical fatigue can be related in a very simple manner. The relationship is structure dependent and is altered by such factors as grain size, ductility, and aging reaction. In the absence of metallurgical instabilities, it is not temperature dependent; therefore it is possible to correlate results of the thermal and mechanical strain-fatigue studies.

---

[9] C. R. Kennedy, W. O. Harms, and D. A. Douglas, *Multiaxial Creep Studies on Inconel at 1500°F*, ORNL-2622 (in press).

[10] C. K. Liu and W. D. Jordan, University of Alabama progress reports Nos. 1–12.

[11] R. W. Swindeman and D. A. Douglas, *The Failure of Structural Metals Subjected to Strain-Cycling Conditions*, ORNL-2619 (in press).

WELDING AND BRAZING

P. Patriarca

R. E. Clausing
E. A. Franco-Ferreira
R. G. Gilliland
A. E. Goldman
R. L. Heestand
A. P. Litman
G. M. Slaughter
J. W. Tackett

Gas-Cooled Reactor Program

Summary of Preliminary Investigations Relative to the ORNL Gas-Cooled Reactor (P. Patriarca, R. L. Heestand, and E. A. Franco-Ferreira). – In order to provide information and data pertinent to the ORNL Gas-Cooled Reactor study, preliminary investigations were conducted in the major fields of interest. The results of these studies are included in detailed form in ORNL-2500,[1] and are summarized briefly below:

Fuel Element Fabrication.[1] – A fuel-capsule assembly procedure was developed, and a typical seven-capsule element was fabricated. The construction of this element enabled Laboratory personnel to gain an appreciation of the required fabrication procedures and to determine the problems to which special attention should be devoted in future work.

Thirty industrial concerns were given the design parameters of the elements, along with several suggested methods of manufacture, and were asked to submit estimates of fabrication costs commensurate with their facilities and capabilities. The vendors' figures were compiled, and representative fuel element costs were determined. It was shown that the fuel element could be fabricated for $30.89 per kilogram of uranium.

Selection of Materials for Pressure Vessel.[2] – A literature survey was conducted and several industrial sources were consulted regarding field erection of a thick-walled 50-ft-dia pressure vessel. Although high-strength steels were given serious consideration, it was concluded that the choice of ASME SA212 grade B made to SA300 fine-grained practice represented the best possible compromise between the advantages and disadvantages inherent in the materials which were considered.

Beryllium Welding Studies[3] (R. L. Heestand). – A special isolated facility for the preparation and joining of beryllium was set up. The equipment consists of a large hood, two dry boxes for manual welding, one dry box for automatic welding, a manual hydraulic press, and other auxiliary equipment.

Initial studies consisted in the fusion welding of plugs into machined tubes for fuel-containment capsules. Leak-tight seals were made by using both the edge-fusion and the plug-type joint designs. However, attempts to butt-weld 0.040-in.-thick sheet material were unsuccessful unless a 700°F preheat temperature was used. No testing of welds for ductility or strength has been conducted to date.

Electron-Beam Welding (E. A. Franco-Ferreira). – A study was made to determine the applicability of electron-beam welding[4] to the fabrication of beryllium and other advanced reactor materials. A literature search was conducted and a survey of potential manufacturers was made; it was decided that the purchase of a laboratory model would be highly desirable. A purchase specification is being prepared for the apparatus, which consists primarily of an electron gun and the associated vacuum system.

Aircraft Nuclear Propulsion Program

Welding of Columbium (R. L. Heestand). – An investigation was initiated to study the characteristics and the corrosion resistance of columbium welds, both with and without the addition of filler metal.[5–7] Suitable welding dry-box equipment has been constructed or modified to permit the evaluation of welds made under carefully controlled conditions. Since weld metal deposited with columbium wire has been subject to corrosion and leaks

---

[1] *The ORNL Gas-Cooled Reactor*, ORNL-2500(Pt. 2), pp 4.4, 4.11–4.22 (April 1, 1958).

[2] *The ORNL Gas-Cooled Reactor*, ORNL-2500(Pt. 2), p 3.23–3.35 (April 1, 1958).

[3] *The ORNL Gas-Cooled Reactor; Advanced Concepts*, ORNL-2510, p 15.21–15.23 (Sept. 18, 1958).

[4] W. L. Wyman, *Welding J. (N.Y.)* 37(2), 49-s–53-s (1958).

[5] R. L. Heestand, *ANP Quar. Prog. Rep. Dec. 31, 1957*, ORNL-2440, p 160–66.

[6] R. L. Heestand, *ANP Quar. Prog. Rep. Sept. 30, 1958*, ORNL-2599 (in press).

[7] R. L. Heestand and E. E. Hoffman, *Welding of Niobium Progress Report No. 1*, ORNL-2423 (to be published).

in thermal-convection loops, other filler metal systems were also investigated. Wire of the 85% Zr–15% Cb composition exhibited good welding characteristics and possessed good corrosion resistance to lithium. Other filler metal compositions, including several columbium-base alloys, are also being studied.

High-Temperature Brazing Alloy Development (R. G. Gilliland and G. M. Slaughter). – Refractory-metal-base brazing alloys are being investigated for a high-temperature reactor application in which they would be exposed to lithium coolant.[8,9] A literature survey was conducted to determine which refractory metal binary systems possessed eutectics or minimums, and the most promising systems are under investigation. Vacuum-brazing equipment has been constructed, and the brazing characteristics and corrosion resistance of a large number of potential brazing alloys are being determined. A diffusion study has also been initiated for the purpose of effecting a rise in the remelt temperature of the brazing alloy, thereby increasing the maximum service temperature attainable.

Molten-Salt Power Reactor Program

Welding Studies on INOR-8[10–13] (G. M. Slaughter). Extensive tests have indicated that INOR-8 is readily weldable under conditions of high restraint. Several different heats of the material were studied, and only one (a high-boron heat) exhibited cracking. A procedure specification for the welding of INOR-8 tubing was developed, and several pump loops and related components have been fabricated from this material.[14] Mechanical property studies on INOR-8 weld metal have shown that it possesses excellent strength and ductility up to 1200°F, but that the average ductility at 1300°F and above is 10% or less. In an effort to increase this high-temperature ductility, the influences of carbon content and ingot melting practice are being investigated. Other filler metal compositions of interest to the program, such as those for joining dissimilar metals, are also being studied.

Component Fabrication (G. M. Slaughter). – Procedures applicable to the back-brazing of heat exchangers containing thick tube sheets are being studied. A special joint design[15] has been developed which prevents premature flow of the brazing alloy before the tube sheet has reached the brazing temperature. Studies of the materials problems associated with a cast-metal-sealed flanged joint were made;[16,17] this joint consists of a seal which is cast in place in an annulus provided to contain it. Preliminary wetting and diffusion tests of potential combinations of cast metals and base metals were made, and recommendations were made for the materials to be used in a large-scale seal test at Y-12.

Development programs are also under way to investigate the fabrication problems associated with bearing construction, with pump shaft construction, and with core-shell construction.

Sherwood Project Assistance

R. E. Clausing J. W. Tackett

The materials problems associated with the successful achievement of thermonuclear plasmas and ultimate thermonuclear power were reviewed, and the most urgent problems were selected for study. Special materials and techniques are required in order to achieve and maintain the ultrahigh vacuum required for the operation of many of the experimental devices. Ultrahigh vacuum apparatus must be baked at 400°C or higher to remove the last traces of absorbed gases; therefore conventional sealing techniques cannot be used, and new methods for making ultrahigh vacuum components must be devised. Also, the very high pumping speeds necessary for the successful operation of some experimental devices may be obtained only by very special techniques, several of which involve the absorption of gas particles by metals.

---

[8] G. M. Slaughter, *ANP Quar. Prog. Rep. March 31, 1958*, ORNL-2517, p 33–35.

[9] R. G. Gilliland and G. M. Slaughter, *ANP Semiann. Prog. Rep. Sept. 30, 1958*, ORNL-2599 (in press).

[10] G. M. Slaughter and P. Patriarca, *MSR Quar. Prog. Rep. Oct. 31, 1957*, ORNL-2431, pp 18, 21–28.

[11] G. M. Slaughter, *MSR Quar. Prog. Rep. Jan. 31, 1958*, ORNL-2474, p 65–72.

[12] *Molten Salt Reactor Progress Status Report*, ORNL CF-58-5-3, p 125–31 (May 1, 1958).

[13] P. Patriarca *et al.*, *MSR Quar. Prog. Rep. June 30, 1958*, ORNL-2551, pp 69–70, 73.

[14] G. M. Slaughter, *MSR Quar. Prog. Rep. Jan. 31, 1958*, ORNL-2474, p 73–75.

[15] R. L. Heestand, *ANP Quar. Prog. Rep. Dec. 31, 1957*, ORNL-2440, p 159–62.

[16] G. M. Slaughter, *MSR Quar. Prog. Rep. Jan. 31, 1958*, ORNL-2474, p 64–66.

[17] G. M. Slaughter, *MSR Quar. Prog. Rep. June 30, 1958*, ORNL-2551, pp 71–72, 74.

Experiments are under way to determine suitable methods of fabricating quick-disconnect seals for ultrahigh vacuum systems. Since the seal must be stable at temperatures up to 400°C, cast-metal and liquid-metal sealing materials are of particular interest. Prototype valve test assemblies have been constructed, and basic wetting and operational tests are under way. A program has also been initiated to determine the outgassing characteristics of various metals and to study means of obtaining high-purity vacuum atmospheres.

A large number of short-range studies were also conducted to provide information and assistance to the Sherwood Project. These included (1) fabrication assistance and failure analyses on a water-cooled copper DCX liner, (2) the fabrication of a large number of ceramic-to-metal seals, and (3) the degassing of several samples for the Geneva exhibit. In addition to the above research and developmental work, a great amount of service work and consultation has been done for the Thermonuclear Experimental Division. The bulk of this work involves the development of special techniques for joining or fabricating unusual combinations of metals, assistance in the proper selection of materials, and the use of equipment.

Merchant Ship Reactor Program

R. L. Heestand

End closures in fuel tubes for the N S "Savannah" core are scheduled to be manufactured by the edge-fusion welding of an inverted cup to the fuel tubes, the inert-gas tungsten-arc procedure being used. The weldability of this joint, as well as that of two plug-type closures, was investigated, with inspection of the joint a primary factor in the considerations. Typical brazed samples similar to the proposed fuel element design were also fabricated and evaluated, and the effects of overheating and underheating during brazing were determined. A more detailed summary of this work is presented by W. C. Thurber in another section of this report, "Process Metallurgy."

Welds joining type 304 stainless steel end caps to both boron-free and boronated (240 ppm) type 304 stainless steel were made. The joints were well inspected for defects by the dye-penetrant method, helium leak testing, radiography, and metallography. Welds produced with each type of closure were equally sound, and no difference in quality was noted between welds produced with the boronated and boron-free stainless steel. Radiographic inspection techniques were devised to provide for 90% weld inspection on a two-exposure basis or 100% inspection on a three-exposure basis, with a sensitivity of 2 to 3%.

Remote Welding

E. A. Franco-Ferreira

Activities have been centered mainly in two areas: a survey of the state of the art and a preliminary experimental program.[18,19]

The survey has consisted primarily of a determination of the level of advancement at other installations, including GE-ANP at Arco, Idaho; HAPO at Richland, Washington; the Savannah River Project; and the Westinghouse PAR Project. In addition, possible vendors of remote welding equipment have been contacted. These surveys enable the Welding and Brazing Laboratory to act in an advisory capacity to projects interested in remote welding.

The experimental program was designed to investigate the possible application of the inert-gas-shielded metal arc-welding process to remote welding situations. The work was aimed at the use of the process for the welding of titanium.[20] The results of the program appeared quite promising, and it might be said that the application of the process to remote welding would be advantageous.

Chemical Technology Division Liaison

A. E. Goldman A. P. Litman

Assistance was given to the Volatility Pilot Plant and its supporting groups in Chemical Development Section A and the Unit Operations Section in their efforts to reprocess spent reactor fuels by the hydrofluorination, fluorination, and volatilization of uranium.

---

[18] E. A. Franco-Ferreira, *An Investigation of the Applicability of Remote Welding to the Maintenance Requirements at ORNL*, ORNL CF-57-9-81 (Sept. 24, 1957).

[19] E. A. Franco-Ferreira, *Tentative Project Outline for Remote Welding and Inspection Development*, ORNL CF-57-12-6 (Dec. 3, 1957).

[20] E. A. Franco-Ferreira and P. Patriarca, *The Inert-Gas Shielded Metal-Arc Welding of Titanium*, ORNL-2612 (to be published).

A series of 30 internal memos were issued covering materials of construction, welding and brazing, corrosion, and failure analysis of fluorinators, hydrofluorinators, and associated equipment used by the above groups. In addition, all operational and construction drawings were reviewed, and materials were supplied for the fabrication of numerous vessels and corrosion test samples.

The results of corrosion testing, to date, indicate the most suitable materials of construction to be "L" nickel for the fluorinator and INOR-8 for the hydrofluorinator.

APPLIED METALLURGY

J. E. Cunningham

PROCESS METALLURGY

R. J. Beaver

C. F. Leitten
W. J. Kucera
J. H. Cherubini
E. C. Edgar[1]
W. C. Thurber
J. T. Lamartine
J. H. Erwin
D. T. Bourgette

ARMY PACKAGE POWER REACTOR (APPR) PROJECT

Procurement of Low-Cobalt Type 304L Stainless Steel

C. F. Leitten E. C. Edgar

Recent experience with core I of the Army Package Power Reactor (APPR-1) has indicated potential maintenance difficulty because of gamma activity buildup in the primary loop system. One of the major causes of this radiological hazard has been traced to $_{27}Co^{60}$, a long-lived transmutation product of $_{27}Co^{59}$, which is a tramp constituent in stainless steel. The concentration of cobalt in stainless steels normally ranges from 0.03 to 0.3 wt %; the cobalt content in the type 304L stainless steel which was employed in core I of the APPR is estimated to be 0.07 wt %. It was felt that this activity level could be substantially reduced in core II by simply specifying stainless steel fuel elements with a cobalt content of less than 0.006 wt %. The price of stainless steel with a guarantee of such a specification is exorbitant. However, by close cooperation with the vendor and careful selection of low-cobalt materials for charging the furnace, it was possible to produce a type 304L stainless steel containing 0.005 wt % Co. The steel heat was prepared by the Allegheny Ludlum Steel Corporation, Pittsburgh, Pennsylvania, and consisted of 16,000 lb of the charged material. A yield of 76% in plate, sheet, and usable scrap was realized from the charge materials at a cost of approximately $2.00 per pound of finished product.

The type and cobalt content of the various materials selected for preparing this heat of steel are itemized in Table 32. The composition of the finished product, based on the results of chemical analysis, is given in Table 33.

[1]Loanee from ALCO Products, Incorporated, Schenectady, New York.

Table 32. Type and Cobalt Content of Charge Materials for Preparing a Low-Cobalt Heat of Type 304L Stainless Steel Alloy

Charge Material	Weight Per Cent Cobalt
Armco iron	0.005
Mond nickel	0.0005
Electrolytic chromium	<0.001
High-purity ferrosilicon	0.002
Electrolytic manganese	<0.001
Iron ore	<0.001
Aluminum	<0.001
Fluorspar	<0.001
Limestone	<0.001
Periclase furnace lining	<0.001
Magdolite	<0.001

Table 33. Chemical Composition of Final Product

Element	Weight Per Cent
Cobalt	0.005
Carbon	0.018
Iron	68.2
Nickel	9.57
Chromium	18.70
Manganese	1.72
Silicon	0.82
Phosphorus	0.010
Sulfur	0.020
Copper	0.100
Tantalum	<0.001

Measurements of the mechanical properties of the 1-in.-thick plate stock revealed yield and tensile strengths of 34,000 and 83,000 psi, respectively, with a reduction in area of 80%. This compares favorably with commercially available type 304L stainless steel.

These results demonstrated that, by careful monitoring of the makeup materials, steels of this general type can be produced with a maximum cobalt content of 0.006 wt % at a cost which is not unreasonable.

Incorporation of Boron in Advanced Core Loadings for APPR-1

J. H. Cherubini

A desirable change in future core loadings of APPR-1 is to increase the boron concentration in the fuel-bearing section of the composite plate from 0.11 to approximately 0.25 wt %. To determine the effect of this increase in concentration on potential solid-state reactions and diffusion during fabrication of the stainless steel fuel plates,[2] B_4C, BN, ZrB_2, and a 0.25 wt % boron–stainless steel master alloy were investigated. Compacts containing varying amounts of boron, with a nominal concentration of 0.25% natural boron as a reference, were prepared by standard powder-metallurgy procedures. After enclosure in stainless steel frames and cover plates, the compacts were roll-clad at 1100, 1150, and 1200°C and heat-treated for 1, 2, and 3 hr at their respective fabrication temperatures.

Results of metallographic examination of the samples after treatment are summarized below:

1. Boron nitride shows a strong tendency to stringer during fabrication.
2. A solid-state reaction occurs between zirconium diboride and the type 304B stainless steel matrix. The degree of interaction is proportional to time and temperature.
3. After two 1-hr heat treatments at 1150°C, boron carbide will completely react with the matrix material to form complex carbides and borides with the elements in the stainless steel.
4. The interaction is manifested by the presence of a precipitate randomly dispersed in the stainless steel matrix. The precipitate is in the form of small globules and appears to be intermetallic in nature.
5. Similar reactions are observed with ZrB_2 and BN dispersions in stainless steel. No evidence of liquation or melting is found.
6. No positive sign of a molten phase was observed in any of the studies. Boron has a definite tendency to diffuse into the cladding from the type 304B stainless steel matrix. The nature and appearance of the precipitate are illustrated in Fig. 98. Migration appears to increase with increasing time and temperature.

Because of the inherent instability of the various boron-bearing compounds in contact with stainless steel at the elevated temperatures required for fabrication, an alternative solution to the problem was devised. It consisted in substituting boron enriched in the B^{10} isotope for the natural grade and incorporating it in the form of a stainless steel alloy, which would be more compatible with the stainless steel matrix. Calculations revealed that the desired B^{10} content could be obtained by adding to the type 304B stainless steel powder a sufficient quantity of a 0.25 wt % boron–stainless steel master alloy powder to obtain a stainless steel containing 0.045 wt % boron. Metallographic examination of composite plates containing such cores revealed an absence of the diffusion band observed with the boron compounds after similar heat treatments. However, additional data revealed very large boron losses during sintering of the cores under hydrogen.

Boron losses can be minimized by sintering either in an inert atmosphere or in a vacuum. The effect of the sintering atmosphere on recovery is shown in Table 34. The losses from the samples sintered in helium and in a vacuum appear to be within the limits of accuracy of the analytical procedures and, therefore, may not be true losses; hence, these initial results strongly indicate that a solution to the problem is imminent.

Development of Dispersions of Eu_2O_3 in Stainless Steel

C. F. Leitten

Dispersions containing 38 wt % Eu_2O_3 in stainless steel have been successfully prepared, and manufacturing specifications are being developed for the production of full-size absorber sections for core II of APPR-1. The previously reported reaction of Eu_2O_3 with prealloyed stainless steel

[2] R. J. Beaver, R. C. Waugh, and C. F. Leitten, *Specifications for Army Package Power Reactor (APPR-1) Fuel and Control Rod Components*, ORNL-2225 (July 24, 1958).

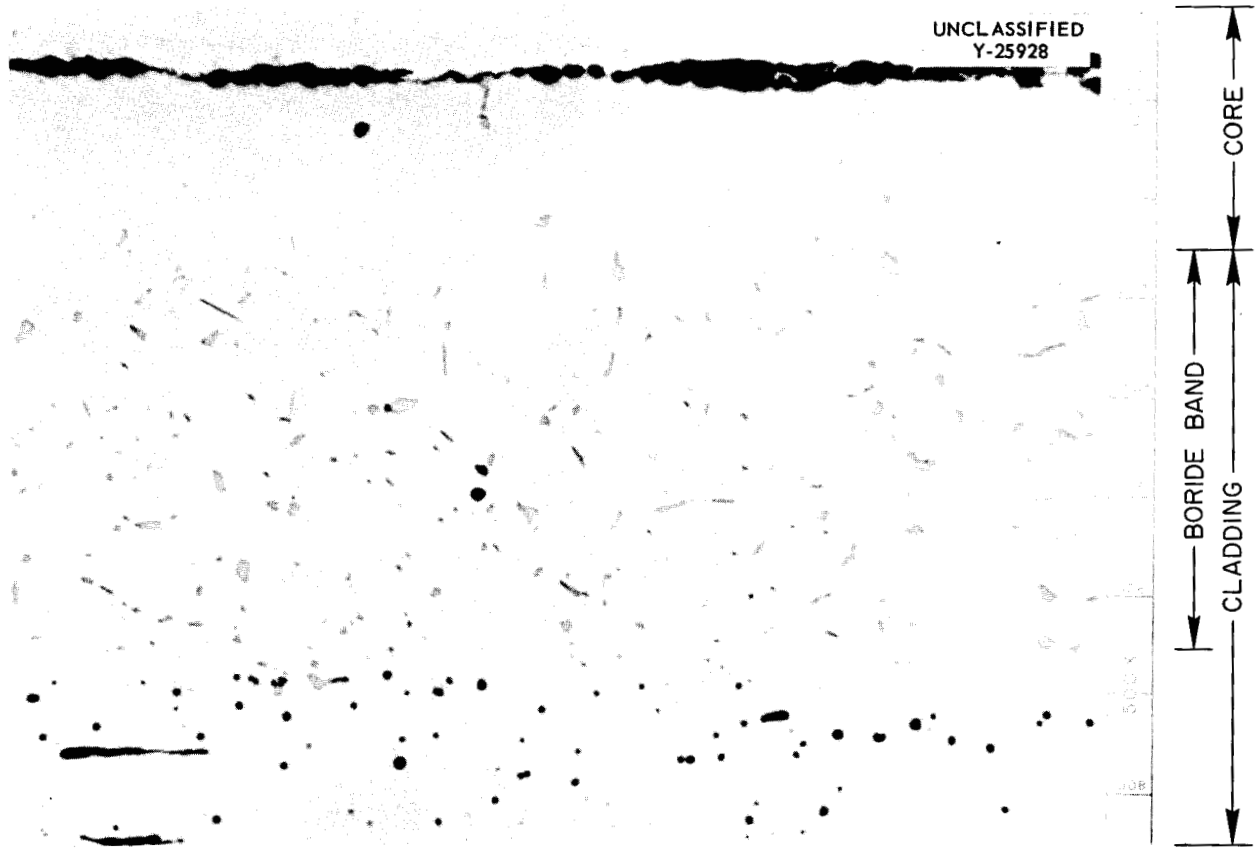

Fig. 98. Longitudinal Section of Composite APPR Fuel Plate Containing 0.25 wt % BN in Type 304B Stainless Steel Matrix, Showing Boron Diffusion into Wrought Type 304L Stainless Steel Cladding After 3 hr at 1150°C.

Table 34. Boron Losses in 0.04 wt % Boron–Stainless Steel Compacts Prepared with the 0.25 wt % Boron–Stainless Steel Master Alloy After Sintering 75 min at 1150°C

Experiment	Matrix Material	Sintering Atmosphere	Per Cent of Boron Lost*
1	304LB	Hydrogen	40
2	304LB	Hydrogen	24
3	304LB	Hydrogen	57
4	304LB	Hydrogen	39
5	304 LoSi	Hydrogen	50
6	304LB	Hydrogen	25
7	304LB	Vacuum	4
8	304LB	Helium	8
9	304LB	Vacuum	5

*Average of three samples.

powder[3] was traced to silicon in the stainless steel, and a specification of less than 0.03 wt % Si in the prealloyed stainless steel powder was established. Difficulties in the procurement of prealloyed stainless steel powder with such a low concentration of silicon led to the selection of low-silicon iron, nickel, and chromium powders (in the proportions found in type 304 stainless steel) as the matrix material.

Although small ½-in.-dia experimental compacts of the elemental powders together with 38 wt % Eu_2O_3 were stable at the 1230°C sintering temperature, difficulties were encountered in sintering the 2 × 2.25 × 0.3 in. compact required for full-scale composite plate. The problem was that a significant volume increase of the core during sintering made subsequent coining of the compact impossible without an intervening machining operation. Experimentation revealed that cold compacting under light pressure followed by sintering,

[3]C. F. Leitten, *Met. Ann. Prog. Rep. Oct. 10, 1957*, ORNL-2422, p 136–37.

coining, resintering, and recoining results in an acceptable compact. The steps in the selected process are listed below:

1. Cold-press the blended powders at 9.4 tsi to provide sufficient green strength for subsequent handling.
2. Sinter under hydrogen for 1½ hr at 1230°C.
3. Repress the sintered compacts at 31.4 tsi.
4. Resinter the compacts under hydrogen for 1½ hr at 1230°C.
5. Coin the compact under 31.4 tsi for final shaping and densification.

The "elemental" compacts prepared in this manner were found comparable in densification to prealloyed compacts manufactured by the previously established procedure.[3]

Miniature compacts of Eu_2O_3 in "elemental" type 304 stainless steel were fabricated into composite plate by roll bonding at 1150°C. Metallographic examination of the hot-rolled plates showed no indication of a reaction between the Eu_2O_3 and the "elemental" stainless steel; however, a reaction was observed between the Eu_2O_3 and the wrought stainless steel at both the cladding-core and core-frame interfaces. This interfacial reaction was prevented by encasing the compacts in stainless foil of low silicon content prior to fabrication.

Full-size plates were subsequently manufactured successfully by use of techniques described previously.[3]

MARITIME SHIP REACTOR PROJECT

Introduction

W. C. Thurber

In January 1958 a program was instituted in the Metallurgy Division for providing technical support and experimental assistance to the Maritime Reactors Branch (MRB) of the Atomic Energy Commission. A major portion of the effort to date has been concerned with the evaluation and proof testing of specific aspects of core I for the N S "Savannah," which is to be the first United States nuclear powered merchant ship. The prime contractor for the "Savannah" core is the Babcock & Wilcox Company, and the mission assigned to ORNL is solely to supply technical assistance to the MRB.

Materials development has been confined to (1) brazing, (2) welding, and (3) ceramic materials (see "Ceramics Research," this report).

Brazing Studies

J. T. Lamartine W. C. Thurber

The reference design for the N S "Savannah" fuel elements stipulates a 6 × 7 array of 6-ft-long × 0.500-in.-OD × 0.035-in.-wall type 304 stainless steel fuel tubes spaced by 1-in.-long hollow ferrules on an 8-in. pitch. The tubes are filled with slightly enriched UO_2 pellets sintered to 91% of theoretical density. Joining the ferrules and fuel tubes into an integral bundle is accomplished by brazing in hydrogen with Nicrobraz No. 50, a nickel-base alloy containing 13 wt % Cr and 10 wt % P.

A metallographic study was conducted to determine whether or not the Nicrobraz No. 50 would undercut the tube wall significantly and also whether or not extensive phosphorus diffusion from the braze metal would occur, with consequent impairment of the stainless steel. To implement this study, tube-to-ferrule joints were prepared by using the Nicrobraz No. 50–type 304 stainless steel combination and several brazing conditions listed as follows:

Sample No.	Brazing Conditions
1	980°C, ½ hr
2	1010°C, ½ hr
3	1010°C, ½ hr, cool, and rerun
4	1040°C, ½ hr
5	1065°C, ½ hr

No appreciable undercutting of the tube wall was observed in any of these samples. Evidence of the quality of the fillet on a typical sample can be seen in Fig. 99. Although the braze metal did not attack the tube wall, one defect – a hairline crack can be seen in the fillet. This condition emphasizes the brittle nature of this brazing alloy.

Microhardness traverses were made across the braze metal and adjacent base metal in each of these specimens to determine whether or not the properties of the stainless steel were affected. A typical traverse is indicated in Fig. 100. The

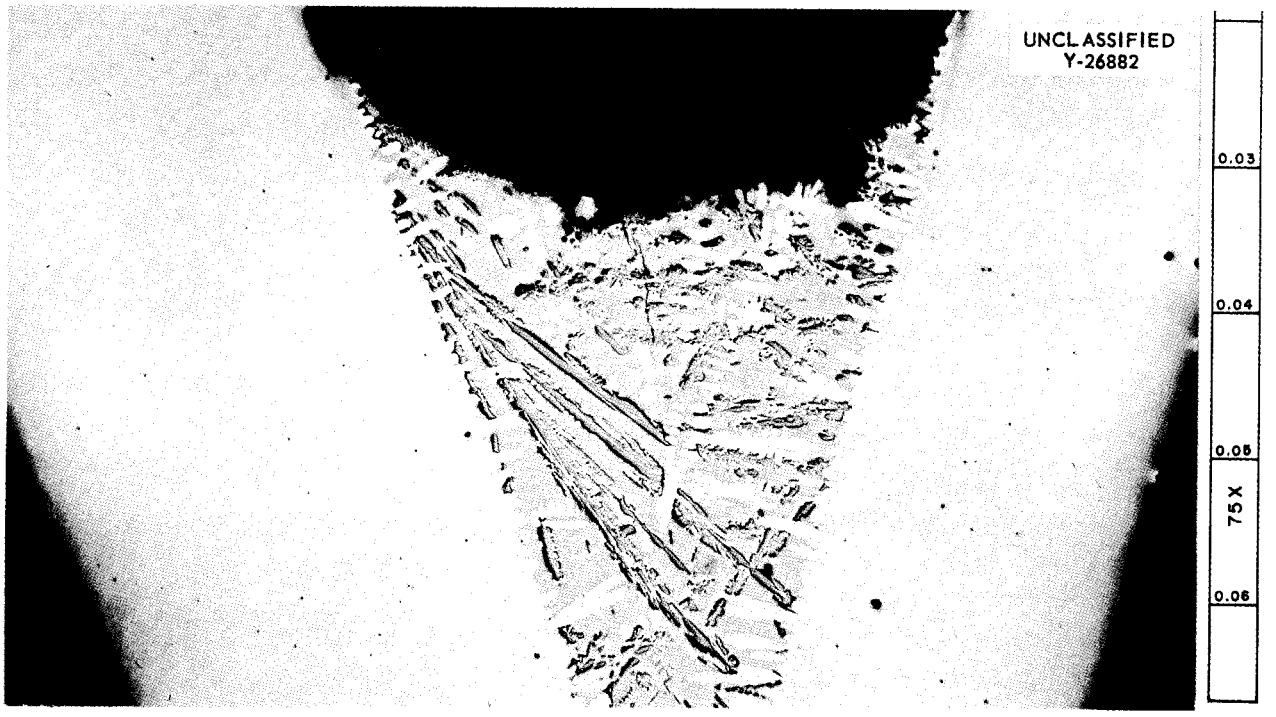

Fig. 99. Tube-to-Ferrule Joint Obtained with Nicrobraz 50 by Brazing in H_2 for $\frac{1}{2}$ hr at 1040°C. Note absence of undercutting of tube wall and hairline crack in braze fillet. As polished.

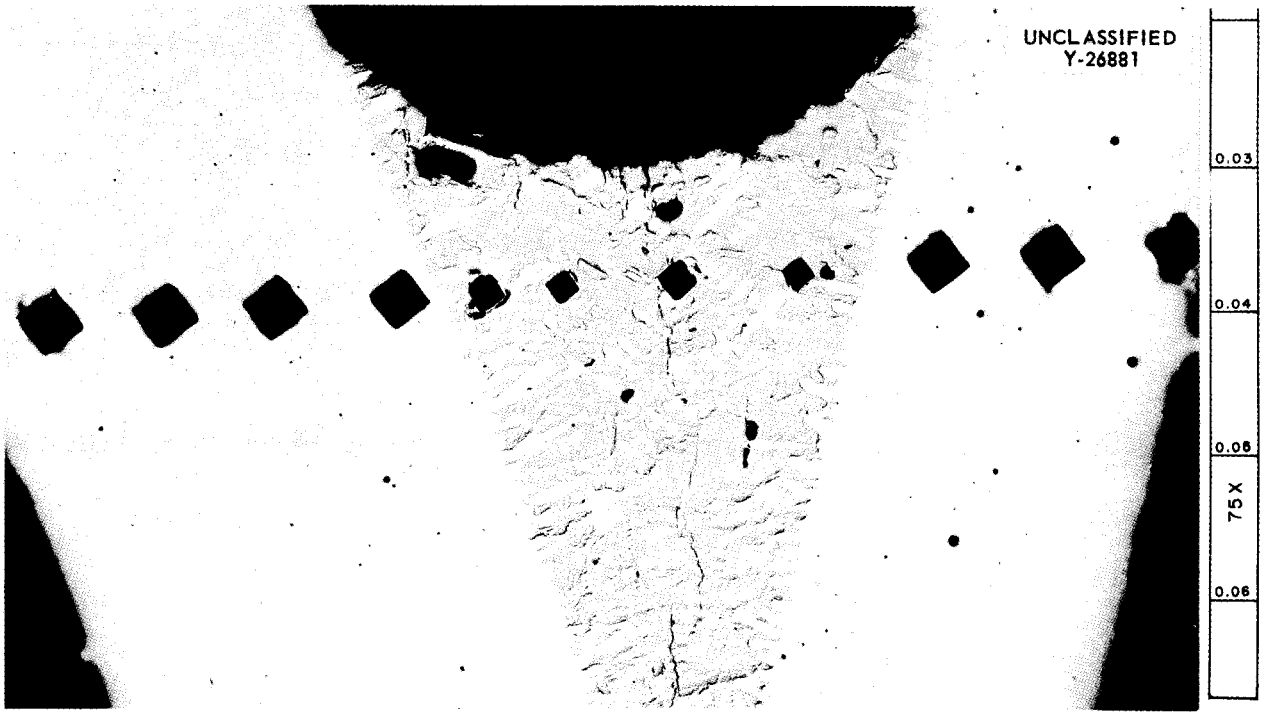

Fig. 100. Microhardness Traverse Across the Material Illustrated in Fig. 99. Refer to text for hardness values. As polished.

diamond pyramid hardness numbers associated with this traverse from right to left were:

Location	Diamond Pyramid Hardness
1	145
2	143
3	148
4	159
5	533
6	599
7	401
8	660
9	165
10	153
11	151
Base Metal (opposite braze joint)	150

The data indicate that the mechanical properties of the base metal are essentially unaffected by the conditions investigated.

A semiquantitative test was also devised for evaluating the shear strength of joints brazed under the described conditions. The testing rig and specimen are shown in Fig. 101. This test was intended for evaluating effects which might stem from differences in total expansion of various fuel tubes operating at different temperatures; results are summarized in Table 35. These data indicate that a rerun of the brazing cycle exerts no deleterious effects on the strength of the brazed joints (tests 2 and 3) and that loads of 900 to 1300 lb are required to initiate failure in reference joints (tests 4 and 5).

The reference design for NMSR fuel tubes may require type 304 stainless steel containing 300 ppm natural boron. It is possible that some deboronization could occur during the brazing operation required for assembling the tubes into fuel bundles.[4] In order to investigate this possibility, approximately 30 ft of boronated type 304 stainless steel tubing of the reference design was obtained from the Babcock & Wilcox Company for heat-treating studies. Samples from two 6-ft lengths of this tubing were analyzed by wet chemistry techniques, and results on each tube indicated 240 ppm boron. The accuracy of this analysis is estimated to be ±10%.

[4] J. C. Shyne and E. R. Morgan, *Metals Progr.* 65(6), 88 (1954).

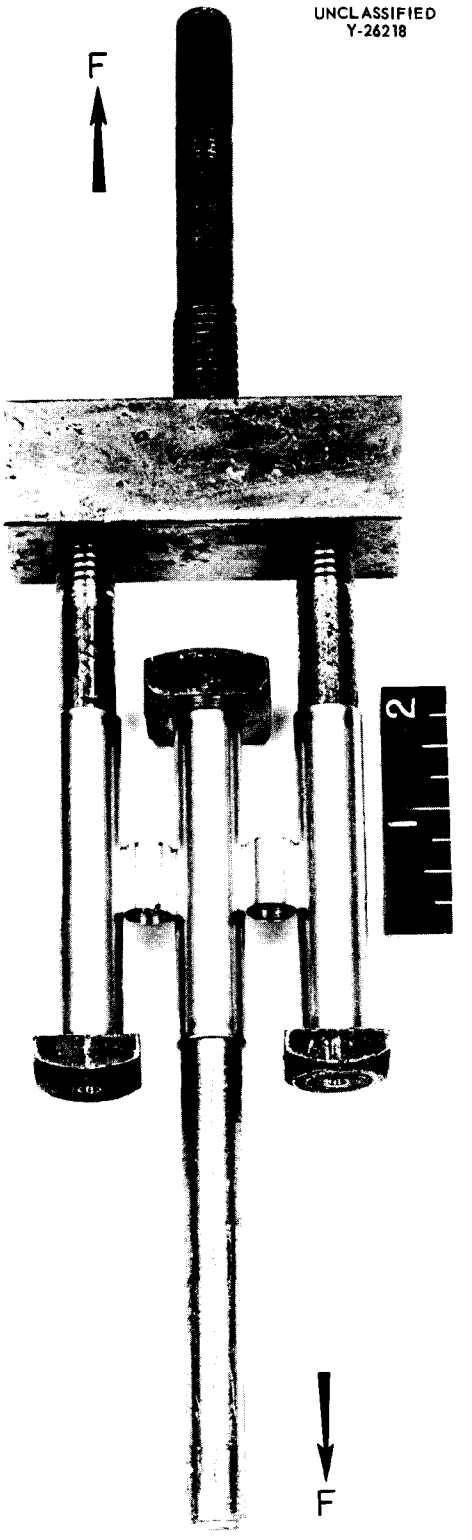

Fig. 101. Shear Test Rig for Brazed Joints.

To determine the effect of temperature and atmosphere on the extent of deboronization, samples of tubing were held at 1010, 1065, 1120, and 1175°C for 1 hr in atmospheres of dry hydrogen, wet hydrogen, argon, and vacuum and then analyzed for boron. The results of this study are summarized in Table 36. These data represent single determinations under each condition.

The analytical results listed in Table 36 are limited, but give strong indications that:

1. No deboronization occurs at 1010°C in any of the atmospheres investigated.
2. No deboronization occurs in vacuum or argon in the temperature range 1010 to 1175°C.
3. Significant boron losses occur in the hydrogen atmospheres at temperatures of 1065°C and higher, the losses increasing with temperature.
4. In hydrogen atmospheres, boron losses appear to increase with moisture content of the hydrogen.

FUEL ELEMENT DEVELOPMENT

Application of 20%-Enriched Uranium for Plate-Type Aluminum Research-Reactor Fuel Elements

R. J. Beaver

The objective of this investigation has been to develop and ultimately select a materials combination considered optimum for aluminum plate-type fuel elements requiring 20%-enriched uranium. The systems considered have been (1) uranium-aluminum alloys, (2) uranium-silicon-aluminum alloys, and dispersions of (3) UO_2 in aluminum,

Table 35. Strength of Joints Brazed with Nicrobraz No. 50 in Hydrogen

Test	Number of Specimens	Ferrule Size*	Tube Material	Brazing Cycle	Average Failure Load (lb)
1	6	10-mil wall, ½ in. long	304 SS	½ hr at 1010°C	240
2	6	15-mil wall, ½ in. long	304 SS	½ hr at 1010°C	280
3	5	15-mil wall, ½ in. long	304 SS	½ hr at 1010°C cool and repeat	260
4	4	20-mil wall, 1 in. long	304 SS	½ hr at 1010°C	1330
5	5	20-mil wall, 1 in. long	304 SS with 330 ppm B	½ hr at 1010°C	880

*Ferrule material, 304 SS.

Table 36. Deboronization of Stainless Steel Tubing

Temperature (°F)	Boron Content (ppm) After Treatment*			
	Dry Hydrogen (dew point, −95°F)	Wet Hydrogen (dew point, −40°F)	Vacuum (less than 1 in.)	Argon (dew point, +6°F)
1840	250	231	275	254
1950	197	127	260	262
2050	180	153	210	266
2150	115	39	270	266

*Initial boron content, 240 ± 24 ppm.

(4) U_3O_8 in aluminum, and (5) uranium carbides in aluminum.

It was demonstrated that U-Al alloys in the range of 35 to 50 wt % U were not entirely acceptable because of inherent fabrication difficulties.[5] Yet, by substitution of 3 wt % of silicon, it was possible to completely suppress the formation of the intermetallic compound UAl_4, thus changing the alloy structure to one containing the intermetallic UAl_3 in the eutectic.[6] The significantly smaller volume of the intermetallic compound markedly decreased fabrication difficulties and increased the reliability of fuel element manufacturing as well as of the reactor performance.[7] In addition to the MTR loading of elements of this type manufactured by the Babcock & Wilcox Company, Lynchburg, Virginia, miniature specimens containing the 48% U–3% Si–Al alloy were prepared at ORNL and are presently under irradiation in the MTR.

Because of the high density of uranium carbides and the resulting lower volume occupied by the fissile material, an extensive investigation of dispersions of these fuel compounds in aluminum was made.[8] The investigation revealed that (1) uranium dicarbide is a superior selection as compared with uranium monocarbide, (2) vacuum degasification of the powder-metallurgy compact is required in order to avoid blistering in subsequently fabricated and heat-treated composite plate, (3) fuel elements can be manufactured with little difficulty, and (4) in the event of a cladding defect, the fuel dispersion will corrode catastrophically in water at 60 to 100°C.

Experimentation with dispersions of oxides of uranium, UO_2 and U_3O_8, in aluminum have included compatibility as well as fabrication studies. The compatibility studies are discussed in detail by R. C. Waugh in another section of this report ("Advanced Engineering and Development of Reactor Materials"). Emphasis on the UO_2-Al system has been primarily on reaction mechanism and compatibility studies because of the previously reported reaction of UO_2 with aluminum at 600°C.[9] Although compatibility studies of the U_3O_8-Al system have been conducted, the major effort has been directed at establishing fabrication conditions and developing manufacturing specifications. Of the two systems, the U_3O_8-Al combination is the more attractive, particularly when the fuel elements are to be joined by brazing. A fuel element containing this dispersion has been produced and delivered to the MTR for performance testing in the active lattice of the MTR.

Fuel Element Fabrication of Dispersions of U_3O_8 in Aluminum

C. F. Leitten W. J. Kucera

The objective of the present study is to demonstrate the feasibility of U_3O_8 as a dispersed fuel in plate-type aluminum fuel elements manufactured according to conventional processing by roll cladding and brazing. Preparation of the fuel core was originally confined to simple dry blending of −100 +325 mesh U_3O_8 powder and −100 mesh aluminum powder and cold compacting under 33 tsi into the desired core size. Composite alclad fuel plates were metallurgically bonded by roll cladding at 600°C after a total hot reduction of 92% in the thickness. It was observed that this type of composite had very little tendency to blister during subsequent elevated-temperature treatments prior to joining the plates into an array by brazing. Thus, with this materials combination it is possible to completely eliminate the undesirable flux-annealing treatment which is required for composites containing air-induction-melted U-Al alloys.

Original investigations were directed at dispersions of 45 vol % of U_3O_8 in aluminum; however, this high-volume-percentage dispersion exhibited a marked tendency to segregate, and reproducibility of plate homogeneity was not possible. Decreasing the volume occupied by the fissile compound to 37% solved the problem and resulted in reproducible plate homogeneity.

---

[5] W. C. Thurber, J. H. Erwin, and R. J. Beaver, *The Application of a Nominal 48 wt % U–Al Alloy to Plate-Type Aluminum Research Reactor Fuel Elements*, ORNL-2351 (Feb. 25, 1958).

[6] W. C. Thurber and R. J. Beaver, *Development of Silicon Modified 48 wt % U–Al Alloys for Aluminum Plate-Type Fuel Element*, ORNL-2602 (to be published).

[7] D. R. deBoisblanc and R. S. Marsden, *Preliminary Evaluation of the 20% Enriched Uranium Core for the Materials Testing Reactor*, IDO-16459 (June 3, 1958).

[8] W. C. Thurber and R. J. Beaver, *Dispersions of Uranium Carbides in Aluminum for Plate-Type Research Reactor Fuel Elements*, ORNL-2618 (to be published).

[9] J. E. Cunningham *et al.*, *Fuel Dispersions in Aluminum-Base Fuel Elements for Research Reactors*, TID-7546, p 269–97 (March 1958).

One of the major problems in the fabrication of roll-clad composites is the spalling of the fuel-bearing compact, which causes particles of U_3O_8 to be trapped between the frame and the core plate. The result is an erratic stringering of U_3O_8 particles beyond the fuel portion of the plate, because of which the fuel may be exposed to the coolant at the end of the finished fuel plate. Reduction in this tendency to spall was possible by sintering the cold-pressed compacts in air at 400°C.

Although some difficulty has been observed because of slight warpage of plates during the conventional furnace brazing process used in joining the plates into a fuel element, the problem is not considered insurmountable. Test elements containing 20%-enriched uranium incorporated as a 37 vol % dispersion of U_3O_8 in aluminum have been successfully made. One such element is presently operating in the active lattice of the MTR with no reported difficulty after two MTR cycles.

Development of High-Strength Aluminum Fuel Elements

J. H. Erwin

The operation of aluminum ORR-type fuel elements is limited by their ability to withstand differential pressures developed at high cooling-water flow rates within the reactor core. The strength of an aluminum fuel element may be increased by adding additional metal to the external fuel plates and the supporting side plates, as in the present mark XI design, or may be increased by substituting stronger aluminum for the present dead-soft type 1100 material. An addition of metal would be at the expense of the metal-to-water ratio; therefore, a substitution of higher-strength aluminum appears to be more desirable. A number of fuel elements containing depleted uranium core material were fabricated by use of types 5050, 6061, and 6951 cladding and side-plate aluminum and subjected to pressure tests in comparison with the standard mark XI MTR fuel element. These tests were conducted by applying air pressure on the inside of the element, and data were obtained by measuring the deflection and permanent set of the outer plates.

The data presented for high-strength aluminum fuel elements in which the thickness of the fuel plates was reduced to 45 mils and the side-plate thickness decreased to $\frac{1}{8}$ in. is an example of improvements which may be accomplished in fuel element design. As is shown in Fig. 102, a differential pressure of 14 psi applied to the standard mark XI fuel element causes a permanent set of 12 mils, which is considered the permissible maximum. On the same basis, the high-strength fuel element withstood a differential of 21 psi. The substitution of an element of this design permits an increase of 5% in fuel loading and a 23% improvement in the metal-to-water ratio as compared with the mark XI design.

The advantages of the higher-strength elements are also apparent in Fig. 103, which shows the deflection of the plates as a function of differential pressure.

The fuel element designated FRD-19 contains a 48 wt % U–Al alloy "meat." The additional resistance to pressure differentials is a result of the high strength of this fuel alloy.

Development of Mechanically Joined Plate-Type Aluminum Fuel Elements

J. H. Erwin

Sections of both curved- and flat-plate aluminum fuel elements were assembled by mechanically joining the fuel-bearing aluminum plates to the supporting spacer side plates. The inactive edge of the fuel plate is provided with a partial dovetail joint, which, as shown in Fig. 104, is locked into the side plate when pressure is applied across the side-plate width. Joint strength of dead-soft aluminum prepared in this manner is approximately 200 lb per inch of joint.

The pressure applied to the edge of the side plate is transmitted throughout the width of the side plate as deformation takes place. This action distributes the locking force over all the plates in the fuel unit. The side plate is increased in thickness to prevent buckling, but can be slab milled to the thickness stipulated in fuel element specifications.

Investigation of Uranium Contamination in Reactor Cooling Water from Aluminum Research-Reactor Fuel Elements

J. H. Erwin

Data presented by Moeller and Leddicotte[10] indicated that a possible source of uranium contamination in the LITR cooling water was uranium on

[10] D. W. Moeller and G. W. Leddicotte, *Source of Fission Products in LITR Cooling Water*, ORNL CF-57-3-120 (March 26, 1957).

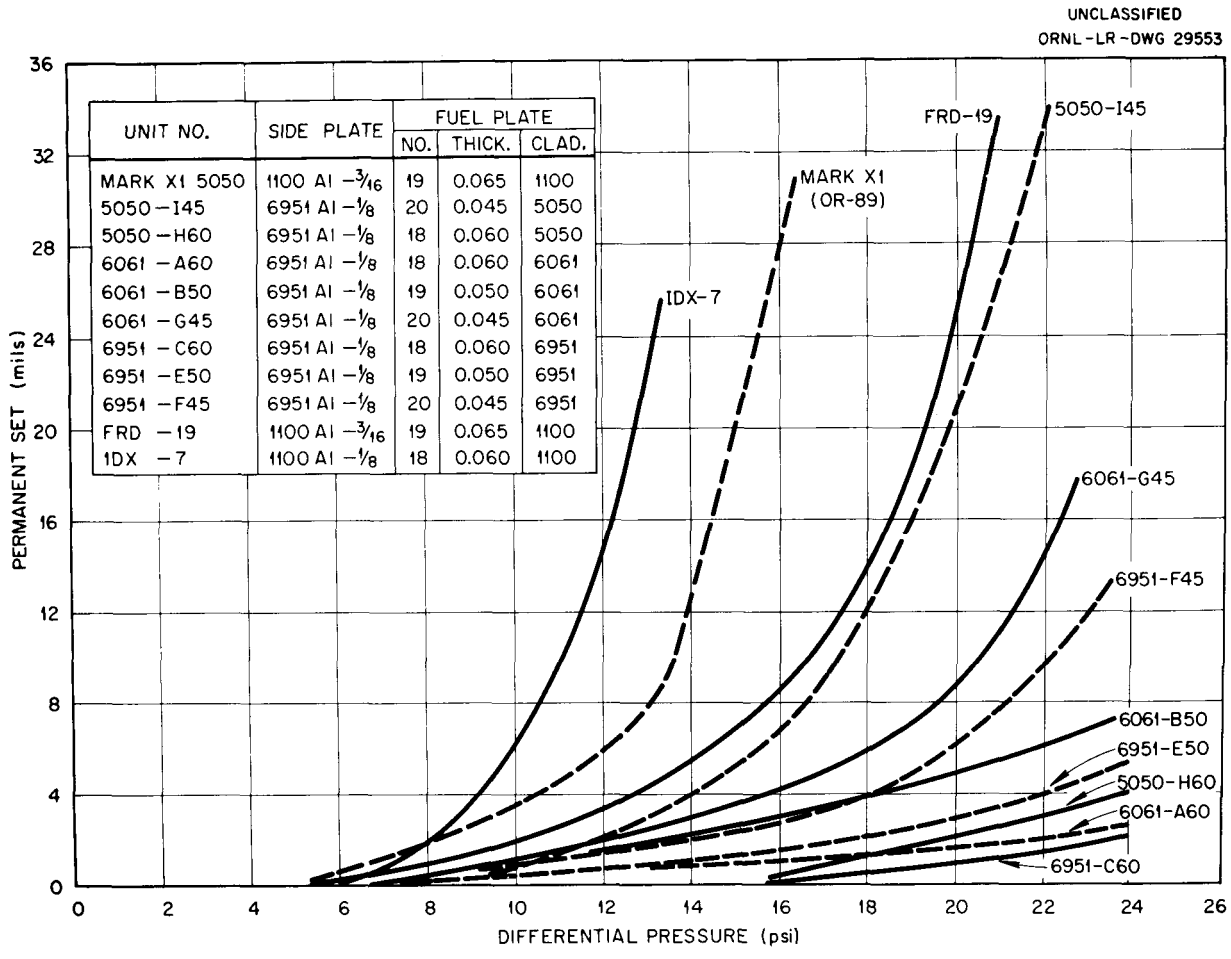

UNIT NO.	SIDE PLATE	FUEL PLATE NO.	FUEL PLATE THICK.	FUEL PLATE CLAD.
MARK X1 5050	1100 Al $-\frac{3}{16}$	19	0.065	1100
5050-I45	6951 Al $-\frac{1}{8}$	20	0.045	5050
5050-H60	6951 Al $-\frac{1}{8}$	18	0.060	5050
6061-A60	6951 Al $-\frac{1}{8}$	18	0.060	6061
6061-B50	6951 Al $-\frac{1}{8}$	19	0.050	6061
6061-G45	6951 Al $-\frac{1}{8}$	20	0.045	6061
6951-C60	6951 Al $-\frac{1}{8}$	18	0.060	6951
6951-E50	6951 Al $-\frac{1}{8}$	19	0.050	6951
6951-F45	6951 Al $-\frac{1}{8}$	20	0.045	6951
FRD-19	1100 Al $-\frac{3}{16}$	19	0.065	1100
IDX-7	1100 Al $-\frac{1}{8}$	18	0.060	1100

Fig. 102. Permanent Set of Top and Bottom Plates of Brazed Curved-Plate Aluminum Fuel Elements After Designated Differential Air Pressurization. Age-hardening alloys solution-treated, air-quenched, and aged.

the surfaces of the fuel element. To investigate this problem, samples have been removed from the surfaces of composite fuel plates, as well as from solid aluminum plates at each step in the conventional fabrication process,[11] in order to determine (1) the extent and source of contamination and (2) the action required to reduce the contamination to an acceptable limit. The uranium in the aluminum samples was determined by neutron activation analysis. The results are tabulated in Table 37.

The values listed for fabricated fuel composites represent the average of data which had significant scatter, and the results are considered preliminary in nature. However, a definite trend can be observed, particularly in the results for fuel plates rolled through a 2-high mill generally used for breakdown of uranium-aluminum alloy billets, as compared with composites rolled through a relatively clean mill. It is, therefore, recommended that (1) composite plates be rolled through non-contaminated rolls and (2) after final cleaning, the completed fuel element be sealed within a container to prevent recontamination of the fuel element surface from air-borne alpha particles.

As is shown, the concentration of U^{235} in the aluminum stock appears to be 0.002 ppm.

[11] J. E. Cunningham and E. J. Boyle, *Proc. Intern. Conf. Peaceful Uses Atomic Energy, Geneva* 9, 203–7 (1956).

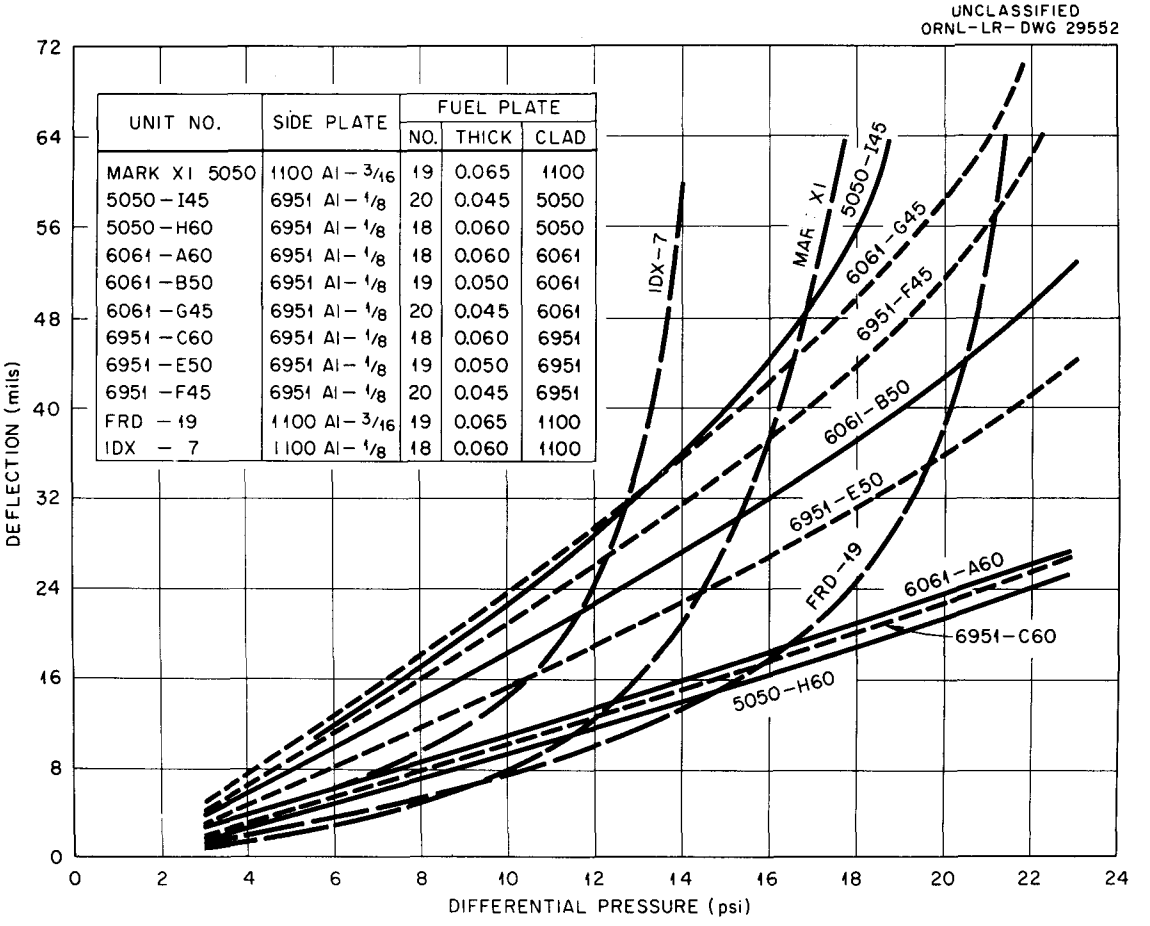

UNIT NO.	SIDE PLATE	FUEL PLATE		
		NO.	THICK	CLAD
MARK XI 5050	1100 Al – 3/16	19	0.065	1100
5050 – I45	6951 Al – 1/8	20	0.045	5050
5050 – H60	6951 Al – 1/8	18	0.060	5050
6061 – A60	6951 Al – 1/8	18	0.060	6061
6061 – B50	6951 Al – 1/8	19	0.050	6061
6061 – G45	6951 Al – 1/8	20	0.045	6061
6951 – C60	6951 Al – 1/8	18	0.060	6951
6951 – E50	6951 Al – 1/8	19	0.050	6951
6951 – F45	6951 Al – 1/8	20	0.045	6951
FRD – 19	1100 Al – 3/16	19	0.065	1100
IDX – 7	1100 Al – 1/8	18	0.060	1100

Fig. 103. Deflection of Top and Bottom Plates of Brazed Curved-Plate Aluminum Fuel Elements After Designated Differential Air Pressurization. Age-hardening alloys solution-treated, air-quenched, and aged.

Table 37. Preliminary Data on Surface Contamination of Aluminum Fuel Elements

Origin of Plate	U^{235} Contamination (ppm)	Remarks
Hot-rolled plate	180	Rolls apparently contaminated by rolling U-Al alloy
Flux annelaed	4.2	Plate processed through fluxing step, including acid rinse
Cold rolled	4.7	Plate taken from cold mill after previous cleaning
Hot rolled	0.86	Rolls cleaned with kerosene and by rolling aluminum stock
Flux annealed	0.40	After processing through flux-annealing and cleaning step
Cold rolled	0.37	Plate given final rolling on United mill
Production plate	0.24	Plate given final anneal and acid cleaning prior to brazing
Stock	0.008	Aluminum from plant stores
ORR	0.39	Enriched fuel plate prepared for reactor use
BSR	0.16	Enriched fuel plate prepared for reactor use

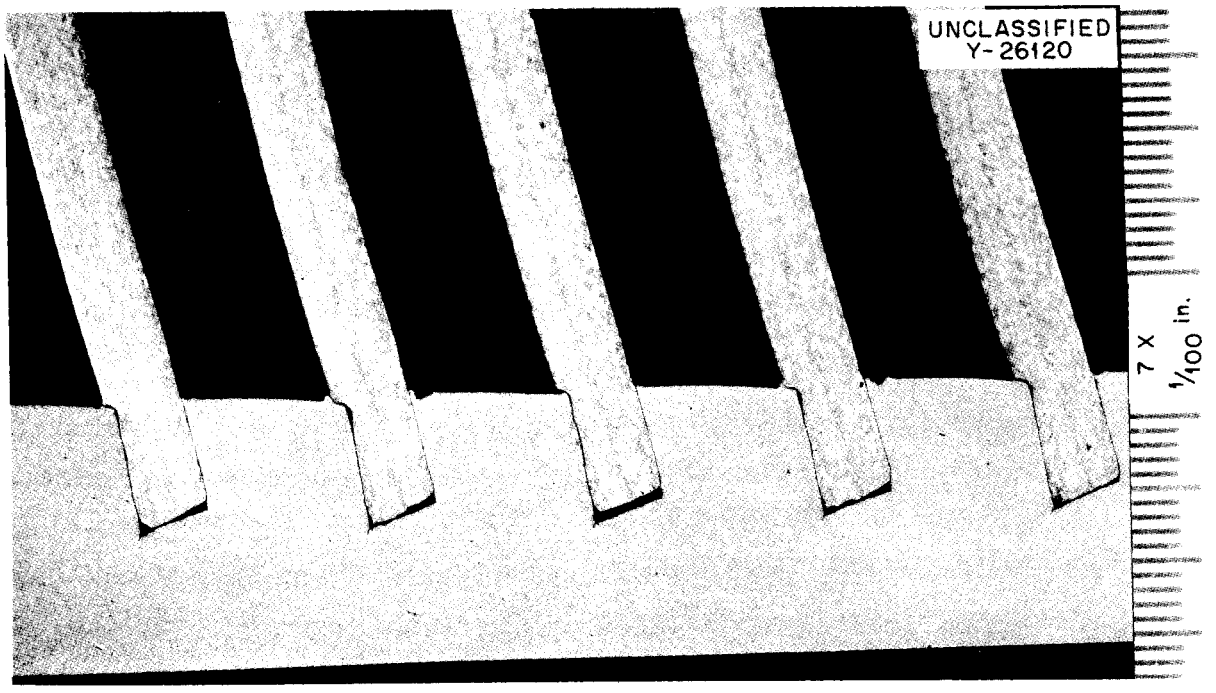

Fig. 104. Cross Section of Mechanically Joined ORR-Type Fuel Assembly.

IRRADIATION TESTING

C. F. Leitten

Miniature Specimens of APPR-1 Absorber Plates Containing 3 wt % Enriched Boron in Electrolytic Iron Clad with Stainless Steel

The preliminary investigation into the irradiation behavior of miniature absorber plates of the APPR-1 type has been completed. The postirradiation evaluation given previously[12] revealed that significant differences existed between the calculated burnup values and those based on chemical analysis, as is shown in Table 38. Because of these differences, the samples presently under irradiation in the MTR have been re-evaluated in order to study the effect of irradiation in the range 4 to 25% B^{10} burnup, in place of the originally selected 11 to 32% range.

Upon completion of the irradiation, these samples will be heated at 500°F for varying periods of time, under pressure, to more closely simulate actual reactor conditions. Dimensional measurements as well as metallographic examination will be employed to determine the extent of irradiation damage.

Table 38. Comparison of Calculated and Determined Burnup for the Miniatures Containing 3 wt % Enriched Boron in Iron

Sample No.	Calculated B^{10} Atom Burnup (%)	Determined B^{10} Atom Burnup* (%)
6	11	4.0
7	32	11.5
8	41	17.6
5	68	37.0
1	66	32.9

*Based on lithium analyses.

Miniature Aluminum Plates Containing 20%-Enriched Uranium

A program has been initiated to study the effects of irradiation on various fuel combinations applicable to foreign reactor service. The program consists in irradiating miniature fuel plates to burnups

[12] C. F. Leitten, *Met. Ann. Prog. Rep. Oct. 10, 1957*, ORNL-2422, p 143.

of 20, 40, 60, and 80% of the U^{235} atoms. The fuel combinations now under irradiation, or to be inserted in the MTR in the near future, are: (1) 48 wt % U–3 wt % Si–49 wt % Al alloy, (2) dispersions of UC_2 in aluminum, and (3) dispersions of U_3O_8 in aluminum.

Upon completion of the irradiation, the samples will be examined for surface defects and dimensional stability.

MTR Plate-Type Elements Containing a 10 wt % Pu–Al Alloy

One of these elements which was irradiated in the active lattice of the MTR to an approximately 29% burnup of plutonium has been examined. Post-irradiation examination included measurements of actual dimensions of the element, observations of the exposed surfaces, and evaluation of surface contamination. No damage was observed.

MANUFACTURING OF REACTOR COMPONENTS

J. H. Erwin

TSR No. 2 Fuel Elements

The second Tower Shielding Reactor (TSR-2) core design embodies an array of segmented fuel elements assembled into a spherical shell. The fuel units for this reactor are novel in that they are angular and require fuel plates of 71 different sizes and curvatures. The fabrication technique for the fuel units was developed as described previously.[13] This technique was used to fabricate successfully a complete loading of highly enriched fuel elements for the spherical reactor core design.

---

[13] J. H. Erwin, *Met. Ann. Prog. Rep. Oct. 10, 1957*, ORNL-2422, p 144.

ADVANCED ENGINEERING AND DEVELOPMENT OF REACTOR MATERIALS

R. C. Waugh

R. E. Adams J. I. Federer

T. S. Lundy

Fuel Irradiation Program

R. C. Waugh J. I. Federer

R. E. Adams T. S. Lundy

A long-range solid-fuel irradiation program, independent of current reactor programs, has been started. The initial phase is a study of the effects of irradiation as a function of exposure temperature and burnup in miniature stainless steel–uranium dioxide dispersion fuel plates. Tentative upper limits of interest are 1700°F irradiation temperature and 3 at. % (33% U^{235}) burnup of the fuel core. Additional variables to be studied include:

1. UO_2 loading, 15, 23, 31, and 40 wt %;
2. UO_2 particle sizes, −100 +140 and −170 +325 mesh;
3. fabrication conditions, as-hot-rolled and nominal 25% cold reduction.

Fuel specimens identical to those used above will be irradiated in "leaky rabbit" capsules at ORR bulk water temperature. Postirradiation studies will determine the effects of annealing time and temperature on the fuel specimens, and the low-temperature data will be correlated with that from the elevated-temperature study.

A reference miniature fuel specimen with over-all dimensions of 2 × 0.875 × 0.030 in. and core dimensions of 1 × 0.625 × 0.020 in. has been established. Fabrication techniques, primarily to minimize stringering of the UO_2 particles, are being developed.

A suitable irradiation capsule is being developed for elevated-temperature use. The fuel specimens will be in liquid metal within a double-walled stainless steel capsule containing thermocouples. Temperature will be automatically controlled by using electric immersion heaters in the liquid metal and by varying the composition of the helium-argon mixture in the annulus between the capsule walls. Heat-transfer bench tests are being conducted.

The required irradiation facilities have been assigned in the ORR, and mapping of the unperturbed flux has been completed.

Intergranular Diffusion of Magnesium in Zirconium

J. I. Federer

A study of grain-boundary diffusion of magnesium in zirconium and of the application of the phenomenon to a method for removal of zirconium cladding from reactor fuel elements has continued. Zirconium and Zircaloy-2 can be penetrated intergranularly by magnesium in the temperature range 570 to 640°C. The resulting material is brittle due to the magnesium-rich grain boundaries.

Zirconium and Zircaloy-2 specimens were exposed to magnesium vapor for various times at temperatures from 570 to 640°C. The depth of grain-boundary penetration was measured metallographically, and the results are summarized in Table 39.

Table 39. Grain-Boundary Penetration of Zirconium and Zircaloy-2 by Magnesium

Temperature (°C)	Time (hr)	Depth of Penetration (in.)	
		Zirconium*	Zircaloy-2**
570	2		0.005
600	2	0.012	0.010
625	0.5	0.010	
		0.011	
625	1	0.016	0.012
		0.017	0.015
625	2	0.025	0.023
			0.027
625	3	0.035	0.032
		0.038	0.034
625	4	0.042	0.043
625	7.5	0.059	
640	2	0.034	0.036

*Grain size ASTM 5, 6, 7.

**Grain size ASTM 7, 8.

The data indicate that about 2.5 hr at 625°C is required for magnesium to penetrate a nominal cladding of 0.030-in.-thick zirconium or Zircaloy-2.

Chemical dissolution experiments were performed to determine the susceptibility of the grain-boundary material to acid attack. Selective grain-boundary attack might result in disintegration of the fuel cladding, exposing the uranium-bearing core for further chemical treatment. The dissolutions were made with acid solutions for which a reprocessing technology already existed: 16 *M* HNO_3, 5 *M* HNO_3–2 *M* HCl, 6 *M* HCl, 4 *M* H_2SO_4, and 13 *M* HNO_3–0.04 *M* HF. Specimens were prepared by exposure to magnesium vapor at 625°C for times in excess of that required for complete penetration. The susceptibility of the specimens to grain-boundary attack was evaluated by weight-change measurements and metallographic examination. The results are summarized in Table 40.

The results of the dissolution tests indicate that the presence of magnesium at the grain boundaries of zirconium and Zircaloy-2 does not significantly accelerate their corrosion in the acid solutions used. Metallographic examination did not reveal selective grain-boundary attack except on the zirconium specimen exposed to the 5 *M* HNO_3–2 *M* HCl solution for 91 hr. Control samples of pure zirconium and Zircaloy-2 were exposed to the 13 *M* HNO_3–0.04 *M* HF solution after it was observed that penetrated samples experienced considerable weight losses. The weight losses were the result of general attack, and the data show that pure samples are corroded at about the same rate as penetrated samples of the same material. The 9.0% weight loss of the penetrated Zircaloy-2 sample exposed to 5 *M* HNO_3–2 *M* HCl solution was attributed to large cracks originally present in the material. This was substantiated in a subsequent test in which the weight loss of an uncracked sample was only 0.2%.

The one sample of penetrated zirconium which showed evidence of grain-boundary attack lost 4.1% of its weight during an initial 48-hr exposure to 5 *M* HNO_3–2 *M* HCl solution, but during the subsequent 43-hr exposure no additional weight loss occurred. The observed weight loss was apparently the result of localized corrosion of a part of the sample. Examination of the attacked region revealed many voids having the same size and shape as adjacent grains, which strongly suggests grain-boundary attack. The localized nature of the attack and its termination during testing indicate that the sample was not homogeneous with respect to magnesium. This experiment demonstrated that magnesium-penetrated zirconium is subject to intergranular attack. The conditions required to promote complete grain-boundary attack are not established.

Magnesium-embrittled zirconium cladding can be removed by mechanical deformation. In one test about 90% of the cladding was removed from a uranium rod subjected to the flexing and rolling action of a rotary tube-and-rod straightener.[1] In another test a 4-in. length of uranium rod clad with 0.015-in.-thick zirconium was exposed to magnesium vapor for 3 hr at 625°C and subjected to the action of a small ball mill using 0.25- to 0.75-in.-dia porcelain balls. Under the relatively mild conditions of this test, about 20% of the cladding was removed, exposing the core in several localized areas. More severe ball-milling conditions would probably increase the degree of cladding removal.

Solid Moderator Study

R. C. Waugh D. T. Bourgette
T. S. Lundy J. H. Cherubini

A general survey of potential solid moderators was made. The criteria used for screening purposes were:

1. stable solid at 300°C,
2. moderating ratio greater than 20,
3. neutron age less than 500 cm^2.

Application of these criteria resulted in a list of 17 elements and compounds. Table 41 lists these materials in order of decreasing moderating ratio. The neutron age values are included. Age values for nonhydrides were obtained by using slowing-down theory incorporated into an Oracle code by Tobias.[2] Age values for hydrides were obtained by using the Flügge-Tittle method[3] incorporated into an Oracle code by W. E. Kinney of the Neutron Physics Division. In both cases, ages were calculated in the interval between the energies corresponding to the U^{235} fission spectrum and the

[1] J. I. Federer, *Met. Ann. Prog. Rep. Oct. 10, 1957*, ORNL-2422, p 149.

[2] M. Tobias, *An Oracle Code for Calculation of Fermi Ages by Numerical Integration*, ORNL CF-56-4-53 (April 10, 1956).

[3] C. W. Tittle, *Nuclear Shielding Studies. I. The Slowing Down and Diffusion of Neutrons in Hydrogenous Media*, NP-1418 (Aug. 31, 1949).

Table 40. Results of Dissolution Experiments on Zirconium and Zircaloy-2 Specimens Penetrated with Magnesium at 625°C

Specimen Thickness (in.)	Penetration Time (hr)	Dissolution* Time (hr)	Weight Change (%)				
			16 *M* HNO_3	5 *M* HNO_3–2 *M* HCl	6 *M* HCl	4 *M* H_2SO_4	13 *M* HNO_3–0.04 *M* HF
			Zirconium				
0.06	3.5	4	+0.16	+0.08	+0.05	+0.07	
0.02	2.5	3	−0.26	−0.86			−23.5
0.02	2.5	4			−5.8	+2.6	
0.02	2.5	4					−20.0
		19					−58.0
0.02	None**	4					−19.0
		19					−59.1
0.06	6	48	−0.01	−4.1			
		60	−0.04				
		91		−4.1			
			Zircaloy-2				
0.06	7	3	−0.01	−8.3	+0.06	+0.02	−12.7
		7		−9.0			−33.3
0.06	None**	10					−30.0
0.06	7	3		−0.1			
		7		−0.2			

*Solutions boiling (106–120°C) under total reflux condition.

**Control specimen.

Table 41. Calculated Moderating Ratio and Neutron Age Values for Potential Solid Moderators

Material	Moderating Ratio	Density (g/cc)	Age to 250°C (cm^2)
BeO	217	2.80	115.8
Graphite	191	1.62	342.3
Be_2C	169	2.20	82.5
Be	164	1.85	79.9
BeF_2	86	1.986	387.9
Li^7H	65	0.82	26.9
MgH_2	64	1.42	29.0
$Mg(AlH_4)_2$	59	3.5	3.4
AlH_3	57	2.5	5.7
ZrH_2	55	5.0	25.9
CaH_2	43	1.7	49.5
CeH_2	34	4.0	70.8
YH_3	29	4.0	17.7
ZnH_2	27	5.0	12.9
SrH_2	26	2.5	72.5
BaH_2	25	4.21	56.6
RbH	23	2.0	210.4

energy corresponding to a neutron temperature of 250°C.

A literature survey on the hydrides of Table 41, other than those of zirconium and yttrium, was completed.

Compatibility of Uranium Oxides in Aluminum

R. C. Waugh

U_3O_8-Al. – The reaction of U_3O_8 with aluminum at 600°C appears to occur in two steps as shown below:

(1) $$3U_3O_8 + 4Al = 9UO_2 + 2Al_2O_3$$

(2) $$3UO_2 + 16Al = 3UAl_4 + 2Al_2O_3$$

Although not detected by x-ray diffraction in limited experiments, UAl_2 and UAl_3 should be involved at intermediate stages of reaction 2.

Compatibility studies were continued at 600°C on fuel plates containing 55.7 wt % U_3O_8 in an aluminum matrix.[4] Figure 105 shows the growth curve obtained after a 3000-hr heat treatment at 600°C. A portion of each curve is drawn as a dotted line to indicate the uncertainty of representation. The identities of the core constituents at selected times are noted and illustrate the two steps of the proposed reaction. The –325 mesh U_3O_8 reacts faster, as anticipated from its comparative surface/volume ratio. Reaction 2 is complete in both cases after 3000 hr. At no time during the course of reaction 1 were U-Al intermetallics detectable; that is, the UO_2 formed did not react with aluminum until all the U_3O_8 had been reduced. The observed growth appears to be an order of magnitude less than that for UO_2-Al plates of the same uranium content. The reasons for these two phenomena are not presently established.

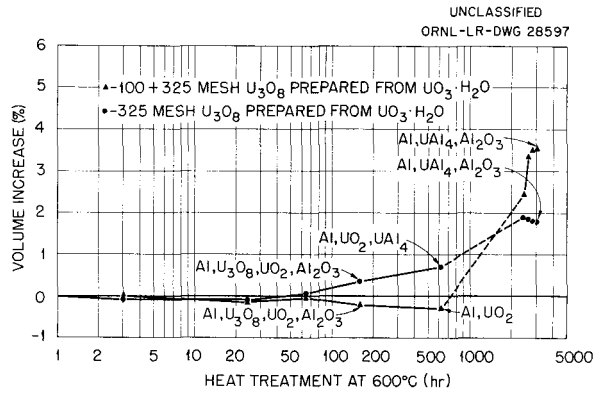

Fig. 105. Growth Characteristics of 55.7 wt % U_3O_8–Al Fuel Plates.

UO_2-Al. – The reaction of UO_2 with aluminum at 600°C occurs as shown below:

$$3UO_2 + 16Al = 3UAl_4 + 2Al_2O_3$$

in which UAl_2 and UAl_3 are intermediate products in the formation of the UAl_4.

Compatibility studies were continued on fuel plates containing 52.3 wt % UO_2 in an aluminum matrix.[4] Growth curves were established at heat-treatment temperatures of 600, 575, 550, 525, and 500°C for fuel plates containing –100 +325 mesh UO_2 reduced from $UO_3 \cdot H_2O$ in hydrogen and high-purity argon. Figures 106 and 107 show the growth

[4] R. C. Waugh, *Met. Ann. Prog. Rep. Oct. 10, 1957*, ORNL-2422, p 139.

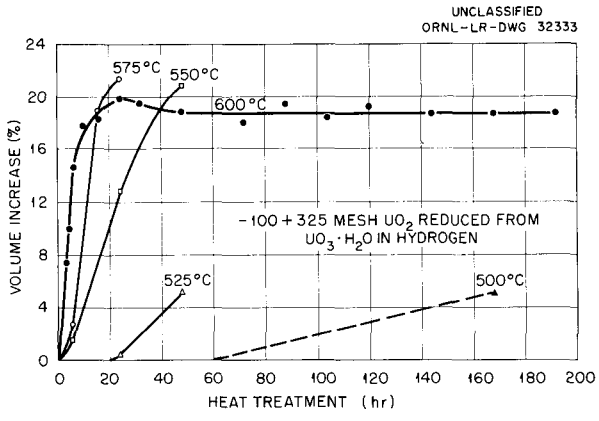

Fig. 106. Growth Characteristics of 52.3 wt % UO_2–Al Fuel Plates at Selected Temperatures.

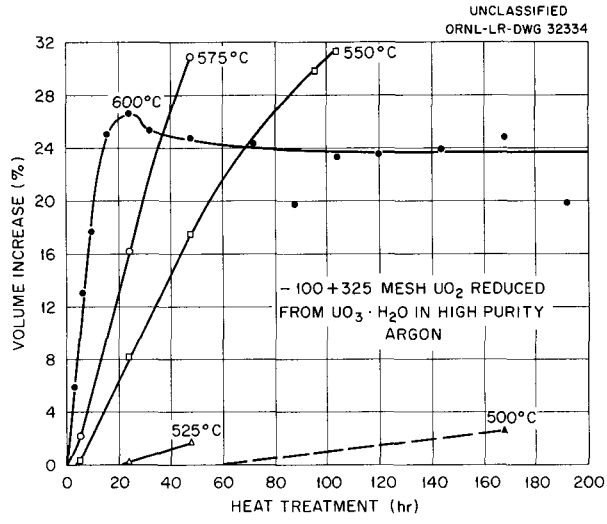

Fig. 107. Growth Characteristics of 52.3 wt % UO_2–Al Fuel Plates at Selected Temperatures.

curves established for the hydrogen- and argon-reduced UO_2, respectively. Each point represents a separate fuel plate. The growth rates decrease with temperature. Growth at 600°C is seen to increase rapidly to 20–26% after 24 hr and decrease slightly to a final value. The reaction products present in hydrogen-reduced UO_2 plates after 3 and 6 hr at 600°C were UAl_2, UAl_3, UAl_4, and Al_2O_3. Reaction was complete after 16 hr on the basis of x-ray diffraction. The reasons for the greater growth of the argon-reduced UO_2 at 600°C and the increased growth at 575 and 550°C for both oxides have not been established. An analytical chemistry method for determining reaction kinetics is at the final stage of development. Figure 108 shows the pronounced warpage that accompanies growth of the hydrogen-reduced UO_2 plates. The argon-reduced UO_2 plates behave similarly.

The compatibility of −100 +325 mesh hydrogen-reduced UO_2 with aluminum in 50 wt % UO_2 cores cold-pressed to ~95% densification has been studied at 600°C for times up to 80 hr in static vacuum-capsule tests. The primary reaction products in all cases were UAl_3 and Al_2O_3, with small amounts of UAl_2 and UAl_4 present in several instances. An average of 76% reaction was determined after 80 hr of heat treatment. The absence of UAl_4 as a primary product is surprising in light of the results from reacted UO_2-Al fuel plates.

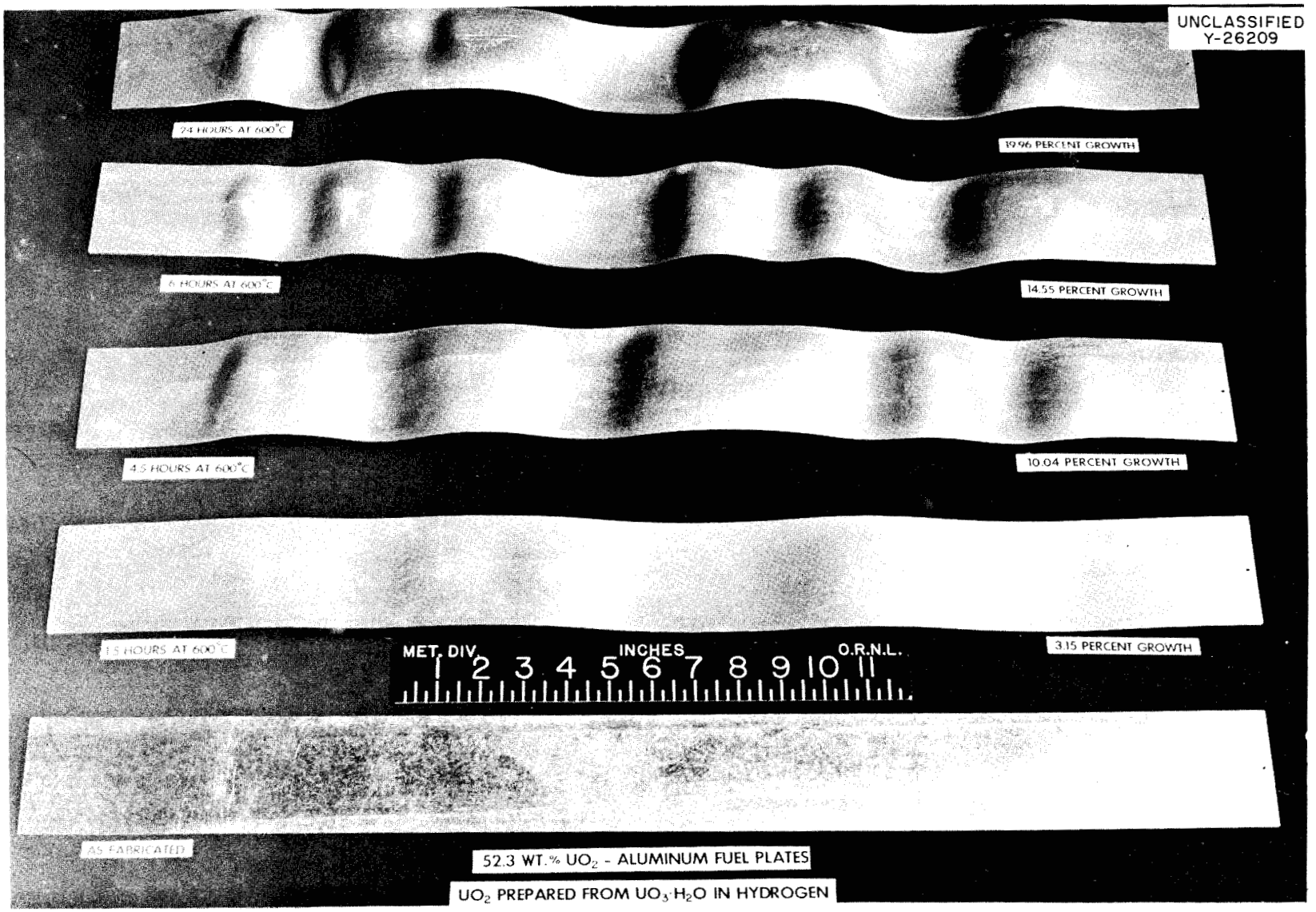

Fig. 108. Warpage of 52.3 wt % UO_2–Al Fuel Plates.

CERAMICS RESEARCH

L. M. Doney

F. L. Carlsen, Jr.
C. E. Curtis
S. D. Fulkerson
R. L. Hamner
L. A. Harris
M. P. Haydon
R. E. Meadows
J. M. Kerr
R. A. Potter
A. J. Taylor
A. G. Tharp
G. D. White

BERYLLIUM OXIDE FABRICATION

R. L. Hamner R. A. Potter

Beryllium Oxide with Selected Additives

Nearly all fabrication studies during the year involving beryllium oxide were directed toward support of the GE-ANPD shielding program.[1-3] The program consisted of two phases: the incorporation of boron in high-density BeO and the densification of BeO by the use of additives. A number of borides were synthesized and incorporated in high-density BeO. The stability of the resulting ceramic bodies in air at 1300°C was investigated. Densification studies were also made with pure BeO and BeO with B_4C, Fe_2O_3, and MgO used as additives.[1-3]

A tentative program in further support of the GE-ANPD effort has been outlined as follows: (1) the production of a high-purity, highly sinterable grade of beryllium oxide and the definition of its sintering qualities, (2) microstructure control studies of beryllium oxide based on the premise that grain growth may be inhibited by purity control, (3) water-vapor corrosion studies of beryllium oxide, and (4) coating studies on the inhibition of water-vapor corrosion.

Pure Beryllium Oxide

In the interest of possible future fabrication requirements it was considered advisable to compile information on the comparative fabrication characteristics of commercially available grades of beryllium oxide. Previous experience has shown that fabrication of Brush's G.C. and Luckey S.P. grades to a high-density product could be accomplished only by hot pressing or by the use of additives. A quantity of highly sinterable LOH grade BeO was received from the Brush Beryllium Company for experimentation. This material is obtained by calcining the hydroxide at low temperatures (<1000°C) to maintain a very fine particle size, approximately 0.1 μ. Densities of 94, 97, and 98% of theoretical were obtained by hot pressing at 1050, 1150, and 1250°C, respectively. Upon sectional examination, however, a marked discoloration was noted due to some undetermined impurity which was hygroscopic when fired below 1150°C. After leaching with HCl the discoloration was not noted, but the densification properties of the material were markedly changed to 68, 86, and 97% of theoretical at 1050, 1150, 1250°C, respectively. The hot-pressing temperatures required for obtaining 97% of theoretical density are given below for LOH and for Brush's G.C. and Luckey S.P. grades:

Grade	Temperature (°C)
LOH	1250
G.C.	1750
S.P.	1950

The differences in densification properties of these materials are traced primarily to differences in particle size of the starting materials, which are compared in Figs. 109 to 111.

Samples of Brush's experimental UOX grade BeO and BeO from the Beryllium Corporation of America have been received, but the sintering characteristics have not been determined.

GAS-COOLED REACTOR

A. J. Taylor J. A. Griffin
S. D. Fulkerson F. P. Jeffers

The initial concept of the GCR stressed economy very strongly. Materials and equipment for every phase of the design were to be, as nearly as

---

[1] L. M. Doney and R. L. Hamner, *ANP Quar. Prog. Rep. Dec. 31, 1957*, ORNL-2440, p 180.

[2] L. M. Doney, R. L. Hamner, and R. A. Potter, *ANP Quar. Prog. Rep. March 31, 1958*, ORNL-2517, p 45–46.

[3] L. M. Doney, R. L. Hamner, and R. A. Potter, *ANP Semiann. Prog. Rep. Sept. 30, 1958*, ORNL-2599 (in press).

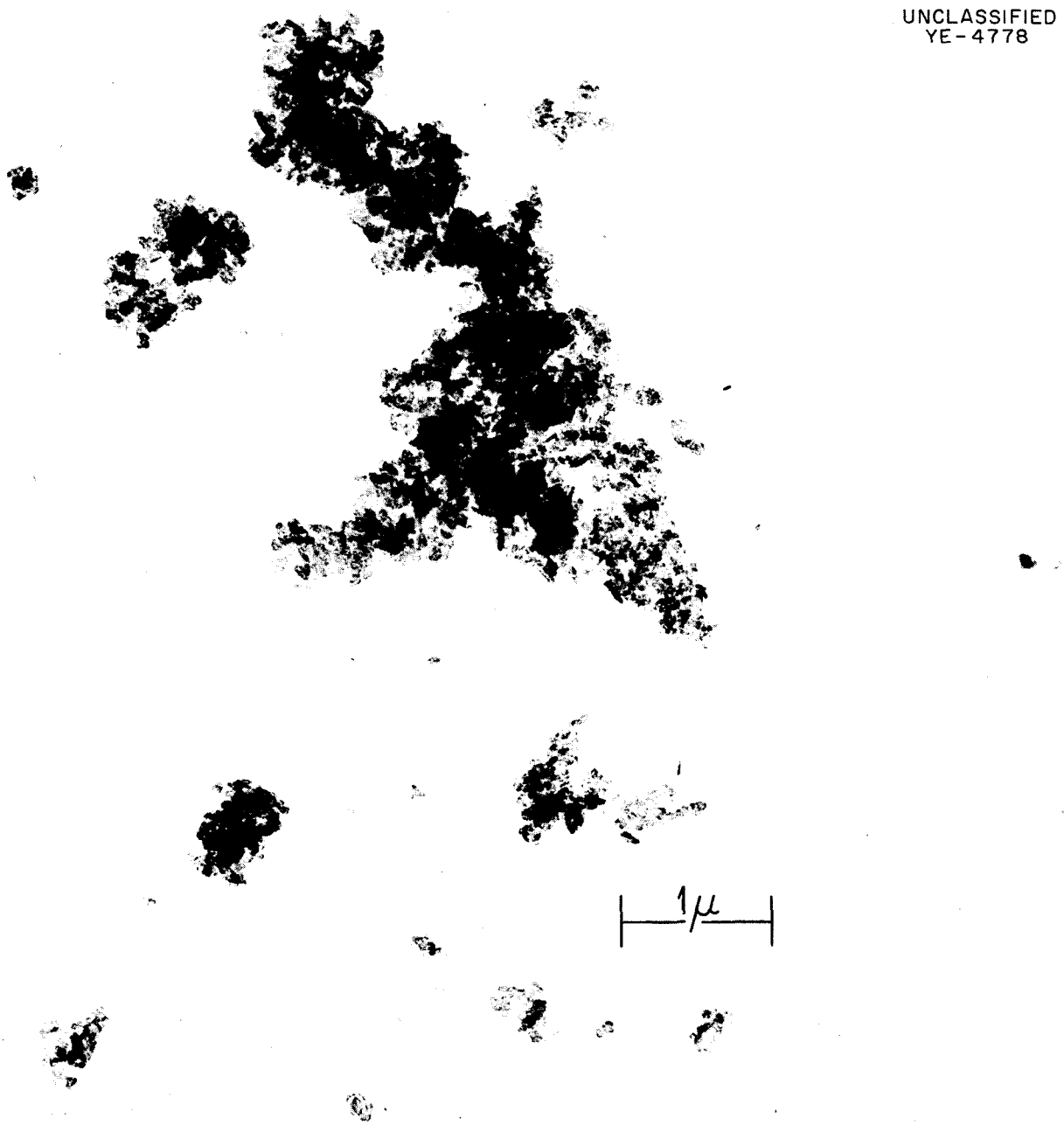

Fig. 109. Brush's LOH Grade Beryllium Oxide.

possible, existent, obtainable, and technically usable. The fuel was fixed as a low-enrichment UO_2 bushing or slug whose cost was to be minimized as much as possible. The task of the Ceramics Laboratory was to determine the feasibility of fabricating the fuel to within tolerance of some specified density and size and, if necessary, to fabricate specimens for the irradiation test program. Elimination of the need for machining was deemed the most necessary part of the effort to reduce fuel fabrication costs, since the best figures obtainable indicated that machining costs would be ~40% of total fabrication costs.

Existing knowledge of fabrication techniques and of types of UO_2 available indicated that it would be quite possible to sinter UO_2 to the specified

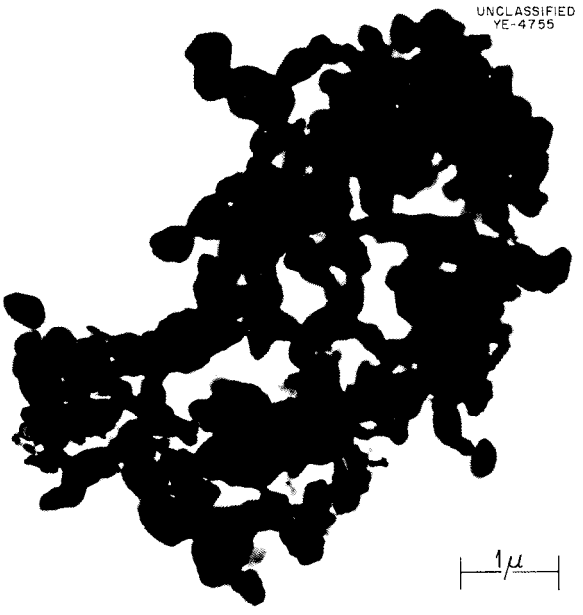

Fig. 110. Brush's G.C. Grade Beryllium Oxide.

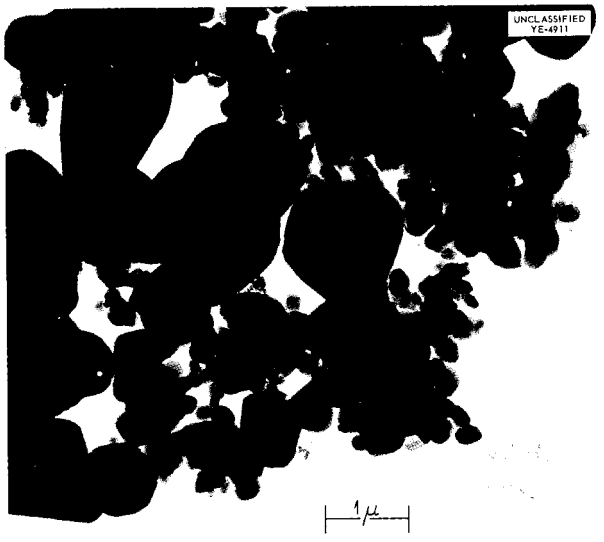

Fig. 111. Brush's Luckey S.P. Grade Beryllium Oxide.

size and density provided that the specified tolerances were not too severe. A type of UO_2 made from ammonium diuranate precipitated from a nitrate solution had been used quite successfully in the Ceramics Laboratory for several years in fabricating high-density bulk shapes of UO_2. This material was characterized by its high green strength when formed at moderate pressures and by its shrinkage to high densities on sintering. This type of oxide was selected as the one most suitable for fabricating the GCR fuel; the forming technique was arbitrarily established as cold pressing, and the only major problem remaining was to develop a process for producing this type of oxide in large quantities with constant qualities.

Pressing dry is preferred to the wet method because it is the simplest forming method which yields high-density pieces, is amenable to forming a great variety of shapes, and is very adaptable to production-line operations.

Fuel Processing

All ceramic fabricating techniques are composed of three basic steps: powder preparation, forming, and sintering. The fabrication process selected for the GCR is one that requires the fewest operations and the least expenditure of energy for each of these basic steps and should therefore be the most economical. Successful implementation of this approach depends strongly on the availability of a particular grade of oxide which is conducive to processing in this manner.

Powder Preparation

For a cold-pressing operation, the powder-preparation step consists in granulating the powders so as to have a free-flowing material which will charge a die uniformly. The techniques employed in the granulation process can vary widely, depending on the material and somewhat on the forming and sintering operations. If additives such as moisture, lubricants, binders, sintering aids, or burnout material are to be used, these ingredients must be blended in during the powder-preparation step. The usual granulation procedure for UO_2 is to blend moisture and a soluble binder into the material and to follow this with drying, breaking up, screening, and blending-in a lubricant. Since UO_2 must be sintered in a nonoxidizing atmosphere, the organic lubricant and binder must be removed by vaporization in a bakeout or preheating operation or by presintering in a CO_2 atmosphere so as to minimize the free-carbon residue. Since the type of UO_2 chosen for the GCR slugs compacts readily into a piece of moderately high green strength without the use of organic additives, it was possible to eliminate this portion of the granulation procedure. In addition, the procedure was further modified to compact as-received UO_2 at a low

pressure (15,000 psi), followed by breaking the compact through a 35-mesh screen. The screened material, including the fines, is a fairly free-flowing powder, containing no additives, ready to charge into a die. Therefore the granulation process eliminates blending, drying, and bakeout or presintering operations while adding only a compacting operation.

Pressing

Of the several techniques available to form the required shape for the GCR fuel, only extrusion and dry pressing are adaptable to a rapid and economical production-line forming operation. Extrusion was eliminated because at present it is very difficult to achieve a high sintered density from extruded pieces; also, it seemed very improbable that the machining operation could be eliminated if the extrusion process were used. The dry-pressing operation is merely one of compacting powders in a die. To achieve high sintered densities, it is ordinarily necessary to compact UO_2 to a fairly high green density, ~60 to 75% of theoretical density. The green density needed will vary with the sinterability or amount of shrinkage which can be expected from any particular type of oxide. Again, depending on the particular type of UO_2, the pressure required in compacting to a high green density ordinarily ranges between 20 and 125 tsi. At these pressures it becomes necessary to add a lubricant to the oxide to aid in the compacting; without a lubricant, pressure cracking, pressure caps, and laminations become a big problem. The green compact must have sufficient strength to withstand a moderate amount of handling without the geometry-destroying effect of crumbling or flaking the corners and edges. Firmness and green strength are usually obtained by including a binder in the powder to be compacted.

In compacting pieces of any appreciable length, the length-to-diameter ratio can become very important. An increasing wasp-waist or hourglass effect is noted in the sintered piece as the length-to-diameter ratio increases and as forming pressures increase. When the sintered piece is to be machined to its finished diameter, this hourglass effect is relatively unimportant, but when the piece is to be sintered to its final dimensions, as with the GCR fuel, this effect becomes very important and must be either minimized or eliminated. The hourglass effect is caused by a density differential between the ends and the center of the pressed piece. With pressure being applied at the ends of the piece in forming, the ends will always be compacted to a density higher than that at the center, and a fairly uniform density gradient will exist between center and ends. When the piece is sintered to its final density, shrinkage is greater in the center than at the ends, and the result is a sintered piece with uniform density, having its least diameter at the center and its greatest diameter at the ends. This is the hourglass effect, and, when large, it destroys the possibility of sintering to within close tolerances of a specified size.

In view of the discussion above, some limits were set for forming the GCR fuel slugs; forming pressure was set at a maximum of 10 tsi, and the maximum length-to-diameter ratio was set at 1. Within these maximums the selected UO_2 forms a low-density green piece that has sufficient green strength for easy handling. At near the required size, experience has established that a pressure of 7500 psi and a length-to-diameter ratio of ~0.65 yield a piece with a density ranging between 40 and 50% of theoretical, with the better grades of oxide yielding density values closer to 48% of theoretical. Formed in this manner, the better oxides give sintered densities ranging from 93.5 to 95% of theoretical. In general, the hourglass effect does not exceed 2 mils on the diameter of a piece which sinters to ~$^3/_4$ in. in diameter. Low pressures are used and are necessary in forming the GCR slugs because light and relatively inexpensive presses and dies can be used, the hourglass effect is minimized, and the oxide selected for this process cannot be pressed at high pressures in steel dies without the addition of some type of organic lubricant to prevent the lamination which occurs in the vicinity of 15,000 psi.

Sintering

Sintering decreases the volume of the mass by crystal growth and agglomeration and thus increases the density of the green piece to the final density desired. The degree of shrinkage obtained depends on the characteristics of the material being sintered and, to a lesser extent, on the conditions of forming the material. There is a practical limit as to the effectiveness of temperature alone in promoting shrinkage. With a fairly sinterable oxide, density increases quite rapidly with

increasing temperature, until a density in the vicinity of 90% of theoretical is attained. Above this temperature the density will continue to increase but at a rapidly decreasing rate, which soon becomes so small that it is impractical to sinter the oxide to the extremely high temperatures which could make any appreciable difference in the final density.

At any given temperature, density will increase with time; however, the effect of time is not so marked as that of temperature, and, unless absolutely needed, long soaking times can be detrimental to the economics of the fabrication process.

Sintering of the GCR fuel is done at 1750°C with a soak time of 1 hr. These conditions are sufficient to sinter the oxide selected for this fabrication process. In general, 1750°C is a fairly standard temperature for sintering UO_2, but depending on the type of UO_2 being sintered, soaking time usually ranges between 2 and 10 hr. Sintering is done in an induction-heated atmosphere furnace with graphite used as the susceptor. This type of furnace was chosen over the usual molybdenum-wound alumina-refractory furnace for several reasons. On a laboratory scale, sintering is done on a batch rather than a continuous basis, and, since the development work requires many firings and the results from the previous firing before the conditions for the following run can be determined, a short-cycle furnace is needed. The one-day cycle of the induction furnace fills this need when compared with the four-day cycle of the molybdenum-wound furnace. The induction furnace allows experimentation at well above 2000°C when it is needed, whereas the molybdenum-wound furnace is limited to a maximum of 1800°C. The induction furnace is a light, small, inexpensive unit which can be replaced with a spare in a few minutes when repairs are needed, while repairs to the molybdenum-wound furnace constitute a major operation and require about four days. It seems very probable that the induction-heated furnace could be scaled up from the laboratory size to a larger, continuous-production furnace.

In general, it has not been considered good practice to sinter UO_2 in the presence of carbon; but experience has shown that it can be done very successfully, with very minor, if any, carbon pickup. The only requirements are that the furnace be kept scrupulously clean and that the atmosphere be carefully controlled. The atmosphere consists of a mixture of nitrogen and hydrogen in the ratio of 7 to 3, although a better mixture would consist of a mixture of hydrogen and either argon or helium. Small quantities of hydrogen are an aid in sintering the oxide, because hydrogen alone can cause the formation of a considerable carbide film on the UO_2, since it entrains carbon in its passage through the furnace. As part of the over-all effort to maintain economy in the fabrication process, inexpensive nitrogen, rather than helium or argon, was used as part of the sintering atmosphere. The disadvantage in using nitrogen is that, if carbide is formed, it will decompose to form the more stable nitride, and the consequent change in density and volume can be catastrophic to the piece being sintered.

Flow Diagram

The fabrication process outlined above (Fig. 112) is a simplified process involving the fewest operations possible. It is entirely dependent upon the availability of a particular type of oxide, but with

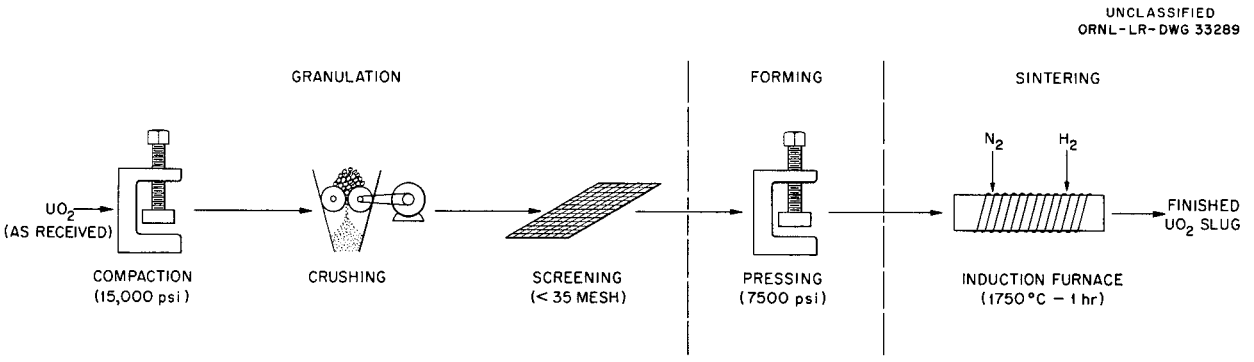

Fig. 112. Minimized Fabrication Process Proposed for GCR Fuel.

the selected oxide it appears very probable that UO_2 shapes, up to the size specified for the GCR, can be fabricated to within tolerances of the specified density and dimensions.

As can be seen from the foregoing discussion, some very stringent requirements have been placed on the UO_2 powder so that it will fit the fabrication process. If the powder is to be produced in the large quantities anticipated, its characteristics will have to be controlled very closely, since slight variations from lot to lot make density and size tolerances difficult to maintain.

Some generalized specifications for the type of oxide needed are that it can be granulated for flowability of the powder and compacted in steel dies at pressures of 20,000 psi or less without the use of either an organic binder or lubricant, that the compacted piece have sufficient green strength for easy handling, and that the material be highly active and sinterable so as to achieve the required high density (95% of theoretical) and the uniform shrinkage which are needed for sintering to within tolerances.

As previously mentioned, the type of powder desired has been known and worked with in the Ceramics Laboratory for several years. This powder, always produced in relatively small batch lots, is made by a standardized method at the Y-12 plant. As shown in Fig. 113, the UO_2 is made from calcined ammonium diuranate, $(NH_4)_2U_2O_7$ (ADU), which has been precipitated from a uranyl nitrate solution. However, since the GCR fuel calls for a low enrichment, a method had to be devised to produce powders of the same quality and characteristics from a fluoride source, because the most economical route for tonnage production was to take UF_6 at the proper enrichment and proceed by the most direct method to UO_2. Making UO_2 from UF_6 is a straightforward and well-established process, but the product does not meet the requirements for the GCR.

With the close cooperation of the Y-12 Production Group, a double precipitation process was evolved (Fig. 114) which did yield several good powders. This is a batch process and the reproducibility is not as good as is needed. The best oxide made by this process was never reproduced. The process was refined to the point that a fairly good oxide could be made by the batch process with fairly good reproducibility, but the powders still varied sufficiently that changes would have to be made in the fabrication process to produce the same sintered piece from each different batch of powder.

A second process (Fig. 115), which is continuous, was started when it was obvious that much tighter control would have to be maintained over the various chemical and calcining conditions. This process, which was established and worked out by the Y-12 Development Group, is proving to be much better from the standpoints of control and reproducibility and will be preferred from the standpoints of cost, quantity, and time. The process

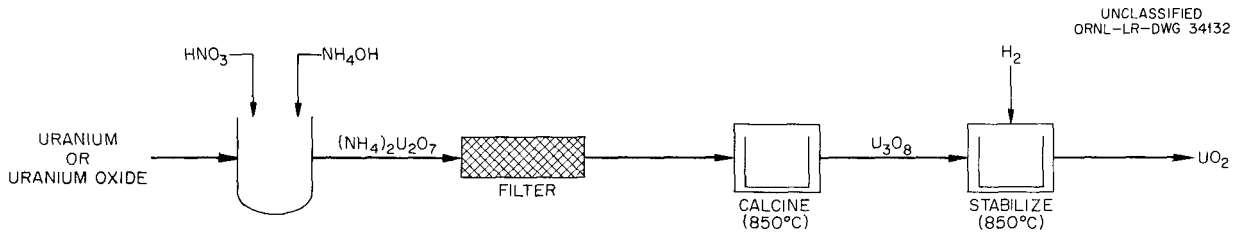

Fig. 113. Standard Y-12 Batch Process for Producing UO_2 from Nitrate Solution.

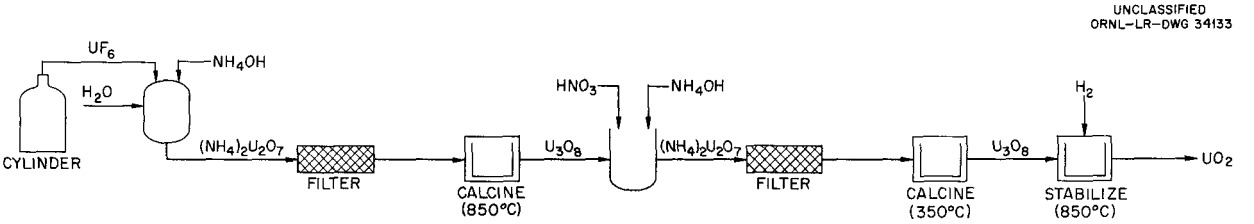

Fig. 114. Batch Process for Producing Highly Sinterable UO_2 from UF_6.

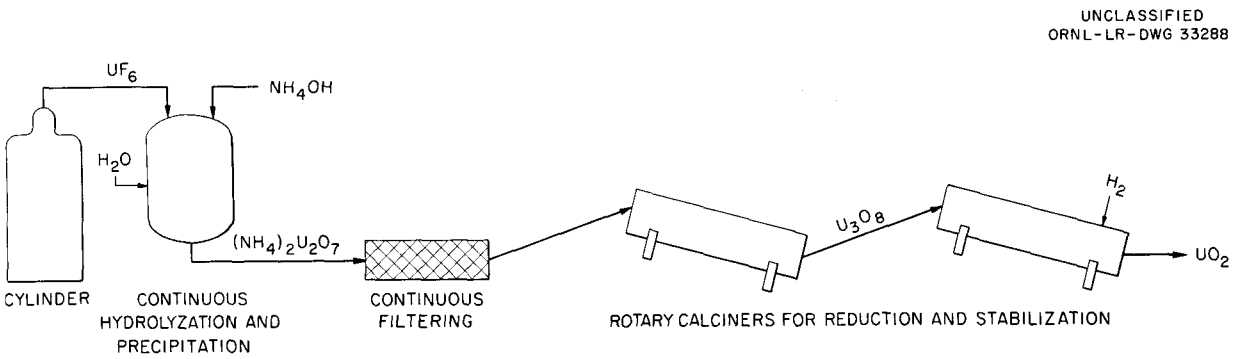

Fig. 115. Continuous Process for Producing Highly Sinterable UO_2 from UF_6.

should lend itself well to the concept of a production facility which starts with UF_6 and ends with a sintered, finished UO_2 shape.

Recently, powders from this process have reached the high quality needed, and the process is now in the refining stage where small variations in chemical and calcining conditions are being investigated for quality control. Oxide powders from the process apparently have the forming and sintering characteristics to produce UO_2 shapes at 95% of theoretical density by the minimized fabrication process used in the Ceramics Laboratory.

Quality Control

Testing of the powders consists in combined thermogravimetric and differential thermal analyses, followed by forming and sintering under the stated conditions. The thermogravimetric analysis, in which weight changes are recorded as a function of thermally induced reactions or changes in the material, gives information on the stoichiometry of the oxide. The stoichiometry is related to crystallite size, surface area, and other surface characteristics such as perfection of crystallite faces and surface activity. The differential thermal analysis, in which the temperature is noted when thermally induced reactions or changes occur, gives information on reactivity and changes in reactivity caused by changes in the processing history of the material.

These analyses are a valuable tool when employed collectively, for they give a rapid check on the effect of changes in the processing history of the material, the completeness of the reduction process, and the reproducibility of the oxide. Figure 116*a* shows analyses of an oxide made under very poor reducing conditions in the calciner. The poorly defined peaks and extremely low over-all weight gain through the oxidation steps from UO_2 to U_3O_8, coupled with the weight change pattern being continually depressed because the weight gain through the oxidation steps is continually offset by a weight loss, indicate that the reduction in the calciner has been essentially incomplete. The sample is composed of a mixture of UO_3, U_3O_8, and UO_2. In Fig. 116*b* and 116*c* are shown patterns of this same material after recalcining under good reduction conditions. Note the effect of temperature of the reduction process on the shape and position of the peaks and on the over-all weight gain of the sample. Figure 117 shows the effect of a change in the atmosphere used during the reduction while all other conditions remained constant. Figure 118 shows a reproducibility check; in this example reproducibility has been rather good.

Forming and sintering the oxides complete the testing. The materials are granulated by compacting at 15,000 psi followed by breaking through a 35-mesh screen; they are formed at 7500 psi and are finally sintered at 1750°C for 1 hr. Observations are made on the powder for graininess, for how well it compacts at 15,000 psi, and for how well it granulates in the breaking up and screening operations. Note is made of the relative strength of the formed piece and the length to which a given amount will compact; after sintering, checks are made on the density, the degree of the hourglass effect, and the uniformity of shrinkage.

At the present stage of development, a continuous process has been established for producing UO_2 from UF_6. Among the last few oxides made,

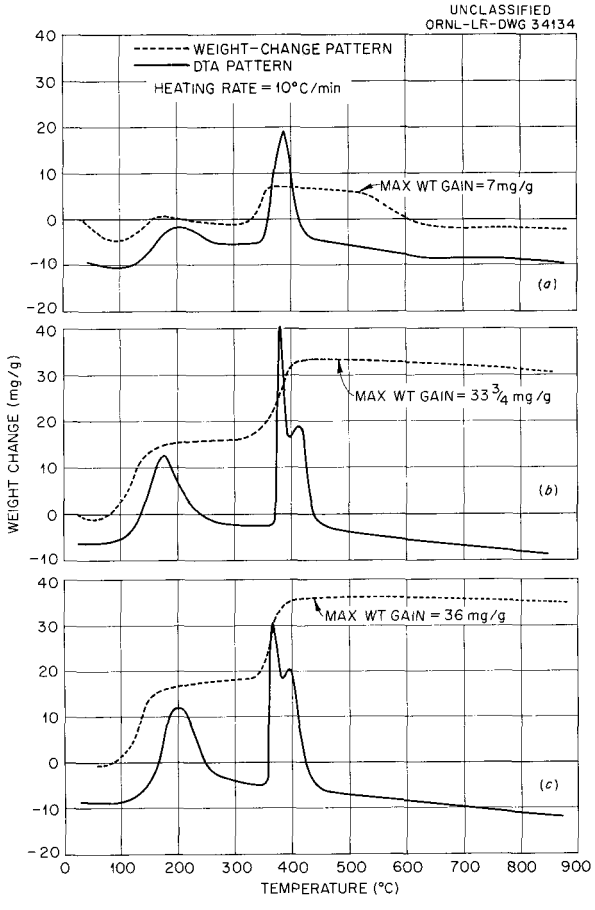

Fig. 116. Thermogravimetric and Differential Thermal Analyses of Samples of UO_2 No. 80 Prepared Under Various Reducing Conditions. (*a*) 650°C for 1 hr, poor conditions; (*b*) 650°C for 1 hr, good conditions; (*c*) 850°C for 1 hr, good conditions.

powders of excellent quality, tailored to fit the fabrication process, have been made. Reproducibility of these powders seems fairly good and is improving, and the entire process of producing the powder and a finished UO_2 shape that does not require machining seems to be quite feasible.

Fabrication of the GCR irradiation test specimens is in progress. The miniature prototype specimens (0.156-in. OD × 0.078-in. ID × 0.25-in. length) are being fabricated. The oxide powders for prototype (0.705-in. OD × 0.323-in. ID × 0.5-in. length) and reduced prototype (0.500-in. OD × 0.230-in. ID × 0.5-in. length) specimens are in process and should be in the fabrication stage soon. These powders are being prepared by the continuous process outlined above.

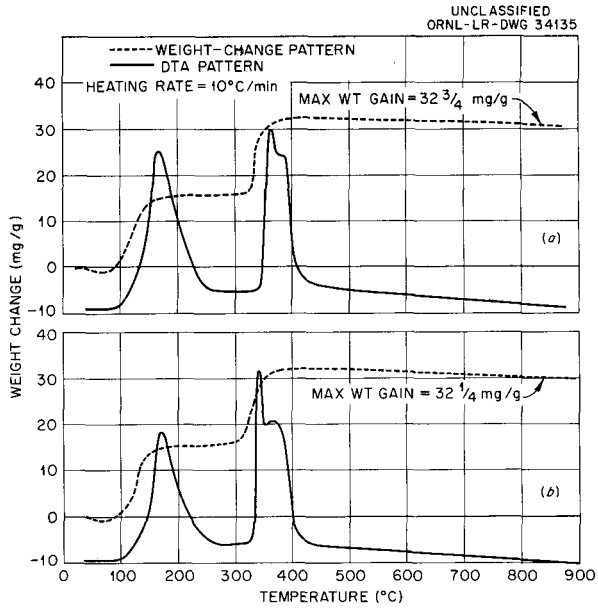

Fig. 117. Thermogravimetric and Differential Thermal Analyses of Samples of UO_2 Prepared in Different Atmospheres. (*a*) UO_2 No. 103 reduced in H_2; (*b*) UO_2 No. 104 reduced in 1:1 N_2-H_2. Oxides were processed identically except for atmospheres.

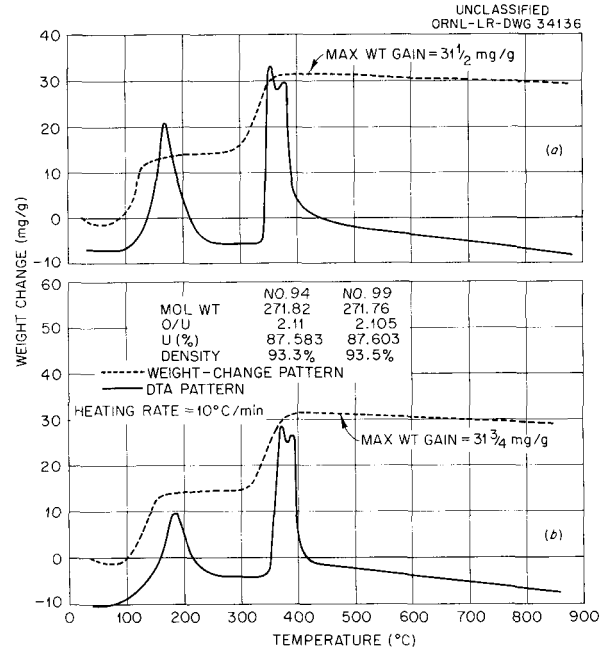

Fig. 118. Reproducibility Check on Two Batches of Oxide. (*a*) UO_2 No. 94; (*b*) UO_2 No. 99.

The extrusion of UO_2 as a fabrication technique is also being investigated. This work is being done by the Electric Auto-Lite Company, Fostoria, Ohio, under contract to ORNL. The initial stage of this work consists in finding the binders and plasticizers which can be used in the least quantity to yield the highest density. The investigation is being restricted to two types of UO_2, one low-calcined and the other dead-burned. It is felt that the optimum extrusion mixture may be a combination of these two types; this will be investigated at a later date. The later stage of this work will be to investigate the possibility of fabricating larger and longer shapes than can be readily obtained by dry pressing and to note the possibility of sintering these shapes to within tolerances of the correct diameter, leaving only raw ends to be finished by machining.

CERAMIC MATERIALS DEVELOPMENT

G. D. White R. E. Meadows

Of considerable importance in the reactor performance of a UO_2 pellet-type fuel element is a knowledge of the temperature to which the material is subjected during consumption or burnup. A method of determining the approximate temperature is to incorporate into the pellet metal wires with significantly different melting points. By metallographic examination of irradiated pellets containing these wires it is possible to observe whether or not the metal wires have melted and therefore to determine whether the temperature of the pellet reached the melting temperature of the specific metal wire. An irradiation test of a Savannah fuel element bundle has been proposed for testing in the G-E Vallecitos Boiling Water Reactor which will contain pellets with temperature-monitoring wires. Gold, nickel, vanadium, platinum (later rejected), and columbium have been selected for melting-point determinations. The metal wires are 0.020 in. in diameter and will be inserted in the center of the pellet as well as along the radius at distances of $\frac{1}{3}$ and $\frac{2}{3}$ from the center to establish a temperature profile.

In order to obtain standards of comparison for postirradiation inspection and to verify the compatibility of the selected wires with UO_2, pellets containing each wire have been heated to the melting temperatures, 100°C above and 50°C below the reported melting temperatures. After being heated through the required cycle, the pellets were sectioned and polished; then photomicrographs were made of the wire-UO_2 interface at both low and high magnifications. Typical UO_2 pellets containing nickel wires are illustrated in Fig. 119. The nickel was observed by optical pyrometry to melt at 1380°C. The specimen held at 1330°C indicates signs of incipient melting, but the wire has not filled the ultrasonically drilled cavity.

Platinum was rejected as a temperature monitor because of its apparent reaction with UO_2. A marked lowering of the fusion temperature of the

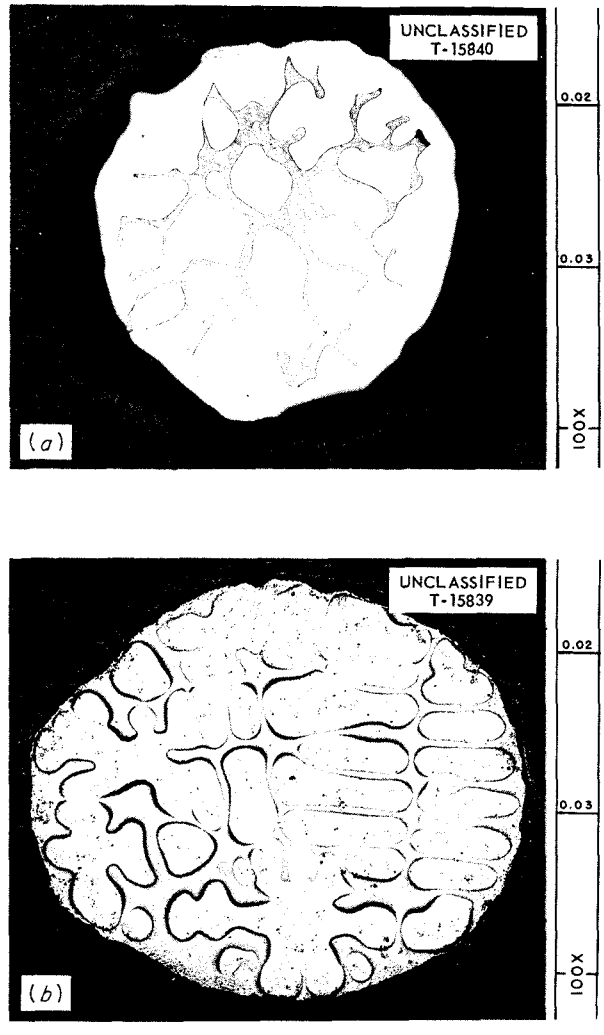

Fig. 119. Appearance of Nickel Temperature-Monitor Wires in UO_2 Pellets. (*a*) Wire heated to 1330°C shows signs of incipient melting but has not filled cavity; (*b*) wire heated to 1380°C has dendritic structure indicative of total fusion. Etchant: 10% KCN + 10% $(NH_4)_2S_2O_8$ solution.

wire was observed even when heating was conducted in vacuum. It was not determined whether this lower melting point was the result of a reaction with UO_2, per se, or with a volatile product such as UO_3 which was vaporized during sintering. When a UO_2 pellet containing platinum was heated in vacuum, a large rise in pressure occurred just before the wire melted at about 1400°C. Specimens heated in helium behaved similarly.

Techniques for fabricating UO_2 pellets containing boron as a burnable poison are also being developed. A major portion of the effort has been directed toward incorporation of 60 ppm of natural boron as ZrB_2 into the UO_2. The boride was added to the UO_2 and intimately mixed in a rubber-lined ball mill with alumina balls for 4 hr. To date, 600 ppm of boron has been added to facilitate preparation and analysis. Spectrographic analyses indicate that the mixing procedure produces a uniform distribution of the boride. Pellets pressed from this material have been sintered in helium, hydrogen, and a $7N_2:3H_2$ mixture at 1700 to 1750°C. Data presented below, which were determined spectrographically, illustrate the boron retention after sintering for pellets initially containing 600 ppm of boron as ZrB_2:

Boron Retention (ppm) in Three Atmospheres

He	H_2	$7N_2:3H_2$
100	5	100
150	5	15
120	<5	Trace
100	<5	200
80	<5	
80	<5	

These results reveal that extremely high losses occur under the experimental conditions cited. Although boron retention in all the atmospheres was unsatisfactory, the results under hydrogen were extremely poor.

Concurrent with these studies, an investigation was conducted to determine the retention of boron in UO_2 to which the burnable poison is chemically incorporated as a controlled impurity during precipitation of ammonium diuranate (ADU). To produce this material, orthoboric acid was added to the uranyl nitrate solution prior to ADU precipitation. Approximately 30% of the boron was lost during precipitation and subsequent reduction to UO_2. The UO_2 ultimately produced was found to contain 62 ppm of boron. Pellets prepared from this material were sintered at the same temperature and in the same environments described in the ZrB_2-UO_2 investigation. In every case the boron was totally lost.

CALCINATION OF THORIUM OXIDE FOR THE HRP

C. E. Curtis

The Ceramics Department has assisted the HRP by the loan of a gas-fired kiln to supplement the calcination facilities of the Chemical Technology Group, assistance in obtaining refractory containers suitable for ThO_2 calcination at 1600°C, assistance in constructing a small zirconia-lined furnace for high temperatures, and calcination of various experimental batches containing ThO_2.

Listed below are results from other work done during the period:

1. Contamination of powdered ThO_2 at 1600°C by alumina containers from three different sources was negligible.[4]
2. To reduce contact between the container and the thoria in calcining, the ThO_2 may be pressed into bars at low pressure (1300 psi was used). Reduction of the thoria to powder after calcination is facilitated if 10 wt % of cellulose flour is blended into the ThO_2 previous to pressing.
3. An easily powdered ThO_2 is produced by blending 10 wt %, or more, of the oxalate precipitate with calcined ThO_2. When calcined directly to 1600°C, the wet oxalate itself also produces an easily powdered product. Use of wet oxalate would eliminate one stage in production (precalcination) but would increase the volume of material going into the 1600°C furnace per unit volume of product.
4. Thorium oxide can be calcined very rapidly (1 hr to 1600°C) in an induction furnace. The product obtained by heating thus in a covered container of pure alumina appeared white and uncontaminated. Its properties have not yet been tested.
5. Repeated attempts to calcine ThO_2 by spraying it through an oxyacetylene torch failed because the process is slow and not readily controllable.

---

[4]C. E. Curtis, *A Brief Investigation of the Contamination of Thorium Oxide Powder by Alumina Containers in Heating at 1600°C*, ORNL CF-57-11-116 (Nov. 19, 1957).

6. Thoria which had been blown through a hollow carbon into an electric arc gave evidence of some carbide formation. The calcined powder is being tested by the Slurry Corrosion Group.

7. Investigation of some possible causes of the formation of lumps in calcining thoria at 1600°C showed that irregular compaction of the powder in the containers prior to calcination might be a cause and that steam (as from wet thoria) had little or no effect in causing lumps when it was introduced into powdered ThO_2 during heating to 1600°C and subsequent cooling below red heat.

SiC-Si FUEL ELEMENTS

J. M. Kerr F. L. Carlsen, Jr.

Development of an SiC-Si fuel element has progressed some in the past few months, but the main problem of incorporating more than 10% of UO_2 in the core still remains. Some success has been achieved in solving many of the problems concerning the fabrication of the fuel elements.

Results indicate that the most critical pressing problem in the fabrication of the SiC-Si fuel elements is the impregnation step in which the green bar is immersed in molten silicon, which must be controlled for several reasons. When the bar is immersed in the molten silicon it is necessary for the reaction between silicon and graphite to go as nearly to completion as possible, yet the temperature must be low enough for the reaction between silicon and UO_2 to be held to a minimum. With bars containing only SiC with minor amounts of graphite (~3% of the binder used), the temperature of the melt must be much higher than with bars containing appreciable graphite. However, bars made of graphite alone have such a highly exothermic reaction that even though the temperature necessary to initiate the reaction is low, the temperature attained during the reaction is extremely high and leads to an excess of uranium silicide formation. In an effort to combine the low initiation temperature and the low temperature of reaction, a body containing a 10% addition of graphite was used. This led to reasonable temperatures at which the reaction would start and at the same time held the reaction temperature in check.

Another aspect of the temperature control problem is that if the UO_2 grains are large and dense, reaction with the silicon is held to a minimum, but if they are overexposed to the molten silicon there will be appreciable reaction. One method to combat silicide formation, then, is to have the reaction proceed rapidly up the bar so that the fuel will not be exposed to the silicon any longer than is absolutely necessary. With the 10% addition of graphite to the SiC body the reaction progresses at a moderate rate, and metallographic examination of polished sections of these fuel elements showed that formation of the silicide was very slight and was confined to the core. The problem of accurate melt-temperature control can be overcome by the use of proper equipment, which will be imperative should it become necessary to produce more than research quantities of these fuel elements.

The Engineering Properties Section of the Solid State Division will receive six each of SiC-Si bars, $1\frac{1}{2} \times 1 \times \frac{1}{8}$ in., with loadings of 0.44 and 0.88 g of fully enriched UO_2, which constitute ~5 and 10% of UO_2, respectively. The fuel elements will be irradiated in the ORR. It is anticipated that there will be a burnup of at least 9 at. % with a heat flux of 300 w/in.^{2} at 1000°C. It is not certain how many thermal cycles will occur, but there will possibly be as many as 50.

Future work on SiC-Si fuel elements will include investigations on reaction rate control in the immersion technique and investigations into the possibility of producing these elements by a process called "dry shooting." This process involves the incorporation of the silicon as a fine powder in the element, with subsequent firing to melt the silicon and cause it to react with the graphite. This will entail investigations of the amount of silicon necessary to have a complete reaction, the optimum temperature at which this will take place, and procedures which must be used in getting the element in and out of the temperature zone quickly. It is anticipated that dry shooting will hold more promise in the future than the immersion technique, since it lends itself to closer control of the silicon content and reaction temperature.

WASTE DISPOSAL

T. N. McVay[5] J. M. Kerr
M. P. Haydon R. L. Hamner

The waste disposal work for the past year has been covered in topical reports.[6]

[5]Consultant, Bureau of Mines.

[6]T. N. McVay *et al.*, *The Fixation of Radioactive Wastes in Ceramic Masses. Part I. Fixation of Radioisotopes Present in Hope Solution; Part II. Purex Wastes*, ORNL-2611 (in press).

RESEARCH IN RARE-EARTH CERAMICS

C. E. Curtis A. G. Tharp

Europium Oxide

Since the work on europium oxide is being reported in the open literature,[7] it will not be described here.

Samarium Oxide

Ceramics of Sm_2O_3 when fired at above 1300°C tended to react with boiling water as previously reported. This tendency was not obviated by firing the oxide at 1500°C in an oxygen atmosphere to prevent reduction to a lower oxide.

Ceramics of 13 Rare-Earth Oxides

The oxides of the entire rare-earth series (except promethium) in 99 to 99.9% purities were heated in the form of small pressed pellets at 1300, 1500, and 1600°C in both hydrogen and oxygen atmospheres. Some tentative conclusions reached are the following:

1. Sintering of the oxides of the five elements of lower atomic number (CeO_2 to Eu_2O_3) occurs most rapidly at 1300 to 1500°C; the other eight oxides (Gd_2O_3 to Lu_2O_3) are more refractory and sinter more rapidly between 1500 and 1600°C.
2. In compacts sintered at 1600°C, the densities of the rare-earth oxides do not increase regularly with increase in atomic number; they may be grouped as shown in Table 42.
3. Oxidizing and reducing atmospheres in firing at 1300, 1500, and 1600°C appeared to have no consistent effect on any of the 13 oxides.
4. All the fired compacts were resistant to moist air except the Pr_2O_3 and Nd_2O_3 compacts, which disintegrated in moist air at room temperature. As previously reported, Sm_2O_3 (ref 8) and Eu_2O_3 (ref 9) fired at above 1300°C react with boiling water at atmospheric pressure.

STUDIES OF OXIDE AND FLUORIDE SYSTEMS

The studies carried out in this past year entailed an investigation of the system ThO_2-SiO_2 and crystal structures of some fluoride compounds, and have been reported elsewhere.[10–14] Two papers are awaiting publication.[15]

---

[7] C. E. Curtis and A. G. Thorp, "Ceramic Properties of Europium Oxide," to be published in *J. Am. Ceram. Soc.*

[8] C. E. Curtis and J. R. Johnson, *J. Am. Ceram. Soc.* 40, 15–19 (1957).

[9] C. E. Curtis and A. G. Tharp, "Ceramic Properties of Europium Oxide," to be published in *J. Am. Ceram. Soc.*

[10] L. A. Harris, *The Crystal Structure of* Rb_3UF_7, ORNL CF-58-1-26 (Jan. 6, 1958).

[11] L. A. Harris, *The Crystal Structure of 7:6 Type Compounds of Alkali Fluorides with Uranium Tetrafluoride*, ORNL CF-58-3-15 (March 6, 1958).

[12] L. A. Harris, *A Preliminary Survey of Some Fluoride Compounds. I*, ORNL CF-58-3-44 (March 10, 1958).

[13] L. A. Harris, *A Preliminary Survey of Some Fluoride Compounds. II*, ORNL CF-58-5-17 (May 14, 1958).

[14] L. A. Harris, *The Crystal Structure of* RbU_6F_{25}, ORNL CF-58-5-63 (May 15, 1958).

[15] L. A. Harris, "A Preliminary Study of the Phase Equilibria Diagram of ThO_2-SiO_2" and "The Crystal Structures of Na_3ZrF_7 and Na_3HfF_7," to be published in *J. Am. Ceram. Soc.*

Table 42. Density of Rare-Earth Oxides Sintered at 1600°C

Oxides	Atomic Numbers of Elements	Density at 1600°C Range
CeO_2, Pr_2O_3, Nd_2O_3	58, 59, 60	6.5 to 7.0
Sm_2O_3, Eu_2O_3, Gd_2O_3, Tb_2O_3, Dy_2O_3, Ho_2O_3, Er_2O_3	62 to 68	7.0 to 7.7
Tm_2O_3, Yb_2O_3, Lu_2O_3	69 to 71	8.7 to 9.4

METALLOGRAPHY

R. J. Gray

R. S. Crouse
E. L. Long, Jr.
W. H. Bridges
C. Hays
T. M. Kegley
J. R. Riddle
J. E. VanCleve

Electron Microscopy

E. L. Long, Jr. W. H. Bridges

High-Magnification Work. – The RCA model EMU-3B electron microscope has recently been equipped with a high-magnification adapter which makes possible a direct magnification of up to 200,000X and a total magnification approaching 1,000,000X. While such magnifications have limited application in ordinary electron metallography, they are useful in studying submicroscopic particulate materials, thin films, and thin foils.

Modified Replication Technique. – Since bulk metallic specimens are not directly viewable in the electron microscope, it is necessary to prepare a thin, accurate replica of the surface for indirect observation. The most easily prepared replicas are those made of thin plastic materials which can be cast on the surface and stripped dry. Replicas of this nature suffer from two major defects: a resolution of better than 200 Å is difficult to attain, and the plastics which are suitable tend to strain and give rise to artifacts. The common cast replica materials employed in this group are Formvar in chloroform or dioxane, and collodion in amyl acetate. The plastic solution is flowed over the sample surface, drained off, and allowed to dry. A 200-mesh grid, $\frac{1}{8}$ in. in diameter, is placed on the surface and then moistened, usually by allowing breath moisture to condense on it. After scotch tape is applied and is tightly adhering to the coated surface, the entire replica, with the grid, is carefully pulled from the sample. The grid with its plastic film is teased from the scotch tape and shadowed in vacuum with a metal having a high scattering cross section for electrons. The replica is now ready for examination in the electron microscope.

Unfortunately, the plastic replicas will not strip readily from the surface of the zirconium-alloy specimens of interest to the HRP Group. It has, therefore, been necessary to use a different replication technique. Thin carbon films have excellent resolution of at least 50 Å and do not give rise to strain artifacts. The greatest difficulty in their use is in removing them from the sample surface. The standard technique is given on the left of Table 43. Pieces of carbon film large enough to examine are successfully removed about 25% of the time. In other instances, either nothing comes off or the film breaks into extremely small pieces as a result of the violent acid treatment. Obviously, the acid etch precludes the re-replication of the surface without repolishing and its attendant difficulties.

Grube and Rouze[1] were successful in replicating steel surfaces with carbon without the necessity of acid treatment by first coating the surface with a wetting agent, Victawet 35B.[2] While such a technique introduces another step in vacuum, the evaporation of the Victawet 35B onto the sample, it eliminates the many washes required after replica removal. In applying the method to the zirconium-alloy samples, replicas have been successfully removed at least 90% of the time. Moreover, the replicas were not disrupted and broken, but usually remained in a raft from which pieces from various locations about the sample could be selected for examination. If necessary, the sample could be re-replicated without repolishing. The modified procedure, listed in the right column of Table 43, has been adopted for standard use in this laboratory. According to the original description,[1] a small amount of Victawet (0.5 to 1 mg) was placed in a conical basket for evaporation. Unless the greatest care was exercised in heating, the material would tend to spit and sputter and jump from the basket. This difficulty has led many researchers to abandon its use and seek other methods or materials, the latest case in point being Boswell,[3] who changed to B_2O_3. Our success with the Victawet is believed to be due to the novel filament used for its evaporation. Six to ten turns of 26-gage tungsten wire are wound into a pancake coil, and the

[1] W. L. Grube and S. R. Rouze, *Am. Soc. Testing Materials Proc.* 52, 573 (1952).

[2] Made by the Victor Chemical Works, Chicago, Ill.

[3] F. W. C. Boswell, *Rev. Sci. Instr.* 28, 723 (1957).

Table 43. Comparison of Steps for Original and Modified Carbon Replication

Original	Modified
1. Sample placed in vacuum chamber	1. Sample placed in vacuum chamber
	2. Victawet evaporated onto sample
2. Shadowing material evaporated onto sample	3. Shadowing material evaporated onto sample
3. Carbon evaporated onto sample	4. Carbon evaporated onto sample
4. Sample removed from vacuum chamber	5. Sample removed from vacuum chamber
5. Scribed into $\frac{1}{8}$-in. squares	6. Scribed into $\frac{1}{8}$-in. squares
6. Sample exposed to acid vapor	
7. Sample is slid into water	7. Sample is slid into water
8. Individual pieces of replica picked up	8. Individual pieces of replica picked up
9. Replica washed	
10. Replica washed	
11. Replica washed	
12. Replica dried	9. Replica dried
13. Replica examined	10. Replica examined
(To be re-replicated, sample must be repolished and etched)	(Sample may be re-replicated without additional effort)

Victawet is "buttered" on. Since the initiation of evaporation can be observed, the danger of overheating is greatly reduced. Our experience indicates that, where Victawet is properly employed, no serious loss in resolution occurs.

Specimens which have rough surfaces or contain many voids do not replicate well, even under the best conditions. For such specimens, a primary replicating material is needed which is very strong. Such a material is thin (0.005 in.) cellulose acetate. A solution of cellulose acetate in acetone is flowed over the specimen surface and the thin sheet of cellulose acetate is pressed firmly over it. After drying a short time, the film is removed. Because the sheet of cellulose acetate is entirely too thick to view directly in the electron microscope, a carbon replica is made of the area that was in contact with the specimen. It had been the general practice to dissolve the cellulose acetate film away from the carbon replica, the greatest hindrance being that the film swelled and ruptured the replica. By replicating the film with our modified technique, which employs a wetting agent, the replicas are removable in water, thereby decreasing the difficulty.

In contrast to the difficulties of a year ago, the replication of specimens is no longer a major problem. Techniques have been developed which yield good replicas most of the time from properly prepared specimens. The major stumbling block has now become the preparation of samples from which certain specific information is desired: the observation of minor phases in many alloys is an example. While many of these phases are visible in light microscopy by virtue of being stain etched, this is of no assistance in electron microscopy; hence, suitable etchants must be developed which do not leave surface films and yet will delineate the various phases.

The Structure of Electropolished and Anodized Aluminum Surface. – The surface appearance of anodized aluminum is seemingly optically anisotropic in nature when viewed under polarized light. (It is known that aluminum oxide is not optically active.) A Faxfilm replica of an anodized aluminum surface, when viewed optically with transmitted light, also behaves actively. That fact would indicate that the character of the surface, rather than the oxide itself, is responsible for the apparent activity. A sample

of superpurity aluminum was anodized to give a coating less than 500 Å in thickness. It was then replicated with carbon and the replicas were examined. The surface was composed of at least two differently appearing structures, as shown in Fig. 120. While both structures had the same general characteristics, one was aligned with a remarkably uniform spacing, that of a furrowed structure not unlike a plowed field; and the other was random, very similar in appearance to "crinkle finish" paint. It would seem, then, that the optical activity is the result of the aligned structure acting as a grating when viewed with plane-polarized light.

In the literature, opinions vary as to the reasons for the development of such structures.[4,5] While, in general, the experimental results of the investigators are similar, their theories for the development are divided into two groups. It is the consensus that the "furrow" structure is orientation dependent. The remarkably uniform structure develops on the (110) planes in the <100> direction. On the (100) planes, a dotlike structure is developed. Some investigators feel the structure is definitely related to the structure of the metal. The other group is convinced that the cause is solely the action of the electropolishing and anodizing baths. There is much evidence supporting the two schools of thought; so confusion still exists. It appears desirable to perform a set of experiments to verify the results of previous investigations and to establish a basis for future work. In addition to the initial experiment, in which various structures were observed, a second experiment should be performed in an attempt to definitely relate the anodized structure to crystal orientation. Spherical single crystals of aluminum are under investigation. The sphere will be oriented by x-ray diffraction techniques, after which flats will be cut into the spheres on the (100), (110), and (111) planes. After electropolishing and anodizing, the indexed flats will be replicated and examined. Results of these examinations will then be compared with the previous results as to orientation dependence.

One by-product of the work thus far is that the replica can be used as a convenient calibration grating particularly useful at high magnifications. When the aluminum is anodized at 35 v for 30 sec,

[4]N. C. Welsh, *J. Inst. Metals* **85**, 129 (1957).

[5]M. Paganelli, *Alluminio* **27**, 3 (1958).

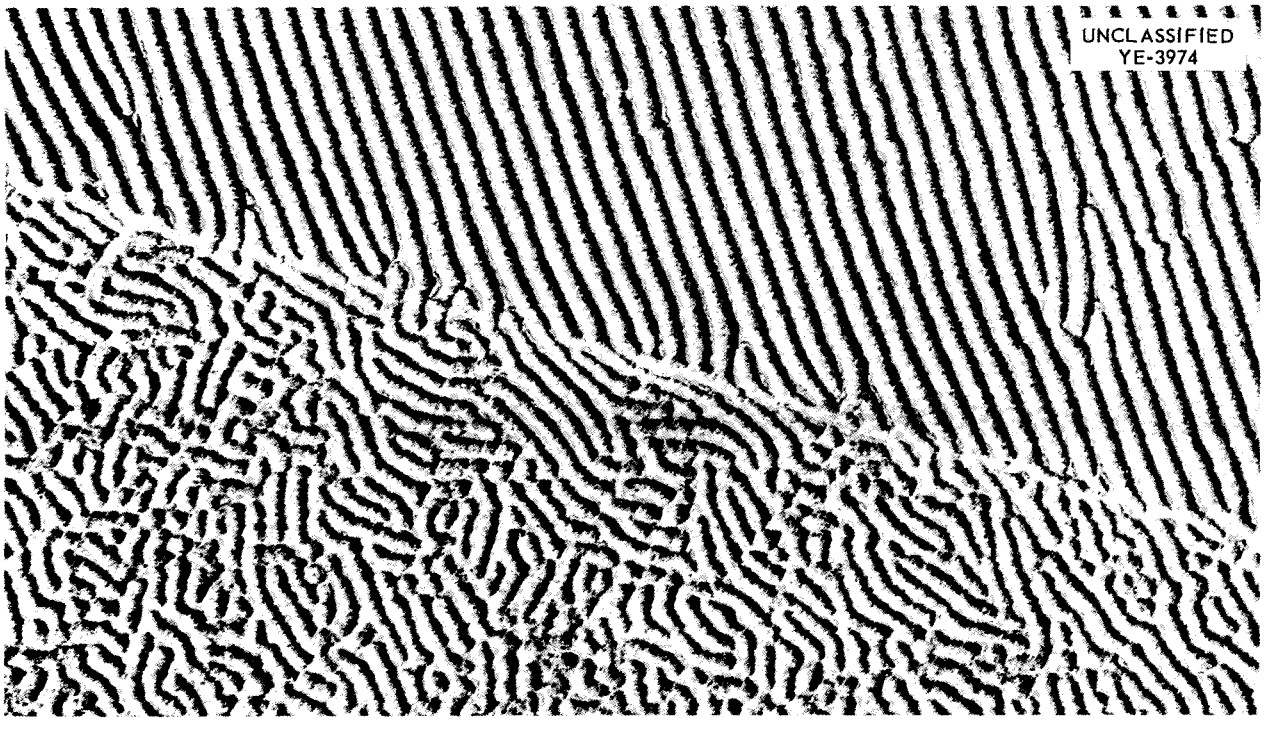

Fig. 120. Electron Micrograph of an Electropolished, Anodized, Super-Purity Aluminum Surface. Note the difference in the two structures separated by a grain boundary. Palladium-preshadowed carbon replica. 43,000X.

the "furrow" spacing is ~11,000 lines/mm. The replicas of ruled gratings commercially available have 28,500 lines/in., or 1122 lines/mm, which limits their use at 30,000X or above. By using an anodized aluminum replica, such as that of Fig. 121, calibration can be conveniently extended by a factor of almost 10.

Electron Microscopy in Color. – Color photographs inherently have two advantages over black-and-white pictures: (1) The eye is more sensitive to slight variations of color than to shades of gray, and (2) after development, all the silver grain in the emulsion is replaced with transparent dyes. The lack of grain tends to increase the useful enlargement of the picture. Unfortunately, there is no color associated with electrons, because they affect a photographic film only by penetration. Ordinary black-and-white film has a single emulsion, but color film has three – one for each of the primary colors. Therefore, any color image present after development would be the result of the depth of penetration of the electrons into the successive layers. In type B Ektachrome, the first layer is blue-sensitive, the second is yellow-sensitive, and the bottom layer is red-sensitive. It would be expected that the electron energy would be relatively homogeneous even after passage through the specimen and that the photograph would be monochromatic, the color being the result of total layer penetration. Some type B Ektachrome was put into the electron microscope and exposed in order to test the hypothesis. The exposure to 50-kv electrons resulted in a blue photograph with very good contrast. Exposure to 100-kv electrons gave a photograph predominantly olive green; but in areas where the replica was thin, there was a faint reddish hue. From these preliminary experiments, it is indicated that color film does indeed have a use in electron microscopy.

Postoperation Examinations of Heat Exchangers and Radiators

J. E. VanCleve

This work is a continuation of work done in 1957.[6] During the past report period, numerous pieces of power-generating equipment were examined after performance testing, and results are summarized below.

[6] J. E. VanCleve and R. J. Gray, *Met. Ann. Prog. Rep. Oct. 10, 1957*, ORNL-2422, p 156.

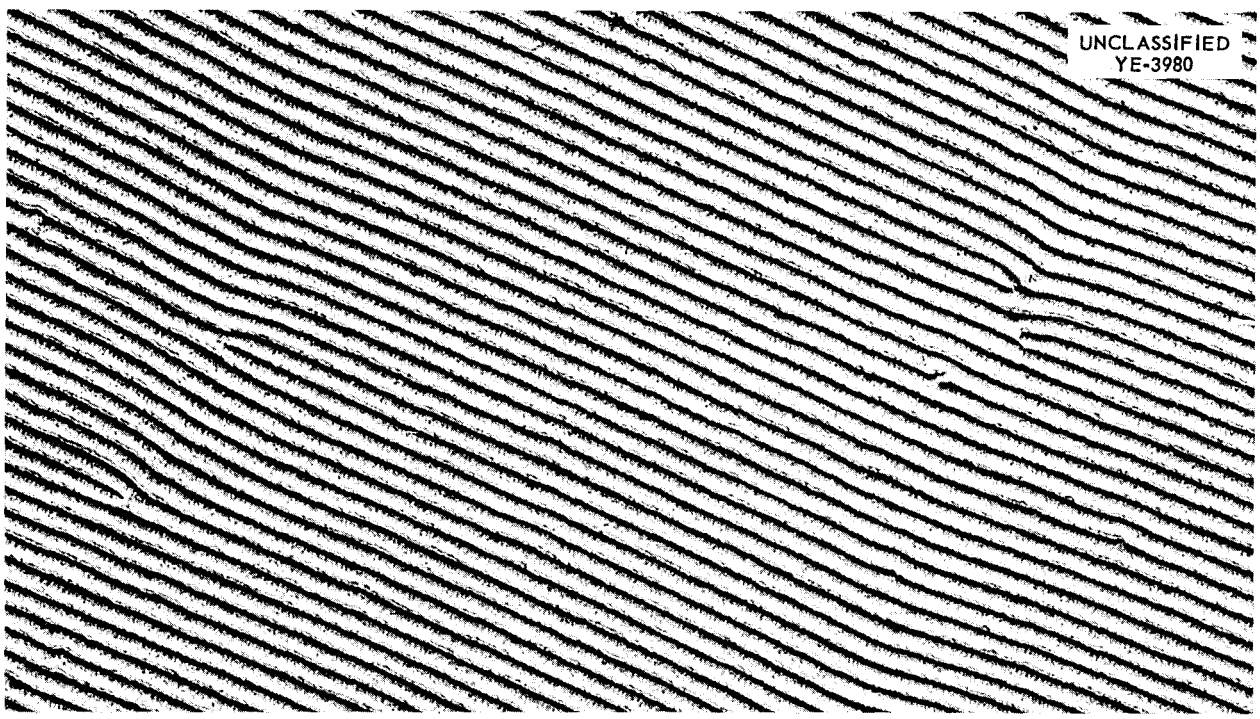

Fig. 121. Electron Micrograph of an Electropolished, Anodized Aluminum Surface. This particular oriented structure makes a convenient grating for high-magnification calibration. "Furrow" spacing is ~11,000 lines/mm. Palladium-preshadowed carbon replica. 34,400X.

York Radiator No. 11. – York radiator No. 11 operated in conjunction with Black, Sivalls & Bryson Nos. 1, 2, and 3 type IHE-8 heat exchangers for 2122 hr, of which 800 were under nonisothermal conditions. The radiator survived 173 thermal cycles and did not fail in test. The results of the examination for integrity of the fin-to-tube braze joints are presented in Table 44. Mass transfer and corrosion data were not obtained because the primary effort was directed toward the examination for imminent failure. This examination disclosed no sign of incipient failure.

York Radiator No. 12. – York radiator No. 12 operated in parallel with York No. 11, and both radiators were examined concurrently. The results of the examination for integrity of the fin-to-tube braze joints are presented in Table 44. The mass transfer and corrosion data again were not obtained. No evidence of incipient failure was observed.

York Radiator No. 17. – York radiator No. 17 operated 723 hr, of which 288 were under nonisothermal condition. The radiator endured 123 thermal cycles and failed in test.

The failure was in the same general location as in the York No. 16 and ART No. 16 radiators, that is, between the NaK inlet header and the fin matrix. No residue was found in these tubes to indicate the presence of a fuel-bearing plug, nor was any evidence of incipient failure detected. The cause of this failure remains undetermined.

York Radiator No. 18. – York radiator No. 18 operated for 344 hr, of which 114 were under nonisothermal conditions. The radiator endured 71 thermal cycles and failed in test. The failure location was again between the NaK inlet header and the fin matrix. Examination of the tubes for the presence of fuel-bearing plugs gave a negative result. Grain-boundary corrosion of the Inconel by NaK was found to extend to a maximum depth of 0.005 in.; however, this degree of corrosion did not seem to be sufficiently severe to have initiated the failure alone. The cause of this failure is still uncertain.

ART Radiator No. 2. – ART radiator No. 2 operated for 862 hr, of which 741 were under nonisothermal conditions. The radiator endured 181 thermal cycles and failed in service. A failure was located between the NaK inlet header and the fin matrix. One tube out of the 40 examined revealed deep penetration of the tube wall by grain-boundary voids. This condition has been associated with the previous failures. The exact cause of the failures observed is not completely understood, yet this type of failure is generally associated with grain-boundary voids which in time develop into fissures. The mechanism by which grain-boundary voids are formed is still somewhat uncertain. The results of the fin-to-tube braze-joint integrity examinations are presented in Table 44.

Black, Sivalls & Bryson No. 2 Type IHE-8 Heat Exchanger. – This heat exchanger operated successfully for 2122 hr, of which 800 were under nonisothermal conditions. The heat exchanger endured 173 thermal cycles and did not fail in test. Forty-eight samples were removed for examination. Corrosion on the fuel side of the tube ranged from a minimum of 0.001 in. in the cool zone to a maximum of 0.012 in. in the hot zone, as indicated by subsurface void formation. Corrosion on the NaK side

Table 44. Comparison of the Examinations for Integrity of Fin-to-Tube Braze Joints for Various Radiators

	Radiator		
	York No. 11	York No. 12	ART Test No. 2
Number of joint areas examined	2470	2714	1781
Per cent of joint areas having 75–100% adherence	89.6	58	95.8
Per cent of joint areas having 50–74% adherence	6.2	10	2.9
Per cent of joint areas having 25–49% adherence	1.2	4	0.5
Per cent of joint areas having 0–24% adherence	3.0	28	0.8
Per cent of joint areas having nonoxidized copper fins	56	30	80
Per cent of joint areas having slightly oxidized copper fins	16.6	20	12.7
Per cent of joint areas having heavily oxidized copper fins	27.4	50	7.3

ranged from a general roughening of the surface in the cool zone to 0.008 in. in the hot zone. This heat exchanger operated as the cold leg of the test loop, and no evidence of fissuring in the tube wall was found.

Black, Sivalls & Bryson No. 3 Type IHE-8 Heat Exchanger. – This heat exchanger operated for 1131 hr, of which 253 were under nonisothermal conditions. The heat exchanger endured 168 thermal cycles and did not fail in test. Forty-five samples were removed and examined. Corrosion on the fuel side ranged from a minimum of 0.001 in. in the cool zone to a maximum of complete penetration of the tube wall by grain-boundary voids at some boundaries. The NaK side of the tubes showed a general roughening of the surface in the hot zone and a maximum mass transfer deposit 0.010 in. thick. This heat exchanger showed evidence of failure, although a leak between the fluids was not picked up by the regular daily analysis of the fluids.

ORNL No. 1 Type SHE-9 Heat Exchanger. – This heat exchanger operated for 1139 hr, of which 400 were under nonisothermal conditions. The heat exchanger endured 194 thermal cycles and failed in test by a NaK-to-fuel leak. Thirty samples were removed and examined. The fractures were detected in three tubes in the "tension side." The fissures seemed to be the result of the progression of grain-boundary voids, which culminated in cracks. The fuel-side corrosion ranged from a minimum of 0.001 in. in the cool zone to complete penetration of the tube wall in the hot zone. The NaK-side corrosion ranged from complete penetration of the tube wall (at the fissures where the types of voids are indistinguishable) to a general roughening of the surface in the cool zone.

Metallography for Homogeneous Reactor Project

T. M. Kegley, Jr.

Metallographic work for the Homogeneous Reactor Project has been concerned chiefly with corrosion, failure analysis, and development problems. A variety of problems were studied metallographically, including those pertaining to valves, pumps, heat exchangers, corrosion test loops, slurry test loops, recombiners, welds, and corrosion specimens. A brief description of some of the work accomplished follows.

The heat exchanger in the HRT mockup consisted of a bundle of thirty-seven $\frac{3}{8}$-in.-dia tubes inside a 6-in.-dia pipe. Uranyl sulfate solution circulated through the tubes, which were of type 347 stainless steel. Associated with heavy scale formation on the inside surface of the tubes was an unusual intergranular oxide penetration (Figs. 122 and 123). Unusual features of this intergranular penetration are grains of corrosion product which appear to consume whole grains of metal without an apparent change in volume, and layers of metallic substance between layers of corrosion product.

Sections of type 347 stainless steel pipe from the HRT mockup letdown heat exchanger were examined. Stress-corrosion cracking was found on surfaces that were exposed to the uranyl sulfate feed stream and the purge-water system.

Two type 347 stainless steel bellows heads from HRT low-pressure bellows valves exhibited cracking after ~2000 hr of operation. Figures 124 and 125 show transgranular cracks found in the bellows head from bellows valve K-46. Cracking may have been due to a chloride-containing asbestos gasket which rested against the top surface of the bellows head.

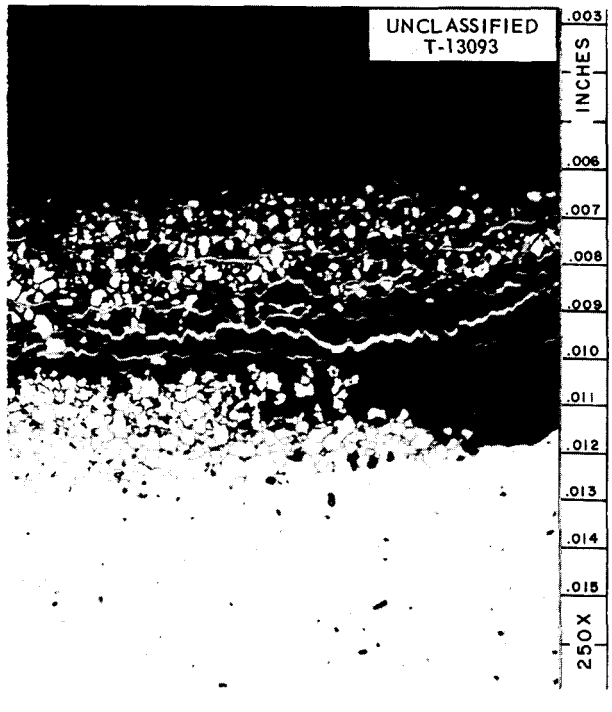

Fig. 122. Intergranular Oxide Penetration Found on Surface of HRT Mockup Heat Exchanger Tubes. As polished.

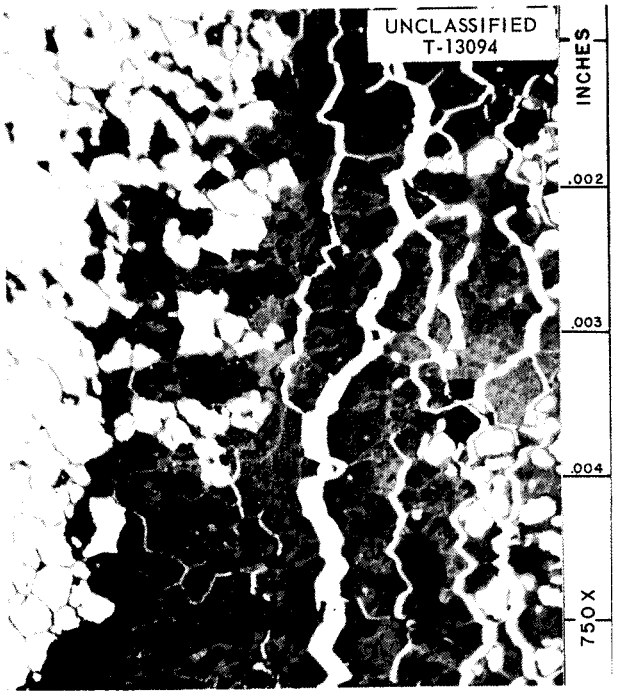

Fig. 123. Portion of Region Shown in Fig. 122 at Higher Magnification. As polished.

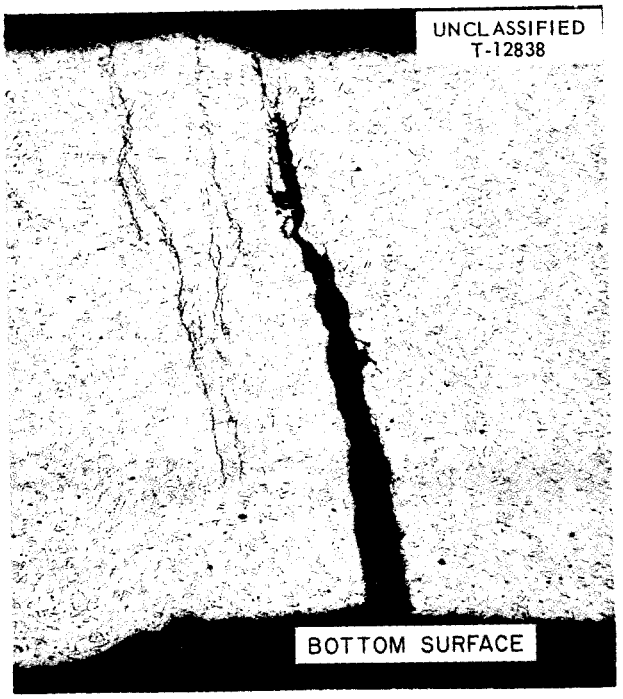

Fig. 124. Transgranular Cracking Found in Bellows Head from HRT Bellows Valve K-46. Etchant: aqua regia. 75X.

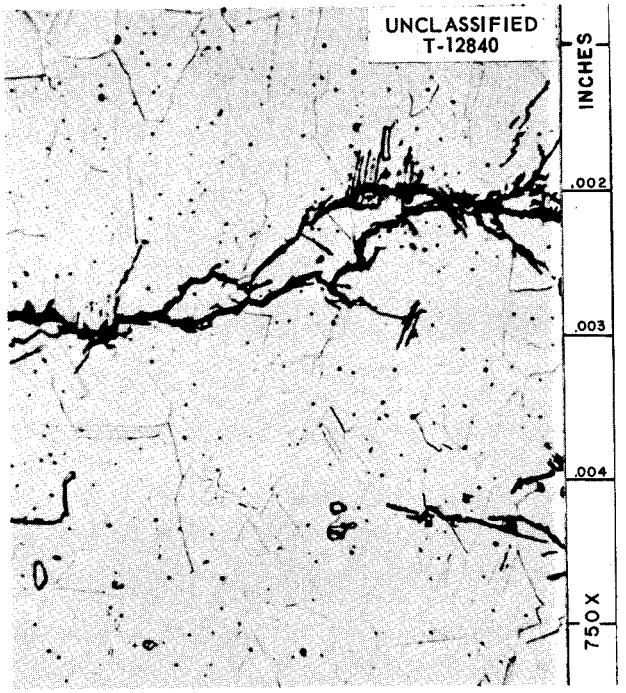

Fig. 125. Magnified View of Cracks Shown in Fig. 124. Etchant: aqua regia.

Cracking occurred in the galvanized iron–stainless steel joints of the HRT cell-top seal pans. The cracking observed in both the stainless steel base metal and the weld material was intergranular in nature. In the case of the base material, the cause of cracking was traced to molten zinc (from the galvanized iron), which attacks the stainless steel intergranularly.

A recombiner boiler of type 347 stainless steel that failed in test by cracking near weld joints was examined. The boiler had operated at 235°C in an environment of 15 to 20% KOH solution, steam, hydrogen, and oxygen. The cracking observed was both transgranular and intergranular in nature. The appearance of cracks found near a weld joint is shown in Fig. 126. Figure 127 illustrates the intergranular type of cracking found. Since cracking occurred only in regions adjacent to the weld joints, it appeared that welding had created high residual stresses which, along with the corroding environment, caused the boiler to fail through stress corrosion.

A steam heater from the dump-valve test loop failed after 6039 hr of operation in contact with uranyl sulfate solution. The heater consisted of a

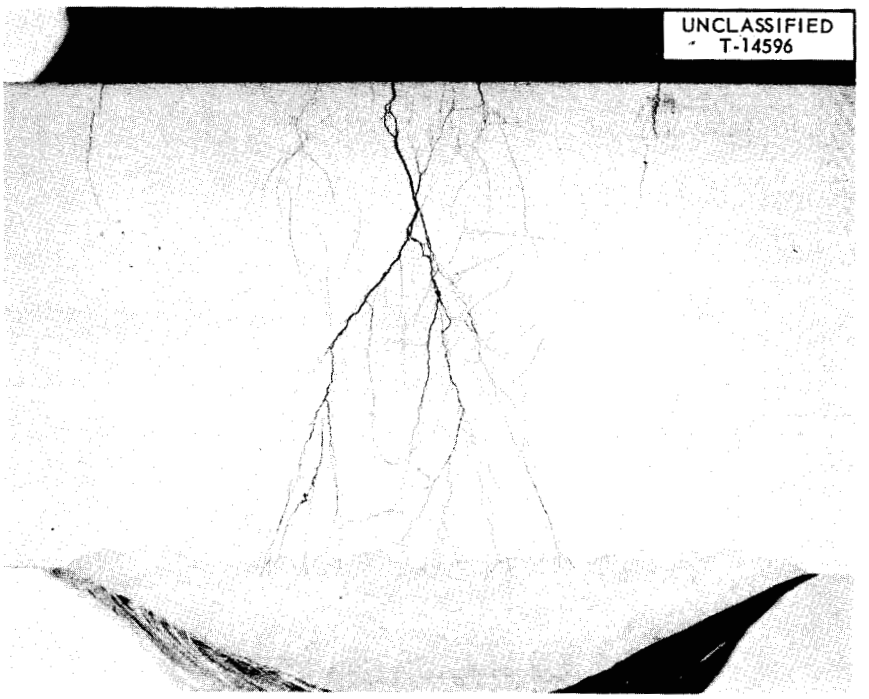

Fig. 126. Cracking Near Weld in Recombiner Boiler. Etchant: aqua regia. 3X.

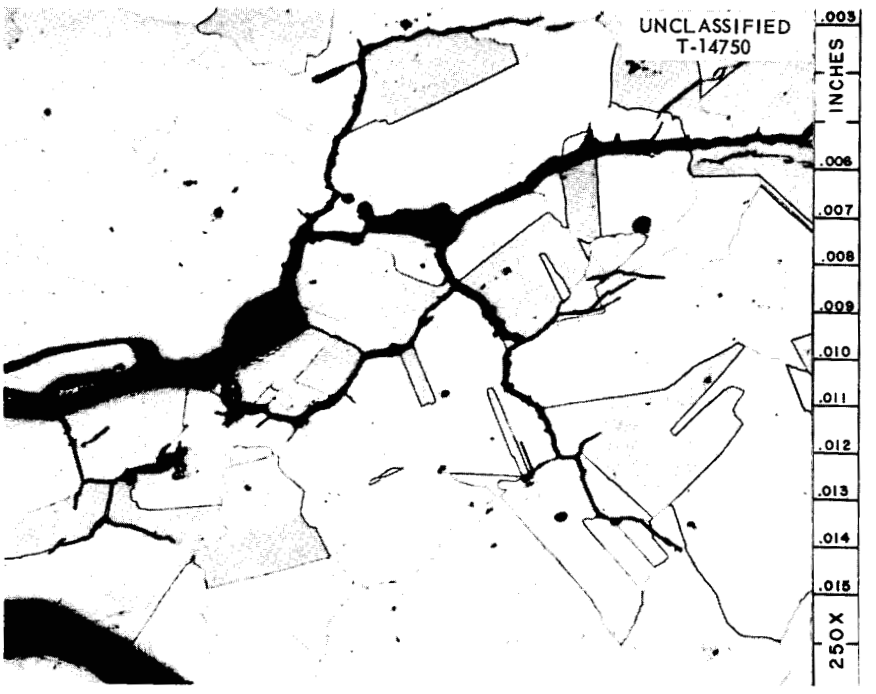

Fig. 127. Intergranular Cracking Found in Recombiner Boiler. Etchant: aqua regia.

½-in. sched 80 type 347 stainless steel fuel line and an outer carbon steel steam jacket. Figure 128 is a macrograph of the fuel line showing that the cracking originated inside, while the photomicrograph in Fig. 129 illustrates the transgranular nature of attack.

A ½-in.-OD heavy-wall type 347 stainless steel pipe served as an addition port to a loop that circulated oxygenated thorium oxide at about 250°C. Transgranular cracks, observed on examination of sections from the addition port, were probably due to chloride stress corrosion.

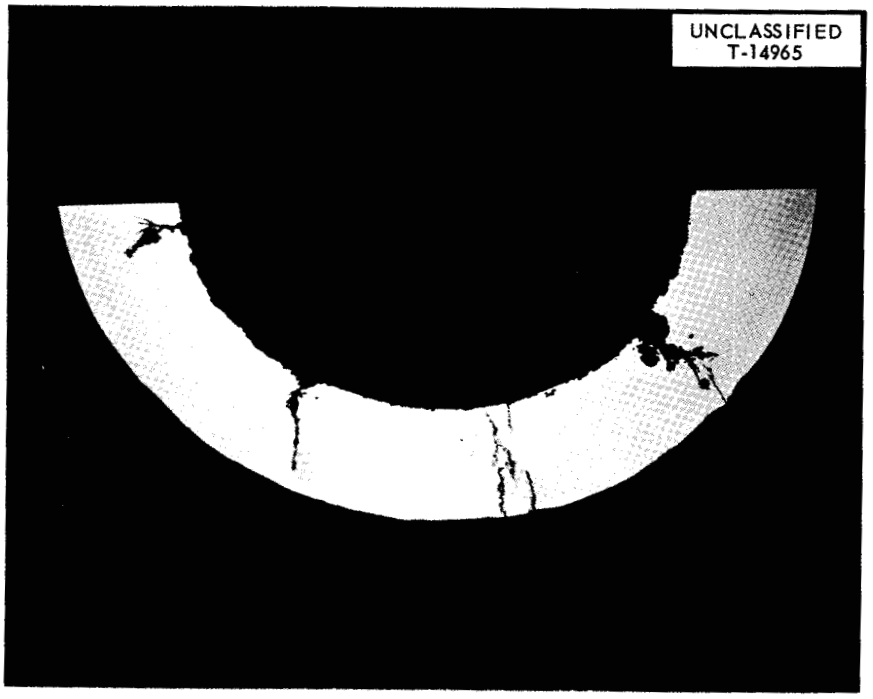

Fig. 128. Cracking in Dump-Valve Test-Loop Steam Heater. 4.5X.

Fig. 129. View of Cracking in Dump-Valve Test-Loop Heater at Higher Magnification. Etchant: glyceria regia.

A type 347 stainless steel bearing ring for a pump exhibited an unusual volume change when cooled in liquid nitrogen prior to insertion in the housing of the pump. Metallographic structures of the steel from which the bearing was made are shown in Figs. 130–132. Before the steel is cooled in liquid nitrogen, it is completely austenitic (Fig. 130). After cooling, martensite has precipitated from the austenite, as shown in Figs. 131 and 132. Figure 133 shows the surface of a specimen of the steel that was first polished and then immersed in liquid nitrogen. The polished surface has been distorted by the formation of martensite during the cooling in liquid nitrogen.

A $\frac{1}{4}$-in.-dia type 347 stainless steel tube, through which uranyl sulfate was circulated, was used in a corrosion loop as a part of a heater leg. The stainless steel tube was surrounded by a cast aluminum alloy jacket and a heater unit. An uncontrolled temperature rise, due to plugging of the tube, caused the aluminum alloy to melt and alloy with the stainless steel. Figures 134 and 135 show the effect of the alloying upon the stainless steel.

A silver-plated type 304 stainless steel wire mesh used as an iodine trap in the HRT mockup was

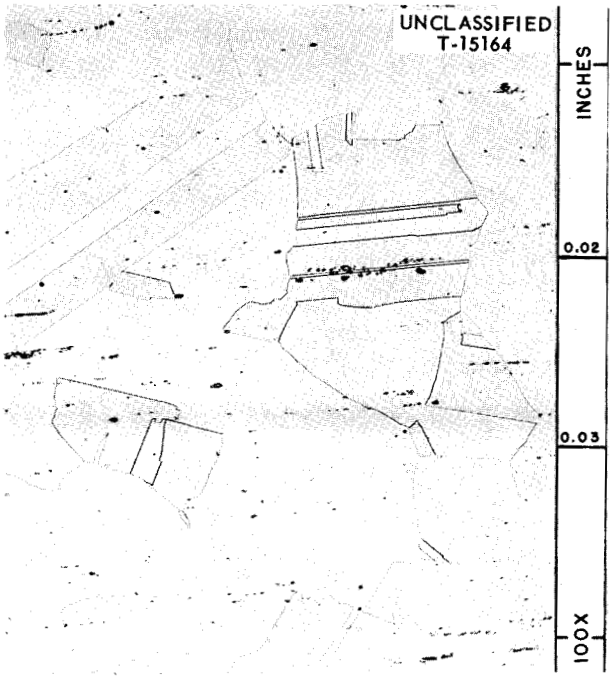

Fig. 130. Structure of Type 347 Stainless Steel Before Cooling in Liquid Nitrogen. Etchant: aqua regia.

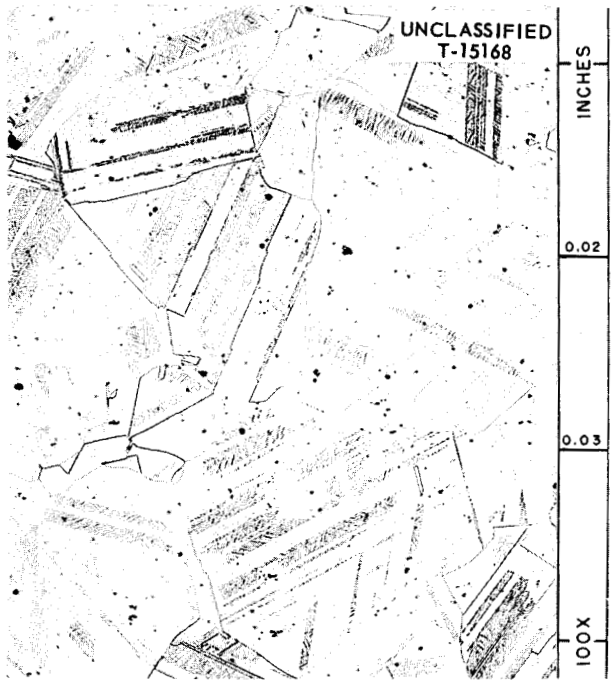

Fig. 131. Structure of Type 347 Stainless Steel After Cooling in Liquid Nitrogen. Etchant: aqua regia.

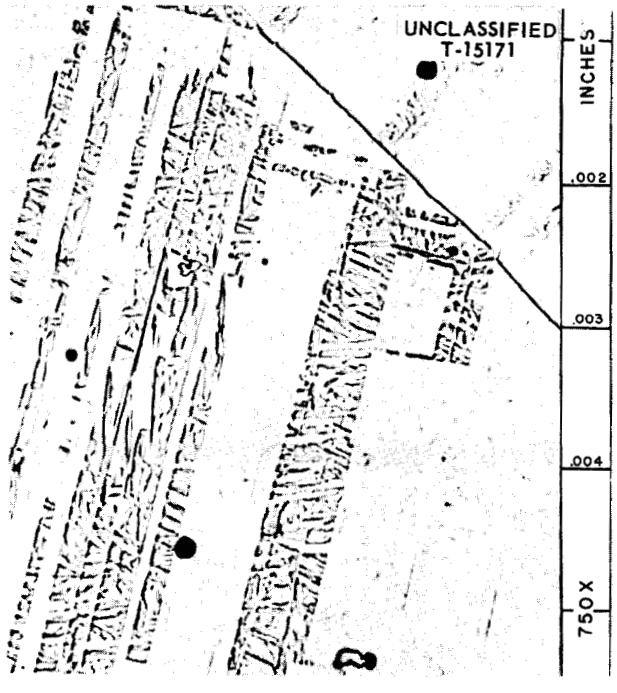

Fig. 132. Martensite Formed in Type 347 Stainless Steel During Cooling in Liquid Nitrogen. Etchant: aqua regia.

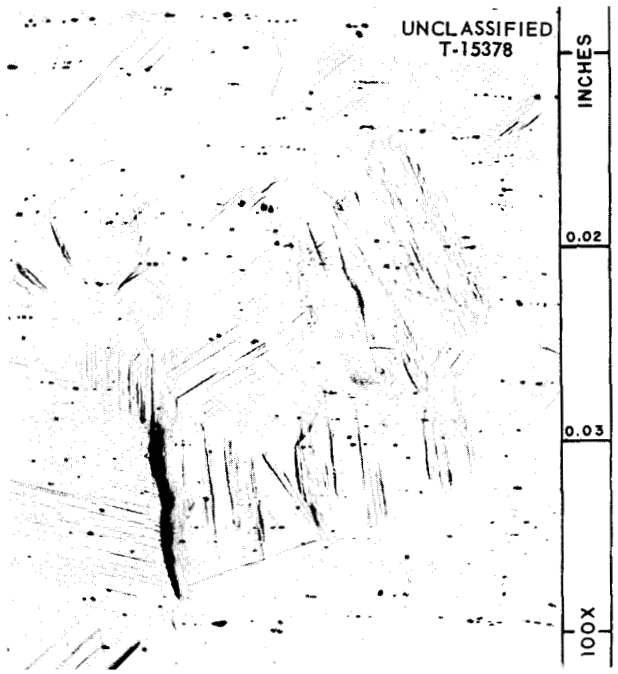

Fig. 133. Polished Surface of Type 347 Stainless Steel Specimen After Cooling in Liquid Nitrogen.

examined. Examination showed some spalling which was probably due to handling rather than to corrosion from steam in the mockup.

A titanium pin holder employed in a corrosion loop cracked upon being clamped to a milling machine table. The pin holder had been exposed to uranyl sulfate solutions for over 9000 hr at 175 to 300°C. It was found that the structure near the fracture contained considerably more hydride than the structure near the end of the specimen holder.

A thermal loop constructed of $\frac{1}{4}$-in.-dia Ti-75A titanium tubing failed while operating at 300 to 600 psi with uranyl sulfate solution. Transformed beta titanium was observed in the microstructure; this indicated that the tubing was heated above the beta transus, which is reported to be 950°C for Ti-75A. Therefore, excessive temperature and pressure were the cause of failure.

A small titanium bomb failed while being tested under water with 2000 psi of oxygen. The seat and plug in the head of the bomb suddenly ignited, probably through the exposure of a fresh unoxidized surface to oxygen. A section taken through the seat exhibited evidence of burning and exposure

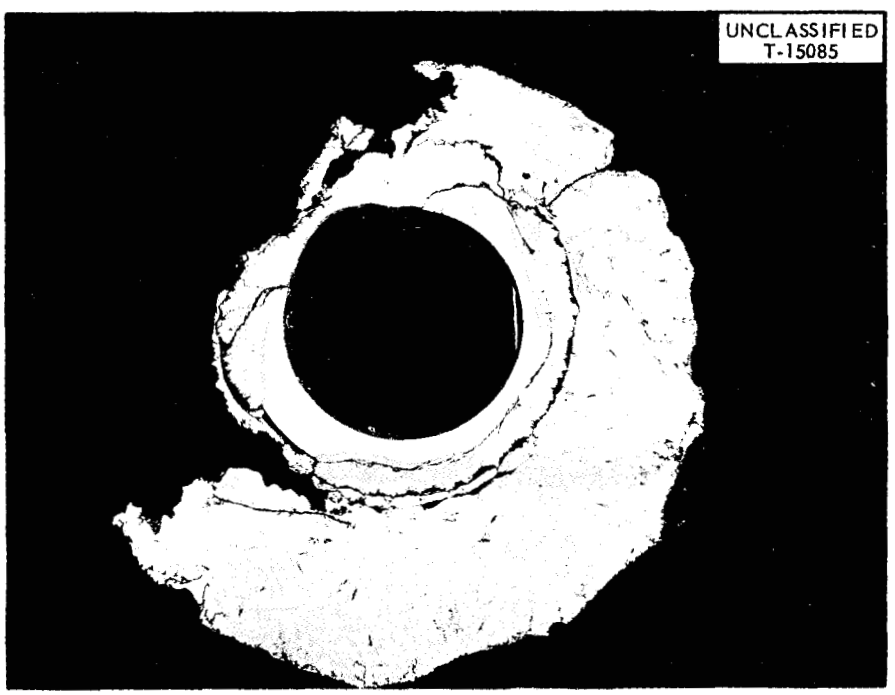

Fig. 134. Cross Section of Heater Leg from Corrosion Loop. Aluminum has alloyed with stainless steel. As polished. 7X.

to high temperature. Figures 136 and 137 are photomicrographs of the oxidized area of the seat.

Metallography for ANP, GCR, and MSPR

R. S. Crouse

Thermal Pulsing Tests. – In an attempt to answer certain questions regarding failures occurring in heat exchangers for the ART, tests were designed to explore the effect of drastic and rapid fluctuations in the temperature of molten fluorides flowing through Inconel tubing. In test, these fluctuations were achieved by pumping alternate slugs of hot and cooler molten fluoride through a section of Inconel tubing. The sole source for heating the test section was molten fluoride salt. The slugs entered the test section through a Y connection and a fast-operating valve, which alternately opened the line from each of two reservoirs, and allowed a constant flow of fluoride with varying temperature at a flow rate of 5 to 8 gal/min. Fluoride salt mixture No. 70 (56 mole % NaF, 39 mole % ZrF_4, 5 mole % UF_4) was employed in all tests except test No. 1, in which fluoride salt mixture No. 30 (50 mole % NaF, 46 mole % ZrF_4, 4 mole % UF_4) was used.

Metallographic examination was the chief means used for determining the extent of structural damage that occurred during test. In several instances, results indicated where design modifications would aid in avoiding trouble in the future. Results of all test data compiled to date are reported in Table 45.

The first four tests used a test section with a wall thickness of 0.029 in. Metallographic examination failed to disclose any cracks other than those at welds; hence, it was decided to use a heavier-walled pipe in subsequent tests. The cracks at welds were due basically to turbulence which caused higher temperature differentials, and thus greater stress.

In test No. V, both heavy wall thickness and numerous welds were used. This test failed below a weld due to rather heavy cracking, which could have been predicted from metallographic examination of previous tests. Deep cracking was found in the heavy-wall section. Therefore another design, with no welds in the test section and very heavy walls, was used through test No. XI.

Metallographic evaluation of tests Nos. VI through XI served to point out several factors that may have led to damage and subsequent failure, but not enough tests were run to determine the influence of the various factors on one another. It is obvious from study of Table 45 that increasing wall thickness, higher cycle amplitude, and higher total number of cycles tend to increase cracking. Tests XII and

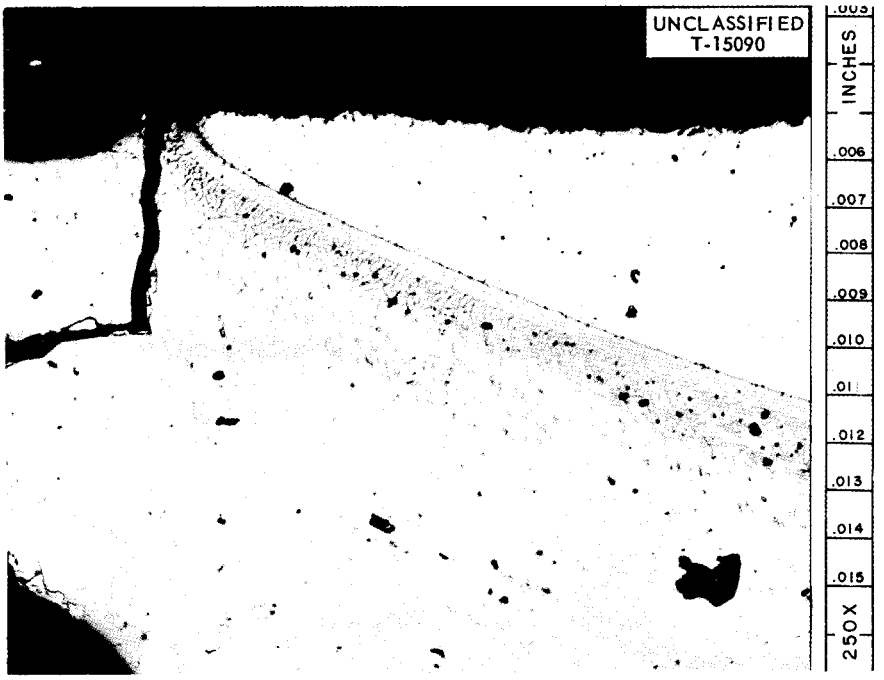

Fig. 135. Area of Complete Alloying at Inner Surface of Heater Leg from Corrosion Loop. As polished.

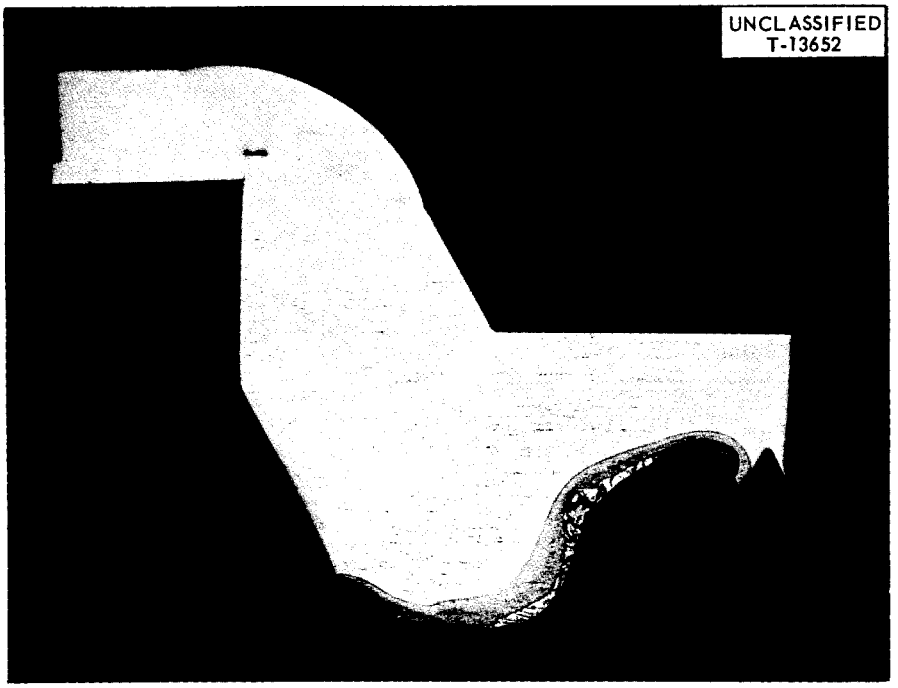

Fig. 136. Burned Seat from Titanium Bomb. Etchant: 5 HF–10 HNO_3–20 glycerin. 4.7X.

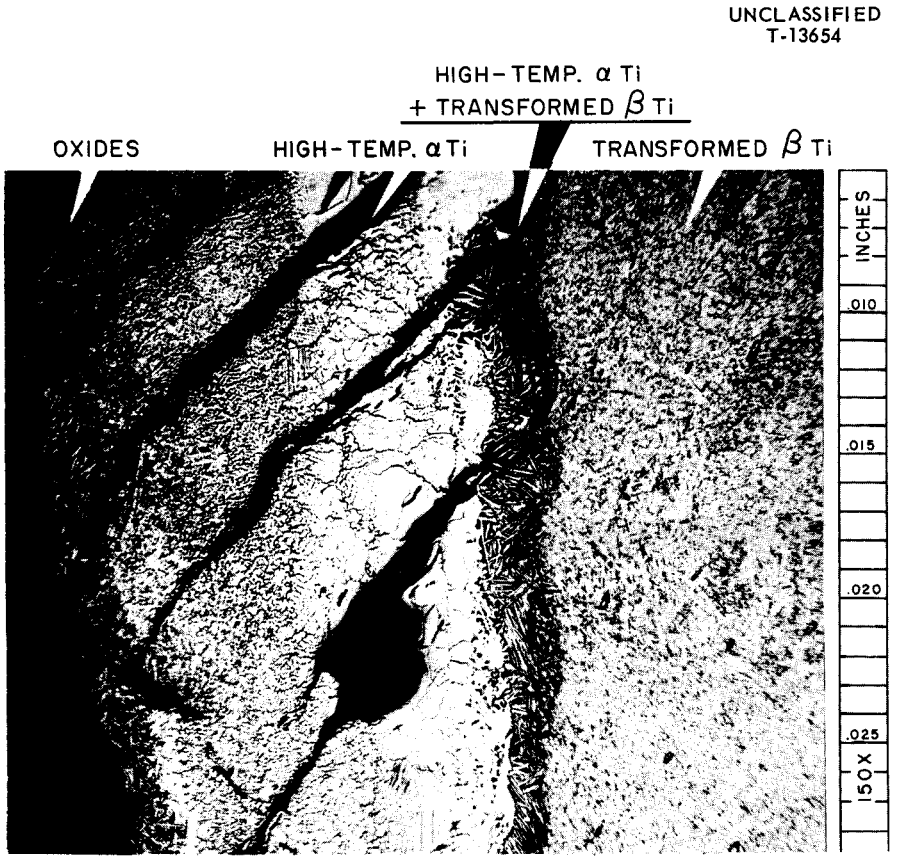

Fig. 137. Burned Surface at Seat of Bomb. Etchant: 5 HF–10 HNO_3–20 glycerin.

Table 45. Results of Thermal Cycle Tests

Test No.	Maximum Temperature (°F)	ΔT (°F)	Time with ΔT (hr)	Frequency (cps)	Total Cycles	Metallographic Results
I	1390	160	2.25	1	8,100	Light voids, no cracks
II	1360	215	0.5	1	1,800	Light voids, no cracks
III	1340	220–280	99.5	1.03	358,200	Scattered light voids; cracks in and near welds
IV	1614	454	250	1	900,000	Heavy cracking in and near weld
V	1658	493	135	0.4	194,000	Failed below a weld; cracks to 72 mils in heavy-wall section
VI	1546	484	22.8	0.4	32,800	Considerable cracking near top of test section
VII	1549	278	155.8	0.4	224,000	No crack in test section
VIII	1548	278.6	351.8	0.4	508,620	Heavy cracking to 85 mils at top of test section
IX	1682	550	200	0.1	72,000	Very heavy cracks to 207 mils, heaviest at bottom of test section
X	1697	569.5	75	0.1	27,000	Moderate to heavy cracks 5 to 103 mils deep
XI	1690	557	25	0.1	9,000	No cracks or attack
XII	1708	580	100	1	360,000	No cracks or attack
XIII	1708	580	214	1	770,100	Moderate cracks to 6 mils; failed due to faulty fabrication

XIII were of a new design and do not present enough data to make an evaluation.

Figures 138 and 139 are typical of the information obtained by metallographic examination of test sections. Figure 138 is a transverse section through the center of a heavy-wall test section removed from test No. IX. It illustrates the extent of cracking due to high cycle amplitude. The intergranular nature of these cracks is illustrated in Fig. 139.

Support Work for Activities Measurements. – The Metallography Group assisted S. Langer of the Chemistry Division in evaluating the data from his activities measurements. He is studying the activities of nickel and molybdenum in the alloy system by electrochemical means. He uses a simple cell setup with electrodes of pure nickel vs electrodes of nickel-molybdenum alloys in an electrolyte of NaCl-KCl eutectic plus $NiCl_2$. Activities are calculated from the measured potential across the cell.

Preliminary to the study of the test electrodes, samples of as received and as-annealed alloys were examined. The alloys were 95% Ni–5% Mo, 90% Ni–10% Mo, 85% Ni–15% Mo, 80% Ni–20% Mo, 78% Ni–22% Mo, 71% Ni–29% Mo, 68% Ni–32% Mo, and 65% Ni–35% Mo. Prior to test, all samples were solution-annealed at 2200°F for 16 hr in H_2. During test, they were held for about three weeks at 1470°F.

Due to the sluggishness of the formation of the β and γ phases, most alloys would be expected to present an essentially unchanged microstructure at the end of the test time, with no new phases appearing. This was true in all but the higher-molybdenum-content alloys. Figures 140 and 141 show a rather peculiar stain-like precipitate of the

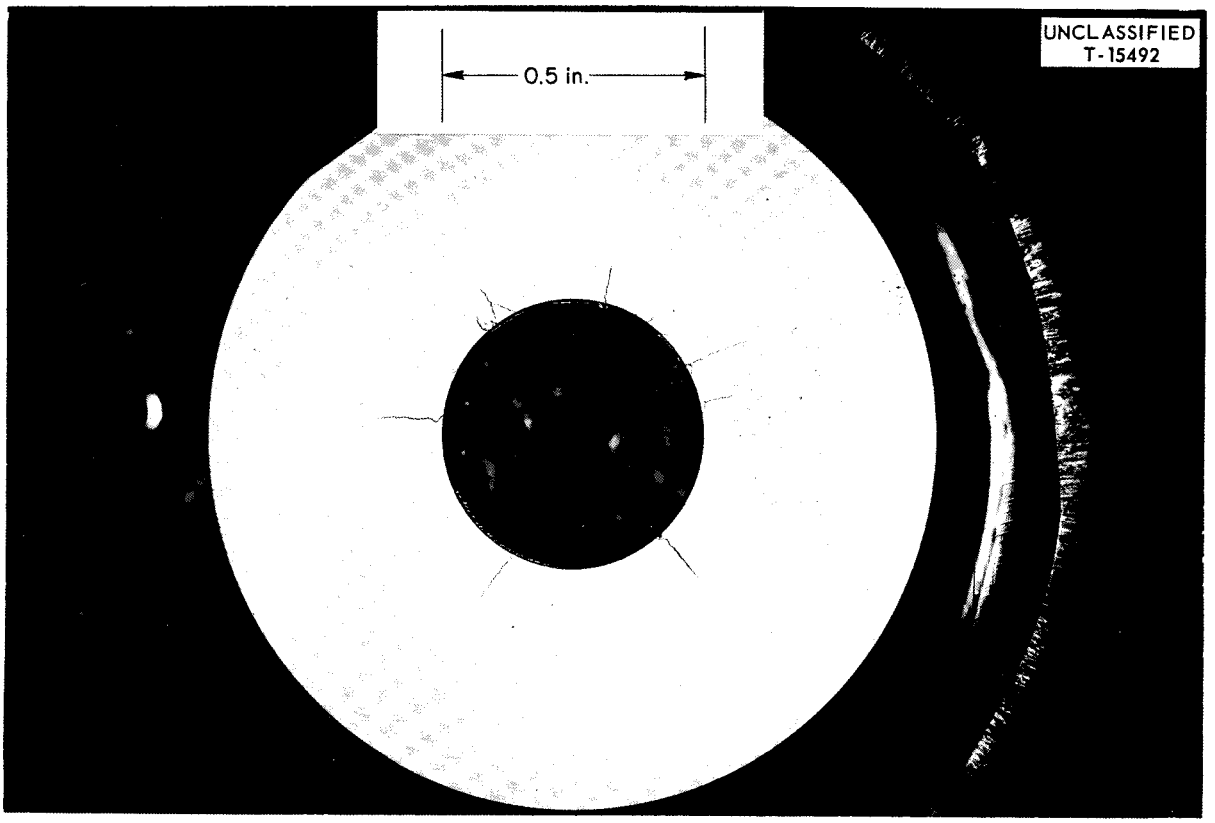

Fig. 138. Macrograph of Typical Heavy Cracking in Thermal Pulsing Test. 3X.

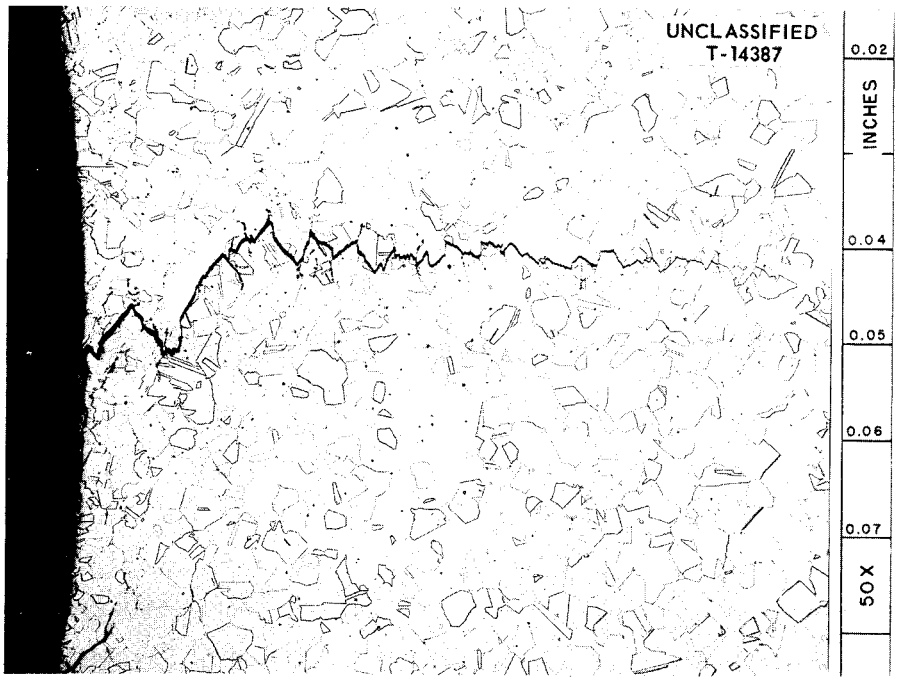

Fig. 139. Typical Crack Found After Thermal Pulsing Test. Note intergranular nature.

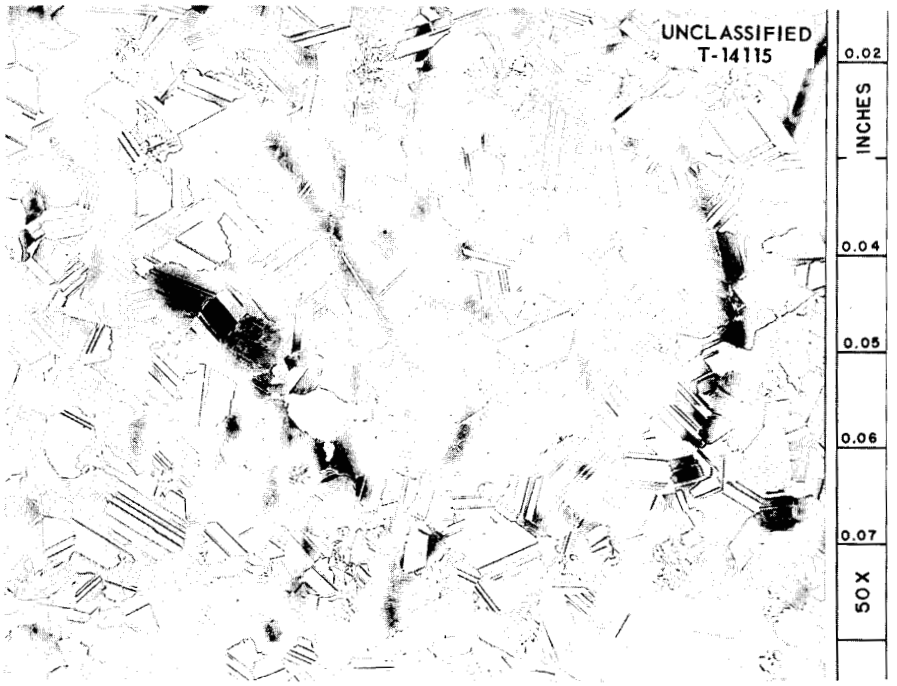

Fig. 140. Peculiar Stainlike Effect in 80% Ni–20% Mo Alloy from Activities Series Experiments.

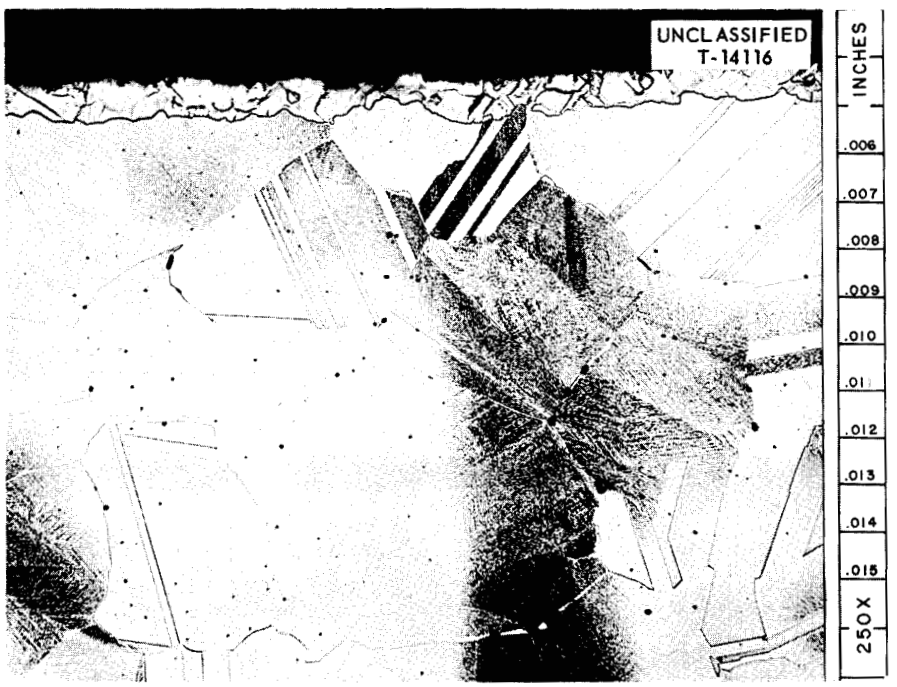

Fig. 141. Effect Shown in Fig. 140 at Higher Magnification.

β phase from an 80% Ni–20% Mo alloy after test. These markings were first thought to be stains; but they reappeared after repolishing and etching, which established them as true structure, not artificial.

Considerable difficulty was experienced in polishing the sample of pure nickel, and apparently patience and prolonged hand polishing with MgO on a Microcloth is the only way at the present time.

The Molten-Salt Power Reactor. – Following the curtailment of the ANP project, the Molten-Salt Reactor program was instigated to explore the possibility that the high-temperature fluoride technology which had been developed might be utilized for stationary power operation. Much of the data obtained in the ANP program was of great importance in starting studies in this program; therefore it was possible to launch directly into the study of long-time loops, with the result that the amount of work on loop examination has been sharply reduced. Only 25 thermal-convection loops have been examined during the past year, as compared with 110 for the prior 12 months. Pump-loop examinations took a corresponding drop from 26 to 8. There has been no change in the type of data required from metallography.

The Gas-Cooled Reactor. – The Gas-Cooled Reactor program is just getting under way this year, and numerous tests of a screening nature have been required. The Metallography Group has been called upon to examine many samples tested at high temperatures in contact with helium and graphite. The samples were wired to a block of graphite in an atmosphere of helium. Both sides of the samples were examined. Table 46 lists the different metals and alloys tested, with some general comments on metallographic observations.

Carburization is the condition most looked for in all the samples. So far, very little obvious carburization has been found, and microhardness traverses are now being made on all specimens. Not enough microhardness data has yet been obtained and assimilated to draw any conclusions.

Extraction and Identification of Microstituents in the Microstructure of Alloys

C. Hays

For some time the Metallography Group has needed a dependable scientific tool to aid in the identification of small particles so often seen in

Table 46. Alloy Screening Tests for Gas-Cooled Reactor

Alloy Tested	Metallographic Observations
Columbium	No attack, no carburization
Croloy 1¼	Apparently oxidized about 2 mils deep; surface rough
Croloy 2¼	Apparently oxidized about 2 mils deep; surface rough
Croloy 3M	Apparently oxidized about 2 mils deep; surface rough
Fe-Cr-Al	No attack, no carburization
Inconel	Erratic results; apparently some carburization
Molybdenum	0.1-mil surface layer of unknown composition
Tantalum	No attack, no carburization
T-1 Steel	Appears decarburized 1 to 1½ mils
Type 304 SS	No attack; slight carbon pickup
Type 316 SS	Grain boundary accentuation due to carbides
Type 410 SS	No attack, no carburization
Zircaloy-2	Attacked to 2 mils on He side of sample
Zircaloy-3A	Considerable grain growth; no carburization
Zr-Cb-Mo	Unexplained structure along surface; awaiting spectrographic analysis
Zirconium	Considerable grain growth

the microstructure of various alloys. These particles may be inclusions, questionable phases, or precipitations of many types. In any case, their mere presence can sometimes create an extremely difficult interpretation problem.

An instrument has been developed recently and placed into operation for limited laboratory use. The word limited is used only because development has not, as yet, been fully completed. Briefly, the apparatus layout consists of the following:

1. an ultrasonic cutting device similar to the type used by the dental profession,
2. two micromanipulators which allow easier handling of both the cutting tip and residue collector,
3. a conventional bench microscope which incorporates a specially built reflecting objective,
4. a wooden microscope base to dampen out undesired vibrations,
5. a voltage stabilizer that controls line-current fluctuations.

Most of these units are depicted in Fig. 142.

In regard to the chisel, the operative techniques are simple. First, a hardened wire, usually on the order of 0.025 in. in diameter, is electrolytically pointed to the desired curvature. The optimum shape desired is shown in the left inset of Fig. 142. Experiments have proved that spring-steel wire (ASTM A 228-41) or high-speed tool-steel drill rods are best suited for this application, since they cause no contamination of the extraction residues.

The pointed wire is attached to an α-brass metallic horn, which, when in contact with the transducer and excited, will transmit sound at a rate of 511,000 in./sec. This increase in the velocity of vibration for α-brass over the value that is normally expected (174,000 in./sec) is attributed to two factors. These are the precision design of the horn and the

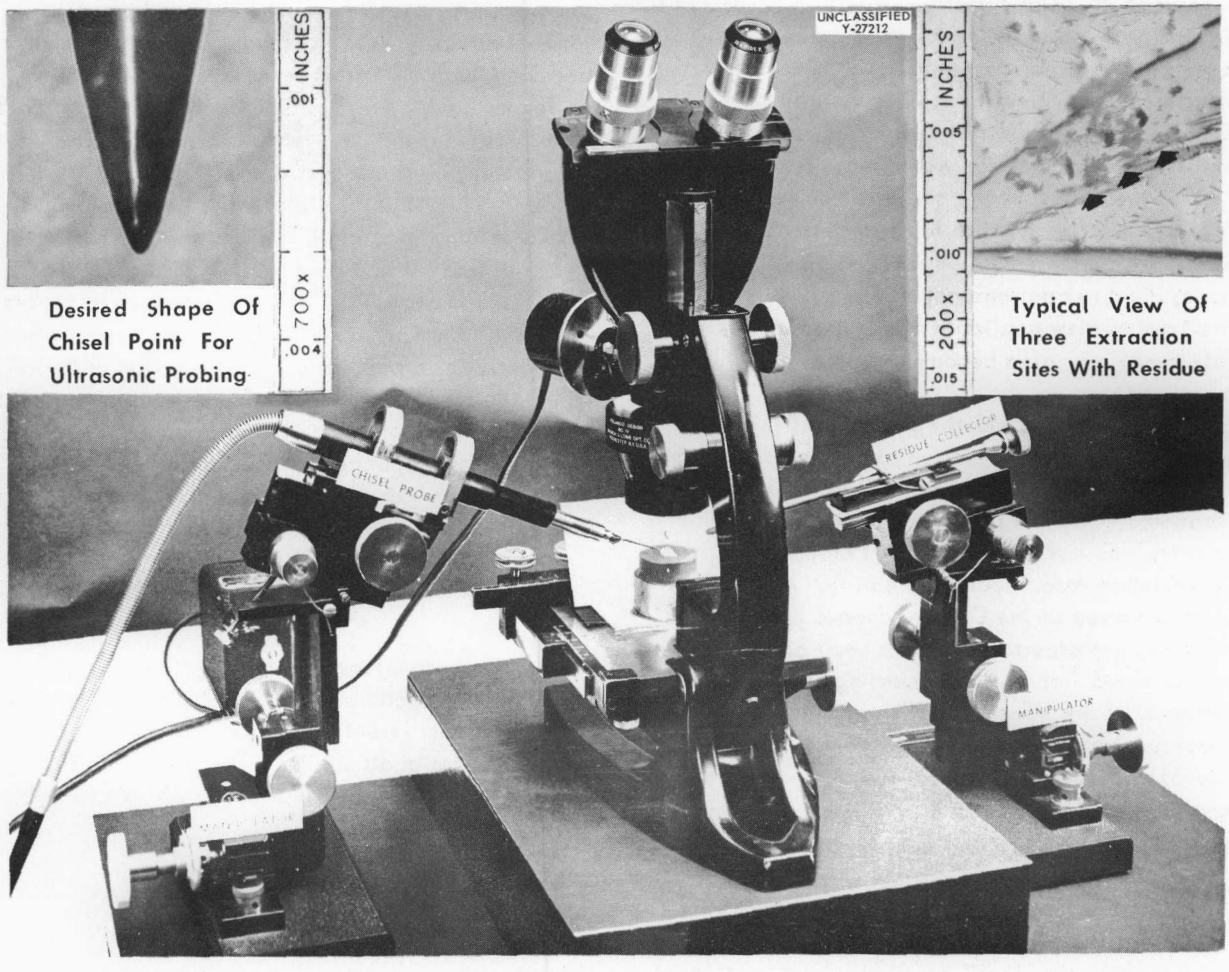

Fig. 142. Microscope Arrangement with the Transducer and Residue Collector in Their Normal Operating Position.

fact that it matches the resonant frequency of the laminated nickel transducer. When in operation, the pointed wire oscillates over a stroke length of 0.0014 in.

Extraction of the unidentified particles, or phases, is carried out in the following manner. Initially, of course, the entire chisel probe must be tuned properly. Thereafter, the point is applied to a particular sample area by moving the controls of a micromanipulator. Immediately upon nicking the metal surface, there is a spray of fine extraction residue around the area of penetration. The appearance of this residue after probe contact is shown in the right inset of Fig. 142. The photomicrograph shows an Al-Fe-Si master alloy in the as-polished state.

To collect the extraction residues, a thin glass fiber coated with petrolatum is maneuvered into the field with another manipulator. When the coated fiber touches the residue, sufficient amounts are dispersed in the petrolatum to allow subsequent transfer to an x-ray camera. Usually 8 to 10 μg of material is needed for a proper film exposure using copper $K\alpha$ radiation for 24 hr. The time required to extract and collect a mass is usually from 15 to 90 min, depending entirely upon the size and composition of the particles extracted.

As to the extent of the chisel's applicability, extractions to date seem to indicate that the practical size limit for the particles is 12 to 15 μ. On occasions, good extractions have been made at 6 μ, but this type of size application is a random operation. This range may also become practical with further improvements.

Perhaps the most startling feature of this apparatus is that no air oxidation of the sample has been experienced to date. In previous work[7] with an ultrasonic chisel, a ceramic transducer of higher velocity was used, and the chief problem was with air oxidation from localized heating. All oxide lines observed in the Debye-Scherrer patterns of extracted samples to date have been confirmed by manual extractions as representing proper constituents of the samples. This was true even in zirconium-base specimens. Another major advantage of this chisel is that no phase transformations from cold working the sample *in situ* have been detected.

Additional work with the chisel calls for the design and installation of an inert-atmosphere system and an improved mechanical stage. The protective atmosphere is needed since it will not always be feasible to determine the proper origin of oxide lines through delicate manual extractions. The stage is required to facilitate the micropositioning of the steel styli to the particular areas of interest.

For the problem in general, more work is scheduled soon for the development of an electrolytic extraction cell. The literature abounds with material on the anodic dissolution of metal samples, but there is a dire need for some better work with further refinements. Ultrasonics, for example, could be one real innovation.

Preparation of Metallographic Specimens by Vibratory Polishing

E. L. Long, Jr.

Work[8,9] on the preparation of metallographic specimens by vibratory polishing has been extended, and at present over 75% of the specimens are completed by this procedure. Five vibratory polishers have been arranged as shown in Fig. 143. The three shown at the left are used in sequence for regular polishing operations. They contain, respectively: (1) silk cloth and Linde A alumina, (2) nap cloth (Microcloth or Gammal) and Linde A alumina, and (3) nap cloth (Microcloth or Gammal) and Linde B alumina. The two assigned to special problems (and shown at the right) can be equipped with a silk or a nap cloth in combination with diamond abrasives and/or oil vehicles. Lucite covers protect all the polishers from air-borne contamination. The two special-problem polishers are equipped with exhaust ports for problems involving toxic materials.

Photomicrography in Color

W. H. Bridges

For the photomicrography of metallographic specimens which depend on color for their interpretation, only color film is satisfactory. There are two basic types of color photography. The first produces a positive, proper image on the film which can be

[7] G. L. Kehl, H. Steinmetz, and W. J. McGonnagle, *An Ultrasonic "Jackhammer" for Removal of Inclusions*, ANL-5545 (March 19, 1956).

[8] E. L. Long, Jr., *Met. Ann. Prog. Rep. Oct. 10, 1957*, ORNL-2422, p 165.

[9] E. L. Long, Jr., and R. J. Gray, *Preparation of Metallographic Specimens Through Vibratory Polishing*, ORNL-2494 (June 13, 1958).

Fig. 143. Vibratory Polishing Units for Metallography. The three units on the left are for regular polishing operations. The two units on the right are reserved for specimens requiring diamond abrasives, oil, or other uncommon techniques.

viewed by transmission or projection. The second results in a negative image with unreal colors. The negative is then printed, either on color printing paper or film, to restore the proper colors. When several copies of a picture are desired, the first type of film is relatively unsatisfactory, since the maintenance of proper color balance in copying is primarily dependent on the color temperature of the illumination, and multiple processing is necessary to produce prints. The second type is well suited to the production of copies. Once the proper filter sequence is determined, prints can be made at any subsequent time with uniform results. The techniques for handling both types of color have been studied, and procedures that will ensure consistent results in the laboratory have been established.

Hot- and Cold-Stage Microscopy

J. E. VanCleve, Jr. J. R. Riddle

The Unitron hot-stage microscope unit[10] has been assembled, and observations to determine the capabilities of the system have been made. Iron, steel, and aluminum have been used in the development of hot-stage techniques. Structures and structural changes of these materials have been observed and recorded at elevated temperatures. The microstructures have been recorded, using both still and motion-picture photography. These films were not suitable for publication because of such problems

[10] J. R. Riddle, *Met. Ann. Prog. Rep. Oct. 10, 1957*, ORNL-2422, p 178.

as the deposition of metal vapor on the viewing window and oxidation of the polished metal surface. Attempts to observe heated samples under various pressures of argon were made; however, thermal convection by the argon resulted in overheating of the O-ring seals. Work with the commercial unit has shown the need of several design changes. The alterations under consideration are: (1) removal of porous ceramics from the furnace chamber, (2) reduction of the hot-zone area by redesign of the furnace, (3) replacement of the heating method, and (4) enlargement of the vacuum port for faster pumping speed. Changes are presently being made in the furnace design but are yet to be evaluated.

A new specimen chamber has been added to the present equipment to permit the observation of materials at low temperatures. The specimen is held under vacuum for thermal insulation and is cooled by being in contact at one surface with a copper container which holds 18 in.^{3} of a liquid coolant such as liquid nitrogen, or dry ice and acetone. Preliminary work indicates that the unit operates satisfactorily.

Dilatometry

J. R. Riddle

Investigations. – Routine investigations were made on 2S aluminum, "A" nickel, Armco ingot iron, INOR-8, Zircaloy-2, Hastelloy B, and Hastelloy W. Examples of the results of this work are shown in Figs. 144 and 145. Figure 144 shows the linear expansion of INOR-8 as a function of temperature, while Fig. 145 gives the linear thermal coefficient of expansion of the alloy. Three samples of yttrium have been tested in the dilatometer; however, the chemical reactivity of this element has prevented the accumulation of accurate data. Yttrium readily oxidizes, and a eutectic reaction between nickel and yttrium results in failure of the thermocouple at the hot junction. There is also evidence that yttrium reacts with quartz, the container and push-rod material used in the dilatometer. Plans to circumvent these problems in future experiments are under consideration.

Several groups have requested thermal expansion data for use in the solution of special problems. These investigations have included the following:

1. The Fuel-Processing Group of HRP required the thermal expansion properties of two high-temperature alloys. This information was employed in calculating the stresses in bolts caused by the relative expansions of two plates and their retaining bolts in heating a receptacle from room temperature to operating temperature.

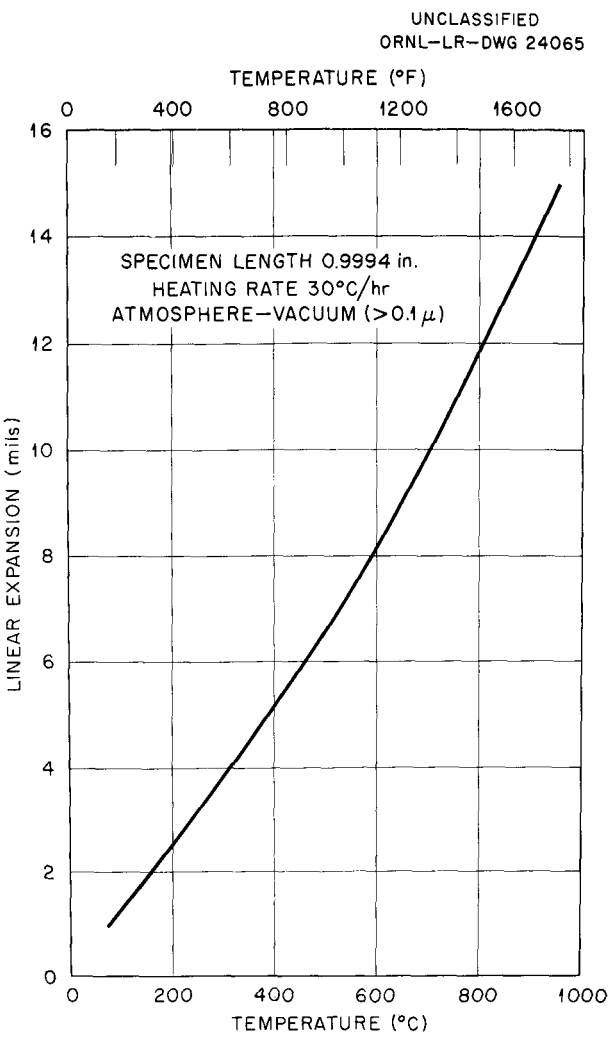

Fig. 144. Linear Thermal Expansion of INOR-8.

2. A titanium alloy exhibited abnormally low impact-strength values in the temperature range of 450°C. The thermal expansion characteristics of the alloy were studied in an attempt to determine a reason for this behavior. There were no anomalies in the thermal expansion curves over the temperature range in question.

3. The Fuel Element Development Group requested thermal expansion data on potential fuel element and cladding materials. The thermal expansion characteristics of 2S Al, 18% U–Al, and 48% U–3% Si–Al were determined. These curves are shown in Fig. 146.

4. The Solid State Division submitted a single-crystal copper-aluminum alloy for the determination of the relationship between thermal expansion characteristics and measurements of electrical resistivity as a function of temperature. Calculations of activation energies for lattice vacancies from thermal expansion and electrical resistivity curves were found to be in excellent agreement.

5. A type 347 stainless steel sample was cooled in liquid nitrogen to determine the dimensional changes associated with the martensite transformation. Cooling curves indicated that martensite forms in a series of steps, and each step resulted in an increase in volume. A quantitative measurement of the volume increase could not be determined; however, the information did support the belief that recent failures in this material were caused by this transformation.

6. The thermal expansion characteristics of uranium samples of various preferred orientations were determined for the Fundamental Metallurgy Group. The "loop" and growth characteristics of

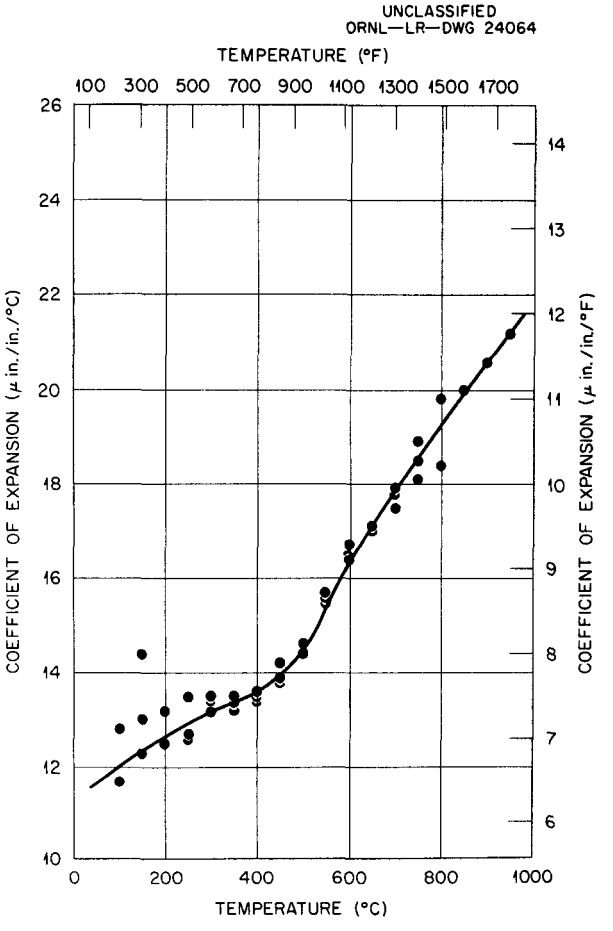

Fig. 145. Linear Thermal Coefficient of Expansion of INOR-8.

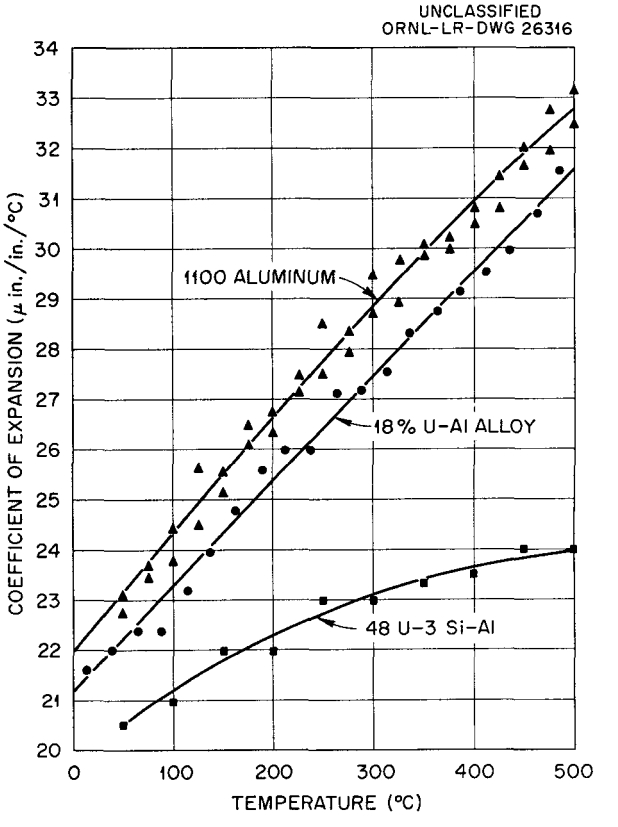

Fig. 146. Linear Thermal Coefficient of Expansion of Potential Fuel Element Material.

five samples have been recorded, and a study is under way to determine the relationship between these preferred orientations and their characteristic curves.

Refinements. – Due to a weakened response of the dilatometer to changes in the position of the microformer core, which is used to transmit the dilation of samples to an X-Y recorder, the dilatometer received a complete overhaul in the instrument repair shop. Worn parts were replaced and a capacitance was added to the circuit between the microformer and the chart drive motor. The capacitance was required to compensate for a phase shift which had reduced the power of the chart drive motor. Subsequent calibrations of the instrument revealed that this work had improved the instrument performance.

A primary concern in dilation measurements is that of instrument accuracy. Several methods of calibration have been investigated. The technique now involves the following steps:

1. A supermicrometer, adjustable to 0.0001 in., is used to move the microformer core through the microformer in steps of 0.001 in. If necessary, the dilation circuit is adjusted until the chart movement corresponds with the displacement of the micrometer.
2. A thermocouple circuit is checked on a potentiometer with an induced emf. When a second check is desired, Armco ingot iron is cycled through the α-γ transformation.
3. The final check is made by dilating a sample furnished by the National Bureau of Standards. The data obtained in this curve are compared with the values furnished by NBS. The results of a recent calibration curve are shown in Table 47.

Table 47. Dilatometer Calibration Data

Temperature (°C)	Linear Expansion (in./in.)		Deviation[c] (in./50°C)
	NBS[a]	Metallurgy[b]	
50–100	0.00083	0.00079	–0.00004
100–150	0.00085	0.00081	–0.00004
150–200	0.00087	0.00082	–0.00005
200–250	0.00088	0.00087	–0.00001
250–300	0.00090	0.00090	0
300–350	0.00092	0.00091	–0.00001
350–400	0.00094	0.00091	–0.00003
400–450	0.00095	0.00095	0
450–500	0.00097	0.00102	+0.00005
500–550	0.00099	0.00100	+0.00001
550–600	0.00101	0.00100	–0.00001
600–650	0.00103	0.00109	+0.00006
650–700	0.00104	0.00106	+0.00002
700–750	0.00106	0.00108	+0.00002
750–800	0.00108	0.00111	+0.00003
800–850	0.00110	0.00108	–0.00002
850–900	0.00111	0.00110	–0.00001

[a]The National Bureau of Standards data were obtained on a 12-in. rod.

[b]The Metallurgy dilatometer data were obtained on a 1-in. rod.

[c]Total deviation (50–900°C) = –0.00003 in./in.

PUBLICATIONS

Adamson, G. M., and W. J. Leonard, "Inert-Gas Tungsten-Arc Welding of Titanium for Nuclear and Chemical Industries," *Welding J. (N.Y.)* **37**, 673–82 (1958).

Allen, J. W., and R. B. Oliver, "Small Diameter Tubing by Eddy Current Methods," *Am. Soc. Testing Materials, Spec. Tech. Publ. No. 223*, 88 (1958).

Allen, J. W., R. A. Nance, and R. B. Oliver, "Eddy Current Measurement of Clad Thickness," *Am. Soc. Testing Materials, Spec. Tech. Publ. No. 223*, 201 (1958).

Betterton, J. O., Jr., and D. S. Easton, "The Silver-Zirconium System," *Trans. Am. Inst. Mining, Met. Petrol. Engrs.* **212**, 470–75 (1958).

Betterton, J. O., Jr., and W. M. Spicer, "The Antimony-Zirconium System in the Range 0–5 At. Pct Antimony," *Trans. Am. Inst. Mining, Met. Petrol. Engrs.* **212**, 456–57 (1958).

Betterton, J. O., Jr., and W. K. Noyce, "The Equilibrium Diagram of Indium-Zirconium in the Region 0–26 At. Pct In," *Trans Am. Inst. Mining, Met. Petrol. Engrs.* **212**, 340–42 (1958).

Betterton, J. O., Jr., and J. H. Frye, Jr., "Factors Affecting the Alpha-Beta Phase Boundaries of Zirconium and Titanium Alloys," *Acta Met.* **6**, 205–11 (1958).

Boston, C. R., and G. P. Smith, "Visible and Ultraviolet Absorption Spectra of $NiCl_2$ Dissolved in Fused LiCl-KCl Mixtures," *J. Phys. Chem.* **62**, 409 (1958).

Boyle, E. J., "Recrystallization of Thorium," *The Metal Thorium* (ed. by H. A. Wilhelm), p 217–24, American Society for Metals, Cleveland, 1958.

Cathcart, J. V., J. J. Campbell, and G. P. Smith, "The Microtopography of Oxide Films on Niobium," *J. Electrochem. Soc.* **105**, 442 (1958).

Cunningham, J. E., R. J. Beaver, W. C. Thurber, and R. C. Waugh, "Fuel Dispersions in Aluminum-Base Elements for Research Reactors," *Fuel Element Conference, Paris, Nov. 18–23, 1957*, TID-7546, p 269–97.

Cunningham, J. E., R. J. Beaver, and R. C. Waugh, "Fuel Dispersions in Stainless-Steel Components for Power Reactors," *Fuel Element Conference, Paris, Nov. 18–23, 1957*, TID-7546, p 243–68.

Cunningham, J. E., and R. E. Adams, "Techniques for Canning and Bonding Metallic Uranium with Aluminum," *Fuel Element Conference, Paris, Nov. 18–23, 1957*, TID-7546, p 102–19.

Cunningham, J. E., "Fabrication and Cladding of Thorium Metal," *The Metal Thorium* (ed. by H. A. Wilhelm), p 225–66, American Society for Metals, Cleveland, 1958.

Curtis, C. E., "Use of Ceramics in Power Reactors. Possibilities as Fuel Elements, Control Rods, Moderators, and Others," *Ceram. Ind.* **71**(1), 76–79 (1958).

Gray, R. J., W. C. Thurber, and C. K. H. DuBose, *Preparation and Metallography of Arc-Melted Uranium Carbides*, ORNL-2446 (Jan. 9, 1958).

Gray, R. J., W. C. Thurber, and C. K. H. DuBose, "Preparation of Arc-Melted Uranium Carbides," *Metal Progr.* **74**(1), p 65–70 (1958).

Hoffman, E. E., and W. D. Manly, *Lithium as a Nuclear Reactor Coolant*, ORNL-2538 (Aug. 8, 1958).

Jetter, L. K., C. J. McHargue, R. O. Williams, and H. L. Yakel, Jr., "Low-Temperature Camera for X-Ray Diffractometer," *Rev. Sci. Instr.* **28**, 1087–88 (1957).

Jetter, L. K., and C. J. McHargue, "Preferred Orientation in Thorium," *The Metal Thorium* (ed. by H. A. Wilhelm), p 161–85, American Society for Metals, Cleveland, 1958.

Kennedy, C. R., and D. A. Douglas, *Plastic Strain Absorption as a Criterion for High Temperature Design*, ORNL-2360 (May 2, 1958).

Long, E. L., Jr., and R. J. Gray, *Preparation of Metallographic Specimens Through Vibratory Polishing*, ORNL-2494 (June 26, 1958).

Manly, W. D., and J. H. Coobs, "New Methods of Powder Metallurgy," *Powder Metallurgy in Nuclear Engineering*, p 165–79, American Society for Metals, Cleveland, 1958.

Milko, J. A., R. E. Adams, and W. O. Harms, "Mechanical Properties of Thorium and High-Thorium Alloys," *The Metal Thorium* (ed. by H. A. Wilhelm), p 186–216, American Society for Metals, Cleveland, 1958.

Oliver, R. B., R. W. McClung, and J. K. White, "Production Inspection of Pipe and Tubing by the Immersed Ultrasonic Method," *Am. Inst. Mining, Met. Petrol. Engrs.* **223**, 62 (1958).

Oliver, R. B., G. M. Tolson, and A. Taboada, "The Use of Penetrants for Inspection of Small Diameter Tubing," *Am. Inst. Mining, Met. Petrol. Engrs.* **223**, 127 (1958).

Page, J. P., and J. H. Coobs, *Shield Plug Assembly for the ART Fuel Pumps*, ORNL-2353 (April 29, 1958).

Patriarca, P., G. M. Slaughter, and W. D. Manly, "Heat-Exchanger Fabrication," *Welding J. (N.Y.)* **36**, 1172–78 (1957).

Pigan, E. A., *An Investigation of the Hot Ductility of Inconel and Inconel X*, ORNL-2571 (Sept. 3, 1958).

Preston, O., C. F. Floe, and N. J. Grant, *Final Report – Development and Testing of Air–Melted Nickel–Molybdenum Alloys with Minor Alloying Additions*, ORNL-2520 (June 16, 1958).

Roche, T. K., *The Influence of Composition Upon the 1500°F Creep-Rupture Strength and Microstructure of Molybdenum–Chromium–Iron–Nickel Base Alloys*, ORNL-2524 (July 9, 1958).

Slaughter, G. M., P. Patriarca, and W. D. Manly, "Bonding of Cermet-Valve Components to Metals," *Welding J. (N.Y.)* **37**, 249–54 (1958).

Smith, G. P., M. E. Steidlitz, and E. E. Hoffman, "Corrosion and Metal Transport in Fused Sodium Hydroxide – Part 3 – Formation of Composite Scales on Inconel," *Corrosion* **14**(1), 65–70 (1958).

Thurber, W. C., J. H. Erwin, and R. J. Beaver, *The Application of a Nominal 48 wt % U–Al Alloy to Plate-Type Aluminum Research Reactor Fuel Elements*, ORNL-2351 (March 11, 1958).

Thurber, W. C., and R. J. Beaver, *Segregation in Uranium-Aluminum Alloys and Its Effect on the Fuel Loading of Aluminum-Base Fuel Elements*, ORNL-2476 (Sept. 5, 1958).

Trotter, L. R., and E. E. Hoffman, *Progress Report on Volatility Pilot Plant Corrosion Problems to April 21, 1957*, ORNL-2495 (Sept. 30, 1958).

White, G. D., and T. N. McVay, *Some Aspects of the Recovery of Lithium from Spondumene*, ORNL-2450 (April 3, 1958).

Yakel, H. L., Jr., "Thermocrystallography of Higher Hydrides of Titanium and Zirconium," *Acta Cryst.* **11**, 46–51 (1958).

PAPERS PRESENTED AT SCIENTIFIC AND TECHNICAL MEETINGS

Adams, R. E., and E. S. Bomar, "Carburization and Chemical Treatments for Recovery of Uranium from Stainless Steel Fuel Elements," American Nuclear Society, Los Angeles, June 2–5, 1958.

Adamson, G. M., and W. J. Leonard, "Inert Gas Tungsten Arc Welding of Titanium for the Nuclear and Chemical Industries," American Welding Society, St. Louis, April 14–18, 1958.

Adamson, G. M., J. O. Betterton, Jr., J. H. Frye, Jr., and M. L. Picklesimer, "Recent Advances in the Metallurgy of Zirconium and Titanium Alloys of Special Interest in Reactor Technology," 2nd International Conference on the Peaceful Uses of Atomic Energy, Geneva, Switzerland, September 1–13, 1958.

Allen, J. W., "Eddy-Current Testing in Practice," 2nd International Conference on Nondestructive Testing, Chicago, November 4–8, 1957.

Allen, J. W., "Eddy-Current Testing in Practice," 1st Southwestern Convention of the Society for Nondestructive Testing, Dallas, May 14, 1958.

Beaver, R. J., and J. E. Cunningham, "Recent Developments in Aluminum-Base Fuel Elements for Research Reactors," Fuel Element Conference, Gatlinburg, Tennessee, May 14–16, 1958.

Betterton, J. O., Jr., and D. S. Easton, "The Silver-Zirconium System," AIME Annual Meeting, New York, February 16–20, 1958.

Betterton, J. O., Jr., and W. K. Noyce, "The Equilibrium Diagram of Indium-Zirconium in the Region 0–26 at. % Indium," AIME Annual Meeting, New York, February 16–20, 1958.

Betterton, J. O., Jr., and W. M. Spicer, "The Antimony-Zirconium System in the Range 0–5 at. % Sb," AIME Annual Meeting, New York, February 16–20, 1958.

Bridges, W. H., and E. L. Long, Jr., "Recent Advances in the Electron Microscopy of Metals," 12th Annual AEC Metallography Conference, Mallinckrodt Chemical Works, St. Louis, February 26–27, 1958.

Bridges, W. H., and E. L. Long, Jr., "A Technique for the Easy Removal of 'Direct' Replicas for Electron Microscopy," American Society for Testing Materials, Boston, May 25, 1958.

Cathcart, J. V., "The Microtopography of Oxide Films Formed on Several Metals of Groups IV and V," Gordon Research Conference on Corrosion, New London, New Hampshire, July 14–18, 1958.

Coobs, J. H., "Solution of Unique Fabrication Problems by Powder Metallurgy," Southern Metals Conference, Gatlinburg, Tennessee, April 21, 1958.

Cunningham, J. E., and R. J. Beaver, "APPR-Fuel Technology," 2nd International Conference on the Peaceful Uses of Atomic Energy, Geneva, Switzerland, September 1–13, 1958.

Cunningham, J. E., R. J. Beaver, W. C. Thurber, and R. C. Waugh, "Fuel Dispersions in Aluminum-Base Elements for Research Reactors," Conference on Fuel Element Technology, Paris, France, November 18–22, 1957.

Cunningham, J. E., R. J. Beaver, and R. C. Waugh, "Fuel Dispersions in Stainless Steel Components for Power Reactors," Conference on Fuel Element Technology, Paris, France, November 18–22, 1957.

Cunningham, J. E., and R. E. Adams, "Alpha Canning of Uranium Slugs for the ORNL Graphite Reactor," Joint French-American Meeting on Graphite Reactors, Brookhaven National Laboratory, Upton, New York, November 14, 1957.

Cunningham, J. E., and R. E. Adams, "Techniques for Canning and Bonding Metallic Uranium with Aluminum," Conference on Fuel Element Technology, Paris, France, November 18–22, 1957.

Curtis, C. E., "Ceramics in Power Reactors," 24th Annual Meeting of the Ceramic Association of New York State, Alfred, New York, October 12, 1957.

Curtis, E. E., and A. G. Tharp, "Ceramic Properties of Europium Oxide," Refractions Division of American Ceramic Society, Annual Meeting, Pittsburgh, April 27–May 1, 1958 [*Am. Ceram. Soc. Bull.* **37**(4), 59 (1958)].

DeVan, J. H., and W. D. Manly, "Corrosion Properties of Fused Fluoride Salt Mixtures," American Nuclear Society, Los Angeles, June 2–5, 1958.

Gray, R. J., W. C. Thurber, and C. K. H. DuBose, "Preparation and Metallography of Uranium Carbides," 2nd World Metallurgical Congress, American Society for Metals, Chicago, November 7, 1958.

Harris, L. A., "A Preliminary Study of the Phase Equilibria Diagram ThO_2–SiO_2," Annual Meeting of the Basic Science Division, American Ceramic Society, Pittsburgh, April 27–May 1, 1958 [*Am. Ceram. Soc. Bull.* **37**(4), 59 (1958)].

Hoffman, E. E., "Lithium as a Nuclear Reactor Coolant," American Chemical Society, San Francisco, April 13–18, 1958.

Jansen, D. H., E. E. Hoffman, and D. M. Shepherd, "Lead-Lithium Alloy-Metallurgical Studies," American Nuclear Society, Los Angeles, June 2–5, 1958.

Kerr, J. M., "Preliminary Tests on Clay Sintered to Retain Reactor Wastes," Annual Meeting of the Basic Science Division, American Ceramic Society, Pittsburgh, April 27–May 1, 1958 [*Am. Ceram. Soc. Bull.* **37**(4), 59 (1958)].

Leitten, C. F., A. E. Richt, and R. J. Beaver, "Stainless Steel-Clad Dispersions of Boron in Iron for Pressurized-Water Reactors," American Nuclear Society, Los Angeles, June 2–5, 1958.

Long, E. L., and R. J. Gray, "Preparation of Metallographic Specimens Through Vibratory Polishing," 12th Annual AEC Metallography Conference, Mallinckrodt Chemical Works, St. Louis, February 26–27, 1958.

Long, E. L., and R. J. Gray, "Vibratory Polishing of Metallographic Specimens for Optical and and Electron Microscopy," American Society for Testing Metals, Boston, May 25, 1958.

Manly, W. D., J. H. DeVan, D. A. Douglas, Jr., J. H. Coobs, H. Inouye, T. K. Roche, and J. L. Scott, "Metallurgical Problems in Molten Fluoride Systems," 2nd International Conference on the Peaceful Uses of Atomic Energy, Geneva, Switzerland, September 1–13, 1958.

McHargue, C. J., "The Effect of Grain Orientation on the Properties and Fabrication of Metals," Southern Metals Conference, Gatlinburg, Tennessee, April 21, 1958.

Oliver, R. B., "Recommendation for Technical Development and Standardization," 2nd International Conference on Nondestructive Testing, Chicago, November 4–8, 1957; North Texas Section of Society for Nondestructive Testing, Dallas, December 17, 1957.

Patriarca, P., "A Survey of the Welding Program at the Oak Ridge National Laboratory," AEC Welding Committee, Chicago, November 7, 1957.

Patriarca, P., G. M. Slaughter, and H. R. Pufahl, "High-Temperature Brazing for Nuclear Reactors," German Welding Society, Mannheim, Germany, June 18–20, 1958.

Patriarca, P., and R. L. Heestand, "A Bulk UO_2–Stainless Steel Fuel Element for a Gas-Cooled Reactor," Fuel Element Conference, Gatlinburg, Tennessee, May 14–16, 1958.

Picklesimer, M. L., R. L. Rittenhouse, and G. M. Adamson, "Transformation Kinetics of Zr-15Nb-X Alloys," American Nuclear Society, New York, October 28–31, 1957 [*Am. Nuclear Soc. , 2nd Winter Meeting*, p 39, 1957].

Slaughter, G. M., P. Patriarca, and W. D. Manly, "Bonding of Cermet Valve Components to Metals," American Welding Society, St. Louis, April 14–18, 1958.

Smith, G. P., "Problems Imposed by Changes in Temperature and Solvent Composition on the Spectrophotometric Analysis of Fused Salts," 11th Annual Summer Symposium of Division of Analytical Chemistry of ACS, Schenectady, June 19–21, 1958.

Smith, G. P., and C. R. Boston, "Absorption Spectra of Fused Nitrates in the Near Ultraviolet I Pure Alkali Metal Nitrates," American Chemical Society, Chicago, September 7–12, 1958 [*Abstracts of the 134th Meeting of the American Chemical Society*, p 46s].

Swindeman, R. W., and D. A. Douglas, Jr., "Improvement of the High-Temperature-Strength Properties of Reactor Materials After Fabrication," American Nuclear Society, Los Angeles, June 2–5, 1958.

Taylor, A. J., and A. G. Tharp, "Large UO_2 Grains from Hydrothermally Grown UO_3 Hydrates," American Nuclear Society, New York, October 28–31, 1957.

Thurber, W. C., and R. J. Beaver, "The Application of Dispersions of Uranium Carbide in Aluminum for Plate-Type Fuel Elements Requiring High Uranium Concentrations," American Nuclear Society, Los Angeles, June 2–5, 1958.

Thurber, W. C., and R. J. Beaver, "Segregation in Uranium-Aluminum Alloys and Its Effect on the Fuel Loading of Aluminum-Base Fuel Elements," Reactor Fuel Measurement Techniques Symposium, East Lansing, June 18–20, 1958.

Van Cleve, J. E., and R. J. Gray, "Metallographic Examination of High-Temperature Radiators" (Secret), 12th Annual AEC Metallography Conference, Mallinckrodt Chemical Works, St. Louis, February 26–27, 1958.

METALLURGY DIVISION
AT
THE OAK RIDGE NATIONAL LABORATORY

OCTOBER 1, 1958

DIRECTOR — J. H. FRYE, JR.; B. F. BYRUM, SEC.

ASSOCIATE DIRECTOR — W. D. MANLY*; J. R. MORRISON,* SEC.

ASSISTANT DIRECTOR — J. E. CUNNINGHAM*; M. B. WHITE,* SEC.

ADMINISTRATIVE ASSISTANT
L. E. BANKER
M. J. BOLINGER, SEC.

FUNDAMENTAL METALLURGY

PHYSICOMETALLURGICAL RESEARCH
L. K. JETTER
B. L. BALLARD,* SEC.

STRUCTURE OF METALS
C. J. MCHARGUE
J. C. OGLE

THEORY OF ALLOYING
J. O. BETTERTON, JR.
G. D. KNEIP, JR.
D. S. EASTON
J. O. SCARBROUGH

X-RAY DIFFRACTION
H. L. YAKEL, JR.
B. L. BALLARD,* SEC.
O. B. CAVIN
R. M. STEELE

MICROSTRESSES IN CRYSTALS
B. S. BORIE
B. L. BALLARD,* SEC.
C. J. SPARKS, JR.
J. C. RICHTER

HIGH-TEMPERATURE REACTIONS
G. P. SMITH, JR.
M. A. BOND,* SEC.
C. R. BOSTON
J. J. MCBRIDE
G. F. PETERSEN
W. M. EWING

METAL SURFACE STUDIES
J. V. CATHCART
J. J. CAMPBELL
J. E. EPPERSON

FUNDAMENTAL CERAMICS STUDIES
G. W. CLARK

HRP METALLURGY

G. M. ADAMSON, JR.
F. LOVING,[1] SEC.

ENGINEERING
E. S. BOMAR, JR.
F. W. COOKE
W. J. LEONARD
J. J. PRISLINGER
C. H. WODTKE
C. M. SMITH, JR.
M. A. WHEELER

RESEARCH
M. L. PICKLESIMER
M. A. BOND,* SEC.
S. G. NELSON
P. L. RITTENHOUSE
R. L. STEPHENSON
P. J. JONES
G. C. NELSON
J. J. WOODHOUSE, JR.

DIVISION SERVICES
R. J. STEERE
R. B. PRATT[4]
M. E. BOTHWELL
K. P. BAYNE
C. E. DUNN

BUDGET ANALYST
R. G. CARDWELL, JR.

TIMEKEEPING
D. B. POE*

CONSULTANTS
N. J. GRANT, M.I.T.
J. L. GREGG, CORNELL UNIV.
W. O. HARMS, UNIV. OF TENN.
W. D. JORDAN, UNIV. OF ALA.
J. KORRINGA, OHIO STATE UNIV.
T. N. MCVAY, BUREAU OF MINES
E. F. NIPPES, R.P.I.
J. W. PRADOS, UNIV. OF TENN.
T. S. SHEVLIN, OHIO STATE UNIV.
E. E. STANSBURY, UNIV. OF TENN.

*MULTIPLE LISTING
[1]ON LOAN FROM REED
[2]ON LOAN FROM HRP METALLURGY
[3]TEMPORARY ASSIGNMENT
[4]ON LOAN FROM E&M DIVISION

REACTOR METALLURGY

W. D. MANLY*
J. R. MORRISON,* SEC.
R. M. EVANS

COORDINATORS

R. E. CLAUSING*	SHERWOOD
J. H. COOBS*	GCR
T. HIKIDO*	ANP
A. TABOADA	MSRP

METALLURGY REPORTS OFFICE
M. R. HILL
F. R. FINN
W. D. MASON
M. D. MONTGOMERY[3]
L. M. PYATT

DYNAMIC CORROSION AND INSPECTION
J. H. DEVAN
E. Q. TAYLOR, SEC.
R. C. SCHULZE
A. J. ROSENBERG
G. M. TOLSON
G. D. BRADY
E. J. LAWRENCE
M. A. REDDEN

NONDESTRUCTIVE TEST DEVELOPMENT
J. W. ALLEN
M. A. BOND,* SEC.
R. W. MCCLUNG
R. A. NANCE
E. A. REED
J. K. WHITE[2]
O. E. CONNER
R. A. CUNNINGHAM, JR.
W. J. MASON

GENERAL CORROSION
E. E. HOFFMAN
D. B. POE,* SEC.
W. H. COOK
J. R. DISTEFANO
D. H. JANSEN
J. L. GRIFFITH
J. W. HENDRICKS
R. E. POTTER
L. R. TROTTER

MECHANICAL PROPERTIES
D. A. DOUGLAS, JR.
J. R. MORRISON,* SEC.
C. W. DOLLINS
C. R. KENNEDY
H. E. MCCOY, JR.
R. W. SWINDEMAN
J. W. WOODS
F. L. BEELER
K. W. BOLING
E. BOLLING
J. T. EAST
J. D. HUDSON
V. G. LANE
B. MCNABB, JR.
E. B. PATTON, JR.
C. K. THOMAS
C. W. WALKER

FABRICATION
J. H. COOBS*
B. L. BALLARD,* SEC.
D. O. HOBSON
H. INOUYE
T. K. ROCHE
W. J. WERNER
J. W. BARNETT
W. R. JOHNSON
J. F. NEWSOME

WELDING AND BRAZING
P. PATRIARCA
M. A. BOND,* SEC.
R. E. CLAUSING*
R. L. HEESTAND
R. G. GILLILAND
E. A. FRANCO-FERREIRA
G. M. SLAUGHTER
J. W. TACKETT
B. MCDOWELL
R. G. SHOOSTER
L. C. WILLIAMS

CHEM. TECH. COORDINATOR
A. E. GOLDMAN
A. P. LITMAN

LIQUID-METAL RESEARCH
J. L. SCOTT
B. L. BALLARD,* SEC.
D. F. TONER

METAL PROCESS PILOT PLANT
T. HIKIDO*
G. E. ANGEL
J. E. POPE
D. E. ROSSON

APPLIED METALLURGY

J. E. CUNNINGHAM*
M. B. WHITE,* SEC.

LONG-RANGE PLANNING
J. P. HAMMOND
M. B. WHITE,* SEC.

PROCESS METALLURGY
R. J. BEAVER
M. B. WHITE,* SEC.
L. L. HALL

METAL FABRICATION
J. H. ERWIN*
G. D. GOLDSTON
T. W. COFFEY

FUEL ELEMENT FABRICATION
J. H. ERWIN*
G. H. CALLAWAY
N. H. FLICKINGER
J. N. HIX
W. W. PROAPS
H. J. WALLACE

ALLOY PREPARATION
D. T. BOURGETTE
J. B. FLYNN
H. W. HOOVER
L. QUEENER

FUEL ELEMENT DEVELOPMENT
C. F. LEITTEN, JR.*
W. J. KUCERA
J. W. GEER
C. HAMBY, JR.

ARMY PACKAGE POWER REACTOR PROJECT
C. F. LEITTEN, JR.*
J. H. CHERUBINI
E. R. TURNBILL

MARITIME SHIP REACTOR PROJECT
W. C. THURBER
J. T. LAMARTINE
C. W. HOLLAND

ADVANCED ENGINEERING DEVELOPMENT OF REACTOR MATERIALS
R. C. WAUGH
D. B. POE,* SEC.
R. E. ADAMS
J. I. FEDERER
T. S. LUNDY
R. A. PADGETT, JR.
J. H. TERRY

CERAMICS RESEARCH
L. M. DONEY
A. S. HOBBS, SEC.

GENERAL CERAMICS
C. E. CURTIS
L. A. HARRIS
M. P. HAYDON
A. G. THARP

FUEL ELEMENT DEVELOPMENT
F. L. CARLSEN, JR.
J. M. KERR

ANP MATERIALS
R. L. HAMNER
R. A. POTTER
W. M. PARKS

GCR CERAMICS
S. D. FULKERSON
R. E. MEADOWS
A. J. TAYLOR
J. A. GRIFFIN
F. P. JEFFERS

MSR CERAMICS
G. D. WHITE

METALLOGRAPHY
R. J. GRAY
W. J. SHOCKLEY
R. S. CROUSE*
E. L. LONG, JR.
W. H. BRIDGES
W. E. DENNY
J. C. GOWER
E. P. GRIGGS
J. T. HOUSTON
R. S. CROUSE*
B. F. DAY
L. G. SHRADER
C. E. ZACHARY
C. HAYS
C. K. H. DUBOSE
E. H. LEE
C. D. MATHES
T. M. KEGLEY, JR.
E. R. BOYD
R. L. FITZGERALD
T. J. HENSON
J. R. RIDDLE
M. D. ALLEN
W. H. FARMER
B. J. REECE
J. E. VANCLEVE, JR.
L. A. AMBURN, JR.
N. M. ATCHLEY
R. A. BOWMAN
B. C. LESLIE

INTERNAL DISTRIBUTION

1. G. M. Adamson, Jr.
2. S. E. Beall
3. R. J. Beaver
4. D. S. Billington
5. F. F. Blankenship
6. E. P. Blizard
7. E. G. Bohlmann
8. E. S. Bomar
9. R. B. Briggs
10. F. R. Bruce
11. J. V. Cathcart
12. C. E. Center (K-25)
13. R. A. Charpie
14. R. D. Cheverton
15. R. E. Clausing
16. J. H. Coobs
17. E. L. Compere
18. F. L. Culler
19. J. S. Culver
20. J. E. Cunningham
21. J. H. DeVan
22. R. R. Dickison
23. L. M. Doney
24. D. A. Douglas, Jr.
25. W. K. Eister
26. L. B. Emlet (K-25)
27. D. E. Ferguson
28. E. Franco-Ferreria
29. J. H. Frye, Jr.
30. C. H. Gabbard
31. W. R. Gall
32. R. J. Gray
33. J. C. Griess
34. W. R. Grimes
35. E. Guth
36. J. P. Hammond
37. P. H. Harley
38. C. S. Harrill
39. P. N. Haubenreich
40. R. L. Heestand
41. T. Hikido
42. M. R. Hill
43. E. E. Hoffman
44. A. Hollaender
45. H. Inouye
46. G. H. Jenks
47. L. K. Jetter
48. W. H. Jordan
49. P. R. Kasten
50. T. M. Kegley, Jr.
51. R. B. Korsmeyer
52. C. F. Leitten
53. W. J. Leonard
54. R. E. Leuze
55. R. B. Lindauer
56. R. S. Livingston
57. M. I. Lundin
58. R. N. Lyon
59. H. G. MacPherson
60. F. C. Maienschein
61. W. D. Manly
62. J. P. McBride
63. C. J. McHargue
64. R. A. McNees
65. R. P. Milford
66. A. J. Miller
67. E. C. Miller
68. K. Z. Morgan
69. J. P. Murray (Y-12)
70. M. L. Nelson
71. E. O. Nurmi
72. R. B. Oliver
73. L. F. Parsly
74. P. Patriarca
75. A. M. Perry
76. M. L. Picklesimer
77. J. J. Prislinger
78. P. M. Reyling
79. A. E. Richt
80. P. L. Rittenhouse
81. R. C. Robertson
82. M. T. Robinson
83. T. K. Roche
84. A. M. Rom
85. H. C. Savage
86. H. W. Savage
87. H. E. Seagren
88. C. H. Secoy
89. C. L. Segaser
90. E. D. Shipley
91. A. Simon
92. O. Sisman

93. M. J. Skinner
94. C. O. Smith
95. G. P. Smith, Jr.
96. A. H. Snell
97. I. Spiewak
98. C. D. Susano
99. R. L. Stephenson
100. J. A. Swartout
101. A. Taboada
102. D. G. Thomas
103. D. S. Toomb
104. W. E. Unger
105. R. VanWinkle
106. R. C. Waugh
107. M. S. Wechsler
108. A. M. Weinberg
109. J. C. White
110. J. K. White
111. G. C. Williams
112. J. C. Wilson
113. C. E. Winters
114. H. L. Yakel, Jr.
115. F. C. Zapp
116. J. H. Koenig (consultant)
117. H. Leidheiser, Jr. (consultant)
118. C. S. Smith (consultant)
119. H. A. Wilhelm (consultant)
120. E. P. Wigner (consultant)
121. Biology Library
122. Health Physics Library
123. Metallurgy Library
124-126. Central Research Library
127. Reactor Experimental Engineering Library
128-142. Laboratory Records Department
143. Laboratory Records ORNL R.C.
144. ORNL – Y-12 Technical Library, Document Reference Section

EXTERNAL DISTRIBUTION

145-148. Air Force Ballistic Missile Division
149. AFPR, Boeing, Seattle
150. AFPR, Boeing, Wichita
151. AFPR, Douglas, Long Beach
152-154. AFPR, Douglas, Santa Monica
155-156. AFPR, Lockheed, Marietta
157. AFPR, North American, Canoga Park
158. AFPR, North American, Downey
159-160. Air Force Special Weapons Center
161. Air Materiel Command
162-163. Air Research and Development Command (RDZN)
164. Air Technical Intelligence Center
165-167. ANP Project Office, Convair, Fort Worth
168. Albuquerque Operations Office
169. Argonne National Laboratory
170. Armed Forces Special Weapons Project, Sandia
171. Armed Forces Special Weapons Project, Washington
172-173. Army Ballistic Missile Agency
174. Army Rocket and Guided Missile Agency
175. Assistant Secretary of the Air Force, R&D
176-181. Atomic Energy Commission, Washington
182. Atomics International
183. Battelle Memorial Institute
184-186. Bettis Plant (WAPD)
187. Brookhaven National Laboratory
188. Bureau of Aeronautics
189. Bureau of Aeronautics General Representative
190. BAR, Aerojet-General, Azusa
191. BAR, Chance Vought, Dallas

192. BAR, Convair, San Diego
193. BAR, Grumman Aircraft, Bethpage
194. BAR, Martin, Baltimore
195. Bureau of Yards and Docks
196-197. Chicago Operations Office
198. Chicago Patent Group
199. Curtiss-Wright Corporation
200. Curtiss-Wright, Quehanna
201. Director of Naval Intelligence
202. duPont Company, Aiken
203. Engineer Research and Development Laboratories
204-211. General Electric Company (ANPD)
212-213. General Electric Company, Richland
214. GE Company, San Jose [AT(30-3)-502]
215. General Nuclear Engineering Corporation
216. Hartford Aircraft Reactors Area Office
217. Idaho Test Division (LAROO)
218-219. Knolls Atomic Power Laboratory
220. Lockland Aircraft Reactors Operations Office
221. Los Alamos Scientific Laboratory
222. Marquardt Aircraft Company
223. Martin Company
224. National Advisory Committee for Aeronautics, Cleveland
225. National Advisory Committee for Aeronautics, Washington
226. National Bureau of Standards
227. Naval Air Development Center
228. Naval Air Material Center
229. Naval Air Turbine Test Station
230. Naval Research Laboratory
231. New York Operations Office
232. Nuclear Development Corporation of America
233. Nuclear Metals, Inc.
234. Oak Ridge Operations Office
235. Office of Naval Research
236. Office of the Chief of Naval Operations
237. Patent Branch, Washington
238-239. Phillips Petroleum Company (NRTS)
240-243. Pratt and Whitney Aircraft Division
244. San Francisco Operations Office
245. Sandia Corporation
246-247. School of Aviation Medicine
248. Sylvania-Corning Nuclear Corporation
249. Technical Research Group
250. USAF Headquarters
251. USAF Project RAND
252. U. S. Naval Radiological Defense Laboratory
253-254. University of California Radiation Laboratory, Livermore
255-266. Wright Air Development Center
267-291. Technical Information Service Extension
292. Division of Research and Development, AEC, ORO

[redacted]

Reports previously issued in this series are as follows:

ORNL-28	Period Ending March 1, 1948
ORNL-69	Period Ending May 31, 1948
ORNL-407	Period Ending July 31, 1949
ORNL-511	Period Ending October 31, 1949
ORNL-583	Period Ending January 31, 1950
ORNL-754	Period Ending April 30, 1950
ORNL-827	Period Ending July 31, 1950
ORNL-910	Period Ending October 31, 1950
ORNL-987	Period Ending January 31, 1951
ORNL-1033	Period Ending April 30, 1951
ORNL-1108	Period Ending July 31, 1951
ORNL-1161	Period Ending October 31, 1951
ORNL-1267	Period Ending January 31, 1952
ORNL-1302	Period Ending April 30, 1952
ORNL-1366	Period Ending July 31, 1952
ORNL-1437	Period Ending October 31, 1952
ORNL-1503	Period Ending January 31, 1953
ORNL-1551	Period Ending April 10, 1953
ORNL-1625	Period Ending October 10, 1953
ORNL-1727	Period Ending April 10, 1954
ORNL-1875	Period Ending October 10, 1954
ORNL-1911	Period Ending April 10, 1955
ORNL-1988	Period Ending October 10, 1955
ORNL-2080	Period Ending April 10, 1956
ORNL-2217	Period Ending October 10, 1956
ORNL-2422	Period Ending October 10, 1957

[redacted]